ATLAS OF CARDIAC MR IMAGING WITH ANATOMICAL CORRELATIONS

SERIES IN RADIOLOGY

VOLUME 22

Atlas of Cardiac MR Imaging

with Anatomical Correlations

CHRISTOPHE DEPRÉ / JACQUES A. MELIN
WILLIAM WIJNS / ROGER DEMEURE / FRANK HAMMER
JACQUES PRINGOT

Departments of Internal Medicine and Radiology
University of Louvain Medical School, Brussels, Belgium

Foreword by
ALEXANDER R. MARGULIS

Springer-Science+Business Media, B.V.

Library of Congress Cataloging-in-Publication Data

Atlas of cardiac MR imaging with anatomical correlations / Christophe Depré ... [et al.]
p. cm. -- (Series in radiology : 22)
Includes bibliographical references.
Includes index.
ISBN 978-94-010-5685-4 ISBN 978-94-011-3784-3 (eBook)
DOI 10.1007/978-94-011-3784-3
1. Heart--Magnetic resonance imaging--Atlases. 2. Heart--Anatomy--Atlases. 3. Cardiopulmonary system --Magnetic resonance imaging--Atlases. 4. Cardiopulmonary system--Anatomy--Atlases. I. Depré, Christophe. II. Series.
[DNLM: 1. Cardiovascular System--anatomy & histology--atlases. 2. Magnetic Resonance Imaging--atlases. W1 SE719 v.22 / WG 17 A8842]
QM181.A67 1991
616.1'207'548--dc20
DNLM/DLC
for Library of Congress 90-13436

ISBN 978-94-010-5685-4

Printed on acid-free paper

Foreword

Magnetic resonance imaging became clinical in 1981 and since that time, has spread in the United States, Europe and Japan like wild fire. The tremendous advantages of the method consisting of safety, superb soft tissue contrast resolution, the ability to study flow, the ability to image in any plane or acquire data in 3D and an almost infinite array of sequences capable of distinguishing between disease and normal tissue, normal and abnormal blood flow make it incomparable for the diagnosis and study of multiple diseases and is particularly valuable in studying the heart and major vessels.

The authors of this book have understood that the secret of success of MR imaging in the study of the heart is to combine the knowledge of anatomy of the heart, the coronary vessels, the pericardium and large vessels with the intricacies of MR imaging. This is why they go deeply into the basic principles of NMR, starting from the essentials and going then into detailed techniques of acquiring images from traditional spin echo to gradient echo and ultra fast imaging approaches, such as the multi shot and EPI. The flow phenomena are also discussed in detail from flow and magnetic field gradients diastolic pseudogating.

The discussion of image quality and possible artifacts is similarly dealt with, conveying to the reader an understanding of how images can be improved and what the causes can be for their degradation. The longest section of this book, however, consists of 122 pages of pure anatomy of the heart by magnetic resonance imaging, from transfers to sagittal to coronal and ROA and LOA equivalent slices. Such detailed treatment will make the reader quite familar with the MR imaging appearances of the heart in all of the conventionally accepted views. In the last chapter, dynamic and functional studies are presented in multiple views as well as at end systole and end diastole.

The reader will find the bibliography arranged very methodically along the various, multiple subjects discussed. The introductory bibliography supplying text book chapters, review articles and technical considerations should be of equally great value to the reader.

Alexander R. Margulis, MD, Dhc Louvain

Contents

Contents

Preface

MR imaging of the heart represents an important advance in clinical cardiology. First, the high resolution of this technique provides a detailed view of cardiac morphology. This anatomical precision is helpful when various diseases are suspected as, e.g. the decrease of wall thickening, pericardial diseases, the diagnosis of congenital abnormalities, thoracic aorta diseases and coronary heart disease. Secondly, the acquisition of several images during the cardiac cycle with cine-MR offers a quite unique model of functional study of the heart.

This book shows that parallelism between the high quality MR images and the pages of an anatomy book is striking. Our aim was to describe the different structures of the heart and the large vessels seen with MR images of normal subjects and to compare them with anatomical slices. This anatomical comparison of normal structures is necessary to read correctly the patients MR images. The structure of this atlas allows to see at the same time the anatomical picture and the corresponding MR slice. More than sixty MR slices are displayed in five different planes of section actually used in MR imaging. The series of tomographic slices clearly delineate cardiac anatomy and the relationships of the heart with surrounding structures. In a second part, about twenty images of cine-MR offer a good comprehension of cardiac functions and dynamics.

Preceding this MR study, the introduction offers a review of normal cardiac anatomy and the principles of cardiac NMR, to assure a better comprehension of the following images.

All the MR images shown in this book were obtained from routine clinical practice (without trying to maximize the resolution of the technique), with a 1.5 Tesla Philips System and ECG-gating. The main structures seen on each image are reproduced on schematic drawings in order to allow a correct interpretation. The graduation seen on most images is in centimeters.

We hope that this book of normal cardiac MR imaging will help the physician in interpreting the different thoracic structures and various pathological findings. We really think that it will be useful and especially for cardiologists, cardiac surgeons, radiologists and students interested by the anatomy of the living heart.

List of authors

Christophe Depré
University of Louvain Medical School
Division of Cardiology
Department of Internal Medicine
54 avenue Hippocrate
1200 Brussels, Belgium

Roger Demeure
University of Louvain Medical School
Department of Radiology and Medical Imaging
10 avenue Hippocrate
1200 Brussels, Belgium

Frank Hammer
University of Louvain Medical School
Department of Radiology and Medical Imaging
10 avenue Hippocrate
1200 Brussels, Belgium

Jacques Melin
University of Louvain Medical School
Division of Nuclear Medicine
Department of Internal Medicine
54 avenue Hippocrate
1200 Brussels, Belgium

Jacques Pringot
University of Louvain Medical School
Department of Radiology and Medical Imaging
10 avenue Hippocrate
1200 Brussels, Belgium

William Wijns
University of Louvain Medical School
Division of Cardiology
Department of Internal Medicine
54 avenue Hippocrate
1200 Brussels, Belgium

Legends with corresponding numbers

1. Left ventricular cavity
2. Myocardium
3. Ascending aorta
4. Aortic arch
5. Descending aorta
6. Coronary sinus
7. Inferior vena cava
8. Superior vena cava
9. Right atrium
10. Left atrium
11. Right ventricular cavity
12. Right ventricular outflow region
13. Left ventricular outflow region
14. Lung
15. Left lung
16. Right lung
17. Main pulmonary artery
18. Left pulmonary artery
19. Right pulmonary artery
20. Ventricular septum
21. Papillary muscle
22. Pericardium
23. Right atrial appendage
24. Left atrial appendage
25. Diaphragm
26. Trachea
27. Thoracic vertebra
28. Left brachiocephalic vein
29. Left common carotid artery
30. Left subclavian artery
31. Aortic infundibulum
32. Atrial septum
33. Left main bronchus
34. Right inferior thyroid vein
35. Larynx
36. Pulmonary infundibulum
37. Left subclavian vein
38. Internal mammary vein
39. Right internal jugular vein
40. Spinal cord
41. Left internal jugular vein
42. Latissimus dorsi muscle
43. Pectoralis major muscle
44. Carina
45. Trapezius muscle
46. Left inferior pulmonary vein
47. Left superior pulmonary vein
48. Brachial plexus
49. Rachis
50. Fourth rib
51. Splenius muscle
52. Erector spinae muscle
53. Sternocleidomastoid muscle
54. Rhomboidus muscle
55. Sternum
56. Manubrium
57. Semispinalis capitis muscle
58. Laryngeal musculature
59. Genioglossus muscle
60. Left lung hilum
61. Longissimus thoracis muscle
62. Middle cardiac vein
63. Liver
64. Azygos vein
65. Intercostal muscles
66. Hemiazygos vein
67. Posterior intercostal vein
68. Dorsal vertebra
69. Rib
70. Spinous process
71. Serratus anterior muscle
72. Esophagus
73. Pleural cavity
74. Right coronary artery
75. Tricuspid valve
76. Right inferior pulmonary vein
77. Internal mammary artery
78. Pectoralis minor muscle
79. Left coronary artery
80. Aortic valve
81. Teres major muscle
82. Circumflex artery
83. Scapula
84. Transversospinal muscle
85. Left upper lobe bronchus
86. Pulmonary valve
87. Right superior pulmonary vein
88. Right lower lobe bronchus
89. Lymph node
90. Subscapularis muscle
91. Segmental bronchus
92. Mitral valve
93. Infraspinatus muscle
94. Right main bronchus
95. Tracheo-bronchial lymph node
96. Pulmonary lymph node
97. Omohyoid muscle
98. Superficial cervical vein
99. Mediastinum
100. Supraspinatus muscle
101. Levator scapulae muscle
102. First rib
103. Subclavius muscle
104. Clavicle
105. Transverse process
106. Sternohyoid muscle
107. Thyroid gland
108. Brachiocephalic trunk
109. Humerus
110. Axillary artery
111. Coracobrachial muscle
112. Vertebral artery
113. Right subclavian artery
114. Right brachiocephalic vein
115. Right subclavian vein
116. Deltoid muscle
117. Right common carotid artery
118. Thebesius valve
119. External jugular vein
120. Pericardosternal ligament
121. Lumbar vertebra
122. Transverse sinus of the pericardium
123. Axillary vein
124. Jugular arch
125. Cervical vertebra

PART ONE

Introduction

CHAPTER ONE

Anatomy of the heart and of the large vessels

Introduction

The heart is situated in the middle of the mediastinum. It has a conical form with the base facing backwards and to the right and with the apex directed downwards, forwards and to the left.

The heart is divided into four chambers, two atria and two ventricles. It is also divided into right and left halves by a longitudinal septum.

Each atrium has a small, conical pouch, called the auricle (or atrial appendage).

The external surface of the heart is covered by a fibroserous sac, the pericardium, which has two layers, visceral and parietal (Fig. I–1).

Internal anatomy

A. *The ventricles*

The two ventricles are situated in front of the atria and are separated from each other by the interventricular (or ventricular) septum. Each ventricle receives blood from the corresponding atrium through an atrioventricular orifice with a valve. The valve consists of cusps, two for the left valve and three for the right valve.

The left atrioventricular valve is called mitral because of its similarity to the bishop's mitre; this consists of two unequal triangular cusps. The right atrioventricular valve, also called the tricuspid valve consists of three cusps. The ventricular surfaces of these valves are attached to the chordae tendinae.

Besides the atrioventricular orifice, the ventricles also have arterial orifices, the pulmonary orifice for the right ventricle and the aortic orifice for the left ventricle. These orifices are guarded by two valves called sigmoid valves. These valves consist of three semilunar cusps, which are attached by their convex margins to the wall of the artery at its junction with the ventricle.

The mechanics of the atrioventricular and arterial valves are different because of their different anatomical features. The atrioventricular valves have the chordae tendinae which prevent the protrusion of these valves into the atria during ventricular systole. With the arterial valves, the blood runs back during protodiastole on to the concave surface of the cusps; the stretching of the three cusps makes them adherent and therefore makes the valve continent.

The ventricular wall projects into the cavity by means of papillary muscles. Their apices are continuous with the chordae tendinae. During ventricular systole, the papillary muscles contract with the rest of the ventricular wall and the chordae tendinae are stretched. This stretching of the chordae tendinae prevents the protrusion of the valves into the atria because of the increase of the ventricular systolic pressure (Fig. I–2).

Any abnormality of the papillary muscle or of the chordae tendinae will thus indirectly cause a dysfunction of the atrioventricular valve. This kind of problem can be seen during acute myocardial infarction, bacterial endocarditis or valvular mitral prolapse. There are two papillary muscles in the left ventricle and three papillary muscles in the right ventricle.

The superior part of the ventricles forms a conical pouch, called the infundibulum, which leads upwards to the arterial orifice.

There are two contiguous regions in the ventricular chamber. The first and inflowing part receives blood from the atrium. The second region is known as the outflowing part. The two parts are nearly perpendicular in the right ventricle and are parallel in the left ventricle.

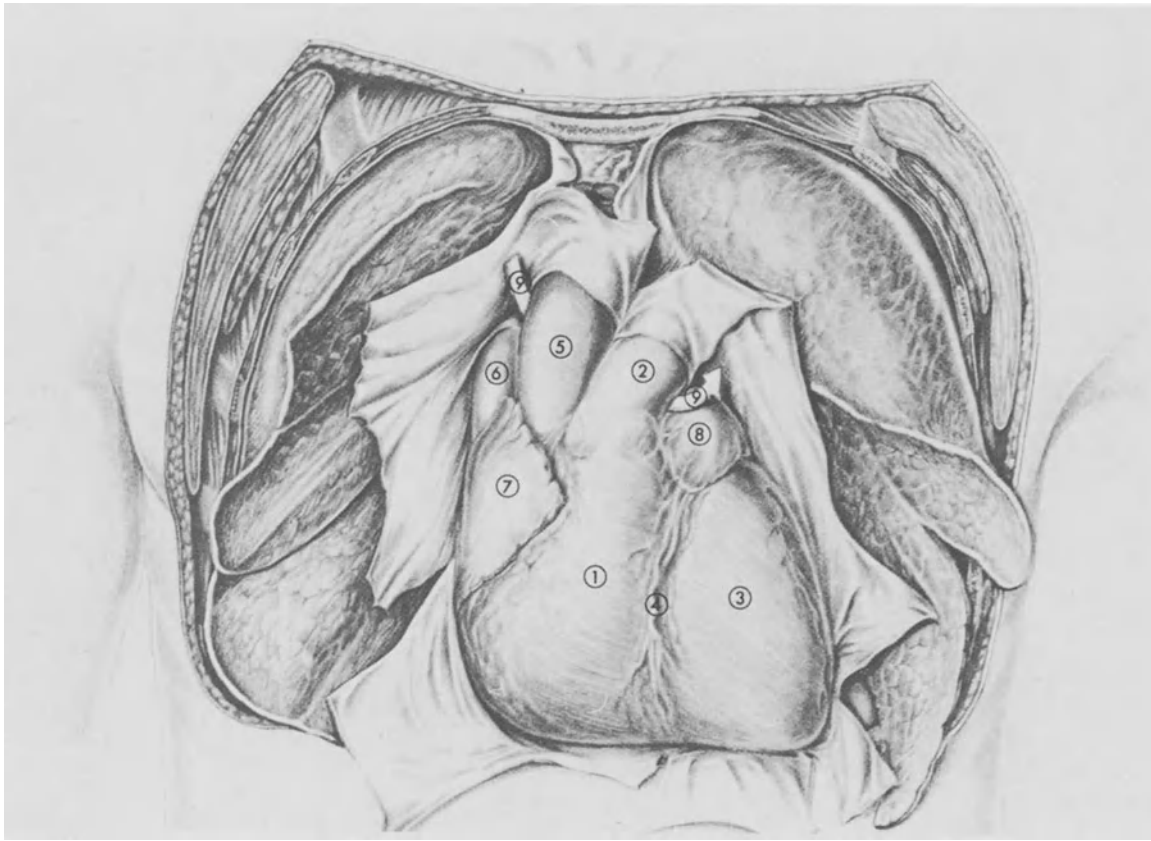

Figure I–1. Situation of the heart in the thoracic cavity. Anterior view.
① Right ventricle; ② Main pulmonary artery; ③ Left ventricle; ④ Interventricular groove; ⑤ Ascending aorta; ⑥ Superior vena cava; ⑦ Right atrial appendage; ⑧ Left atrial appendage; ⑨ Transverse sinus of the pericardium.

B. *The atria*

The atrial cavities are situated behind the ventricles. They are smaller and thinner than the ventricles.

Blood flows into the right atrium from above via the superior vena cava and inferiorly from the coronary sinus and the inferior vena cava. It opens into the right ventricle by the right atrioventricular valve, called tricuspid valve.

The inferior vena cava has a valve – known as the Eustachius valve – situated at the point where it opens into the right atrium. At the opening of the coronary sinus into the right atrium is to be found the Thebesius valve, which prevents the blood from flowing backwards into the coronary venous circulation during the auricular systole.

The superior vena cava, however, does not have this kind of valve and it opens directly into the right atrium. This anatomical feature explains the presence of a jugular pulse in right cardiac failure.

On the anterior wall of the right atrium, close to the auriculoventricular valve, the atrium continues into a narrow pouch called right auricle.

The left atrium presents on its posterior wall the opening of the four pulmonary veins. Usually, these veins flow separately into the cavity.

On the anterior wall of the left atrium, we find the left auriculoventricular valve, or mitral valve. As with right atrium, this anterior wall also presents a small diverticle called left auricle (Fig. I–3).

C. *The coronary vessels*

There are two main arteries supplying the heart, the

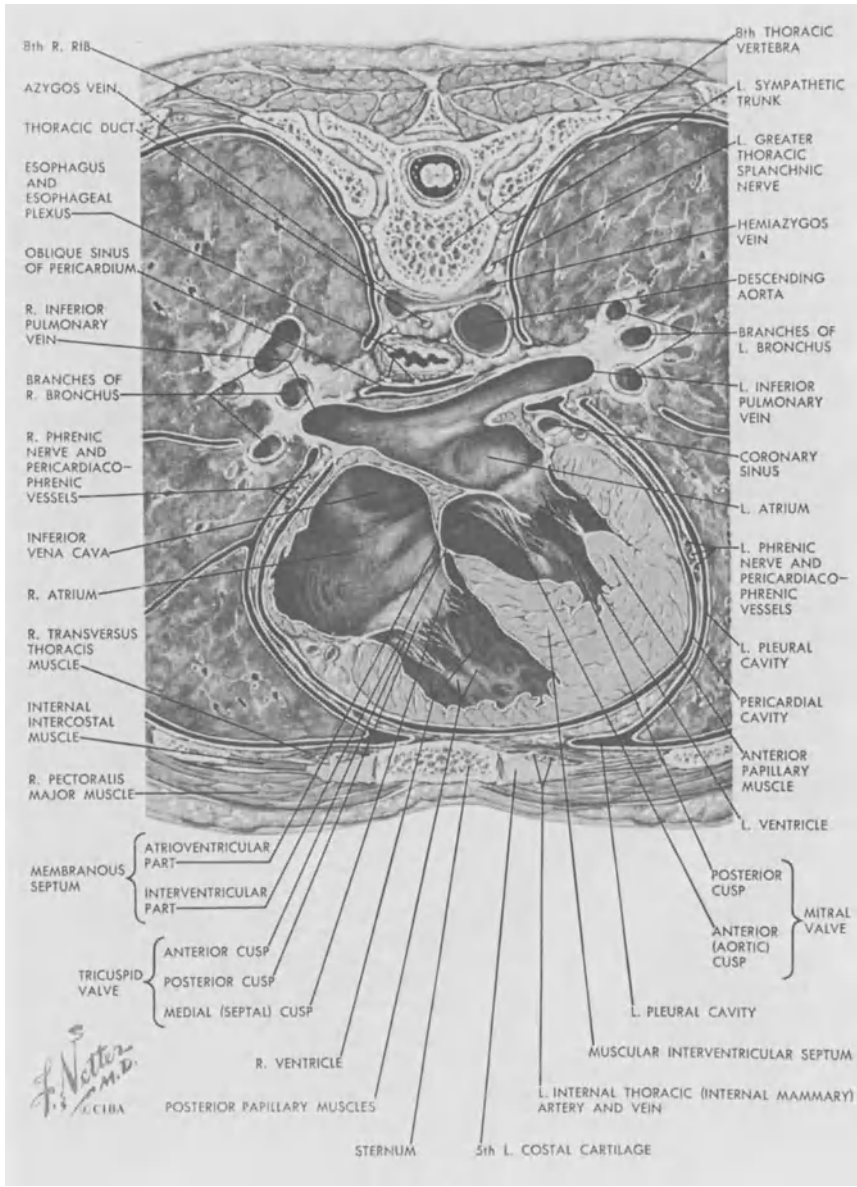

Figure I–2. Transversel section of the heart.

right and left coronary arteries. These are the first arteries to arise from the aorta just behind the sigmoid valves.

The left coronary artery passes horizontally between the main pulmonary artery and the left atrium, and then runs through the anterior interventricular groove to the apex. The two branches of the left anterior artery are the circumflex artery which lies in the left auriculoventricular groove as far as the posterior face of the heart, and the left anterior descending artery, which passes through the anterior interventricular wall to the apex.

The left anterior descending artery supplies the anterior part of the heart, and the circumflex artery

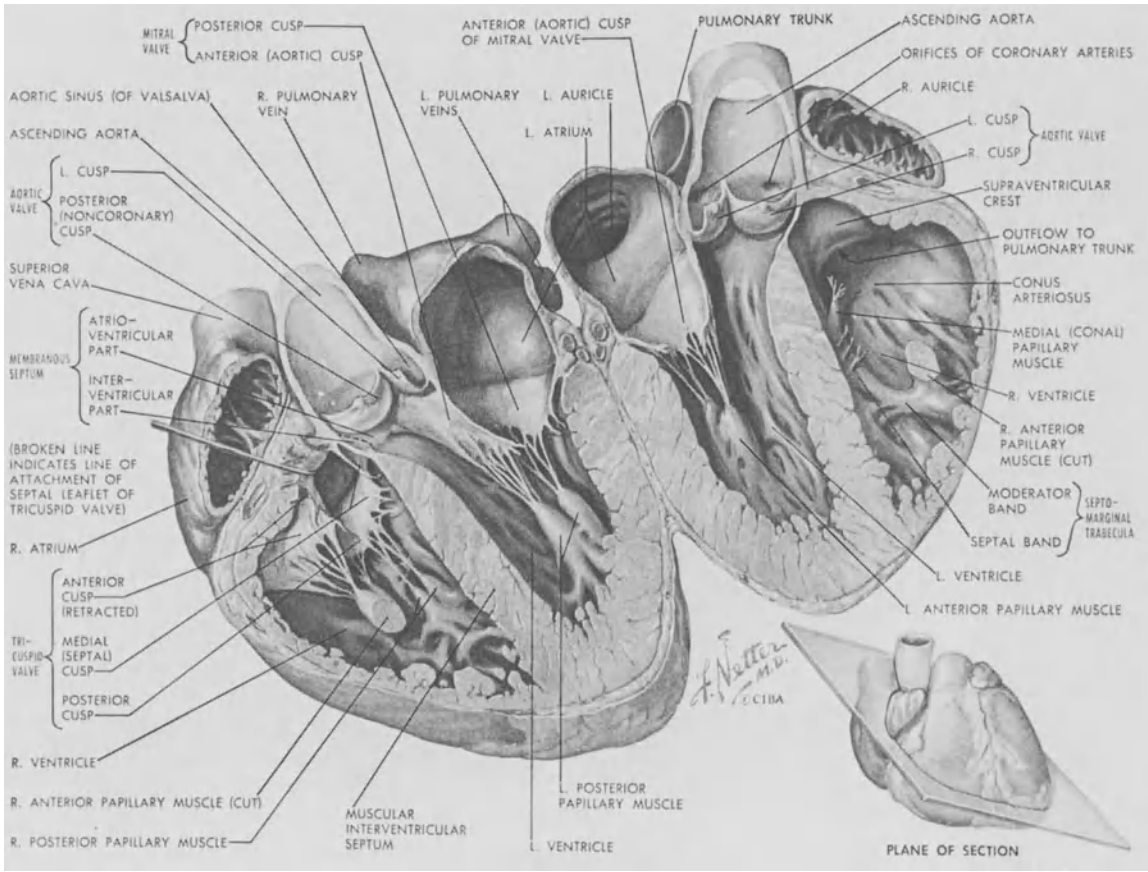

Figure I–3. Longitudinal section of the heart.

supplies the lateral and posterior parts of the heart.

The right coronary artery lies between the main pulmonary artery and the right auricle, then passes through the right auriculoventricular groove and finally descends in the posterior interventricular groove. At the extremity of this groove, the artery turns to the apex and often has an anastomosis with the extremity of the left anterior descending artery (Fig. I–4).

The venous blood comes back principally via the great cardiac vein. This vein originates at the apex of the heart and follows the anterior interventricular groove together with the left anterior descending artery. It continues along the anterior face of the left auriculoventricular groove as far as its posterior aspect until it finally ends in the inferior wall of the right atrium. A widening can be seen at the end of the great cardiac vein a few centimeters before its end. This is called the coronary sinus which opens into the right atrium at the Thebesius valve (described above). At the point where the great cardiac vein becomes dilated and forms the coronary sinus, is to be found the Vieussens valve.

Other veins ends in the coronary sinus, eg the left auricular vein, the left ventricular vein, the posterior interventricular vein (that runs in the posterior interventricular groove, along with the right coronary artery) and the small coronary vein that lies in the posterior part of the right auriculoventricular groove before joining the coronary sinus.

Other small cardiac veins do not drain into the coronary sinus but flow directly into the right atrium. These small veins generally originate in the right ventricle.

Several small veins, called Thebesius veinules, originate in the wall of the heart cavities and flow directly

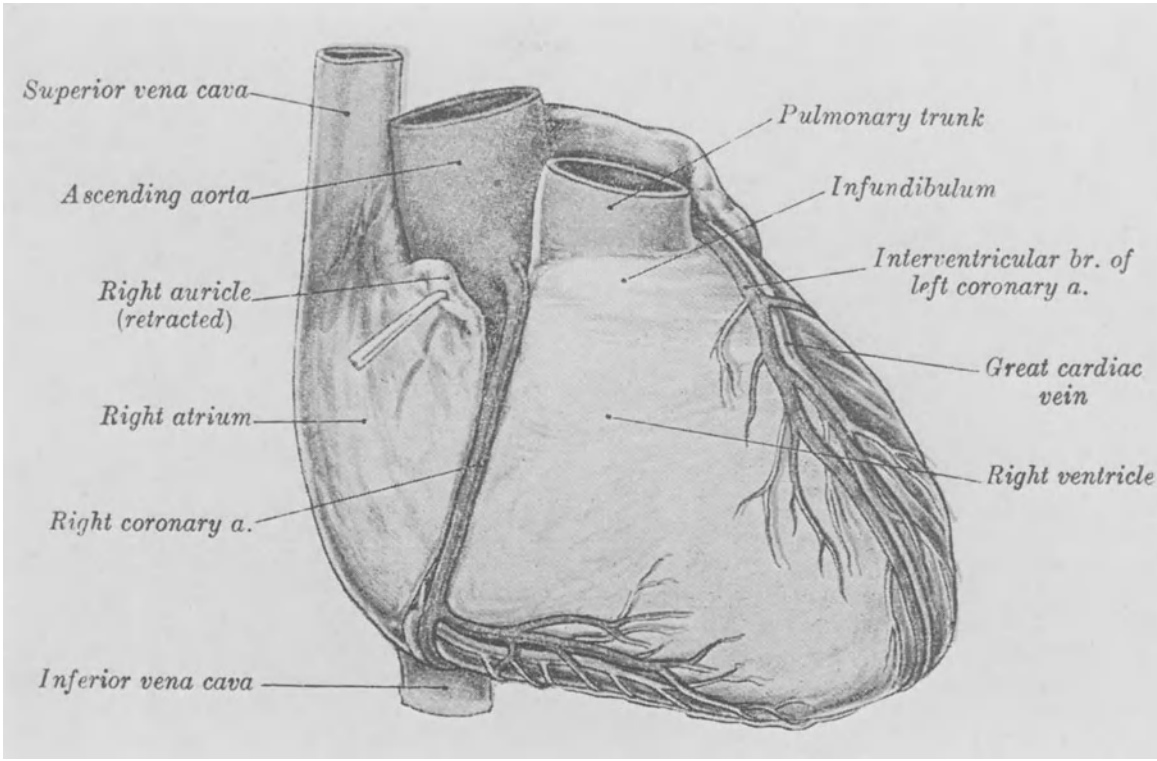

Figure I–4. Right side of the heart.

into the same cavity. These small veins are used, for example, for the venous blood flow of the papillary muscles.

D. *The pericardium*

The pericardium is a thin epithelial tissue formed by two layers, a deep layer adhering to the myocardium, and a superficial layer, called the epicardium. The pericardium is thus a double envelope that contains the myocardial part of the heart.

The pericardium, like the pleura or the peritoneum, is a serous membrane; this means that it is composed of a thin cellular sheet (called mesothelium) similar to vascular endothelium.

The two layers of the pericardium are separated by a virtual space in normal cases. However, this space can be filled by exudative secretions during an inflammation (eg pericarditis). The pericardium can also become fibrous or even calcified (for example, with tuberculosis) and then loses its elasticity. In such pathological circumstances, the diastolic relaxation movements and the ventricular filling of the myocardium are altered.

The deep pericardial sheet covers the coronary vessels and the myocardium from the apex to the base of the heart. At the base of the heart, the sheet continues and covers the first part of the aorta and the main pulmonary artery. It also covers the first part of the pulmonary veins and of the two venae cavae. Then, the deep sheet reflects upon itself and so forms the superficial sheet or epicardium.

At the base of the heart, the pericardium forms a cavity, called the transverse sinus of the pericardium (or Theile sinus). The margins of this sinus are drawn inferiorly by the base of the heart and superiorly by the right pulmonary artery. The posterior border is marked by the superior vena cava and both the ascending aorta and the main pulmonary artery form its anterior aspect (see Fig. I–1).

This transverse sinus has two openings, one to the right and the other to the left. The right orifice is situated between the ascending aorta forwards and the superior vena cava backwards. The left opening is situated between the main pulmonary artery and the left atrium.

The double-sheet structure of the pericardium is contained in a fibrous, very resistant envelope called fibrous pericardium. This fibrous part lies on the epicardium, but does not reflect on itself. At the base of the heart, this fibrous structure ends in the adventitia of the large vessels. This fibrous pericardium has some ligaments that are attached to the diaphragm, the sternum and the vertebrae (from the sixth cervical to the fourth dorsal vertebra). Smaller ligaments go to the bronchi and the esophagus.

On the fibrous pericardium are to be found fatty streaks that can become enlarged in obesity or in corticotherapy (and so increase the cardiac silhouette on a thoracic X-ray).

Blood supply to the visceral sheet of the serous pericardium is from the coronary arteries. The superficial sheet of the pericardium (or epicardium) and the fibrous pericardium are both supplied by the diaphragmatic and bronchial arteries.

E. *The anatomy of the large vessels*

The large vessels are the vascular structures – arterial and venous – that fill the cardiac cavities and arise from them. The coronary sinus and the coronary veins are excluded from this definition. The large vessels include the main pulmonary artery, the aorta, the pulmonary veins and the vena cava.

1. *The main pulmonary artery*

Venous blood flows from the peripheral vessels, through the vena cava, the right atrium and right ventricle and finally reaches the main pulmonary artery (or pulmonary trunk). This blood is then driven under pressure to the lung to be oxygenated in the alveolar wall. The histologic structure of the main pulmonary artery is arterial (though its content is venous or deoxygenated blood) to accomodate the high pressure of blood coming from the right ventricle.

The main pulmonary artery begins at the pulmonary valve, above the right infundibulum. It is situated in front of the ascending aorta (see Fig. I–1) and is completely covered by the pericardium. The posterior wall of this artery represents the anterior limit of the transverse sinus, as described above (see Section D). After a distance of five centimeters, the main pulmonary artery divides into right and left pulmonary arteries. Each of these joins the corresponding lung hilum. The right pulmonary artery is longer than the left because the heart is situated to the left of the thoracic cavity. The diameter of the right pulmonary artery is larger than that of the corresponding left artery.

2. *The aorta*

The aorta has two main parts: the thoracic aorta, which will be described here and the abdominal aorta. The thoracic aorta consists of an ascending segment, an aortic arch, and a descending segment.

– *The ascending aorta:* This arises from the left ventricle at the level of the sigmoid valves. Immediately after, it forms its two first collateral vessels, the right and left coronary arteries. At this level, the aorta is dilated and forms the Valsalva sinus. The coronary ostia are situated at the end of the sinus so that when the aortic valves are opened during systole, they do not occlude the coronary ostia. The ascending aorta reaches as far as the first intercostal space.

– *The aortic arch:* when arriving at the distal part of the trachea, the aorta passes backward and reaches the left edge of the fourth dorsal vertebra, forming an arch from the anterior to the posterior part of the thoracic cavity. Then, it turns around the left bronchus and the left lung hilum. The right wall of the vessel is situated against the left edge of the esophagus.

From the superior wall of the aortic arch arise three vessels. These are, from right to left and from forwards to backwards: the brachiocephalic trunk, the left common carotid artery and the left subclavian artery.

– *The brachiocephalic trunk* passes upwards on the right until it reaches the right sternoclavicular joint. At this level, after a length of three centimeters, it divides into right common carotid artery and right subclavian artery.

– *The left common carotid artery* passes upwards and slightly to the left. When reaching the thyroid cartilage, it divides into left external and left internal carotid arteries.

– *The left subclavian artery* is the third and last

vessel arising from the aortic arch. It reaches the neck, passing under the left clavicle. Numerous collateral vessels originate from this vessel before it becomes the axillary artery.

In summary, the carotid vessels supply the cranio-cerebral structures. The subclavian arteries supply the upper limbs. There is one exception: from each subclavian artery rises a vertebral artery. The two vertebral arteries will join to form the basilar artery. This vessel penetrates the skull by the foramen magnum along with the brainstem. This basilar artery then divides into two posterior cerebral arteries, supplying the cerebellum and the posterior part of the brain. In the brain, the carotid vessels and the posterior cerebral arteries are joined by some collateral vessels ensuring blood supply if one of these arteries became occluded.

– *The descending thoracic aorta:* this begins at the fourth dorsal vertebra, then descends through the posterior mediastinum before reaching the diaphragm. It crosses the diaphragm on the median line by the aortic hiatus. The descending thoracic aorta is in contact with the anterior wall of the rachis and is in proximity to the esophagus, the thoracic duct and the azygos vein. Before leaving the thoracic cavity, the descending aorta gives rise to the bronchial, esophageal, mediastinal and intercostal arteries.

3. *The pulmonary veins*

The pulmonary veins drain the oxygenated blood coming from the two lungs into the left atrium. Despite the fact that they contain 'arterial' (oxygenated) blood, these vessels have a venous structure, because of their low pressure system.

There are four pulmonary veins, consisting of two left and two right veins. From each side, arise a superior and an inferior vein.

The pulmonary veins originate at the lung hilum, with the union of smaller veins running in the pulmonary parenchyme. From the hilum, they go to the left atrium where each of the four veins ends at its own orifice (in some cases, the veins may join before opening into the left atrium).

In some pathological cases, the pulmonary veins drain into the superior vena cava. In consequence, the oxygenated blood coming from the lung arrives in the right atrium, then passes into the right ventricle and goes back to the lung. This is not compatible with life. There is often a shunt between the atria or the ventricles. In some cases, the pulmonary veins fill directly into the right atrium or join the inferior vena cava. The pathophysiological consequences are also fatal.

In contrast to the inferior vena cava and the coronary sinus, the pulmonary veins do not have a continent valve at their entry into the left atrium.

4. *The vena cava system*

The venae cavae are the two vessels bringing back to the right atrium all the deoxygenated venous blood coming from the body (except the venous blood of the myocardium itself which comes back to the right atrium by the coronary veins and the coronary sinus, as described above).

(1) *The superior vena cava* originates at the superior part of the mediastinum, at the junction of the two brachiocephalic veins, just behind the first right rib. Each brachiocephalic vein is itself created by the union of the subclavian vein and the internal jugular vein. The right brachiocephalic vein is very short and vertical. The left brachiocephalic vein is longer and horizontal, due to the situation of the superior vena cava to the right of the median line. The inferior thyroid vein often drains into the left brachiocephalic vein. At the meeting point of the subclavian vein and the internal jugular vein, the thoracic canal also drains on the left, and the right lymphatic duct on the right. Other vessels, like the vertebral, posterior jugular and internal mammary veins drain into the brachiocephalic veins.

The superior vena cava descends along the mediastinum, following the right edge of the ascending aorta. Then it fills into the superior wall of the right atrium. Its length is about 7 centimeters.

The only vessel draining into the superior vena cava is the azygos vein. This vein is the result of the union of the ascending lumbar vein and the twelfth right intercostal vein. It drains the blood of the lumbar and intercostal veins. It follows an ascending path by the right edge of the rachis, beginning at the twelfth rib. When it arrives at the third rib, the azygos vein curves forward (so forming the azygos arch) and ends at the posterior wall of the superior vena cava.

This azygos vein is thus situated on the right side of the rachis, from the twelfth dorsal vertebra to the third dorsal vertebra. It is filled by blood coming from the right lumbar veins (joined to form the right ascending lumbar vein) and from each of the right

intercostal veins. Each intercostal vein opens into the azygos vein at its own orifice, except for the three first intercostal veins that join together before draining into the azygos vein.

On the left side, the azygos draining system is slightly different. The left ascending lumbar vein and the left twelfth intercostal vein form a vessel called hemiazygos vein. At the level of the left seventh rib, the hemiazygos vein curves to the right and forms an arch. This arch terminates on the left wall of the azygos vein. Thus, the hemiazygos vein drains into the azygos vein. The first six left intercostal spaces are drained by an accessory hemiazygos vein (also called small superior azygos vein) that terminates either in the hemiazygos vein or directly in the azygos vein. The term 'azygos' (literally: 'with no sibling') means that this vein is not accompanied by a corresponding artery.

(2) *The inferior vena cava* is formed by the union of the two common iliac veins. Each iliac vein is formed by the junction of an external and an internal iliac vein. The internal iliac vein principally drains the blood coming from the pelvis. The external iliac vein drains the veins of the inferior limb (especially the femoral vein) and the parietal veins of the abdomen (especially the epigastric vein and the iliac circumflex vein).

The inferior vena cava runs upwards along the right edge of the rachis, against the psoas muscle. It crosses the tendinous part of the diaphragm and then directly drains into the inferior wall of the right atrium, just beside the auricular opening of the coronary sinus.

A few collateral vessels terminate at the inferior vena cava, e.g., the lumbar veins. There are five lumbar veins, one right and one left, for each of the five lumbar vertebrae. These veins have, at the abdominal level, the same function as the intercostal veins of the thoracic cavity: they drain the blood coming from the parietal musculature of the abdomen and from the abdominal part of the spine. Before draining into the inferior vena cava (each by its own orifice), the lumbar veins are joined by a vertical anastomosis called the ascending lumbar vein. As explained above (see the superior vena cava), this ascending lumbar vein joins the twelfth intercostal vein to form the azygos vein on the right and the hemiazygos vein on the left. The azygos vein is thus a kind of anastomosis between the superior and the inferior venae cavae.

The other collateral vessels of the inferior vena cava are the renal veins, surrenal veins, spermatic or ovarian veins, hepatic and sub-diaphragmatic veins.

The hepatic veins are the major venous drainage system of the liver. They arise at the junction of the hepatic sinusoids. These sinusoids (perforated, very low-pressure vessels irrigating the hepatocytes) arise from the divisions of the portal vein. The portal vein brings back to the liver all the venous blood coming from the bowels, the stomach and the spleen (thus, essentially blood carrying all the nutrients coming from the digestive processes). The portal vein is formed at the meeting point of three vessels: the splenic vein (draining the blood coming from the spleen, the pancreas and the left part of the stomach), the superior mesenteric vein (draining the blood from the right part of the stomach, the duodenum, the jejunum, the ileum and the proximal part of the colon) and the inferior mesenteric vein (draining the distal part of the colon).

Schematically, the venous circulation ends in three main axes. The superior vena cava drains the blood from the head, the neck, the superior limbs and the thoracic cavity. The inferior vena cava drains the blood coming from the abdominal cavity, the pelvis and the inferior limbs. The portal vein drains the blood coming from the bowels. The portal veins end in the liver and form several sinusoids. These sinusoids join together to form the hepatic veins which end in the inferior vena cava. Thus, the peripheral venous blood drains into the heart by two venae cavae, indirectly bound together by the azygos vein.

In summary, the cardiovascular system is divided in two parts:

- *the small circulation*, connecting the heart with the lungs by the pulmonary arteries and veins. This circulation begins at the right ventricle and ends at the left atrium. Its role is to oxygenate the blood.
- *the large circulation* carries the oxygen from the lung to the tissues. It begins at the left ventricle by the aorta and it ends in the right atrium by the two venae cavae.

CHAPTER TWO

Principles of Cardiac MR imaging

INTRODUCTION

Nuclear Magnetic Resonance (NMR) spectroscopy was discovered around 1945 as a method to determine the magnetic properties of atomic nuclei. In 1952, the Nobel Prize was awarded to Bloch and Purcell for their independent work in developing NMR. It is still successfully applied as a tool in molecular physics and chemistry, revealing molecular structures, chemical reaction rates and diffusion processes. In biochemistry, NMR has made contributions to elucidating the structure of cell membranes, nucleic acids, proteins and viruses. Especially interesting from the medical point of view are in vivo proton, phosphorus and carbon spectra.

After the discovery of differences in the proton NMR parameters (relaxation times) of normal and malignant tissues by Damadian (1971), imaging techniques to depict the magnetic behaviour of protons were developed by Lauterbur (1973) and Ernst (1975) among others, disclosing the field of Magnetic Resonance Imaging (MRI). So the first live image was reported in 1976 of a human finger, rapidly followed by the hand and the thorax in 1977, and the head and the abdomen in 1978. Since then, image quality has improved steadily while imaging time has shown a gradual decrease, bringing MR imaging into clinical practice.

Section I is a brief introduction to the physical basis of MR imaging terminologies without attempting to describe the technical aspects. Section II introduces the most current reconstruction methods of MR images. More specific points of rapid imaging methods, MRI artefacts, image quality and cardiac imaging are overviewed in Section III.

The reader who already knows the basic physical principles and terminologies of NMR can skip the first Section without any loss of understanding of the two following parts.

SECTION ONE
BASIC PHYSICAL PRINCIPLES OF NUCLEAR MAGNETIC RESONANCE

Two pictures of the nuclear spin behaviour will be considered, the *Classical picture* and the *Quantum picture*. They are complementary and necessary to understand the NMR principles.

I–1. Nuclei – Magnetic dipolar moment – Small magnet

Atoms are constituted of electrons and nuclei. The nuclei are made up of protons (p) and neutrons (n). Whereas R.X. tomography is concerned with electrons, nuclear Magnetic Resonance Imaging (MRI) and Spectroscopy (MRS) are related to nuclei of specific atoms. Indeed certain nuclei (H^1, P^{31}, F^{19}, Na^{23}, C^{13}, etc.) generate a small magnetic field in their surrounding. The NMR phenomenon is present only when these atomic nuclei species are considered.

The physical property related to this intrinsic nucleus magnetic field is named *magnetic dipolar moment* (μ) (Fig. 1a). This value defines the nucleus magnetic properties and the ability of nuclei to have a magnetic

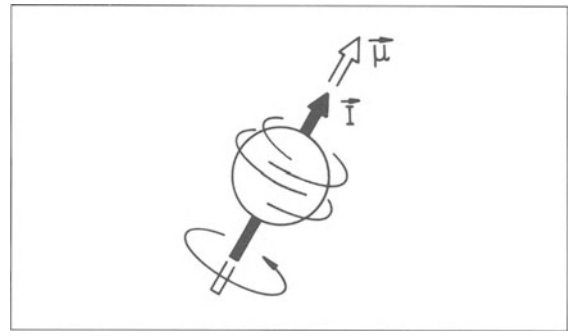

Figure 1a. When an atomic nucleus owns magnetic properties, it is characterized by a magnetic dipolar moment μ and a nuclear spin I.

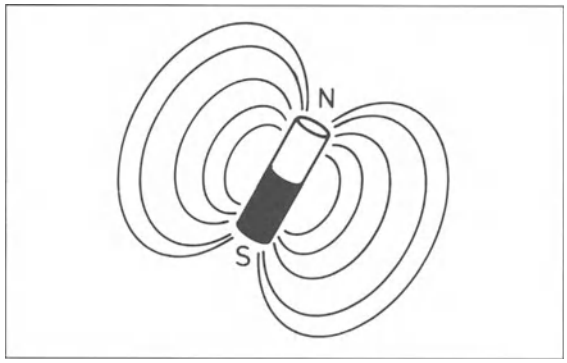

Figure 1b. A nucleus with a spin I can be compared to a small magnetized bar.

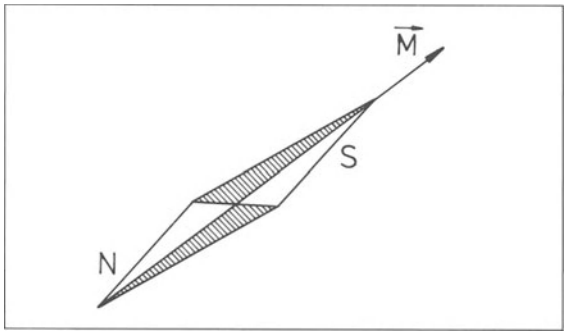

Figure 1c. A nucleus with a spin can also be compared to the magnetized needle of a compass.

behaviour. The nuclei previously shown have this property while other nuclei like O^{16} or Ca^{40} do not have it ($\mu = 0$).

Therefore we can compare the useful nuclei for NMR to small magnetized bars (Fig. 1b) or to the magnetized needle of a compass (magnets) (Fig. 1c). The magnet is characterized by a macroscopic value termed magnetic moment or magnetization (M).

I–2. Spin and gyromagnetic ratio

The atomic nuclei with a net (different to zero) dipolar moment have a *nuclear spin (I)*. This physical value is related to the dipolar moment through the *gyromagnetic ratio (γ)* (1).

$$\mu = \gamma I \qquad (1)$$

We see that different nuclei can have the same spin but different dipolar moments and therefore, different gyromagnetic ratios (Table 1).

Table 1. Variation of gyromagnetic ratio.

Nucleus	Spin	Gyromagnetic ratio (MHz/T)
H^1	1/2	42.58
P^{31}	1/2	17.24
F^{19}	1/2	40.05
Na^{23}	3/2	11.26
C^{13}	1/2	10.71
C^{12}	0	0.00
O^{17}	5/2	5.77
O^{16}	0	0.00

The nuclear spin is said to be a microscopic or quantum value and its aim is to specify potential discrete spatial orientations along which the dipolar moment can orient itself.

Under normal circumstances all spins or dipolar moments have a random orientation which changes rapidly as a result of the thermal Brownian motion. However they have the intrinsic ability of discrete spatial orientations when submitted to magnetic fields.

I–3. Static magnetic fields

By definition the magnetic field (B) is the area surrounding a magnet constituted of current-carrying conductors. This region is endowed with certain properties. The most important one for NMR is the fact that a small magnet in such a region exercices an influence that tends to align it in a given direction. The history of NMR has shown how closely NMR techniques have developed with magnet technology; field homogeneity for chemical shift measurements, field strength for biological molecule NMR, whole body magnets for clinical imaging. The five most important parameters to be considered in specifying a magnet are: (i) field strength, (ii) field homogeneity and the volume of the homogeneous region, (iii) field stability, (iv) access to the magnetic field, and (v) stray magnetic field which is the residual magnetic field which is produced by the magnet outside the examination room. These all interact and, even if the financial cost was not a limitation, some characteristics of these parameters would be impracticable from an engineering point of view. In most cases, the capital cost of a superconducting magnet or the power consumption of a resistive magnet forces a

compromise between the other specifications. The cost and difficulty of installation and the space requirements of large imaging magnets should also not be underestimated.

We will discuss here neither the technical nor the economical problems, but we will overview the three main types of magnet with their principal specifications.

(i) *Superconducting magnets*. These magnets are constituted by wires of superconductor materials like niobium-titane. The main particularity of these materials is that they lose their electric resistance at a temperature of the order of 20 degrees above absolute zero (20 K). To reach this physical property, the wires of the magnet are immersed in a container filled with liquid helium (4.2 K). In this situation, theoretically, the wires can carry electric current during an infinite period of time without any losses. Therefore, once the current is installed in the wires and the field strength achieved, the power supply generating this current can be disconnected, the magnetic field persisting infinitely.

The superconducting magnets provide the highest stable field strength (up to 14 Teslas for small bore magnets and 4.0 Teslas for whole body imagers) that the current technology can achieve. They are relatively expensive but the running costs are low although influenced by the local prices of liquid helium. An inconvenience of this kind of magnet is the important stray field generated although now it can be reduced by a special hardware device termed active shielding.

(ii) *Resistive magnets*. The principle of these magnets is the classical way to generate magnetic fields. A power supply generates electric current which will be carried by low resistance wires (e.g. copper) constituting the magnet. The maximum field strength supplied by this kind of magnet for whole body imagers is currently around 0.28 Teslas. It is limited by the restricted capacity of the cooling-water system that carries off the heat generated by the electric currents in the coils of the magnet.

The field can be less stable than that of superconducting magnets due to variations in the electric current. The purchase prices are relatively low but the running costs are influenced by the price of electricity and cooling water. These magnets are characterized by low stray field whose extent is limited to the magnet sizes.

(iii) *Permanent magnets*. The third class is that of magnets built in a mass of ferromagnetic material (e.g., $SmCO_5$). This material does not need an electric current to generate a magnetic field, it is magnetized (remanant field) thanks to its intrinsic properties and keeps this field constant without any losses. The field strengths are currently 0.5 Tesla. These magnets are relatively expensive and heavy. The running cost is low and is related to the temperature conditioning, the field stability being dependent on the magnet room temperature. These magnets are characterized by a stray field lower than that of resistive magnets.

I–4. Precession – Resonance frequency – Longitudinal and transverse components

We will only focus our further discussions on H^1 which is also named a proton p because this nucleus is constituted of only one proton. This is the most abundant nucleus inside the human body and the most sensitive in terms of NMR information. It is also one of the most simple to study due to its low spin value (½).

4.1 *Larmor precession*

When immersed in a magnetic field, nuclei with a magnetic moment will orient themselves either with or against the field direction (quantum behaviour) (Fig. 2).

Because this alignment within the field is not perfect, the nuclear dipolar moments or the nuclear

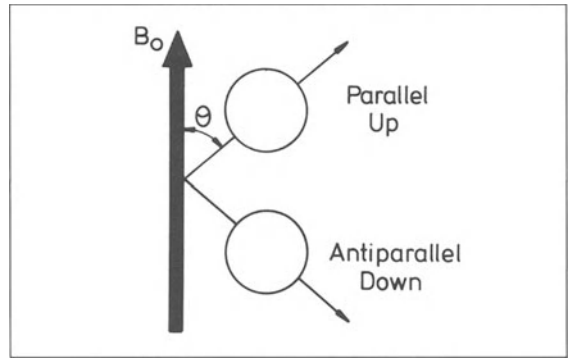

Figure 2. When immersed in a magnetic field, nuclei with a spin can orient themselves either parallel, or antiparallel to the external magnetic field.

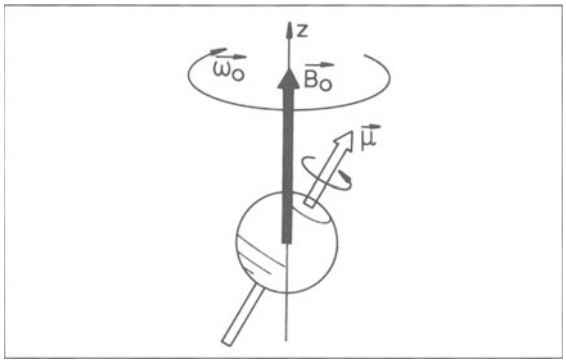

Figure 3. The magnetic dipolar moment precess around the external magnetic field with an angular velocity named Larmor pulsation.

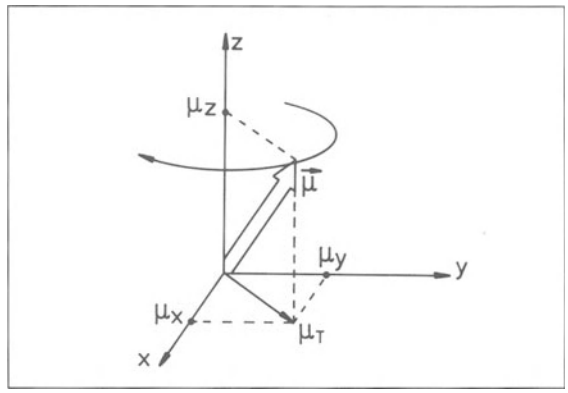

Figure 4. When submitted to an external magnetic field B_0, the magnetic dipolar moment owns two components with respect to the direction of B_0; a longitudinal component μ_z and a transverse component μ_T. The latter one is decomposed into μ_x and μ_y.

spins rotate around the direction of the magnetic field (B_0) with a well defined frequency named *Larmor pulsation* or *frequency* (Fig. 3). This rotation is called the *Larmor precession* and the precession frequency (ω_0) depends on the involved isotope (kind of nucleus characterized by the gyromagnetic ratio γ) and is proportional to the strength of the magnetic field at the site of the nucleus:

$$\omega = \gamma B_0 \qquad (2)$$

4.2 *Resonance frequency*

This Larmor frequency is also named *Resonance frequency* and this precessional movement of nuclear spins submitted to a magnetic field describes their classical behaviour.

4.3 *Dipolar moment components*

This description shows also that dipolar moment vector has always three components relative to a three dimensional reference frame defined from the magnetic field B_0. The component aligned to B_0 (z-axis) is named longitudinal (μ_z) whereas the components perpendicular to B_0 are named transverse (μ_T) (Fig. 4).

I–5. Energy states and net magnetization vector

5.1 *Energy states and Boltzmann Distribution*

Before the application of a magnetic field B_0, there is an equal number of nuclear spins parallel (spins UP) to B_0 than antiparallel (spins DOWN) to B_0. Under normal circumstances of temperature ($\approx$ 37 °C), when a magnetic field ($\approx$ 1 Tesla) is applied, there is, per volume unit of the H^1 nuclei sample, a very little excess of nuclear spins UP relative to the amount of spins DOWN. The relative populations of spins UP and DOWN is well defined by a statistical distribution law named the *Boltzmann Distribution* (Fig. 5a) whose the mathematical expression is given by:

$$N_D/N_U = \exp(\Delta E/kT) \qquad (3)$$

where

$$\Delta E = h\nu_0 \qquad (4)$$

is the *quantum energy* to give to a H^1 nucleus in such a way that, if its spin is UP, (said to be in the resting or low energy state) it becomes a spin DOWN (said to be in the excited or high energy state).

h is the Planck constant,
k is the Boltzmann constant, and
T is the absolute temperature (Kelvin).

This statistical distribution explains also that when nuclear spins are under the influence of an external static magnetic field, there exists a thermodynamic equilibrium between the populations of the low and high energy states. This equilibrium is termed the *thermal equilibrium* of the nuclear spins.

In this equation ν_0 is the frequency of an electromagnetic radiation (Radio-Frequency wave) at which a H^1 spin must be submitted in order to be able to

make a transition between its low and high energy states (Fig. 5a). This explanation describes the quantum mechanical approach of the influence of a magnetic field on a group of nuclear spins.

As ν_0 is also the Larmor frequency met during the classical description, the link between the quantum and the classical approaches of this phenomenon is again established.

5.2 *Macroscopic magnetization*

In a typical MR situation, thanks to the abundant presence of protons inside the human body (hydrogen atoms contained in water, fat, etc.), the relatively small excess between UP and DOWN protons is still sufficient to produce a net *macroscopic magnetization* M. This physical value is a vector with an amplitude equal to the statistical summation of UP and DOWN spins and with the same direction and sense as B_0 (Fig. 5b). By comparison with longitudinal component of the dipolar moment (μ_Z) this magnetization is said to be longitudinal. Under these circumstances we say that the body is magnetized. For a particular tissue of the body the amplitude of this magnetization is given by:

$$M_0 = \chi B_0 \tag{5}$$

where χ is called the *magnetic susceptibility* of this tissue and describes how easy is its magnetization when it is immersed in a static magnetic field B_0.

This equation also shows that, when any interactions other than a static magnetic field is present, the magnetization varies lineary with this field.

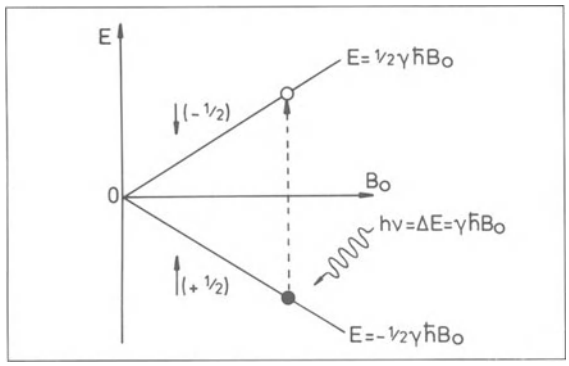

Figure 5a. An em radiation whose the frequency equals the Larmor frequency of a proton submitted to an external magnetic field can induce transitions between the low and high nuclear energy states.

I–6. Electromagnetic radiations – Resonance conditions

6.1 *Electromagnetic radiations*

By definition, an electromagnetic (em) wave is a wave

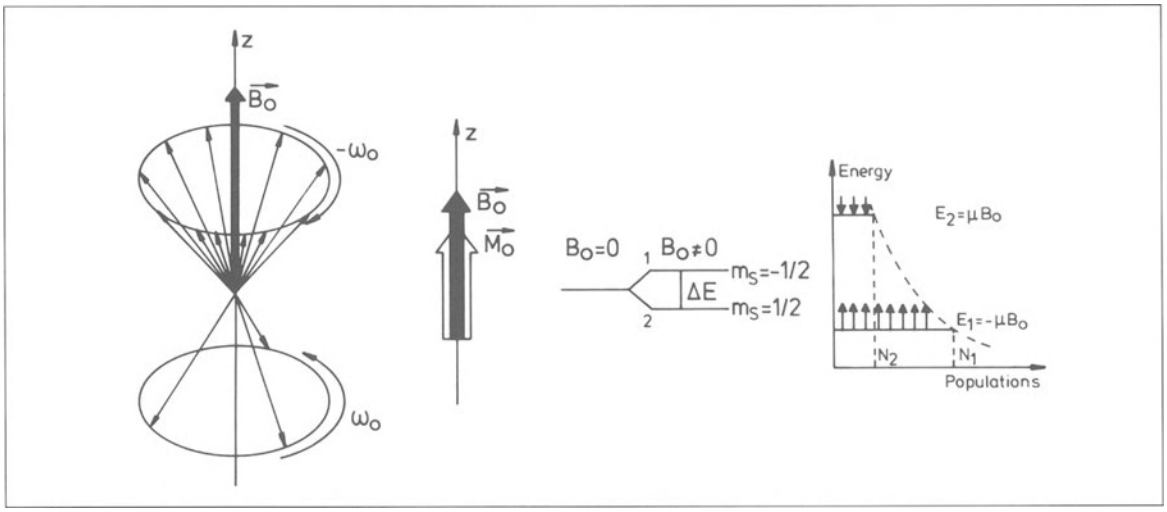

Figure 5b. An external magnetic field permits us to distinguish between the two energy states of a set of protons. The populations of these energy levels are different and defined by the Boltzmann statistics. Therefore, a sample filled with hydrogen nuclei is magnetized and characterized by a macroscopic magnetization M_0.

able to travel through the vacuum, as opposed to mechanical waves requiring a material medium to propagate itself (i.e., a RX is an em wave whereas ultrasonographic waves are mechanical ones). The em wave is constituted by two fields, an electric field E and a magnetic field B_1, oscillating orthogonally each to the other and travelling both perpendicularly to the propagation direction (Fig. 6).

The em wave oscillation is characterized by the frequency ν or the pulsation ω; these two values being related by the equation:

$$\omega = 2.\pi.\nu \qquad (6)$$

In H^1 NMR, the most common values of this frequency range from 10 MHz to 800 MHz. The em waves in this frequency bandwidth are named radiofrequencies (RF). Another particularity of the em wave is its capacity to transport an energy proportional to its pulsation or frequency.

$$\text{Energy} = (h/2\pi)\omega_{em} = h\nu_{em} \qquad (7)$$

In NMR, these two fields operate and have different effects on the patient body but the most important for the NMR principles is the magnetic one.

An em wave and therefore an oscillating magnetic field B_1 can be created by carrying oscillating electric current by electric conducting wires (Cu, Ag, etc.). This device is termed an *RF coil.* In NMR, to be efficient, this B_1 field must be oriented perpendicular to the static field B_0 and it can be considered like a magnetic field having a constant amplitude B_1 and rotating around B_0 at an angular velocity equal to the RF pulsation ω. If B_1 rotates around B_0 exactly at the Larmor pulsation ω_0 and if we observe the behaviour of the nuclear spins from a reference frame bound to B_1 (rotating frame; we can imagine that we are sitting on B_1 and that we are rotating synchronously with it around B_0), we ascertain that the nuclei *see* B_1 as being exactly synchronous with their own precession. Generally when NMR phenomenon is discussed, this rotating frame is always considered because the graphic representations of magnetization behaviour are more simple in this reference frame than in the static frame (also named laboratory frame) bound to B_0. The present discussion permits us again to consider the two representations already discussed of the NMR phenomenon: (i) the classical picture which uses reference frames and the rotating magnetic field B_1, and (ii) the quantum picture with RF radiations and the energy associated with em waves.

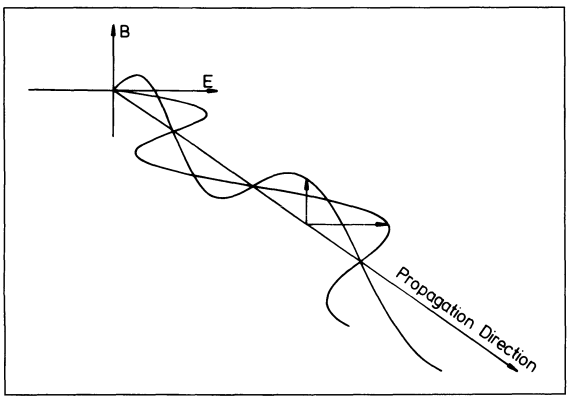

Figure 6. An em radiation is constituted by electric and magnetic fields. These two fields oscillate orthogonally each to the other and travel both perpendicular to the propagation direction of the em wave without need of a material medium.

6.2 *Resonance condition*

In nature, when a perturbation (exciting or emitter systems e.g., rotating field, vibration generators, wind, etc.) has exactly the same frequency as the system submitted to it (excitable or receiver system, e.g., a set of nuclear spins, a pendulum, a bridge), the best situation for the easy transfer of energy from an exciting system to an excitable one is encountered. This particular condition in physics is called the *resonance condition.*

6.3 *Classical picture*

In the laboratory frame, when $\omega_{RF} = \omega_0$, the movement of the net macroscopic magnetization is the combination of a rapid precession around B_0 and a slow precession ($B_1 \ll B_0$) around B_1. The magnetization describes a spiral path on the surface of a sphere having for radius the length of this magnetization (Fig. 7a). In the rotating frame, the movement is very simple, it is just a slow rotation at angular velocity $\omega_1 = \gamma B_1$ around B_1 (Fig. 7b). If B_1 is continuously applied, the magnetization M oscillates slowly between parallel and antiparallel to B_0. Coming back again to dipolar moment components, in this situation the macroscopic magnetization has always two components, a longitudinal one parallel to the B_0 direction and a transverse component perpendicular to this direction.

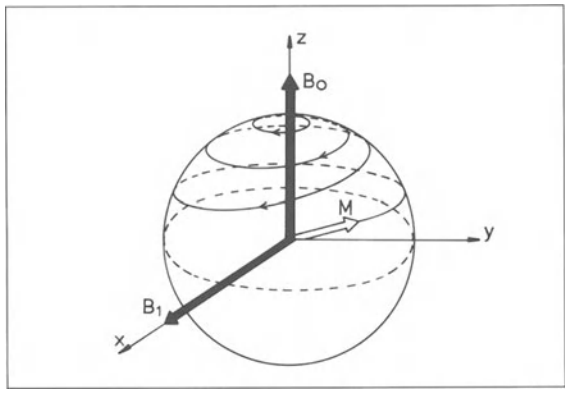

Figure 7a. In the laboratory frame, the magnetization submitted to a static field and a RF field oscillating at the Larmor frequency describes a spiral path on the surface of a sphere having for radius the length of the magnetization.

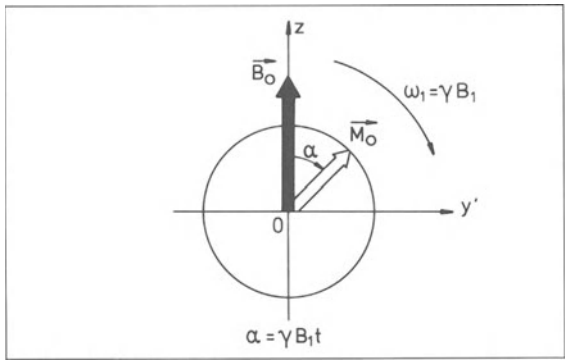

Figure 7b. In the rotating frame, under the resonance conditions, the magnetization describes a slow rotation around the RF field direction.

6.4 *Quantum picture*

In quantum description, the resonance corresponds to a time-dependent combination of both quantum states during and after the application of the RF field. The number of nuclei in each quantum state (i.e., energy levels), in the up and down orientations, is time fluctuating.

6.5 *Radiofrequency coils*

In MRI practice, different kinds of RF coils are used depending on the type of human body regions to be imaged and the spatial resolution to be reached.

6.5.1 *Head, body and knee coils*

The names of these coils are very explicit and they are generally used to produce the exciting RF waves (emitter coils) but also to receive the NMR signal emitted back by the body (receiver coil). These coils are said *quadrature coils* and *mirror coils* which are modifications of the previously explained ones to increase the signal-to-noise (S/N) ratio or, in other words, their sensitivity. *For example, with a quadrature coil, this S/N ratio could be theoretically improved by approximately 40%.*

6.5.2 *Surface coils*

These coils are just receiver coils, the RF emission being generally made by the body coil and they are named circular, rectangular, wrap-around, ... surface coils. They are used to image small well localized parts of the body whose dimensions depend on the coil size and they increase the S/N ratio and therefore the spatial resolution over the imaging regions. The main inconvenience of these coils is the considerable inhomogenous signal distribution over the image plane and along the direction perpendicular to it. Therefore, from body regions located slightly outside a volume proportional to the coil sizes, the S/N ratio falls off very rapidly leading to a null signal collected from all those body regions.

I–7. Radiofrequency pulses

In the classical description, the 90° and 180° RF pulses correspond respectively to the careful application of the RF field during a time that the nuclear magnetization deviates of 90° or 180° from the B_0 direction (Fig. 8).

In the quantum description, the 90° pulse corresponds to the emission of electro-magnetic radiations so that there is equilibrium in the numbers of spins

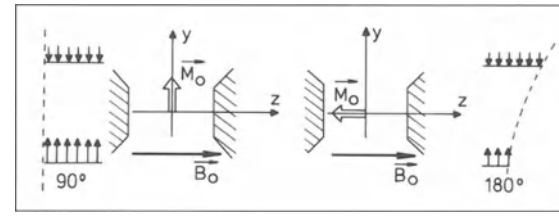

Figure 8. The 90° and 180° RF pulses correspond respectively to the application of the RF field during a time that the nuclear magnetization deviates of 90° and 180° from the B_0 direction.

parallel and anti-parallel to the B_0 direction. On the other hand, the 180° pulse inverts the nuclear state populations. In general, an $\alpha°$ pulse corresponds to the application of the RF field during a period of time of any duration.

When 90° or $\alpha°$ pulses are applied to a sample containing nuclei with spins, respectively the following situations are present: (i) a transverse magnetization with a maximum amplitude equal to the longitudinal magnetization M_0 at the thermal equilibrium and no residual longitudinal magnetization M_z, and (ii) a transverse magnetization $M_{x,y}$ whose amplitude is smaller than M_0 and a remaining longitudinal magnetization M_z with an amplitude smaller than M_0. On the other hand, the 180° pulse does not generate any transverse magnetization.

In any case, the RF pulse at the resonance condition has two important effects on a set of nuclear spins: (i) it creates around B_0 a coherent precession (in-phase) of dipolar moments previously in incoherent rotation (out-of-phase). In this way it creates in the transverse plane a net transverse magnetization that precesses at the Larmor frequency around the static magnetic field, and (ii) it turns the macroscopic magnetization from the B_0 direction of an angle α called *flip angle*. The value of the flip angle depends on the application duration of the RF field, and the amplitude of the generated transverse magnetization is proportional to the sine of this angle.

I-8. Relaxation mechanisms – Relaxation times

B_0 and B_1 are not the only fields that the individual nuclei *see*. In addition, each nucleus *sees* a fluctuating field B_{loc} which adds to B_0 and B_1. B_{loc} is the resultant field that is generated by all other nuclei, especially those located in the close vicinity to a nucleus feeling B_{loc} (Fig. 9).

The effect of the static or slowly varying part of B_{loc} in the z direction (longitudinal) is also to alter the precession frequency, by effectively changing B_0. On the other hand, if the time varying part of B_{loc} has components h_x (t) perpendicular to B_0 with frequencies in the region of ν_0, these will add to B_1 and cause transitions (from the quantum description point of view) or cause the precessions angles, hence M_z, to change (from the classical description point of view).

These fluctuations are due to the thermal motion

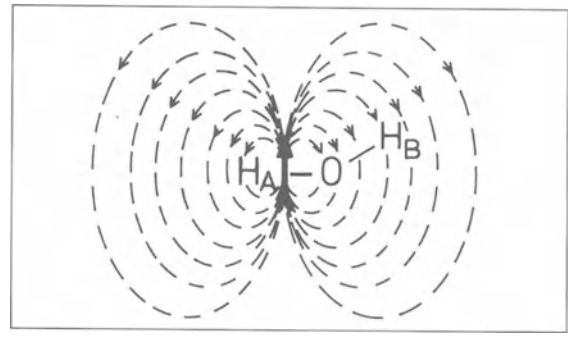

Figure 9. The hydrogen nucleus H_B of a water molecule experiences the local magnetic field h created by the magnetic dipolar moment of its twin brother H_A.

of atoms or molecules which own the nuclear magnets (dipolar moments). This latter process is effectively the mechanism of the T_1 *relaxation* phenomenon (also named spin-lattice relaxation) which drives the system to thermal equilibrium.

Likewise, the slowly varying component $h_z(t)$ adding B_0 destroys any existing M_x and M_y transverse magnetizations by a phasing process; this is the mechanism of the T_2 *relaxation* phenomenon (also named spin-spin relaxation).

Respectively the relaxation times T_1 and T_2 are the constants characterizing these two processes and are intrinsic magnetic properties of biological tissues. These relaxation times are very dependent on the tissue state (solid or more or less liquid, static or more or less mobile, constituted of smaller or larger molecules, the temperature and magnetic field B_0). In Table 2 we summarize the relaxation times of several current tissues encountered in MRI.

Table 2.

Tissue (B_0 = 1.5 T, 37°C)	T_1 (ms)	T_2 (ms)	Proton density (%)
CSF	2400	160	100
Grey matter	920	100	100
White matter	780	90	90
Muscle	870	45	70
Myocardium	870	55	70
Fat	260	80	80
Blood	200	100	100
Bone marrow	400	60	60

In summary, T_1 *relaxation time is the time constant describing the recovery (come back) of the longitudinal magnetization* M_z *to its thermal equilibrium value* M_0.

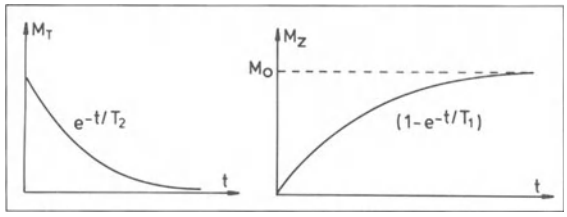

Figure 10. The curves which describe the longitudinal magnetization recovery and the transverse magnetization decay have exponential shapes characterized respectively by the T_1 and T_2 relaxation times.

T_2 relaxation time describes the fall off of the transverse magnetizations M_x and M_y present in the plane perpendicular to B_0 after the application of a RF field.

The curves describing these two relaxation phenomena against time have exponential shapes (Fig. 10).

We mention some ideas of interest about these relaxation times. In mobile fluids, T_2 is nearly equal to T_1, whereas in solids or in slowly tumbling systems (e.g., high-viscosity systems, etc.), static field components induced by neighbouring nuclei are operative and T_2 becomes significantly shorter than T_1. In solids, T_2 is usually so short that the signal has disappeared within the first milliseconds, whereas in fluids, the NMR signal may exist for seconds. To a large extent, this is the cause of the low or absent signal from solid structures in MRI.

I–9. Detection of the NMR resonance signal – FID

Consider the situation where a transverse magnetization M_T is created following the application of a RF pulse on a sample of nuclear spins submitted to a static magnetic field B_0. When this RF is switched off, the M_T makes a Larmor precession only around B_0 and induces a time dependent electric voltage (Lenz law), named *electromotrice force (emf)* V(t) in an aerial (coil) that would be located in the surrounding of the sample containing the nuclear spins (Fig. 11).

This time depending electric voltage is called NMR *F(ree) I(nduction) D(ecay)*. At the beginning of their precession, the spins are in-phase and the FID is maximum, but depending on the sample relaxation characteristics the spins become more or less rapidly out-of-phase. The resulting transverse magnetization decreases proportionally, the FID falling off. Therefore the real FID will be represented by an oscillating curve decaying exponentially versus the time (Fig. 12).

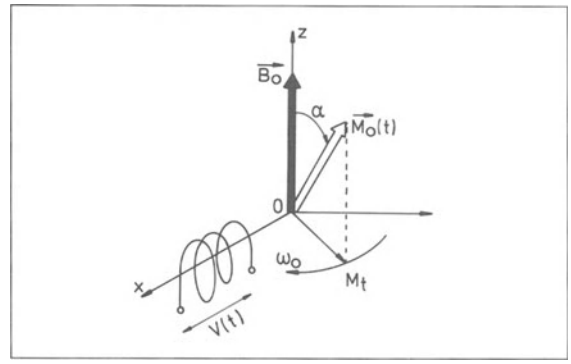

Figure 11. During its precession around B_0, the magnetization M_0 induces an electromotrice force, named FID, at the connections of the receiver coil.

The FID decay time constant is the transverse magnetization time constant, i.e., the transverse relaxation time T_2.

The FID cancellation takes around 4 times T_2, corresponding to the cancellation of the transverse magnetization. During this delay, the longitudinal magnetization, which depends on T_1, has just recovered a part of its equilibrium value ($T_1 < T_2$) M_0.

I–10. NMR Spectrum – Fourier Transform – Chemical Shift

By the FID we have described the behaviour of the transverse magnetization decay against time. But its shape, very simple (exponential) in our simplified exposal, is very complicated in practice. As in other domains, e.g., in optics with the decomposition of white light by a prism, we prefer to transform mathematically the FID in order to obtain its spectral or

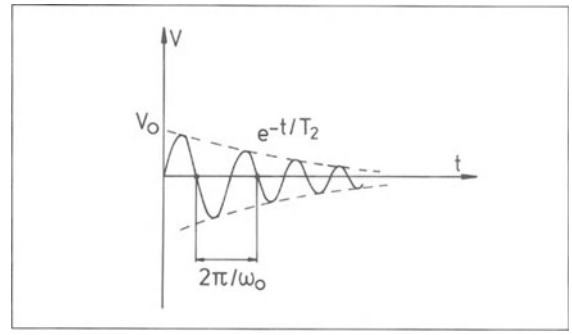

Figure 12. The FID vanishes exponentially with the T_2 time constant.

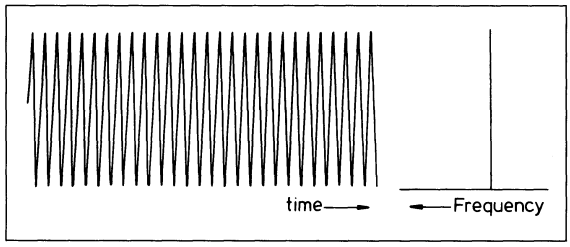

Figure 13. The NMR spectrum of a continuous sine signal is a line centered at the Larmor frequency.

frequency distribution (components) called the spectrum. This manipulation is the result of the *Fourier Transform (FT)* or more practically, because it is less time consuming in terms of computation, the *Fast Fourier Transform (FFT)*. For a spin isochromat (set of nuclear spins of a single atomic or molecular specie precessing at exactly the same Larmor frequency ω_0), the FID shape is a pure sinusoid of cosinusoid (Fig. 13) and its FFT or frequency spectrum is just a line centered on the frequency (pulsation) ω_0. Realistically, due to the relaxation time T_2, the spins do not all precess at the same Larmor frequency, they are spread out from each other, in terms of Larmor pulsation, and the FID shape is a decaying sinusoid or cosinusoid (Fig. 14). Therefore, the frequency spectrum or NMR spectrum is a gaussian or lorentzian with a width proportional to $1/T_2$.

When different species (or different isochromats) are mixed in a same sample, the FFT of the NMR signal is a set of lorentzians or gaussians (also termed peaks) each located at the resonance frequency of each species. One of the most simple examples is the NMR spectrum of H^1 in biological tissues (Fig. 15). It is roughly composed of two peaks, one from the pure water protons and the other from the fat protons. At a field of 1.5 Teslas, the frequency space between these peaks is around 220 Hz (3.5 ppm).

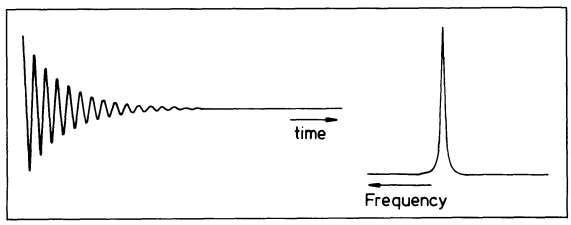

Figure 14. The NMR spectrum of an FID is a gaussian or lorentzian curve centered at the Larmor frequency and whose the width is proportional to $1/T_2$.

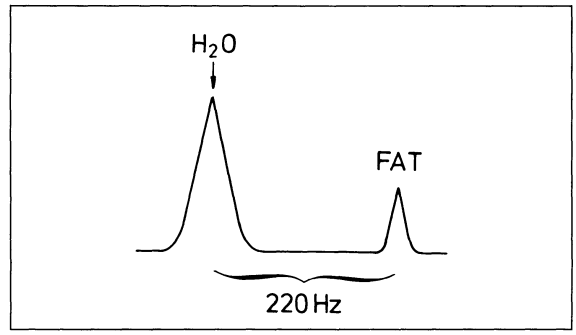

Figure 15. The NMR spectrum of a sample containing a mixing of water and fat is composed of two lorentzian peaks centered respectively at the resonance frequencies of water and fat.

In spectroscopist terminology, the physical phenomenon which characterises the Larmor frequencies of protons present in different molecular species (materials) all contained in one unique sample is called the *chemical shift* (σ).

I–11. Experimental T_2 times

11.1 *Field inhomogeneities*

When we speak about T_2 and T_1 relaxation times, we have seen that T_1 (the time needed for a complete return to thermal equilibrium state) was longer than the time constant (T_2) required for the complete disappearance of the NMR signal (FID) in the transverse plane xy.

We have seen that T_2 was related to the dephasing effect (loss of phase coherence) due to varying intrinsic local fields (B_{loc}) of the studied material. In the previous discussion we had used an unrealistic situation in which the external static magnetic field B_0 was supposed homogeneous (exactly the same at the location of any nucleus in the sample). In practice the decay of the signal in the xy plane is even faster than the decay predicted by the intrinsic T_2 of the examined tissue (Fig. 16). This enhanced loss of coherence results from the slightly different Larmor frequencies induced by small differences in the static magnetic fields (field inhomogeneities) at different locations of the sample. Three main phenomena are responsible for the differences of the static field experienced by the nuclei: (i) the imperfections of the main static magnetic field B_0, (ii) the application of pulsed field gradients for the image encoding, and (iii) the

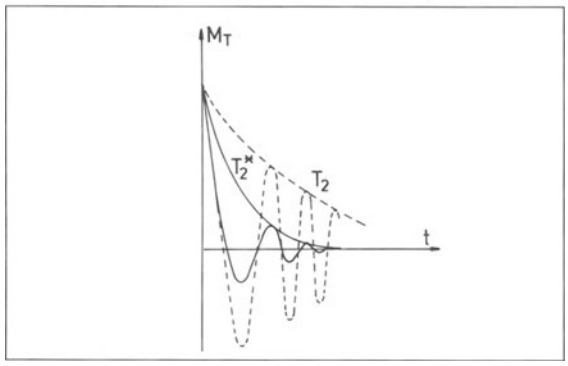

Figure 16. Due to field inhomogeneities, the FID decays with a time constant T_2^* smaller than T_2.

strong variations of local tissue susceptibility (e.g., air, tissue).

Under these circumstances, the observed decay time constant of the FID becomes:

$$1/T_2^* = 1/T_{2tissue} + 1/T_{2inh} = \\ = 1/T_{2tissue} + \gamma\,\delta B_0 \qquad (8)$$

where

$1/T_2^*$: is the observed relaxation rate of the transverse magnetization;
$1/T_{2tissue}$: is the intrinsic tissue relaxation rate;
$1/T_{2inh}$: is the field inhomogeneities relaxation rate (including susceptibility effects);
γ : is the proton gyromagnetic ratio;
δB_0 : is the field inhomogeneities.

From this equation, we see that T_2^* is always shorter than T_2.

11.2 *Notion of phase*

The phase describes the angular displacement around the external field B_0 that the transverse magnetization and the individual nuclear spin accomplish against the time (Fig. 17). At the switch off of an $\alpha°$ RF pulse, the phase is null ($\varphi = 0$) relative to the y-axis of the transverse plane (the transverse magnetization and all the spins are aligned to the y-axis). As the time evolves, the phase increases and is related to the Larmor or resonance pulsation by the equation:

$$\varphi = \gamma B_0 t \qquad (9)$$

where, t is for the time evolution.

Due to the T_2 or T_2^* relaxation times, some nuclear spins dephase faster (F) than others which are slower (S). Therefore, the phase coherence ($\varphi = 0$) which exists just after the RF pulse disappears more or less rapidly with respect to T_2 or T_2^*.

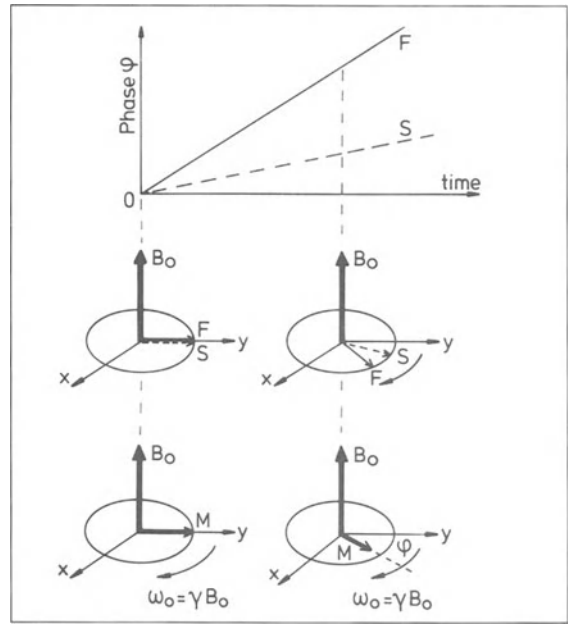

Figure 17. Slow precessing spins accumulate less phase than fast precessing spins.

SECTION TWO
ADVANCED IMAGING TOPICS

II-2. Spin-Echo (SE) pulse sequence – Echo time (TE) and repetition time (TR) – Weightings

1.1 *Spin-Echo pulse sequence*

After the spin system has been excited by a 90° pulse, the spins fan out as time progresses, some spins dephasing faster (labelled F) than others (labelled S) (Fig. 18). Due to the reversible nature of the dephasing process caused by magnetic field inhomogeneities, it is possible to rephase the spin system.

The initial transverse magnetization, reduced only by T_2 decay, can be reestablished by applying a 180° RF pulse along x or y, TE/2 milliseconds (termed the half echo time) after the initial 90° pulse (Fig.

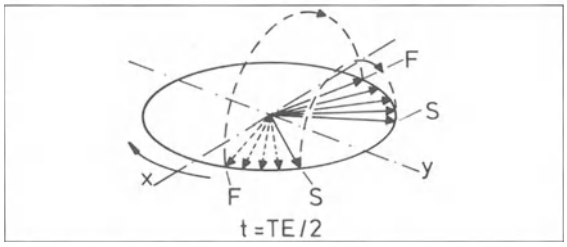

Figure 18. A 180° RF pulse turns the spins over into a mirror image position in the transverse plane.

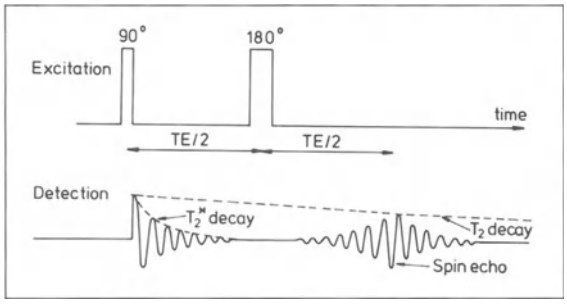

Figure 19. The initial transverse magnetization, reduced by the T_2 decay, can be reestablished by applying a 180° RF pulse TE/2 milliseconds after the 90° RF pulse.

19), turning the partially dephased transverse magnetization over into a mirror image position. In this way, the fast components (F) will catch up the slow ones (S), refocusing at time TE (termed echo time) and creating a spin echo (SE) (Fig. 20).

During MR image data acquisition, the sequence 90°–(TE/2)–180° is repeated 128, 256 or 512 times, each sequence being separated from the next by a period called the repetition time TR (Fig. 21). This pulse sequence 90°–(TE/2)–180°–TR is called a Spin-Echo pulse sequence.

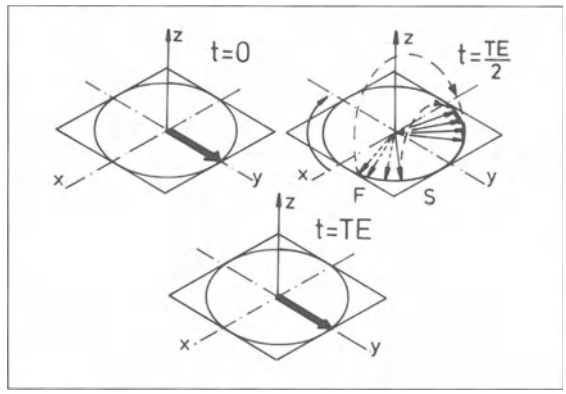

Figure 20. TE/2 milliseconds after the application of the 180° RF pulse, a spin echo is generated.

The echo (NMR signal following the 180° pulse) like the FID (just after the 90° pulse) are both decaying with respect to T_2*. However, the maximum amplitudes of the FID and the echoes decay exponentially with the T_2 time constant (Fig. 21).

An echo train is generated by the application of a series of 180°pulses which follow one unique 90° pulse. The echoes are separated each from the others by a time duration equal to TE (Fig. 21). This imaging sequence is called the multi echoes SE sequence. In this way, and using the maximum amplitude of each echo, we can draw the T_2 decay curve of the imaged tissues.

Because we are waiting for a period of time equal to TR before the new application of the 90° pulse, the longitudinal magnetization M_Z has recovered an amplitude depending on TR and T_1 of the considered tissues. Therefore, the maximum signal intensity of the FID and the echo depend on two experimental

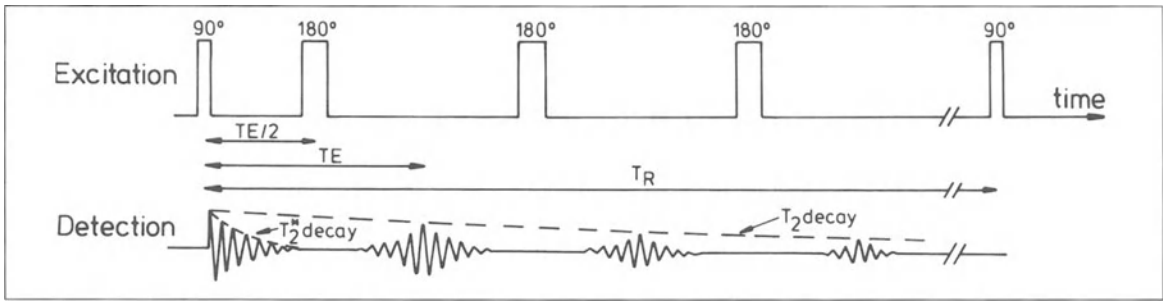

Figure 21. By applying a series of 180° RF pulses, each of them spaced by TE milliseconds, an echo train is generated. Each echo signal decays with T_2* while the maximum amplitudes of the echoes decay with T_2.

parameters (TR and TE) and three intinsic tissue parameters (proton density ρ and relaxation times T_1 and T_2) in accordance with the equation:

$$I \approx \rho\,(1 - 2e^{-(TR - (TE/2))} / T_1 + e^{-TR/T_1})e^{-TE/T_2} \quad (10)$$

From this equation we can see that it is mathematically possible to weight the signal intensity independently T_1, T_2, ρ or by a mixing of these three parameters.

1.2 *Weightings*

If TR is short, routinely from 400 ms to 600 ms, the longitudinal magnetization recovery M_Z, which is the maximum amplitude of the transverse magnetization M_{xy} (FID) following the 90° pulse (TE = 0), depends very strongly on T_1, the FID is T_1 weighted. Therefore, the maximum amplitude of the echo for very short TE routinely in a range from 20 to 30 ms will be T_1 weighted. However by increasing the value of TE, the NMR signal will depend more and more on T_2 with a rapid disappearance of the T_1 effect (Fig. 22). The NMR signal will be then weighted by a mixing of T_1, T_2 and ρ.

On the other hand, if TR is long (greater or equivalent than T_1), the signal intensity does not depend any longer on T_1 because the longitudinal magnetization M_Z has had enough time to recover almost its full amplitude. In this situation, if TE is as short as possible (ideally 0 ms), the maximum amplitude of the echo depends only on proton density (ρ weighted NMR signal). When TE increases, the echo becomes very strongly dependent on T_2 (T_2 weighting). In Table 3 we summarize these results.

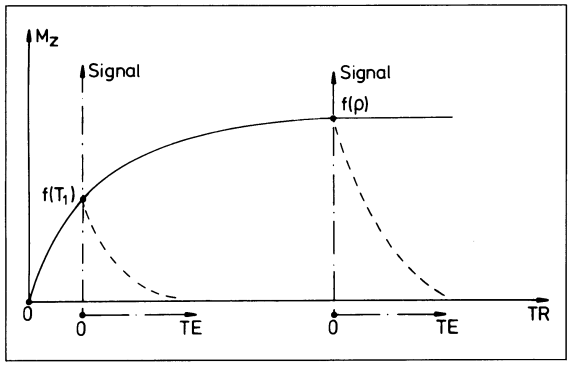

Figure 22. For short TR values, the longitudinal magnetization depends much on T_1. On the other hand, for large TR values, it depends only on the proton density (ρ).

Table 3.

Weighting	TR (ms)	TE (ms)
T_1	Short < 500	Short <30
T_2	Long >1800	Long >30
Proton density	Long >1800	Short <30

1.3 Phase concept

Coming back to the principle of the spin-echo, we see that just at the moment when the 90° pulse is switched off, all nuclear spins are in-phase in the transverse plane. By definition, we will say that the phase of all spins is null: φ=0. After the RF pulse is switched off, due to local fields (in general all field inhomogeneities) and static field, each spin precess around B_0 with an own angular velocity. Therefore, from point to point, the phase of each spin evolves so that at the moment of the 180° pulse switching (T=TE/2) the phase is:

$$\varphi(T=TE/2) = \gamma\,.\,(B_0+\delta B_0)\,.\,TE/2 \quad (11)$$

where δB_0 describes all field inhomogeneities and T is for the time.

The application of the 180° pulse corresponds to a time reversal leading to a phase evolution such that for all time t greater than TE/2:

$$\varphi(T=TE/2+t) = \gamma.(B_0+\delta B_0).(TE/2-t) \quad (12)$$

where t is for time evolution after the 180° pulse.

It is obvious that after a time t=TE/2, the phase becomes again null for each nuclear spin (Fig. 23).

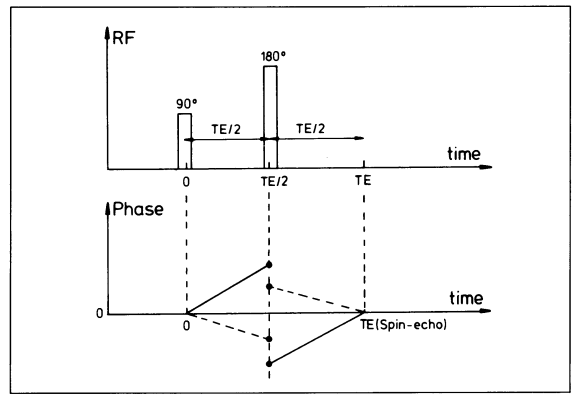

Figure 23. The 180° RF pulse reverses the sign of the spin phase.

That is another definition of the spin-echo signal or more generally another manner to describe the regeneration of the NMR signal.

II-2. Image contrast - Contrast weighting

2.1 *Contrast definition*

We can define the contrast between two adjacent regions of an image as being the apparent brightness difference between them. This subjective definition can take a mathematical form described by the following equation:

$$C = (I_A - I_B) / I_0 \qquad (13)$$

where I_A and I_B are the image pixel values measured in two adjacent regions A and B within the image. I_0 is a normalization factor which could be the signal intensity that would be recorded from a 90° pulse after the complete relaxation of the longitudinal magnetization M_Z prior to this pulse.

2.2 *Contrast weighting*

A clear example in order to understand the principle of signal weighting and the value of this weighting is the comparison between CSF tissue and White Matter (WM) tissue. More particulary, the relaxation times and the proton density of CSF are larger than those of WM (Fig. 24).

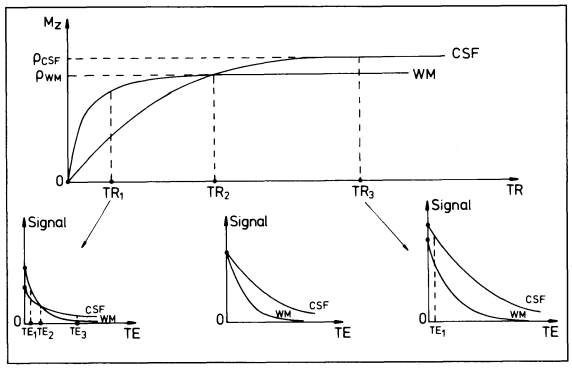

Figure 24. For short TR and TE values, the tissue signals are T_1-weighted, the White Matter (WM) being brighter than the Cerebro-Spinal-Fluid (CSF). For large TR and short TE values, the signals are ρ-weighted and become gradually more T_2-weighted with the increase of TE, the CSF becoming gradually brighter than the WM.

For small values of TR ($TR_1 \approx 500$ ms) and TE values as short as possible ($TE_1 \approx 20$–30 ms), CSF signal is smaller (dark region on the image) than WM (bright on the image); the image is strongly T_1 weighted. For progressively larger TE values, the signals are more and more T_2 weighted, WM becoming progressively less and less bright than CSF until the CSF and WM signals become the same (TE_2). For TE values (TE_3) greater than TE_2, there is a signal amplitude inversion, the WM becoming darker than the CSF. Unfortunately, due to the signal weakness at TE=0 and fast T_2 signal decay the images become rapidly noisy. This is why we do not use this sequence to acquire clinically practicable T_2 weighted images.

There is a TR value ($TR=TR_2$) for which, if TE=0, CSF and WM signals have the same intensities, CSF and WM being thus isointense within the image. For this particular TR value, increasing TE, CSF becomes gradually brighter than CSF.

Finally, for TR values greater than TR_2 ($TR_3 \approx$ 2s) with TE as small as possible ($TE_1 \approx 20$–30ms), we observe a signal amplitude inversion; CSF is brighter than WM and the image is ρ weighted and quasi independent of T_1. Increasing progressively TE, CSF becomes gradually brighter than WM; the image becomes gradually more T_2 weighted. Therefore, for TE around 100 ms, WM is completely dark while CSF remains bright.

2.3 *Contrast curve for two tissues*

Another way to present the above discussion is to draw the contrast curve using the definition equation of contrast. By this curve, we can easily check the

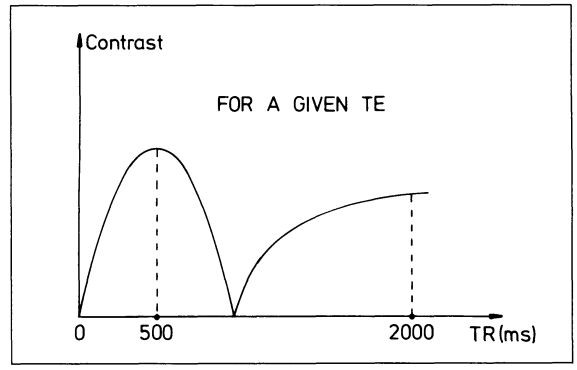

Figure 25. The contrast curve permits us to check the optimal TR and TE values in order to obtain the best contrast between tissues.

optimal values of TR and TE in order to get the best T_1 and T_2 weighted contrast between the tissues of interest (Fig. 25).

This particularity is one of the most important characteristics which distinguishes Computed Tomography from Magnetic Resonance Imaging. MRI has the ability to generate various kinds of contrast between tissues, just by working on the intrinsic magnetic properties of the tissues (by means of experimental parameters TR and TE) and without injection of any contrast product.

Nevertheless, contrast agents are currently required for specific reasons, for example to increase the contrast between tissues which are well vascularized and others which are less well vascularized. The contrast agents also permit to decrease the imaging time.

II–3. Image reconstruction

3.1 *General principle*

Once described the FID generation and the principle of weighting, we now have to explain how MR images are produced from the weighted NMR signals. To create an image it is necessary to have spatial encoding of the radiofrequency signals emitted from the body.

As seen previously, the precession frequency depends linearly on the strength of the magnetic field. Consequently, if the magnetic field differs from voxel to voxel (or pixel to pixel) within the volume of the patient, the frequency of the signal will also differ from voxel to voxel.

The summed signal of all voxels, and that which is measured by a coil outside the patient, would then be built up of components of different frequencies. This complicated signal can be unravelled into its components by Fourier transformation. In this theoretical case, a Fourier transformation of the total signal would reveal entire contributions from all voxels. Unfortunately, by this procedure, a large number of measurements would be required to reconstruct an image. This would lead to a too large imaging time.

3.2 *Slice selection*

The external magnetic field can differ from voxel to voxel just by adding to the static and RF magnetic fields a special hardware device which generates magnetic field gradients. This apparatus is able to generate, parallel to the external magnetic field B_0, a magnetic field, the amplitude of which varies lineary along one selected direction of the 3 dimensional space (e.g., y-direction in Fig. 26).

Suppose that a tube of y axis has been filled with a material characterized by a variable proton density along this axis. Suppose that this tube is placed in a static field of usual homogeneity (10^{-6}) and direction y to which is added a linear field gradient in the y-direction (selection gradient). Every section of the tube perpendicular to the gradient direction has its own precession frequency. Therefore, if we record the FID emitted by the tube and if we Fourier transform it, the computed spectrum is just the projection of the tube proton density along the y-axis (Fig. 27).

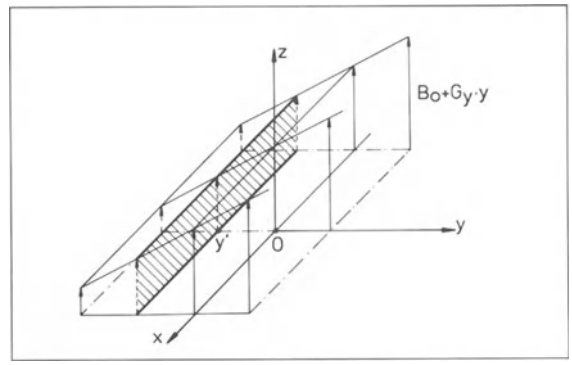

Figure 26. The gradient coils generate linear magnetic field gradients along any direction in a 3-dimensional space (e.g., G_y along the y-direction).

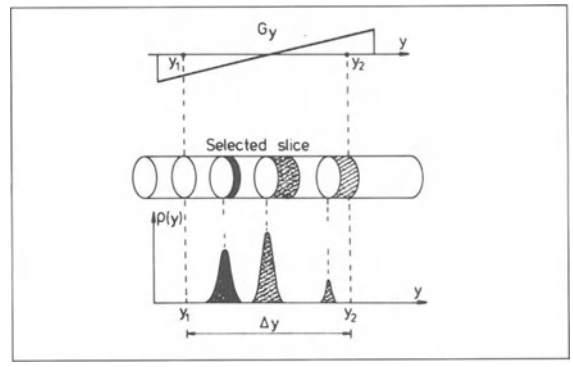

Figure 27. A magnetic field gradient applied along the y-axis of a tube filled with a variable proton density permits us to get the projection of the tube proton density on this axis.

To turn the magnetization of a particular section perpendicular to B_0, an RF pulse with a frequency equal to the Larmor frequency of this selected slice must be applied. Consequently, if an RF pulse with a narrow range of frequency (bandwidth), symmetrically distributed with respect to a central frequency, is applied in the presence of the selection gradient only a narrow band of protons will respond. Therefore, only the magnetization within this band will be turned perpendicular to the external magnetic field and only the protons contained inside this sample band will produce a signal in the detection coil. Remark that the slice thickness depends on the width of the RF pulse frequency bandwidth and the gradient strength.

The decrease of the selection RF bandwidth and the increase of the selection gradient field strength reduce the slice thickness.

3.3 *2-D Fourier imaging (spin-warp imaging) - 2D FT*

This technique which owes its introduction to Kumar, Welti and Ernst employs two orthogonal linear gradients sequentially to encode the image plane. We describe this method only because it is the most commonly employed and is the only one that we have used (Fig. 28).

A particular slice having been selected, each of its voxels must be characterized. As we are confronted with a two-dimensional problem, each of these voxels must be uniquely labelled by two characteristics (Fig. 29).

3.3.1 *Phase encoding gradient*

The excitation of nuclei in the imaging or selected slice is followed by a pulsed gradient oriented in one of the two imaging plane axes, for instance the x-axis. During the period of application of the x-gradient (phase-encoding period t_x), the nuclei inside each column of voxels perpendicular to the x-axis experience a magnetic field slightly different from that experienced by the other columns. Then, the spins contained inside each column precess at the same angular velocity (Larmor pulsation ω_x^i) but that is slightly different from column to column. This Larmor pulsation which characterizes univocally this column is expressed by:

$$\omega_x^i = \omega_0 + \gamma G_x x^i \qquad (14)$$

where i = 1, N_x is the number of each column.

N_x is the image resolution in the x-direction or the total number of columns;
ω_0 is the Larmor pulsation due to B_0;
γ is the proton gyromagnetic ratio;
G_x is the amplitude of the x-gradient.
x^i is the location of the ith column.

When G_x is switched off, all the spins of the selected slice, i.e. all the columns, precess again at the same Larmor pulsation ω_0. However they *remember* the former presence of the G_x-gradient by retaining characteristic-dependent phase angles. Each of these phases (e.g., φ_x^i), corresponds to the angle made by all the spins of each column (e.g., i) with respect to the x-axis. Therefore, for each column labelled i, we have a characteristic phase angle given by:

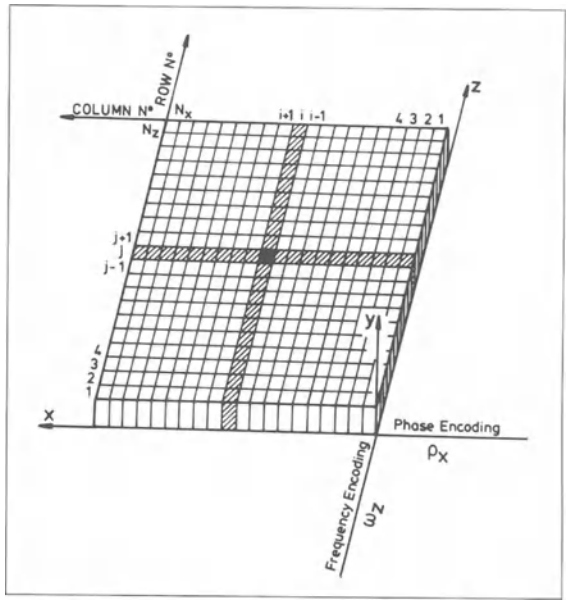

Figure 29. Each pixel (i, j) of the image plane is univocally characterized by 2 parameters, one phase and one frequency.

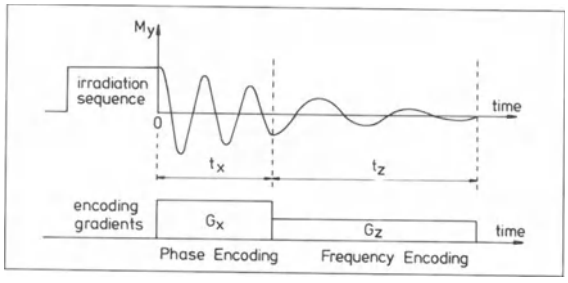

Figure 28. The image plance encoding is realized by means of the phase and frequency encoding gradients.

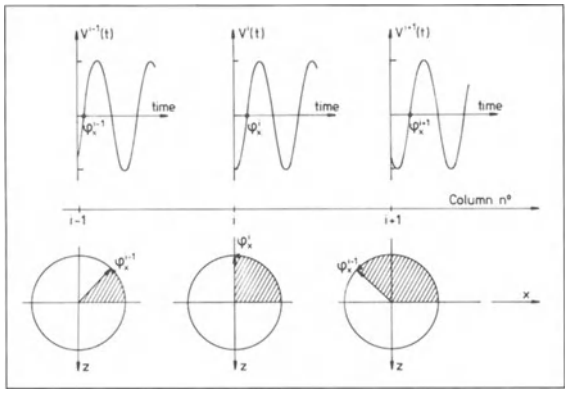

Figure 30. By the phase encoding gradient, each column of the imaging plane generates a NMR signal which is slightly shifted in time from the signals produced by the others.

$$\varphi_x^i = \gamma G_x t_x x^i \tag{15}$$

where

t_x is the period of application of G_x;

x^i is the position of the column i along the x-axis.

When G_x is switched off, if we could measure individually the FID generated by the spins of a particular column, we should have for each column of voxels a sinusoid oscillating at the Larmor pulsation ω_0. But from column to column the recorded sinusoids would be slightly shifted in time each from the others. This small dephasing or time shift is exactly the *memorised phase* φ_x^i that is unequivocally related to the position of nuclei along the x-axis. The FID of the column i could be expressed by:

$$V^i(t) \approx \sin(\omega_0 t + \varphi_x^i) \tag{16}$$

where i=1, N_x.

When movements are present in the direction of the phase encoding gradient, there are uncontrollable additional phases added to the controllable ones imposed by this gradient. This leads to phase misregistration and movement artefacts in the image plane along the preparation gradient direction.

3.3.2 *Frequency encoding gradient*

Following the x gradient, a third gradient is applied along z. This one creates a distribution of frequencies (*readout* or *frequency encoding gradient*) along the z-axis. Now, instead of studying the effect of the G_z-gradient when it is switched off, as done with the phase-encoding G_x-gradient, we are going to examine the nuclear spins within each voxel in each row (perpendicular to the z-direction) of the imaging plane during the application of G_z. The precession frequency (e.g., ω_z^j) will be different from row to row and is given by:

$$\omega_z^j = \omega_0 + \gamma G_z z^j \tag{17}$$

where j = 1, N_z is the number of each row.

N_z is the image resolution in the z-direction or the total number of rows;

ω_0 is the Larmor pulsation due to B_0;

γ is the proton gyromagnetic ratio;

G_z is the amplitude of the z-gradient.

z^j is the location of the jth row.

If we could measure individually the FID generated by the spins of each voxel (i,j) of each row (j) during the application of G_z, we should observe sinusoids given by the equation:

$$V^{ij}(t) \approx \sin(\varphi_x^i + \omega_z^j t) \tag{18}$$

where i=1, N_x and j=1, N_z.

In summary, this signal $V^{i,j}(t)$ *and therefore each voxel* (i,j) *is characterized univocally by two parameters, a phase* φ_x^i *which is related to the x-positions and a frequency* ω_z^j which is related to the z-positions. The univocal encoding of the image plane is reached.

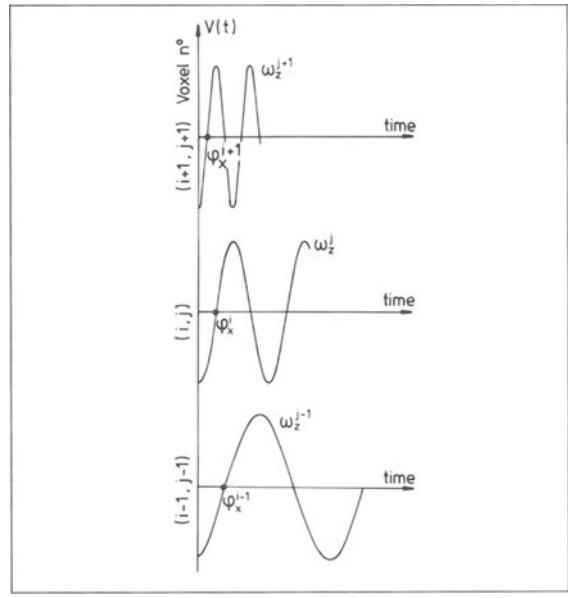

Figure 31. The signal generated by each voxel of the imaging plane is characterized by a phase shift which is related, e.g., to the x-positions and a frequency which is related, e.g., to the z-positions.

3.3.3 *Raw data*

In practice, we must measure the NMR signals, i.e. echoes, only during the existence of the measurement gradient, however, we cannot measure the echo signals voxel by voxel because this procedure would require too much imaging time. Therefore, the MR signals recorded by the RF coil is the superposition of the signals emitted simultaneously by all the slice voxels and we observe very complicated signal shapes instead of simple sinusoids. These signals named interferograms will be sampled by a finite number of points N_z during the G_z-gradient switching time t_z. The data collected by this process are called *raw data* and are stored in the computer memory or on hard disk. Each of these raw data can be expressed by the equation:

$$V(t_k) \approx \sum_{i,j} V_{ij}(t_k) \tag{19}$$

or

$$V(t_k) \approx \sum_{i,j} \sin(\varphi_x{}^i + \omega_z{}^j t_k) \tag{20}$$

where $i = 1, N_x$ and $j = 1, N_z$.

In summary, the NMR signal coming from the selected raw data is encoded for positions in the x-direction by means of a phase angle and for positions in the z-direction by means of a frequency. In addition, this signal gives us information not only about one row and one column but, at the same time, about all the voxels labelled (i,j) constituting the imaging plane.

3.3.4 *Two Dimensional Fourier Transform (2DFT)*

Although this signal contains information from all voxels in the imaging slice, the information gathered from one cycle (excitation, phase-encoding, readout) is not sufficient to determine the signal amplitude required in each voxel to reconstruct an image. Therefore, the cycle will be repeated with different settings (N_{ph} = 128, 256, 512) of the phase-encoding gradient, each separated from the following by a time duration equal to the repetition time TR. The N FID's, each corresponding to a different value of the preparation gradient, will be sampled N_{meas} times during the application of the measurement gradient. Each FID is converted into the frequency domain and consequently in the space domain by a two-dimensional Fourier transform of the 2D raw data (2D spectrum). Finally, this 2D spectrum is encoded in grey levels to give the MR images.

The gradient manipulations to select the slice of interest and to encode the imaging plane is another important characteristic of MRI. We can image any slice plane, transverse, sagittal, coronal, oblique and, very interesting for cardiac examinations in particular the double oblique slice plane.

II–4. Acquisition times – Scan time

4.1 *General expression*

Thanks to the description of the 2D-FT imaging method we are now able to write the equation giving the time (T_{acq}) required to acquire a NMR image.

$$T_{acq} = n_{av} \cdot TR \cdot N_{ph} \tag{21}$$

where

n_{av} is the number of averages or the number of times that we repeat the complete cycle of acquisition;

TR is the repetition time;

N_{ph} is the image resolution or number of phase-encoding steps.

4.2 *Multiple slice (MS) acquisition*

If the repetition time is long enough, we can select and acquire the raw data of several images which are contiguous or not contiguous; each image being separated from the following by a distance proportional to the slice thickness (*slice gap*). More recently, the number of images can be distributed in packages of slices, each pack being located in a different anatomical region and characterized by its own orientation parameters (e.g., if we can use 9 slices for a spine examination, we can create 3 packages of 3 slices, each pack being positioned independently from the others, to image 3 vertebras). The number of images that we can use depends on TR, the machine hardware, TE, the number of echoes and the use of special pre-sequences, e.g. presaturation pulses. When a sequence acquires several slices with several echoes, it is called *multiple slice multi echoes (MSME)*.

SECTION THREE
SPECIAL TOPICS

III–1. Fast imaging methods – Gradient echoes sequences

1.1 *Introduction*

All the classical pulse sequences like SE sequence have relatively long scan times which have two main disadvantages: (i) there is an increase of motion artefacts due to either patient movement or to involuntary motions such that cardiac beats, breathing or stomach and bowel movements. All these motions blur the MR images; (ii) preclusion of 3D imaging.

Therefore, to avoid blurring of an image, the scan time must be less than the time which characterizes the motion. Naturally, the breath can be held for a while, although it is doubtful whether an old or a very sick patient could manage more than 10 s pause. For heart studies, it is possible to gate the data acquisition to the cardiac cycle by triggering events from R-wave. Unfortunately, irregularities in the heart cycle vitiate this approach. There is also the question of patient comfort and management, as well as the economic factor. All of which point to the realization of as short an imaging procedure as possible.

The most simple approach to reducing the scan times is to decrease the repetition time TR. However, in a simple spin echo pulse sequence, although a reduction of TR results in a reduction in the acquisition time in the same proportion, it also results in a diminution of the echo amplitude which is related to the T_1 of the tissues. To reach this aim of reduced scan time without this undesirable loss of signal we have to use special pulse sequences termed *gradient echo pulse sequences.*

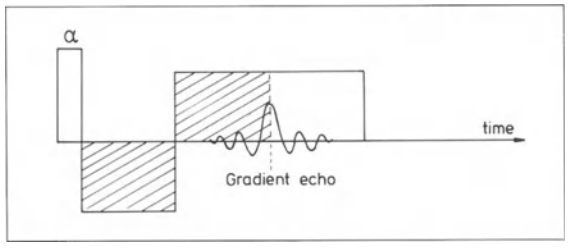

Figure 32. After a RF pulse, a delayed FID or gradient echo can be generated by the application of a dipolar magnetic field gradient.

1.2 *Principle*

There are two important physical properties at the basis of fast imaging methods: (i) the generation of gradient echoes, and (ii) the use of low flip angles.

(i) *Gradient echoes.* It is possible to generate a gradient echo or more strictly speaking a delayed FID by using a read-out dipolar gradient after the excitation pulse (Fig. 32). By this procedure, during the first gradient lobe, the spins accumulate phases but, when the gradient sign is reversed (second gradient lobe), this phase vanishes and an echo is produced (Fig. 33). The maximum echo amplitude (null phase) happens at the center of this second lobe.

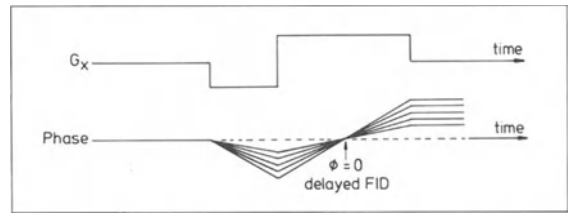

Figure 33. The phase shift accumulated during the first lobe of the dipolar magnetic field gradient is cancelled during the second lobe.

So, the 180° pulse indispensable to create the echoes in the 'classical' SE sequence is no longer needed with fast pulse sequences. Unfortunately, in this situation, the phase resulting from field inhomogeneities are no longer compensated, leading in particular to susceptibility artefacts (*cf.* III–5.2) and T_2* contrast weightings instead of T_2 SE contrast weightings. This is because the sign of the phase is reversed with a 180° pulse (*cf.* II–1.3) but not with a dipolar gradient (Fig. 33).

(ii) *Low flip angle.* According to Bloch equations, that govern the classical movement of the nuclear magnetization, the MR signal increases with the sine of the excitation flip angle whereas the loss of longitudinal magnetization – or saturation – changes with the cosine of the flip angle α (Fig. 34).

When flip angles of less than 90° are used, less longitudinal magnetization is lost and the signal recovers (returns to equilibrium) more rapidly be-

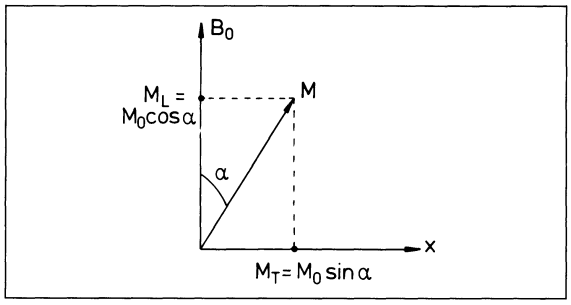

Figure 34. After an $\alpha°$ RF pulse, the longitudinal magnetization changes with the cosine of the flip angle while the transverse magnetization changes with the sine of this angle.

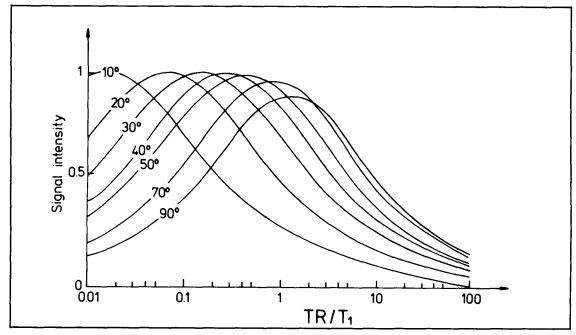

Figure 36. The flip angle must be optimized with respect to the TR/T_1 ratio.

tween excitations. This phenomenon is described by the Ernst curves (Figs. 35 & 36) representing in particular S/N against TR/T_1. As a result, shorter TR's may be used leading to a *steady state* situation.

Remarks that since a flip angle of less than 90° results in residual longitudinal magnetization, it is inappropriate to use again a 180° pulse to generate the spin echo as the latter would also act on the residual longitudinal magnetization and would invert it. Such a situation would lead to a non-equilibrium state. *That is another reason for employing gradient refocusing.*

1.3 *Signal and contrast properties of partial flip angle images*

The contrast and the contrast weighting in the fast imaging sequences are very dependent on how the pulse sequence is implemented in the machine and are thus factory dependent. Currently there are a profusion of different gradient echo pulse sequences

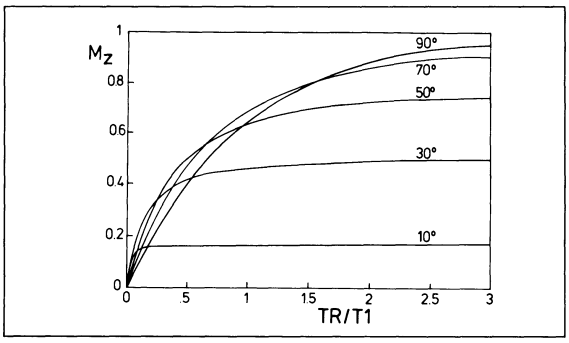

Figure 35. For short values of TR/T_1, the longitudinal magnetization recovery depends strongly on the flip angle.

termed by a very great variety of symbols as: FFE, FLASH, FISP, GRASS, SSFP, etc.

The basic difference of all these pulse sequences lies in the ways (spoiler gradients) used to cancel the residual transverse magnetization existing when very short TR and TE are employed (TR, TE $\ll T_1, T_2$). It is also to be noted that with fast sequences the pure T_2 contrast does not exist any more and is replaced by T_2* contrast which is dependent on the field inhomogeneities, the magnetic susceptibility, the flow effects, ... (generally, non reversible phase perturbations). Therefore, with rapid imaging, the contrast generation depends on several mechanisms, the principal ones being: (i) the relaxation times T_1 and T_2*, (ii) the phasing of water and fat, and (iii) the flow enhancement.

In our images we have used the FFE pulse sequence and the role of the latter mechanisms on the contrast can be summarized as follows.

(i) *Role of relaxation times* (Table 4)
In summary, we observe T_1-weighting for $\alpha > 40°$ and long TR (200–400 ms), T_2-weighting for $\alpha < 20°$ (even with short TE) and short TR (20–50 ms).*

Table 4. Role of relaxation times on TR and TE.

Weighting	Flip angle	TR(ms)	TE(ms)
Density	<20	200–400	8–15
T_1	>40	200–400	8–15
T_2*	<20	200–400	30–60
Heavy T_2*	>30	20– 50	8–15

(ii) *Phase of water and fat spins.* As seen previously, the difference in resonance frequencies of fat and

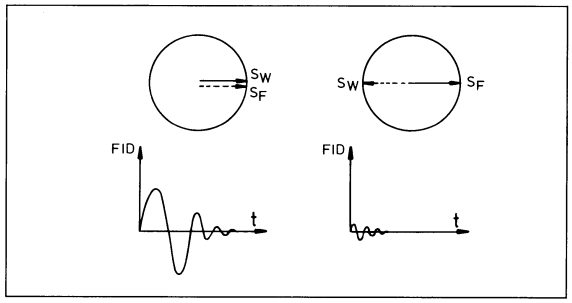

Figure 37. With the fast imaging sequences, depending on the TE values, the fat and water signals can be in-phase or in opposed phase. Respectively, the detected NMR signal will be maximum or almost null.

water protons is about 3.5 ppm. Therefore, depending on the value of TE the resonances of these two species can be in-phase (TE equals a multiple of 4.3 ms at 1.5 Teslas) or in opposed phase (TE equals a multiple of 2.2 ms at 1.5 Teslas), almost cancelling out to produce a theoretically (field homogeneity problems) very small signal (Fig. 37).

(iii) *Flow enhancement.* After several RF excitations, static tissues reach a steady state which produces a *saturation effect.* Strictly speaking, this involves the elimination of all measurable magnetization, in particular if the recorded signal is small. However, rapid circulating spins (high velocity blood) do not saturate because, between two successive excitations, there is a replacement of unsaturated spins inside the imaging plane. Therefore, fast-flowing blood produces high intensity signals (Fig. 38).

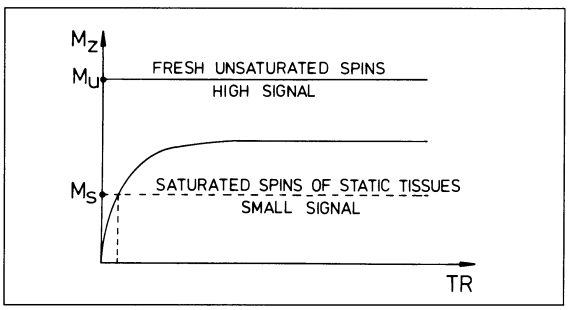

Figure 38. After several RF excitations, stationary tissues are saturated and produce low NMR signals while unsaturated tissues like flowing blood generate high signals.

1.4 *Acquisition time*

For a fast imaging technique like the *FFE pulse sequence* the minimum TR is around 10 ms. Using equation (21) for T_{acq}, the minimum acquisition time for a single slice is theoretically: $T_{acq} \approx 2.56$ s for a number of phase encoding steps $N_y = 256$.

Unfortunately, this acquisition time is again too long to obtain motion free imaging or *real time imaging* (breathing, cardiac beats, abdominal movements) even if we reduce N_y encoding steps or if we employ the *Half Fourier* technique. That is why we have to use again motion synchronized devices, ECG, respiratory monitoring and gating, to reduce those artefacts.

III-2. Ultra fast imaging - The close future

2.1 *Principle*

Currently, thanks to important hardware improvements, it is possible to reduce greatly the repetition time and the echo time as well as the reconstruction (fast array processors) and the data transfer times (computer and data links) between the host computer and the image display. The latter has become more and more important when image acquisition times reach the sub-second level. Two kinds of *ultra fast* techniques can be distinguished: (i) the methods based on the previous fast imaging ones again termed multi-shot techniques, and (ii) those based on the *Echo Planar Imaging* (EPI) procedure again called one-shot or *single-shot* technique.

2.2 *Fast imaging based methods - Multi-shot methods*

They are termed *Snapshot-FLASH, TURBO-FLASH, Fluoroscopy,* etc. and, as in fast imaging procedures, one phase encoding is acquired per RF pulse and the echo is created by gradient reversal also named gradient recall. Their method is the drastic reduction of TR and TE. In the extreme limits, TR and TE can be reduced respectively 5 ms and 2 ms when flip angles lower than 5° are used. With these parameters and for 128 phase encoding steps, the minimum acquisition time for one slice would be: $T_{acq} \approx 320$ ms using the Half Fourier procedure. The main problem encountered with those high speed methods is the almost complete disappearance of T_1 and T_2

contrasts. The NMR signal and the tissue contrast are dominated by proton spin density ρ.

On the other hand, because very short TE are employed, there is one considerable advantage intrinsic to these methods: the susceptibility artefacts (*cf.* III-5.2) as well as B_0 inhomogeneities are no longer visible and the effective spin-spin relaxation time T_2^* is almost T_2.

2.3 *Weighting of ultra fast sequences*

To benefit from the short T_{acq} and the increased pure T_2 dependence of the NMR signal and to improve the T_1 and T_2 contrast weightings, these latter being generally accepted as determinant parameters of all medical and biological applications of MRI, we must use different types of classical MR experiments prior to the fast sequence. In this way, the classical MR sequences produce a *magnetization label*, which is stored as different values of longitudinal magnetization M_Z and then measured by the high speed imaging sequence, e.g., inversion-recovery for T_1 pre-weighting, spin-echo for T_2 pre-weighting, etc. (Fig. 39).

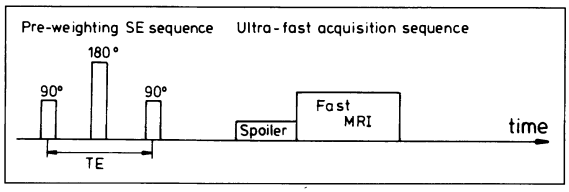

Figure 39. To counterbalance the low weighting of ultra-fast sequences, pre-weighting pulses are used.

2.4 *EPI - Single-shot method*

Instead of using many excitations of the imaging plane, each followed by the recording of one NMR signal (*cf.* III-2.2), MR images can be produced by using a single RF excitation of the imaging plane. This RF pulse is followed by a series of MR signals which are generated by frequent reversal of at least one magnetic field gradient (Fig. 40).

Therefore, using a single RF excitation (single-shot), one complete image can be acquired in an acquisition time $T_{acq} \approx 32$ ms for 64 phase encoding steps. In other words, all the phase encodings are measured by just one radiofrequency irradiation of the imaging plane. Of course, after a recovery period, in a range from 60 ms to 1 s, the process can be

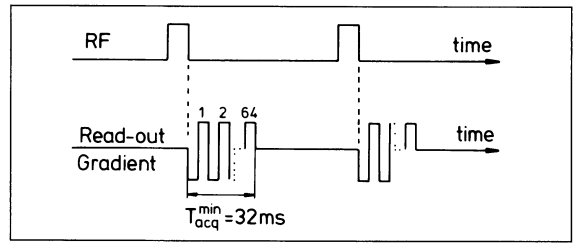

Figure 40. With EPI pulse sequence, the full image raw data are acquired by using a single RF pulse.

repeated and the same phase encodings measured again. This NMR method produces images at a rate 10 times higher than the ultra-fast multi-shot techniques. Unfortunately, it means that the hardware encounters very rigorous conditions, the most important being the use of special gradient coils able to generate gradient with a *rise time* Δt (switch time) less than 1 ms (Fig. 41). Therefore, the gradient coils of the current or classical imagers can no longer be used with this EPI method.

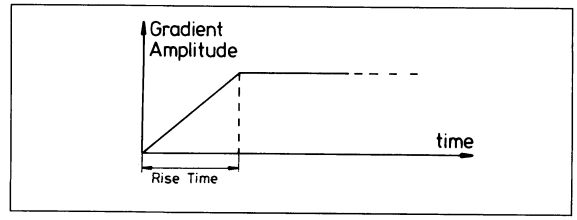

Figure 41. The magnetic field gradient rise time is an important hardware characteristic to allow the EPI pulse sequence application.

III-3. Flow phenomena

The interpretation of the signal from flowing blood is not easy considering the wide number of parameters to be taken into account. The main ones are: (i) the type of flow (pulsatile or not pulsatile), the velocity, the acceleration, a secondary flow and the turbulence; (ii) the sequence parameters (in particular the RF saturation pulse), the gradient strengths and their timings, and the echo time; and (iii) finally, the orientation of the vessel to the imaging plane. Two main causes influence the MR signal inside vessels. The first one is related to the transport of spins into and out of the imaging slice. The second is due to the most current image reconstruction method used, the 2DFT or spin-warp method.

As phase and frequency encodings are used with this method, blood movements in the presence of field gradients (encoding gradients) introduces phase shifts that influence the signal intensity in the image. We are beginning to discuss flow for the classical spin-echo pulse sequence. We will explain further the modifications due to the employment of fast imaging pulse sequence.

3.1 *Phase and flow*

3.1.1 *Flow and magnetic field gradient*

The flow effects due to blood motion in the direction of imaging gradients are recognized as *spin-dephasing, odd-echo dephasing* and *even-echo rephasing*. Under the influence of this phenomenon, MR signal will be either decreased, or increased. As seen previously, after an RF pulse, the spins start to dephase with respect to the resonant frequency. If, in addition, magnetic field gradients are present, the nuclear spins at different locations in the excited slice precess at different frequencies. Therefore, for a given location, the associated phase is proportional to the gradient amplitude and its time duration with respect to the equation:

$$\varphi = \gamma G_x \int_{t_1}^{t_2} x(t')\, dt' \qquad (22)$$

where

$$x(t') = x_0 + v\, t' \qquad (23)$$

where

t_1, t_2 are respectively the moments of the switching on and switching off of the gradient;
x_0 is the spin position at the 90° pulse;
v is the flow velocity;
t' is the time variable.

From this equation we can write more generally the phase as:

$$\varphi = \varphi_{stat} + \varphi_{vel} \qquad (24)$$

where

φ_{stat} is for the stationary phase due to the stationary spins;
φ_{vel} is for the velocity related phase due to the spins with constant velocity.

If flowing blood, moving uniformly for more simplicity, is compared to the surrounding stationary tissues, we can demonstrate that, compared to stationary spins, the moving spins accumulate an extra phase term proportional to the velocity in the gradient direction. In addition, if we consider that there is a velocity profile through the vessel cross-section (e.g., laminar flow), all the protons within this section do not experience the same velocity and thus, do not move at the same velocity through the magnetic field gradient. The result is that the protons within this vessel section precess at different amount of phases leading to dephasing and signal loss. It can be demonstrated that at the moment of the first echo, this dephasing is not cancelled and results in effective loss of signal. In general, in multi-echoes imaging, this signal loss occurs for all odd echoes (*odd-echoes dephasing*). If there are not higher order terms present in the series expansion of the flow phase equation (24) (e.g., an acceleraiton term) or in the field gradient, we can observe a rephasing at the moment of the second-echo but also for all the even echoes (*even-echoes rephasing*). Two interesting remarks are to be made: (i) this rephasing occurs only for *symmetric echoes* (e.g., TE = 20, 40 ms); (ii) the strength of the selection gradient being weaker than the frequency and phase encoding gradient amplitudes, there will be less dephasing for blood flowing perpendicular to the imaging plane than for blood circulating within the slice plane.

3.1.2 *Turbulence*

Turbulence is present when randomly fluctuating velocities are encountered. Without the presence of any magnetic field gradient we meet once again a situation of spin dephasing but now without any chance of rephasing at any echo time. Therefore, turbulence leads to irreversible MR signal loss. This phenomenon is seen for instance surrounding the mitral valve, near vascular obstruction or in giant intracranial aneurysms. *Remark that this effect can appear simultaneously with another flow type (secondary flow) such as the laminar flow in the presence of partial vascular obstruction.*

3.2 *Time-of-flight effects*

Flowing blood can appear bright or dark depending on its velocity, the direction of flow and the imaging pulse sequence employed.

3.2.1 *High velocity loss*
The origin of this phenomenon is the blood movement between the saturation 90° RF pulse and the echo 180° RF pulse. This effect leads to signal loss that depends on the values of the echo time (TE) and flow velocity. As 90° excitation pulse influences only the protons of a slice with a well defined thickness, when the 180° read-out pulse is applied, there is a mixing of two spin populations. One is constituted of excited spins (able to produce MR signal) not yet gone out the imaging plane and another with saturated or non excited spins (unable to generate MR signal) coming from outside the selected imaging plane. Depending on the blood velocity and TE, the proportions of the two populations vary leading to an MR signal loss related to these two parameters.

3.2.2 *Flow related enhancement*
In some cases, flowing blood can also produce a strong MR signal. Two situations of image acquisition must be distinguished to better understand this flow phenomenon.

(i) *Single slice acquisition.* Depending on TR and the T_1 relaxation times of the stationary tissues surrounding a particular vessel, the amount of longitudinal magnetization recovery can be more or less important between two successive sequences (or two RF excitation pulses). In other words, these particular tissues will be partially saturated. On the other hand, during TR, more or less saturated flowing blood will be replaced by fresh unsaturated blood. Therefore, flowing blood produces a higher signal than adjacent stationary tissues. This effect is known as *Flow Related Enhancement* (FRE) or entry phenomenon and is optimum when the flow rate is such that all the blood in the slice thickness (dz) is replaced by fresh blood in the repetition time TR. This occurs when the blood velocity is given by: $v = dz/TR$ (25). In clinical MRI, the FRE is seen for instance with the slow blood of femoral veins while the signal cancels for the rapidly flowing blood of femoral arteries.

(ii) *Multiple slice acquisition.* In this situation the appearance of FRE within MR slices depends on how the multiple slice sequence is programmed in the imager. Let us suppose the simple case where the slices are excited successively by 90° pulses. Now, the blood spins are submitted more frequently to the excitation pulses at a rate given by: mdz/TR (26)

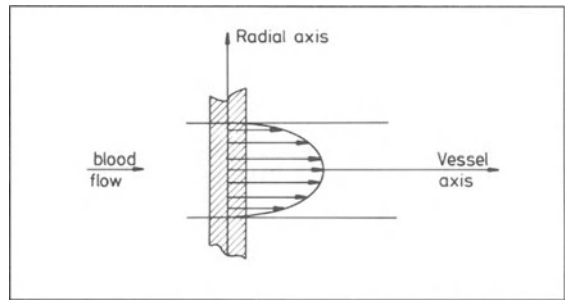

Figure 42. A laminar flow is characterized by a parabolic velocity distribution along the vessel radius.

where m is for the number of slices in the imaging volume. Therefore, we encounter a maximum blood enhancement within the entry slice as seen in the single slice situation. However, when looking at deeper slices, FRE persists but with decreasing MR signal due to the progressive increase of blood spin saturation.

3.2.3 *Signal variations within the vessel section*
In practice, the flow velocity is not the same all over the cross-section of a vessel, there is a velocity distribution that can be parabolic for laminar flow (Fig. 42). Depending on the amplitudes of flow velocities encountered in this distribution and the value of TR, but also TE, the proportions of saturated blood spins which remain inside the imaging slice at the application of the next 90° pulse and fresh unsaturated blood (without any transverse magnetization at the next 90° pulse) vary through the imaged vessel section, along the axes perpendicular to the vessel axis. Therefore, there is a combination of the 'high velocity loss' and the 'FRE' flow effects if we are looking for multiple slices sequence along a vessel. The situation is well described in the Fig. 43. It can happen that in the first slice, at the moment of the 90° pulse application, all the excited flowing spins of the previous sequence (depending on TR) have been replaced by fresh non excited ones. The intraluminal MR signal will be intense all over the vessel cross-section, if TE is not too long. For the second slice, there will remain an amount of previously excited or saturated spins mixed with an important population of unsaturated spins.

This mixing leads to an important bright circular region at the center of the vessel section; the rest of this section remaining dark. In the third slice, there

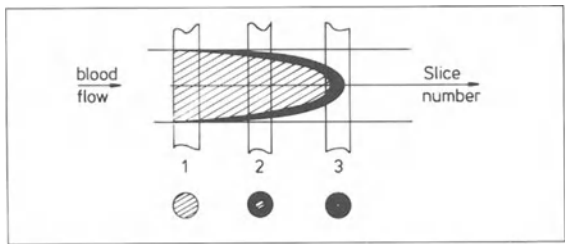

Figure 43. With a multiple slice acquisition, the blood appears as a bright spot at the center of the intraluminal vessel section and a dark MR signal filling the remaining of the vessel section.

is a small quantity of fresh inflowing blood spins and a large number of previously excited ones. The image pattern will be a small bright spot at the center of the intraluminal vessel section and a dark MR signal filling the remaining of this section.

3.2.4 *Diastolic pseudogating*

When an ECG is used to synchronize MRI acquisitions and when the gating is made on the R-wave, an extra enhancement of blood occurs for slices acquired nearest to the diastolic phase. This effect is due to slower diastolic blood flow. Therefore, if we observe the NMR signal generated by the blood of a vessel passing through the imaging volume, we meet firstly a strong signal for slices located at the entry surface. After, the intensity of this signal decreases progressively for the following slices until it increases again just before the diastolic phase. Finally, from this moment in the cardiac cycle, it decreases again within slices acquired during the systolic phase (Fig. 44).

3.3 *Flow and fast imaging*

The flow effects encountered during the former discussions dedicated more particulary to spin-echo pulse sequence are also present with rapid imaging techniques. The differences between SE and *Fast Imaging (FI)* with regards to flow are mainly due to the shorter TR used and the smaller flip angles utilized with FI. Therefore, rapid flow will be seen like an intense MR signal, stationary tissues will be dark and slow flow with intermediate intensities. That is the reason why flow inside the cardiac cavity can be seen brightly with FI whereas it does not give any signal with SE.

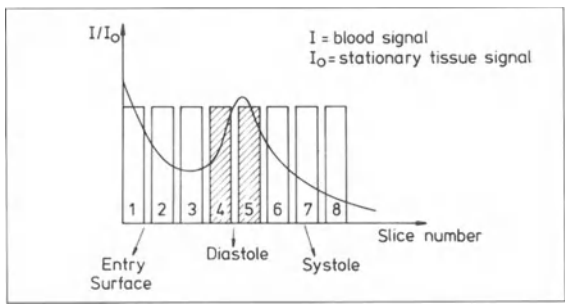

Figure 44. At the diastolic phase, there is an enhancement of the blood signal.

III–4. Image quality

4.1 *Signal-to-Noise ratio*

The basic principle of this ratio is that the NMR signal increases linearly with voxel volume while unstructured noise due to Brownian motion of the molecules increases with the patient volume seen by the detection RF coil and is independent of the voxel volume. Therefore, the S/N ratio is expressed by:

$$S/N \approx 1 / N_{ph} \cdot \sqrt{N_{ph}} \qquad (27)$$

where N_{ph} is the number of phase-encoding gradient steps.

Nevertheless, for larger objects, S/N per unit area rather than per pixel is a more appropriate measure because the eye integrates the pixels in a given area, the number of pixel being proportional to N_{ph}^2. Therefore:

$$S/N \approx 1 / \sqrt{N_{ph}} \qquad (28)$$

leading to a less dramatic drop in S/N with increasing N_{ph}.

4.2 *The number of averages* n_{av}

The signal increases linearly with n_{av} and the noise $\sqrt{n_{av}}$, resulting in an increase of S/N by $\sqrt{n_{av}}$. Signal averaging also appears to be a powerful solution to motion artefacts but penalizes acquisition time.

4.3 *Properties of the detection coil*

The coil causes noise through its resistance, which depends on the frequency (skin effect). In MRI systems, noise is predominantly by the patient. Surface coil produces a higher signal as a result of the

smaller distance between the tissue emitting the signal and the coil, and receives less patient-generated noise as a result of the smaller sensitive volume.

4.4 *Field strength*

After taking into account the properties of the detection coil, electronic equipment and losses in tissue but without any considerations about variations of T_1 against field strength (this is of great importance because what we are studying in MRI is more the C/N which depends very strongly on T_1 and T_2 than the S/N), the S/N is roughly proportional to field strength B_0.

4.5 *Spatial resolution*

The spatial resolution is determined by field homogeneity and the steepness of the gradients employed, and may be increased until the S/N becomes the limiting factor. For example, in high resolution imaging, steep gradients are used. Increasingly spatial resolution, the S/N decreases and more averages are needed, resulting in longer imaging time. Today, resolution has reached the 0.5 mm range in routine clinical MRI.

4.6 *Field of view (FOV)*

To reach the same S/N, there is not a net gain in acquisition time by reduction of the FOV because we have to compensate the S/N drop due to smaller voxel volume by more averages.

4.7 *Summary and example*

There is a compromise solution between the spatial resolution to reach, the S/N acceptance an the acquisition time. The equations related these parameters are:

$$S/N \approx \sqrt{n_{av}} / \sqrt{n_{ph}} \quad (29)$$

$$T_{acq} \approx n_{av} \quad (30)$$

For instance, the FOV remaining constant, when we are increasing the spatial resolution by a factor 2 (e.g., use of 512 phase encoding steps instead of 256), we are recluding the S/N *ratio by a factor 1.4. To compensate this* S/N *drop, we must increase by a factor 2 the number of averages* n_{av} *which leads to increase by a factor 2 the acquisition time* T_{acq}. *That is why, for particular examinations , the surface coils are the solution to obtain better resolution for a reduced FOV without significant* S/N *drop and without acquisition time penalty.*

III–5. Artefacts

In this section we are only overviewing the MRI artefacts which can be corrected by the user himself. Other artefacts can occur within MR images but they generally require the hardware imager specialist and are documented in the dedicated literature. We classify the MRI artefacts that occur with routine imagers in two categories: (i) artefacts occuring mainly along the phase encoding direction, and (ii) those creating distortions mainly in the frequency encoding direction.

5.1 *Artefacts in the phase encoding direction*

5.1.1 *Aliasing or wrap-around artefact*

The MR signal (FID or spin-echo) measured at the coil connections is said to be an analogic or continuous signal against the time. To be treated by a computer, it must be digitized or transformed into a finite set of points that will represent as accurately as possible the measured analogic MR signal. This latter is very complicated because it is the superposition of a set of periodic signals each oscillating with a frequency different from the others. This group of frequencies is characterized by a frequency bandwidth or frequency spectrum. The *Nyquist Therorem* shows that if the sampling frequency, the rate at which the detected MR signal is digitized, is not at least twice the highest frequency of the frequency bandwidth, the computer representation of this signal gives it an erroneous representation. This misrepresentation is called *aliasing* or *wrap-around* phenomenon and means that any frequency greater than one half of the sampling frequency is indistinguishable from some lower frequency included in the frequency spectrum.

Therefore, the frequencies outside the frequency bandwidth are said to be folded over. *In MRI, if the chosen FOV is smaller than the object size, a phase-encoded signal located outside the FOV is interpreted as coming from within and folds over, two regions of tissue becoming superimposed in the image.*

This artefact can happen in the three field gradient

directions and in general, the simplest way to correct it is the signal oversampling (the increase of sampling steps). This procedure is used in the frequency encoding direction (currently made in routine imagers without any user action) whereas it cannot be used automatically for the phase encoding direction because it would lead to extra acquisition time (e.g., employing 512 phase steps instead of 256 steps doubles the acquisition time). There are several ways to cancel this artefact in the preparation direction: (i) the increase of the FOV so that it includes the full object, (ii) the modification of the orientation of the phase encoding direction (that is one of the image parameters to be defined before starting the examination) so that at least the smaller dimension of the object along the phase encoding direction matches with the size of the FOV. *For instance, if the FOV is rectangular (e.g., 200 mm × 300 mm), we use the smaller dimension (e.g., 200 mm) like the FOV image parameter and orient the preparation gradient in this direction.* (iii) the use of surface coils because they have a limited detection extension, (iv) to wrap around the unwanted object parts with Al foils (RF screen) in order to prevent their RF excitation and therefore the detection of any signal coming from them.

5.1.2 *Truncation artefact*

Theoretically, to be accurately imaged, an object requires an infinite range of spatial frequencies associated with it. Unfortunately, in practice this is impossible and an arbitrary *frequency cut-off* is imposed resulting in the frequency bandwidth previously discussed. It can result in an artefact phenomenon called *truncation* or *Gibbs* artefact which appears as striations equally spaced within the MR images. *This artefact has led to pathology misinterpretation, the most common of which is the mimicking of syringomyelia.* This artefact can happen both in the frequency and phase encoding directions and the best theoretical solution to cancel it could be the recording of higher sampling frequencies. In practice, it can be reduced (it will still exist but becomes unperceptible although slightly blurring the whole image) by increasing the number of sampling steps in the both directions. As for the aliasing artefact, this solution can be applied for the frequency encoding direction but can not be used for the phase encoding because it could lead to extra acquisition time.

Therefore, if we think that this artefact appears along the phase encoding direction, we will rotate this direction by 90° in the image plane and will acquire once again the images to see if the artefact follows or not the phase encoding direction and, therefore verify if what we are seeing is an artefact or not. Note that this artefact can also be altered by the filtering of the detected MR signals or reconstructed images (low-pass filter), *but with the disadvantage that the whole image will be modified and not only the artefact.*

5.1.3 *Motion artefacts*

The motion artefacts are the most frequently encountered in MRI and result in MR signals which are inappropriatly distributed in the phase encoding direction whatever the motion direction may be within the 2 DFT image. The motions can be classified into two categories with respect to their apparition during the pulse sequences: (i) the motions that occur between the data acquisition and the 90° excitation pulse which starts the next pulse sequence, (ii) the motions occuring between the 90° excitation pulse and the data acquisition. Respective to these two classes, the image ghosts encountered in the human body are: (i) those due to thorax (breathing and heart beat) and abdominal movements, and (ii) those due to blood and CSF flow. The basis of all those artefacts is the *periodic* or *pulsatile* movements which lead to a series of equally spaced ghosts across the images along the phase encoding direction. They are due to 'incorrect phased' added to the set of phases 'correctly' imposed by the phase encoding field gradient (*cf.* II–3.3). The distance between two successive ghosts depends on the repetition time TR, the frequency of the periodic movement, the encoding field gradient strength and the FOV.

(i) The first type of motion can be totally eliminated by physiological gating, the synchronization between data acquisition and the motion. *For cardiac examinations, triggering of the acquisition by cardiac cycle will be done whereas both cardiac triggering and respiratory gating are necessary to cancel respiratory motions. Unfortunatly, both procedures increase the image acquisition times.* The ghosts arising from breathing can also be cancelled with fast imaging methods associated with respiration suppression or by signal averaging (n_{av}). Finally, these artefacts can be eliminated by using special methods named *phase reordening* (ROPE, CORE) which correct before the image reconstruction the erroneous phases in the acquired data.

(ii) The motion ghosts of the second kind can be reduced by using additional compensating gradients. They have special shapes adjusted in order to compensate uncorrected phase introduced by the movements. By this means we can selectively cancel phase errors coming from the velocity or from the acceleration or from the both.

5.2 Artefacts in the readout direction

5.2.1 *Magnetic field inhomogeneities*

RF Field. The magnetic RF field can not be the same all over the sensitive volume of the RF coils and therefore across the whole imaging FOV. This inhomogeneity depends on the type of RF coils used and will be lower for body and head coils than for circular or surface coils of any shape. Therefore, when they are used to excite the spin system, the amplitude of this excitation varies across the FOV, certain regions experience the correct 90° and 180° pulses whereas other regions experience different flip angle RF pulses. *It results in abnormal variations of the transverse magnetization and therefore of the MR signals* (shadings) *within the images. The only way to reduce this artefact is the use of more homogenous RF coils.*

This phenomenon occurs also when RF coils are only used as receiver even when the RF field excitation is homogenous across the FOV. Under these circumstances, the image shading is due to the inhomogenous sensitivity inside the receiving RF coil. *This artefact can be reduced by filtering the reconstructed images or detected MR signals (Homomorphic filters).*

Applied magnetic field. The magnet building imperfections result in field inhomogeneities that can give similar effects to the RF field ones. This artefact can be corrected by better magnetic field *shimming.* This shimming is of great importance when we wish to use pulse sequences allowing separation of water tissues from fatty tissues. *In this situation, the external static magnetic field shimming must be better than the* H^1 *Larmor frequency separation between these two tissue species* (3.5 ppm) (*cf.* I–10).

Metallic materials. The magnetic field is distorted locally by ferromagnetic implants such as some prosthetic heart valves or inadequate ECG electrodes because they generate spontaneously a magnetic field which adds to the applied one. Non-ferromagnetic objects can also cause magnetic field distortions due to Eddy currents induced inside them by the switching of the gradient devices. *These artefacts appear as a region without signal around a large implant while in other cases just a locally distorted image can occur.*

Magnetic susceptibility. When a tissue is immerged in magnetic field B_0, the magnetic susceptibility tissue constant χ tells us how easily it can be magnetized (*cf.* I–5.2).

$$M_{tissue} = \chi_{tissue} B_0 \qquad (31)$$

When adjacent tissues have very different susceptibilities (air/tissue, bone/tissue, localized concentrations of hemoglobin, overload of iron, etc.), there exists intrinsic magnetic field gradients accross the imaging voxels located in the surrounding of the boundary between the two tissues. *It results in a locally applied magnetic field degradation and artefacts similar to those previously discussed can occur. These are removed partially when the SE pulse sequence is employed but not with the gradient echo pulse sequences* (*cf.* III–1.2).

5.2.2 *Chemical shift artefact*

The chemical shift phenomenon tells us that water and fat protons resonate at slightly different resonant frequencies (*cf.* I–10). In the presence of a linear selection or frequency encoding field gradient, fat protons and water protons that would be content inside a unique image voxel will be displaced and this voxel will be undoubled. The amplitude of this displacement depends on the field strength, the FOV, the field gradient amplitude and the sampling rate; it can be several pixels in the read out direction.

This artefact appears as a signal void at the boundary between fatty and aqueous tissues (myocardium/surrounding adipose). It is more pronounced when higher field strengths are used and can be reduced by using stronger field gradients (with unfortunately a reduction of the S/N *ratio). This artefact will be cancelled by using methods based on saturation or spectroscopic pulse sequences* (CHESS, CHEMSAT, SPIR). *It can also be reduced with gradient echo pulse sequences where the echo time will be adjusted on the phase shift between fat and water transverse magnetizations (cf.* III–1.3). *Finally, we mention that some special techniques can reconstruct separated fat and water images (e.g., the* Dixon method*).*

5.3 *Direction independent artefacts*

Field gradient linearity. The basis of spin-warp MR image reconstruction is the use of linear field gradients because the resonance frequency depends lineary on the magnetic field. *Therefore, any imperfection in the field gradient lineary results in a scaling factor between the recorded images and the real anatomy. Whence, under these circumstances, the MR images appear distorted (image contraction).*

SECTION FOUR
REFERENCES

IV.1 Textbooks

Abragam A: *Principle of Nuclear Magnetism.* Oxford University Press, 1961

Esser PD, Johnston RE: *Technology of Nuclear Magnetic Resonance.* The Society of Nuclear Medicine Inc., 1984

Farrar TC, Becker ED: *Pulse and Fourier Transform NMR.* Academic Press, 1971

Foster MA, Hutchinson JMS: *Practical NMR Imaging.* IRL Press, 1987

Gadian DG: *Nuclear Magnetic Resonance and Its Applications to Living Systems.* Oxford University Press, 1982

Jackson DF: *Imaging with Non-ionizing Radiations*, Vol. 2. Surrey University Press, 1983

Mansfield P, Morris PG: *NMR Imaging in Biomedicine.* Academic Press, 1982

Mc Cready VR, Leach M, Ell PJ: *Functional Studies Using NMR.* Pringer-Verlag, 1986

Morris PG: *Nuclear Magnetic Resonance Imaging in Medicine.* Clarendon Press, 1986

Petersen SB, Muller RN, Rinck PA: *An Introduction to Biomedical Nuclear Magnetic Resonance.* Georg Thieme Verlag, 1985

Rinck PA, Petersen SB, Muller RN: *An Introduction to Magnetic Resonance in Medicine.* Georg Thieme Verlag, 1990

Shaw D: *Fourier Transform NMR Spectroscopy.* Elsevier, 1984

Slichter CP: *Principles of Magnetic Resonance.* Springer-Verlag, 1978

Wehrli FW, Shaw D, Kneeland JB: *Biomedical Magnetic Resonance Imaging.* Principle, Methodology, and Applications. VCH Publishers, 1988

IV.2 Book chapters

Axel L, Morton D: Flow effects in magnetic resonance imaging. *American Association of Physicists in Medicine* 1985 Summer School. The Portland University. 315–327, 1985

Brown MS, Gore JC: MR relaxation in tissue. *American Association of Physicists in Medicine* 1985 Summer School. The Portland University. 189–202, 1985

Dobson KG: Magnet design and technology for MR imaging. *American Association of Physicists in Medicine* 1985 Summer School. The Portland University. 93–110, 1985

IV.3 Review articles

Alfidi RJ, et al: MR angiography of peripheral, carotid and coronary arteries. *AJR* 149:1097–1109, 1987

Bailes DR, et al: Respiratory ordered phase encoding (ROPE). *Society of Magnetic Resonance in Medicine* 1985: 939

Bradley GW: Sorting out the meaning of MRI flow phenomena. *Diagn Imag Inter* 05/1987: 102–111

Edelman RR, et al: New spinal MR strategies overcome motion artifacts. *Diagn Imag Inter* 12/1987: 86–92

Frahm J, et al: Flow suppression in rapid FLASH NMR images. *Magn Reson Med* 4: 372–377, 1987

Haacke E, et al: Reducing motion artifacts in two-dimensional Fourier transform imaging. *Magn. Reson Imag* 4: 359–376, 1986

Haase A: Snapshot FLASH MRI. Applications to T1, T2 and chemical shift imaging. *Magn Reson Med* 13: 77–89, 1990

Handley P: Magnets for medical applications of NMR. *British Medical Bulletin* 40: 125–131, 1984

Hendrick RE, et al: Maximizing signal-to-noise and contrast-to-noise ratios in FLASH imaging. *Magn Reson Imaging* 5: 117–127, 1987

Henkelman RM, et al: Artifacts in magnetic resonance imaging. *Rev of Magn Reson Med* 2(1): 1–126, 1987

Hould D, et al: Mechanisms of contrast in NMR imaging. *J Comput Assist Tomogr* 8: 369–380, 1984

Kraft KA, et al: MR imaging of model fluid velocity profiles. *Magn Reson Imaging* 7: 69–77, 1989

Lanzer P, et al: ECG-synchronized cardiac MR imaging: method and evaluation. *Radiology* 155: 681–686, 1985

Libove JM, et al: The signal-to-noise relationships in NMR imaging in the human body. *J Phys E* 13: 38–43, 1980

Mansfield P: Real-time echo-planar imaging by NMR. *British Medical Bulletin* 40: 187–190, 1984

Mills TC, et al: Partial flip angle MR imaging. *Radiology* 162: 531–539, 1987

Mitsuaki Arakawa BS: Advanced engineering and design expand utility of RF coils. *Diagn Imag Intern* 1986: 133–146

Riederer SJ, et al: MR fluoroscopy:technical feasibility. *Magn Reson Med* 8: 1–15, 1988

Tkack JA, et al: A comparison of fast spin echo and gradient field echo sequences. *Magn Reson Imaging* 6: 373–389, 1988

Unger EC: Partial flip angle imaging finds broader clinical use. *Diagn Imag Intern* 03/1988: 102–107

Van Dijk P: Direct cardiac NMR imaging of heart wall and blood flow velocity. *J Comput Assist Tomogr* 8: 429–436, 1984

Van Der Meulen, et al: Very fast MR imaging by field echoes and small angle excitations. *Magn Reson Imaging* 3: 297–299, 1985

Van Der Meulen, et al: Fast field echo imaging: An overview and contrast calculation. *Magn Reson Imaging* 6: 355–368, 1988

Van Wedeen J, et al: MR velocity imaging by phase display. *J Comput Assist Tomogr* 9(3): 530–536, 1985

Wehrli FW: Time-of-flight effects in MR imaging of flow. *Magn Reson Med* 14: 187–193, 1990

Wood ML, et al: Optimization of spoiler gradients in FLASH MRI. *Magn Reson Imaging* 5: 455–463, 1987

Young IR: considerations affecting signal and contrast in NMR imaging. *British Medical Bulletin* 40: 139–147, 1984

Young IR, et al: Clinical magnetic susceptibility mapping of the brain. *J Comput Assist Tomogr* 11(1): 2–6, 1987

Yuan C, et al: Flow-induced effects and compensation technique for slice-selective pulses. *Magn Reson Med* 9: 161–176, 1989

PART TWO

Cardiac MR imaging

CHAPTER ONE

MRI slices of the heart

Transverse slices 1–13
Sagittal slices 1–10
Coronal slices 1–7
Left anterior oblique (LAO) equivalent slices 1–10
Right anterior oblique (RAO) equivalent slices 1–6

TRANSVERSE SLICES 1-13

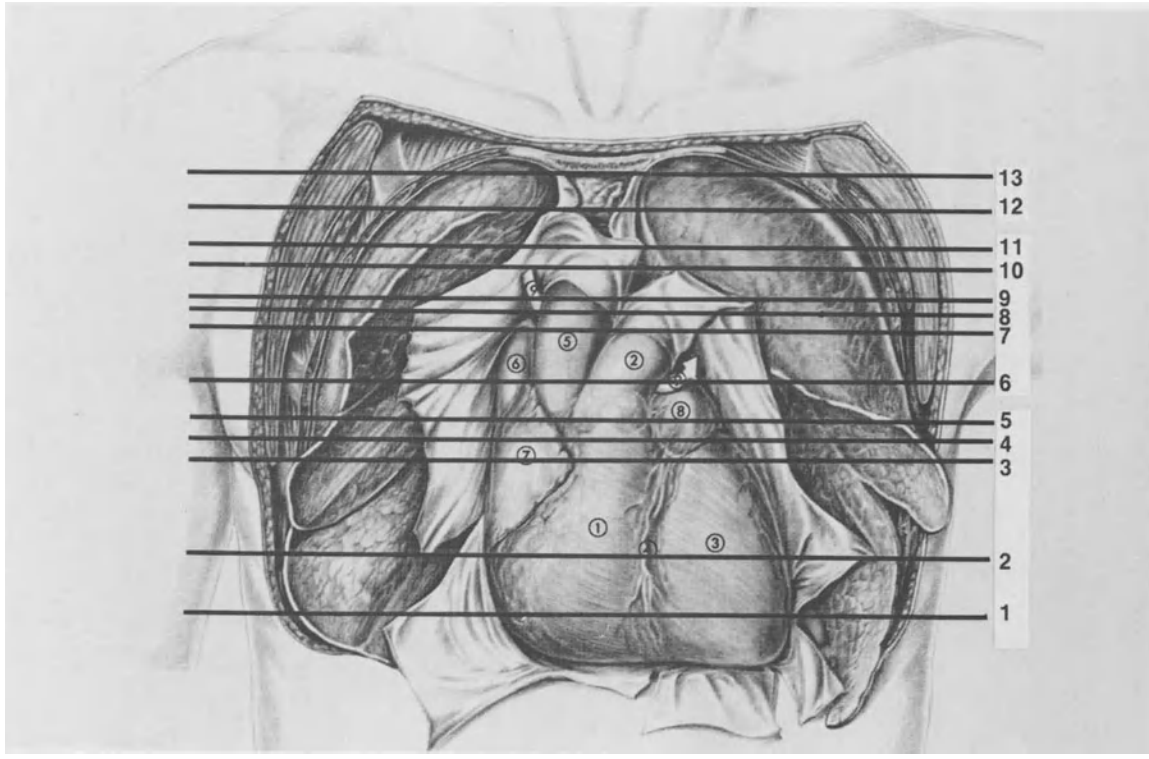

Figure T–0. Plane of section of the transverse slices.

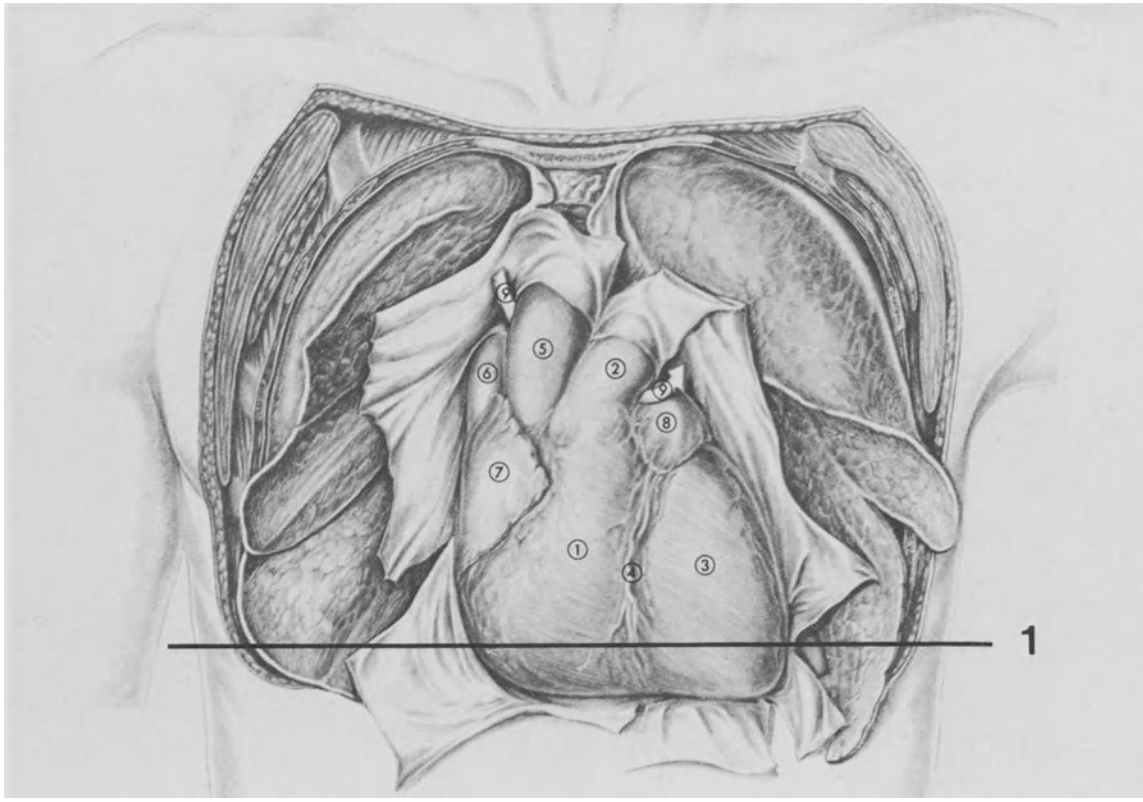

Figure T–1. Plane of section of transverse slice 1.

This transverse slice is close to the diaphragmatic surface of the heart. The two ventricles are shown. The right ventricle is separated from behind by the inferior vena cava which will open into the lowest part of the right atrium. The descending aorta, the azygos vein and the esophagus are also shown on this slice. Note that the esophagus is normally collapsed in the living subject.

The wall of the right ventricle is thinner than that of the left and is rather flat; the left ventricular cavity presents a nearly circular outline with walls about three times as thick as those of the right ventricle.

Note: The same anatomical view as described in figure I-1 (page 4) will be used for the description of the transverse and sagittal planes of section. For legend numbers, refer to page 4.

Transverse slice 1

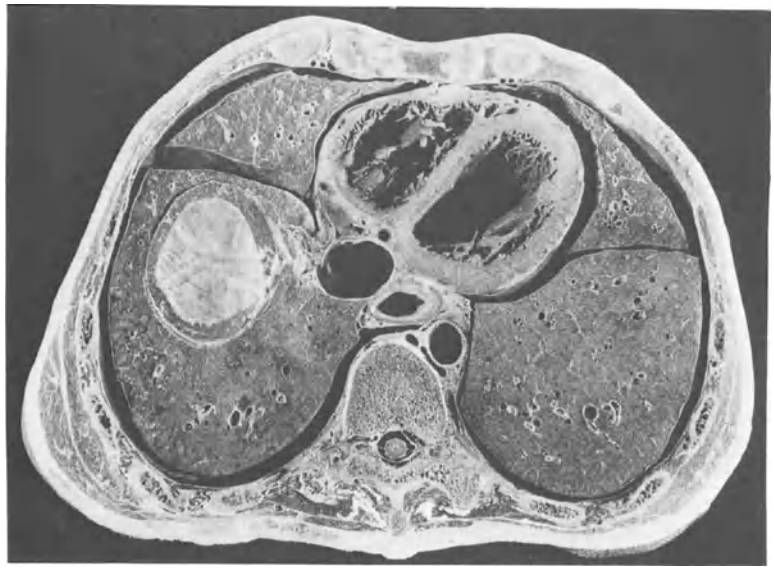

Figure T-2. Anatomical slice.

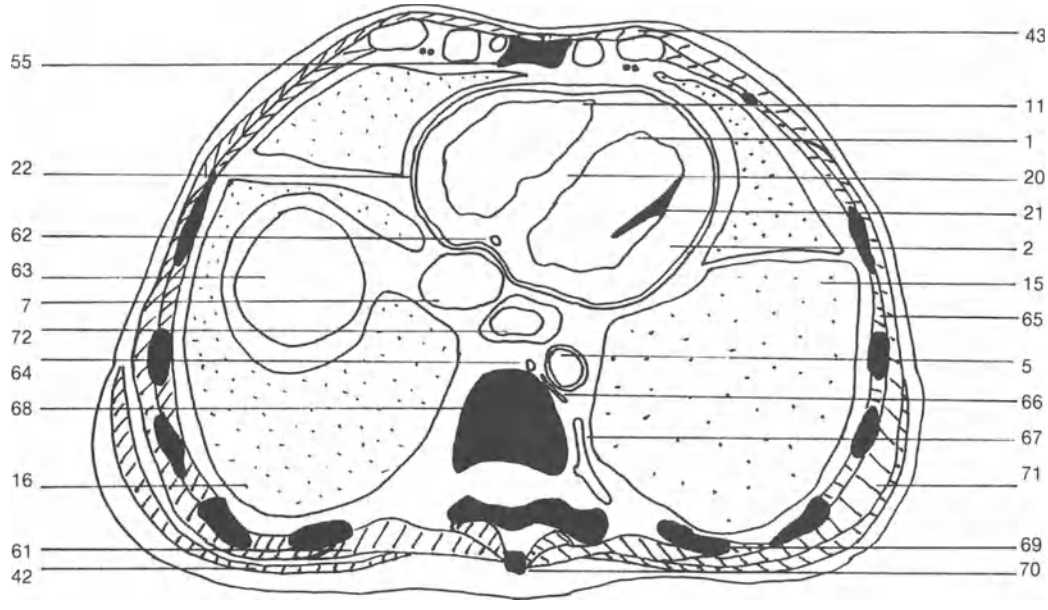

(1) Left ventricular cavity; (2) Myocardium; (5) Descending aorta; (7) Inferior vena cava; (11) Right ventricular cavity; (15) Left lung; (16) Right lung; (20) Ventricular septum; (21) Papillary muscle; (22) Pericardium; (42) Latissimus dorsi muscle; (43) Pectoralis major muscle; (45) Trapezius muscle; (55) Sternum; (61) Longis-

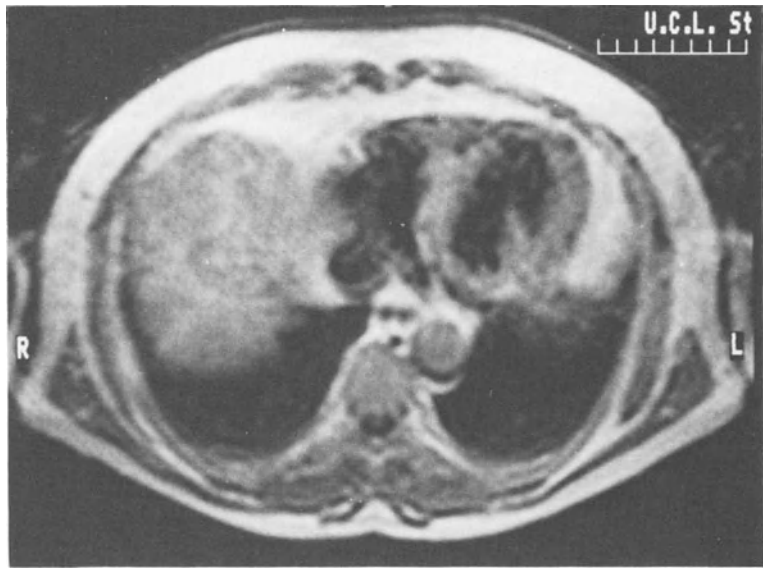

Figure T-3. MR slice.

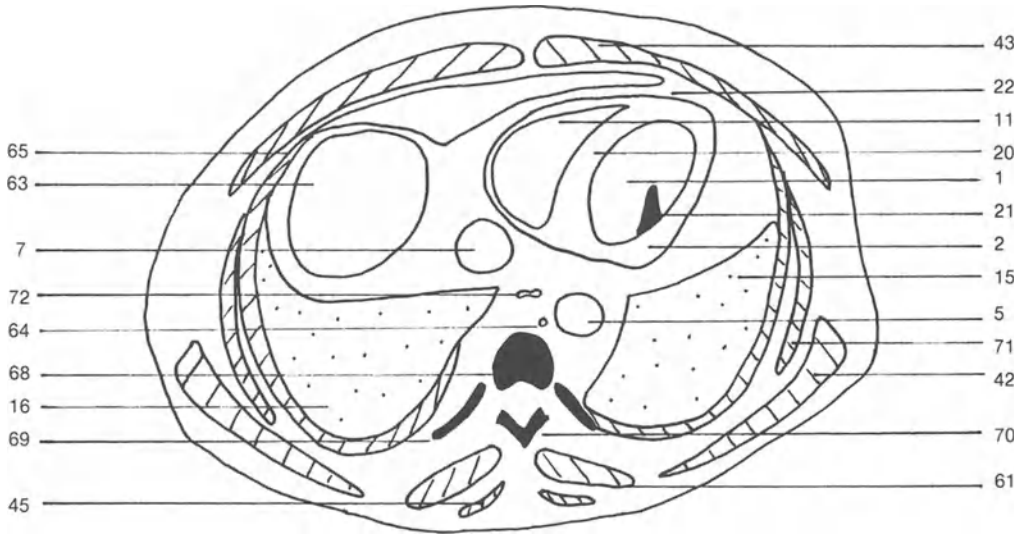

simus thoracis muscle; (62) Middle cardiac vein; (63) Liver; (64) Azygos vein; (65) Intercostal muscles; (66) Hemiazygos vein; (67) Posterior intercostal vein; (68) Dorsal vertebra; (69) Rib; (70) Spinous process; (71) Serratus anterior muscle; (72) Esophagus.

Transverse slice 2

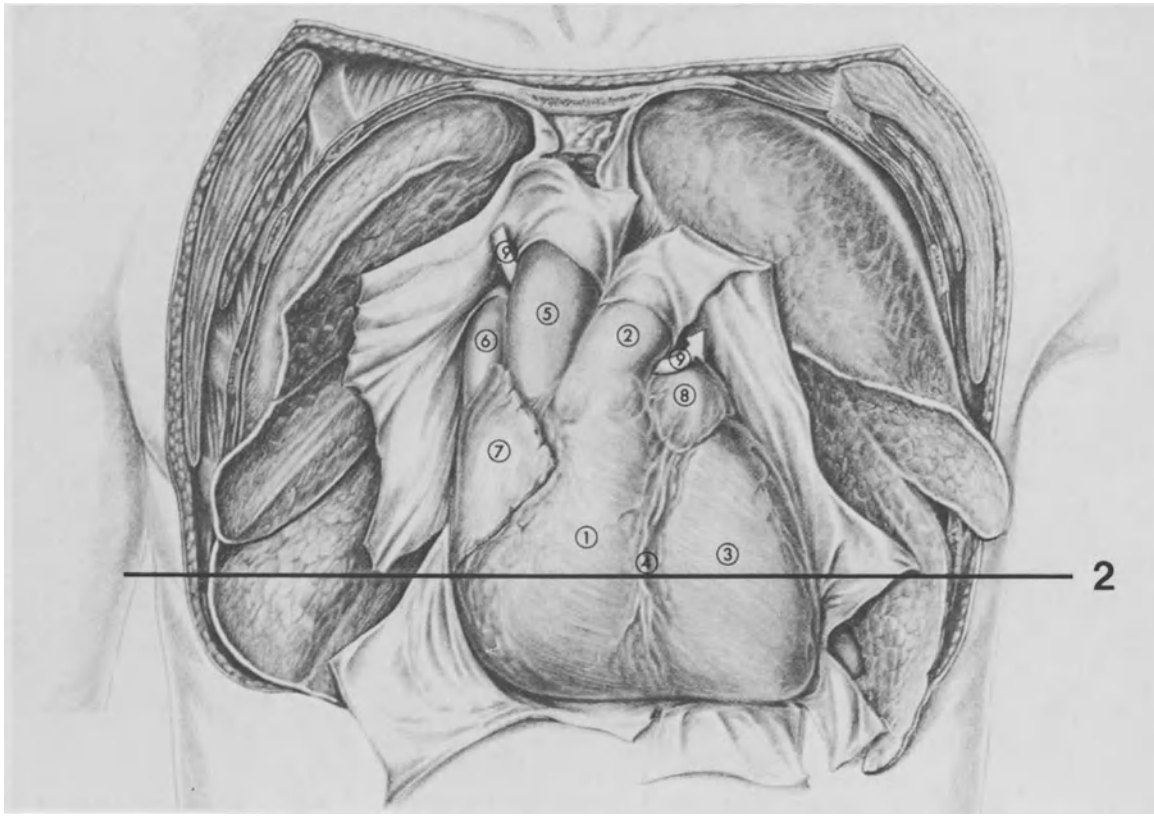

Figure T–4. Plane of section of transverse slice 2.

This slice shows the anatomical level with three cavities: the right ventricle, the right atrium and the left ventricle. At this level, the inferior vena cava opens into the right atrium. Just anterior to the extremity of the inferior vena caval valve, the coronary sinus enters the right atrium. Its orifice is guarded by a valvelike fold, the coronary sinus (Thebesius) valve. The diaphragm is seen on the right.

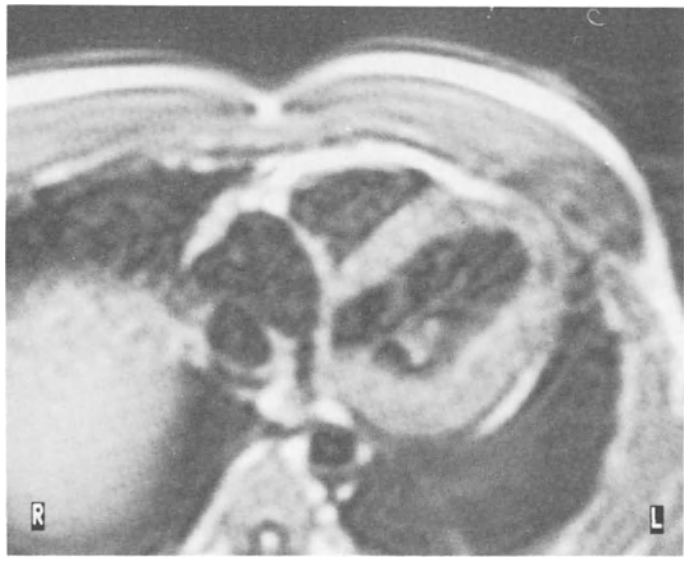

Figure T-5. MR slice.

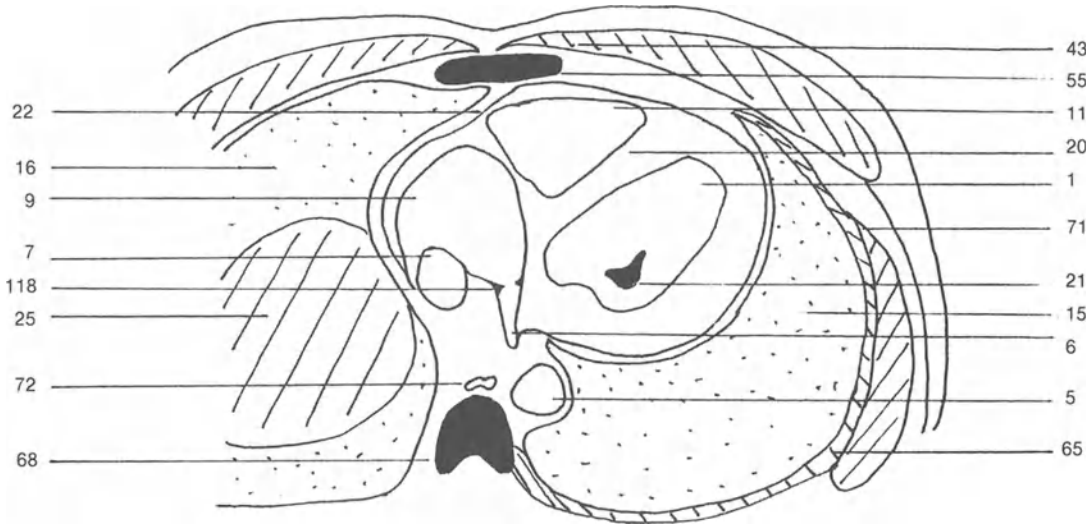

(1) Left ventricular cavity; (5) Descending aorta; (6) Coronary sinus; (7) Inferior vena cava; (9) Right atrium; (11) Right ventricular cavity; (15) Left lung; (16) Right lung; (20) Ventricular septum; (21) Papillary muscle; (22) Pericardium; (25) Diaphragm; (43) Pectoralis major muscle; (55) Sternum; (65) Intercostal muscles; (68) Dorsal vertebra; (71) Serratus anterior muscle; (72) Esophagus; (118) Thebesius valve.

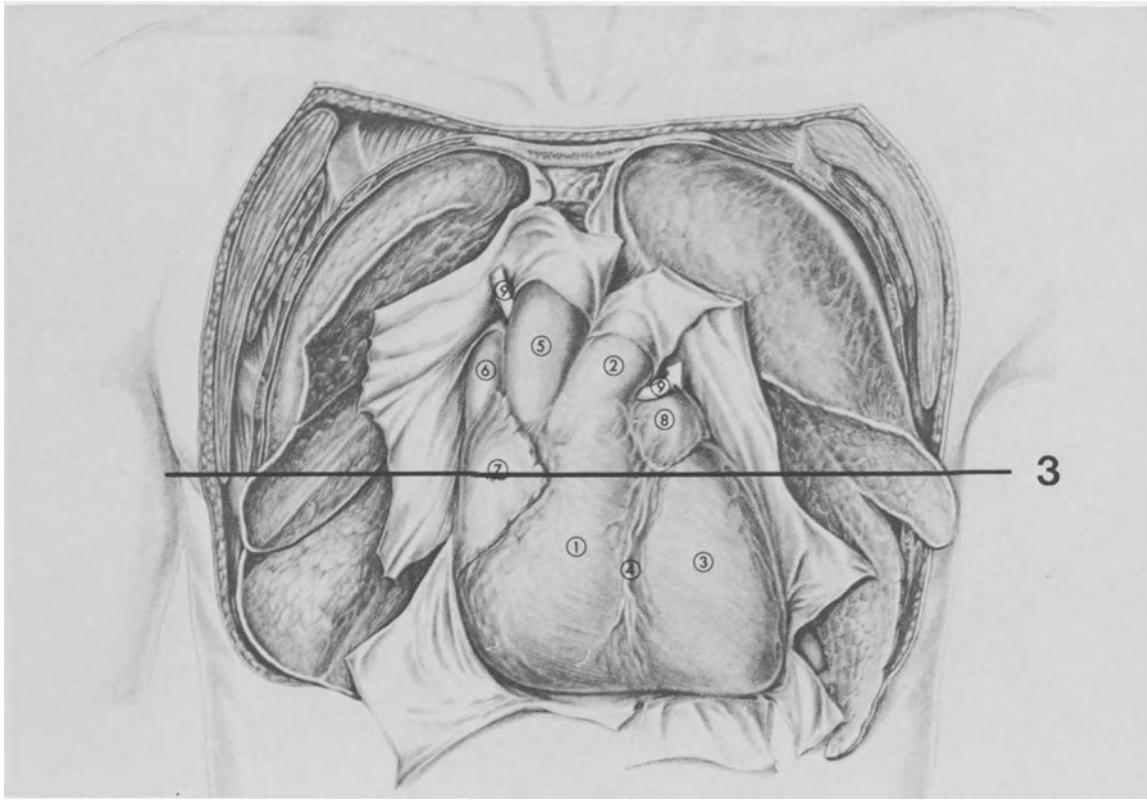

Figure T–6. Plane of section of transverse slice 3.

Slice through the right atrioventricular (tricuspid) and left atrioventricular (mitral) valves. Two NMR transversal slices are necessary to visualize these two structures because the mitral valve is slightly higher than the tricuspid valve.

The left ventricular outflow region may be seen very well at the level of the mitral valve on the NMR slice. This part of the left ventricle is related to the aortic valve which is situated at a superior level.

The opening of the pulmonary veins into the posterior surface of the left atrium can be seen.

Anteriorly, the right ventricle becomes smaller and will form a right ventricular outflow region.

Transverse slice 3

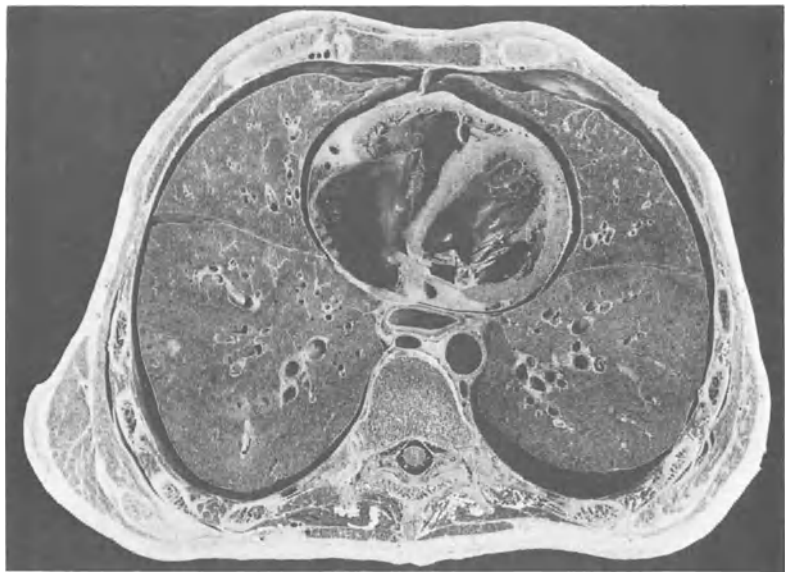

Figure T-7. Anatomical slice.

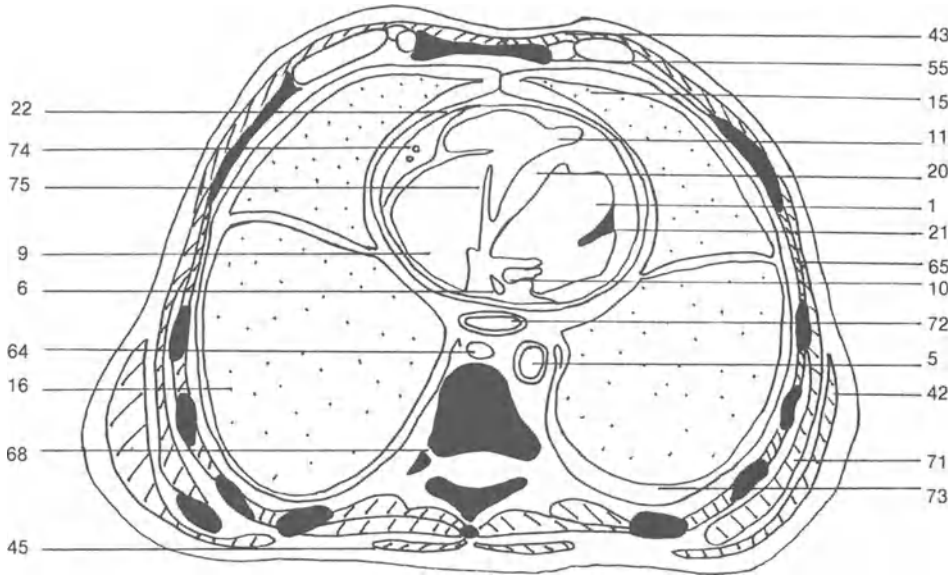

(1) Left ventricular cavity; (2) Myocardium; (5) Descending aorta; (6) Coronary sinus; (9) Right atrium; (10) Left atrium; (11) Right ventricular cavity; (13) Left ventricular outflow region; (15) Left lung; (16) Right lung; (20) Ventricular septum; (21) Papillary muscle; (22) Pericardium; (32) Atrial septum; (42) Latissimus dorsi muscle; (43) Pectoralis major muscle; (45) Trapezius muscle; (55) Sternum; (61) Longissimus thoracis muscle; (64) Azygos vein; (65) Intercostal muscles; (68) Dorsal vertebra; (69) Rib; (70) Spinous process; (71) Serratus anterior muscle; (72) Esophagus; (73) Pleural cavity; (74) Right coronary artery; (75) Tricuspid valve; (76) Right inferior pulmonary vein; (78) Pectoralis minor muscle; (92) Mitral valve.

Figure T–8. MR slice.

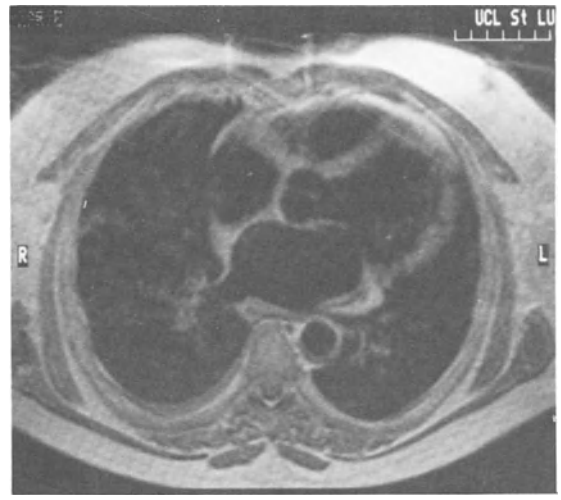

Figure T–9. MR slice.

T–8

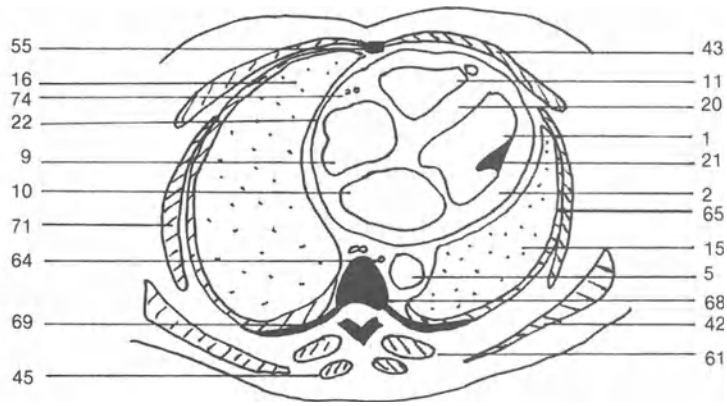

T–9

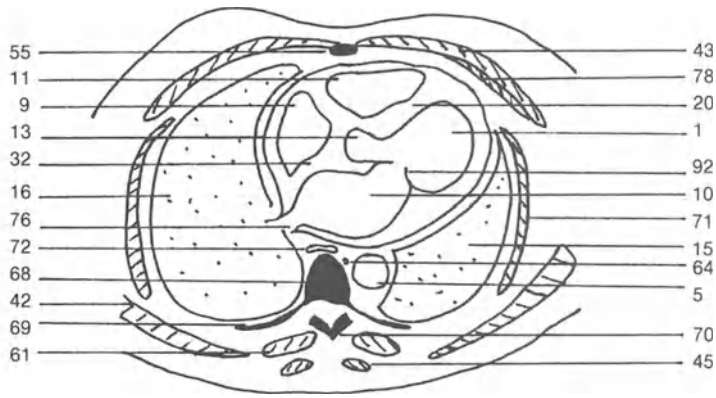

Transverse slice 4

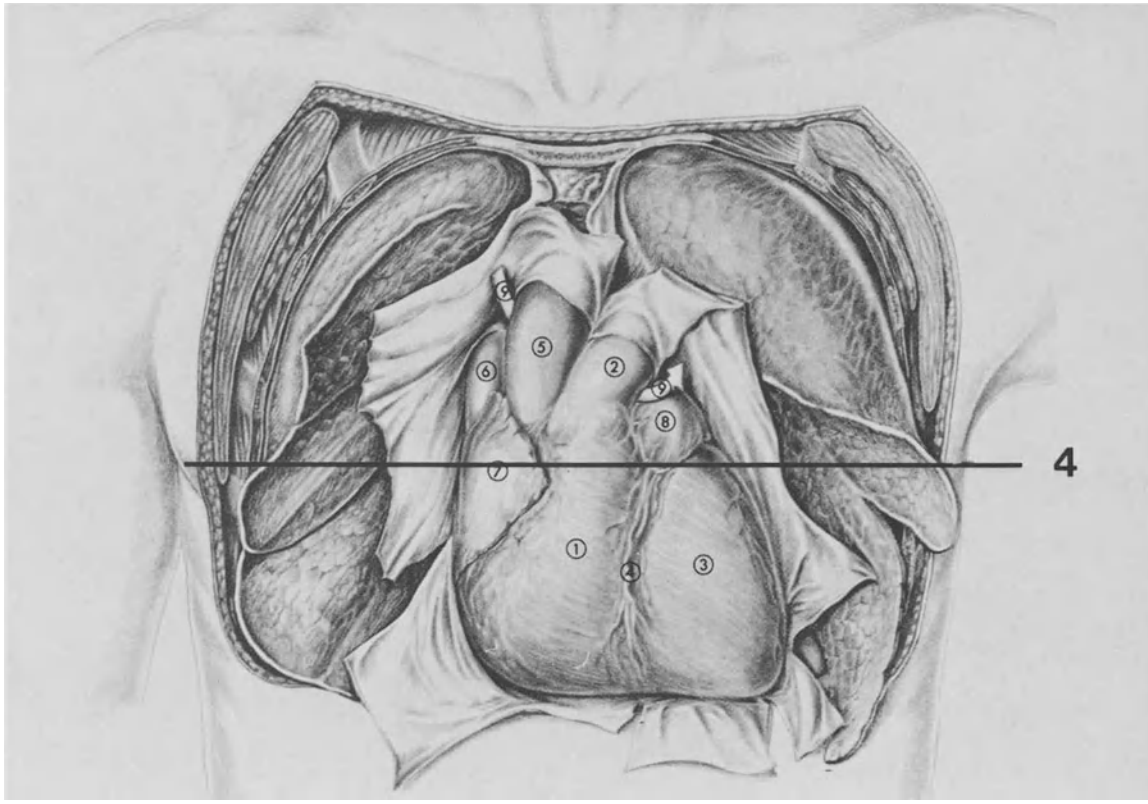

Figure T–10. Plane of section of transverse slice 4.

This slice shows the outflow regions of the right and left ventricles. The right ventricular outflow region is situated anteriorly.

The left atrium is widest at this level. The right atrium is smaller than on the previous level and the superior vena cava opens into the upper and posterior part of the atrium.

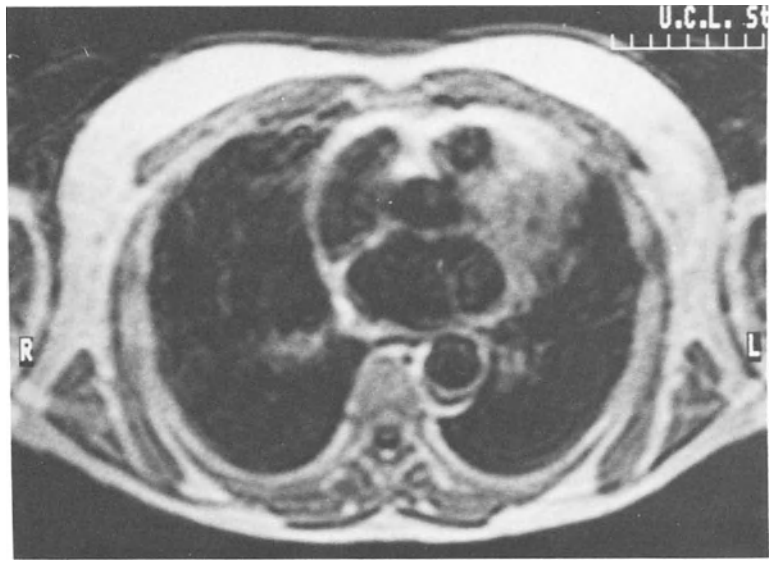

Figure T-11. MR slice.

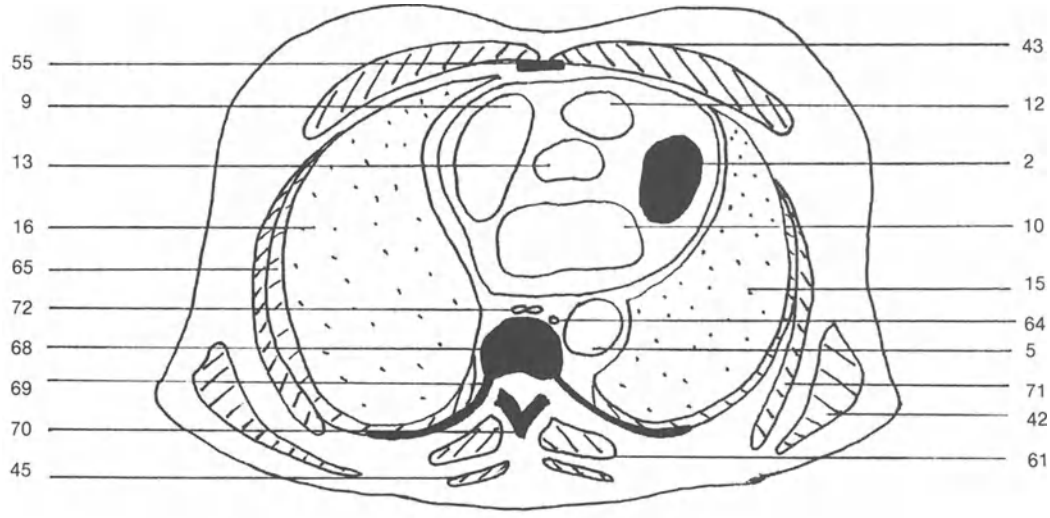

(2) Myocardium; (5) Descending aorta; (9) Right atrium; (10) Left atrium; (12) Right ventricular outflow region; (13) Left ventricular outflow region; (15) Left lung; (16) Right lung; (42) Latissimus dorsi muscle; (43) Pectoralis major muscle; (45) Trapezius muscle; (55) Sternum; (61) Longissimus thoracis muscle; (64) Azygos vein; (65) Intercostal muscles; (68) Dorsal vertebra; (69) Rib; (70) Spinous process; (71) Serratus anterior muscle; (72) Esophagus

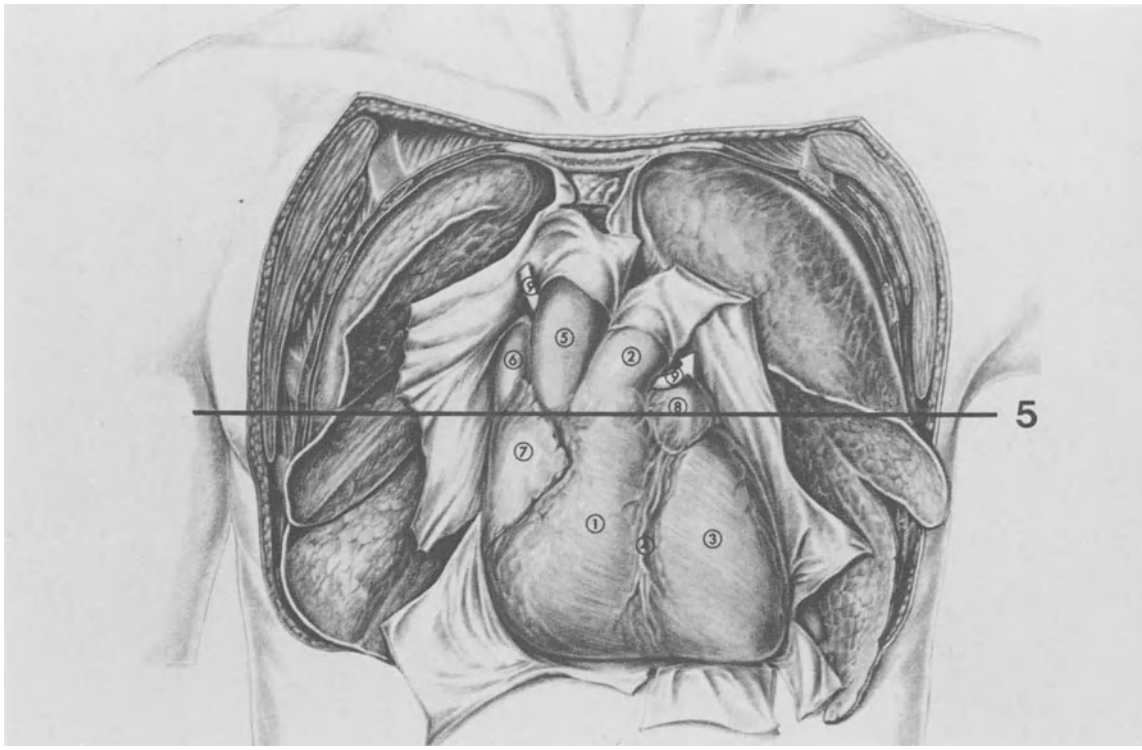

Figure T–12. Plane of section of transverse slice 5.

The pulmonary veins open, at this level, into the left atrium, two on each side of its middle line; their orifices do not have valves. The superior vena cava opens into the posterior part of the right atrium.

The two ventricles lead to the pulmonary and aortic orifices. The three NMR slices show respectively the ventricular outflow region, the valves and the infundibulum.

Transverse slice 5

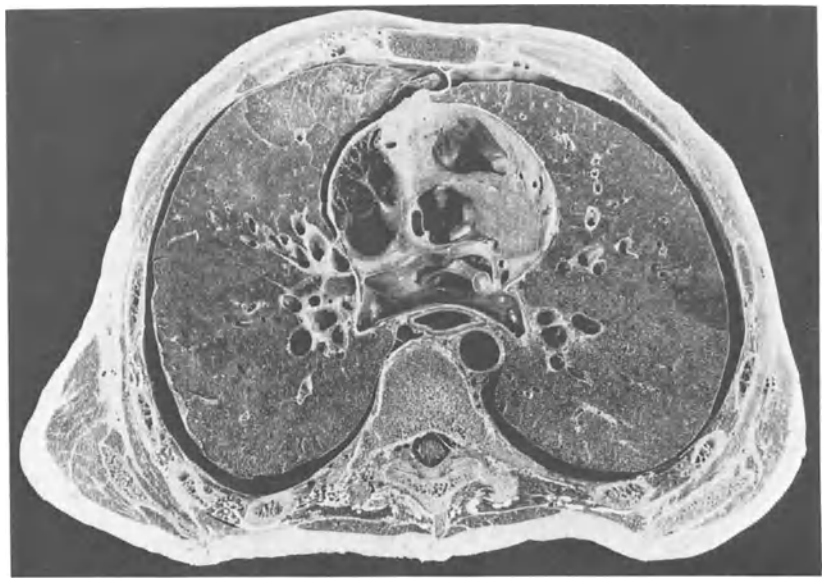

Figure T-13. Anatomical slice.

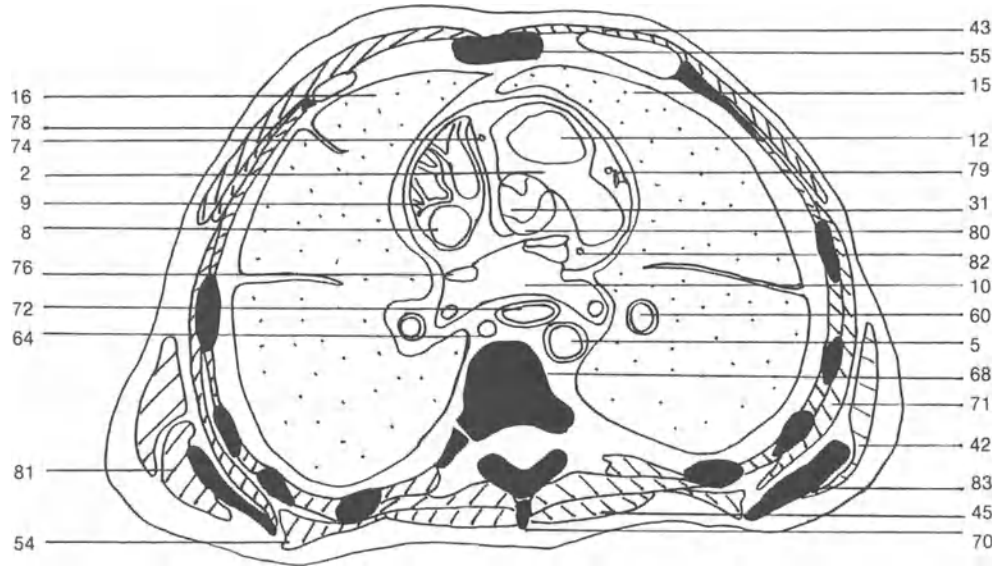

(2) Myocardium; (5) Descending aorta; (8) Superior vena cava; (9) Right atrium; (10) Left atrium; (12) Right ventricular outflow region; (15) Left lung; (16) Right lung; (31) Aortic infundibulum; (42) Latissimus dorsi muscle; (43) Pectoralis major muscle; (45) Trapezius muscle; (54) Rhomboidus muscle; (55) Sternum; (60) Left lung hilum; (61) Longissimus thoracis muscle; (64) Azygos

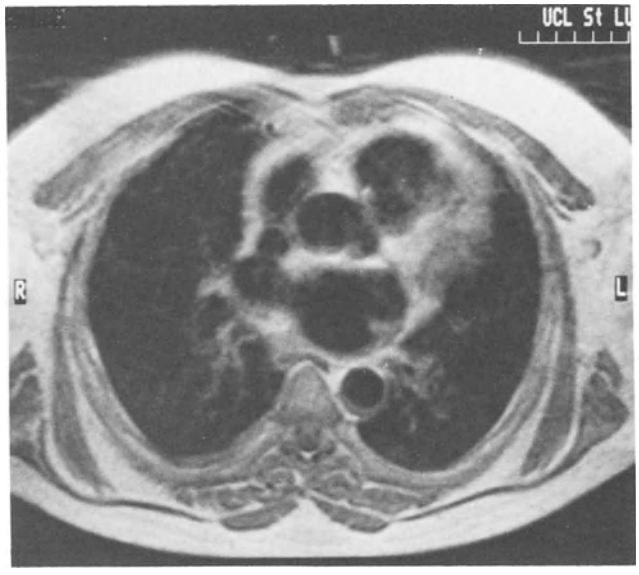

Figure T-14. MR slice.

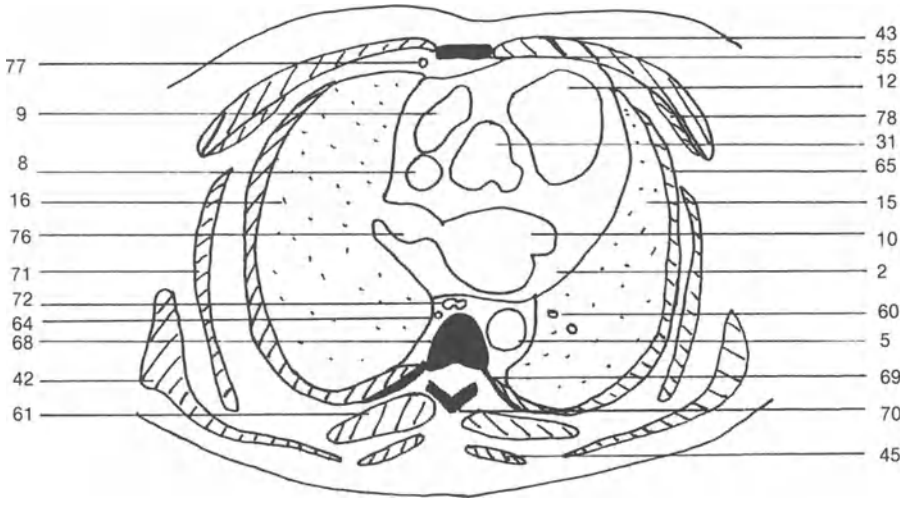

vein; (65) Intercostal muscles; (68) Dorsal vertebra; (69) Rib; (70) Spinous process; (71) Serratus anterior muscle; (72) Esophagus; (74) Right coronary artery; (76) Right inferior pulmonary vein; (77) Internal mammary artery; (78) Pectoralis minor muscle; (79) Left coronary artery; (80) Aortic valve; (81) Teres major muscle; (82) Circumflex artery; (83) Scapula.

Transverse slice 5

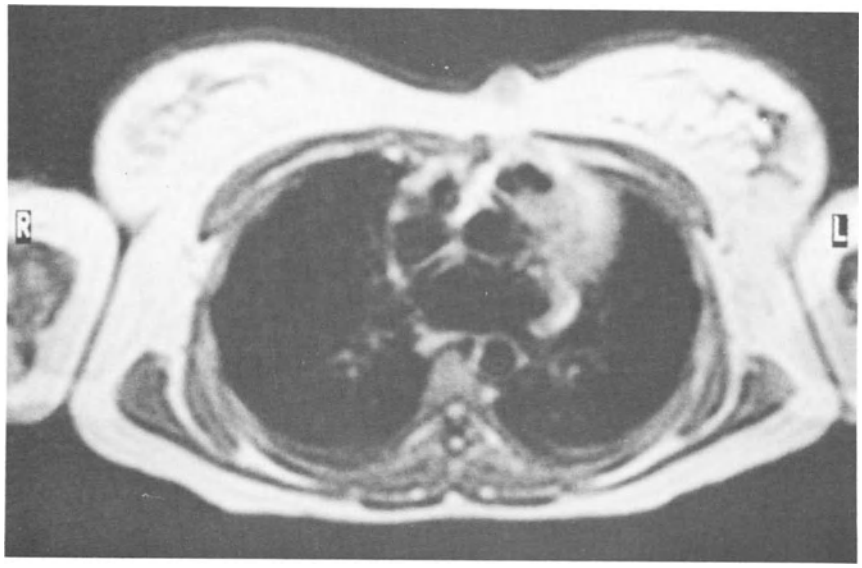

Figure T–15. MR slice.

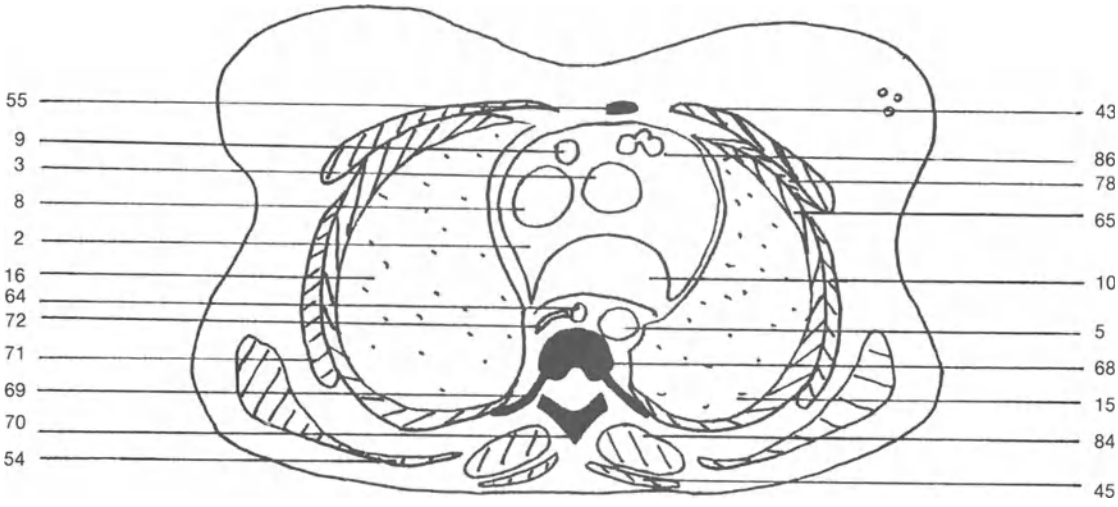

(2) Myocardium; (3) Ascending aorta; (5) Descending aorta; (8) Superior vena cava; (9) Right atrium; (10) Left atrium; (15) Left lung; (16) Right lung; (17) Main pulmonary artery; (22) Pericardium; (42) Latissimus dorsi muscle; (43) Pectoralis major muscle; (45) Trapezius muscle; (46) Left inferior pulmonary vein; (54) Rhomboidus muscle; (55) Sternum; (61) Longissimus thoracis

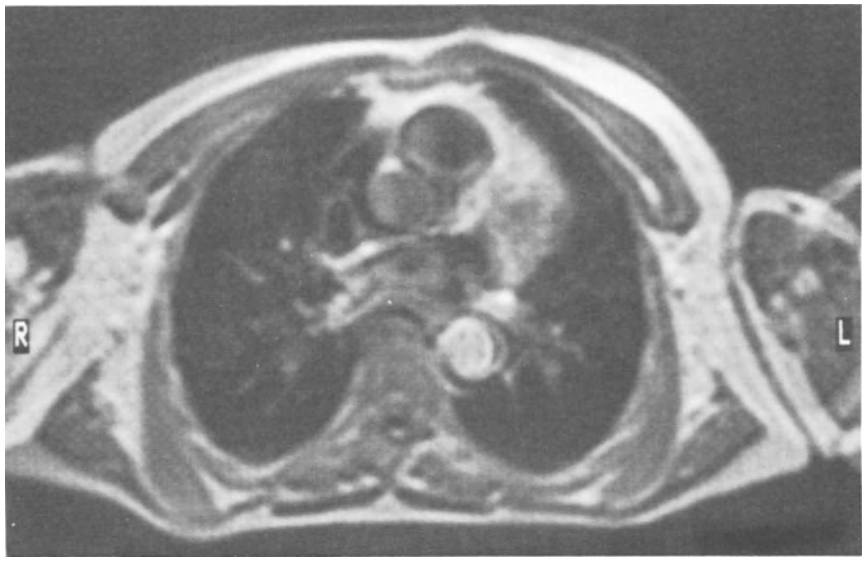

Figure T-16. MR slice.

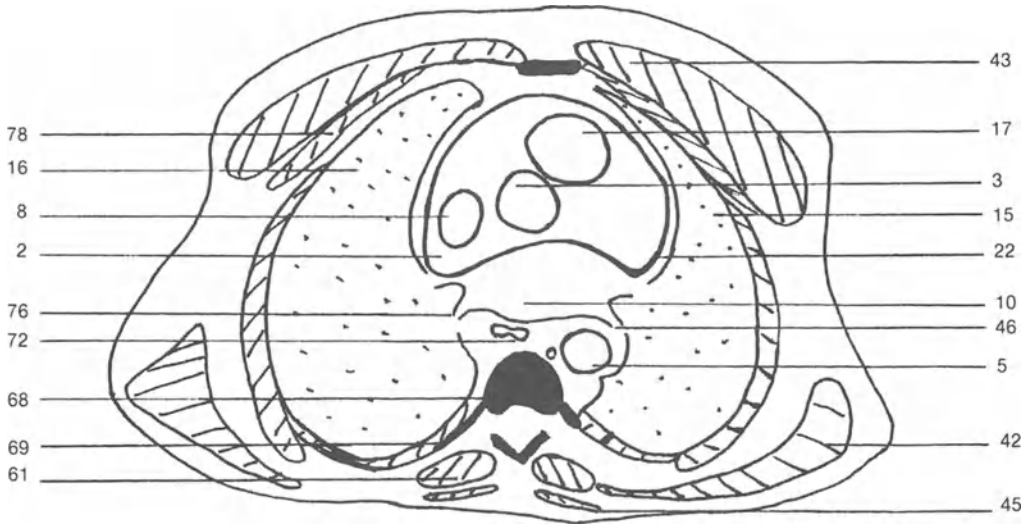

muscle; (64) Azygos vein; (65) Intercostal muscles; (68) Dorsal vertebra; (69) Rib; (70) Spinous process; (71) Serratus anterior muscle; (72) Esophagus; (76) Right inferior pulmonary vein; (78) Pectoralis minor muscle; (84) Transversospinal muscle; (86) Pulmonary valve.

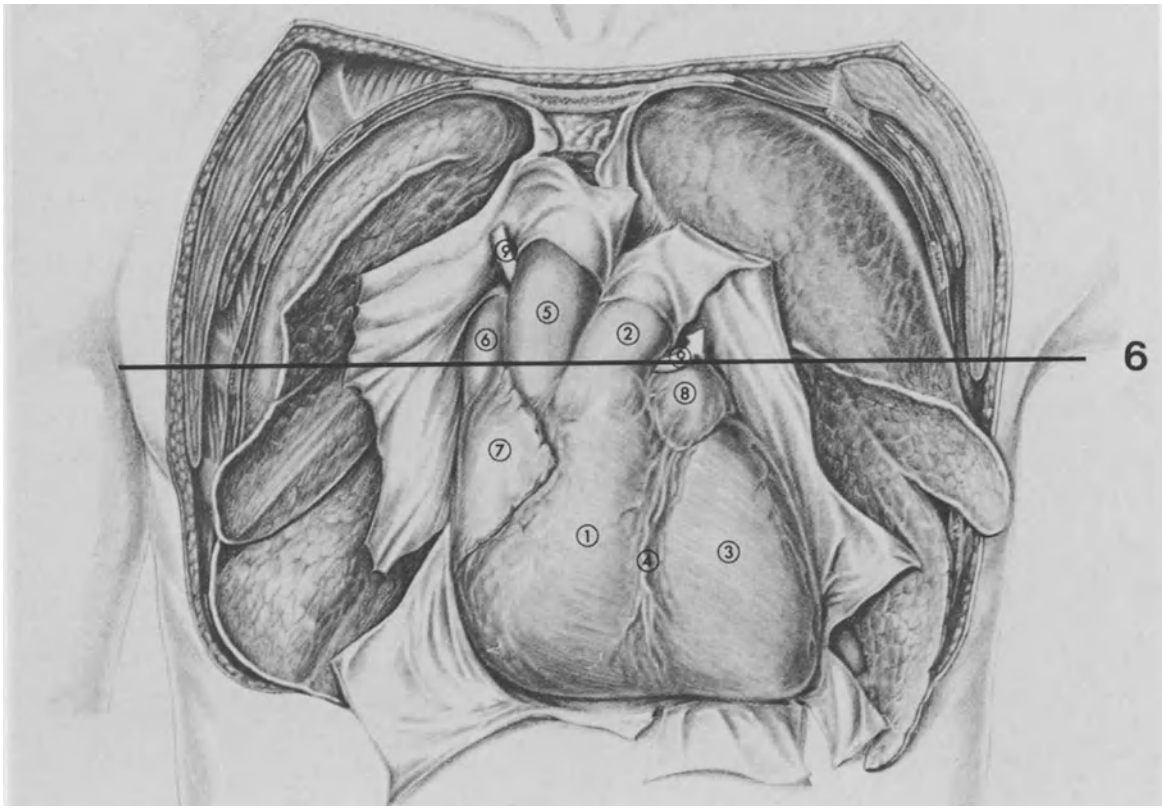

Figure T–17. Plane of section of transverse slice 6.

Approximately at the level of the sixth thoracic vertebra, the ascending aorta and the pulmonary trunk arise from the heart. The ascending aorta is related on its right side to the superior vena cava.

Posteriorly, the superior pulmonary veins open into the left atrium. The pulmonary veins are related to the two main bronchi. These latter bronchi divide into lobar bronchi (two left and three right).

Transverse slice 6

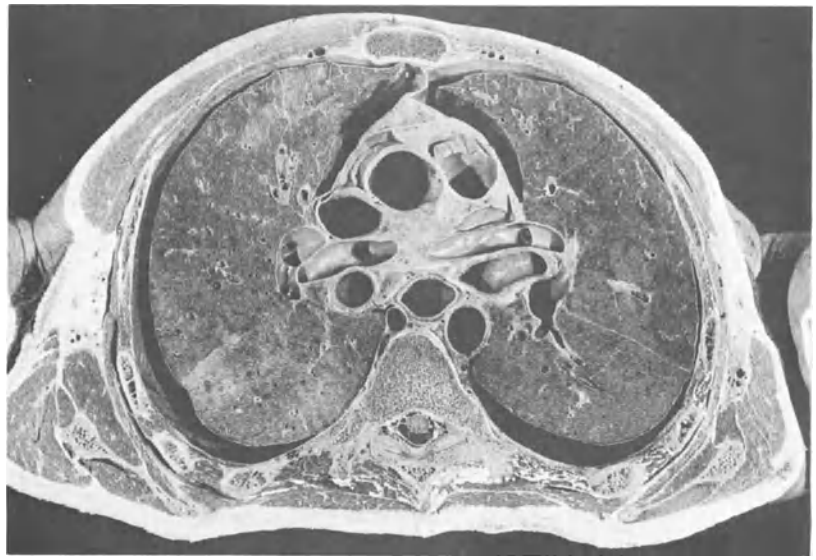

Figure T–18. Anatomical slice.

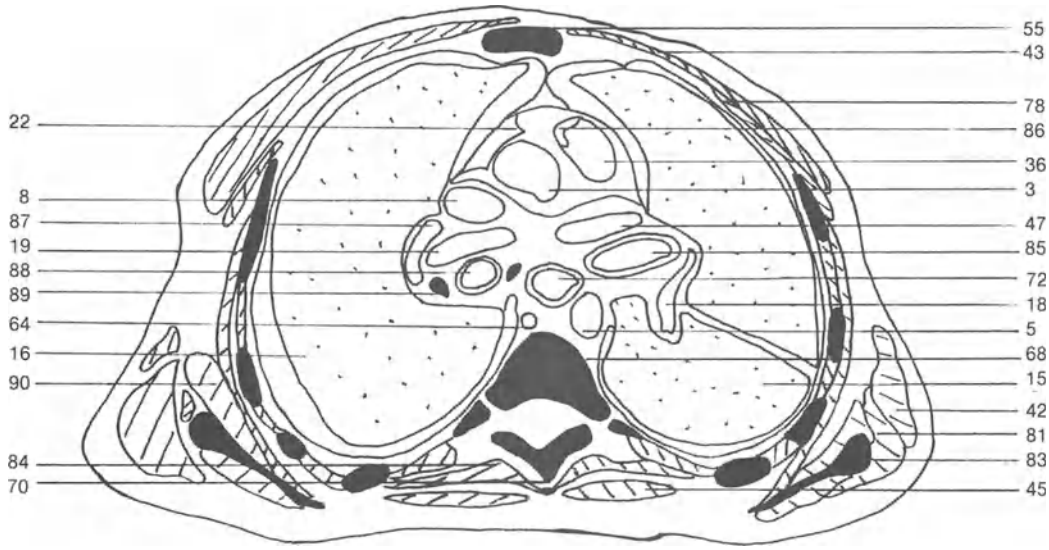

(3) Ascending aorta; (5) Descending aorta; (8) Superior vena cava; (10) Left atrium; (15) Left lung; (16) Right lung; (17) Main pulmonary artery; (18) Left pulmonary artery; (19) Right pulmonary artery; (22) Pericardium; (36) Pulmonary infundibulum; (42) Latissimus dorsi muscle; (43) Pectoralis major muscle; (45) Trapezius muscle; (47) Left superior pulmonary vein; (55) Sternum; (61) Longissimus thoracis muscle; (64) Azygos vein; (65) Intercostal muscles; (68) Dorsal vertebra; (69) Rib; (70) Spinous process; (71)

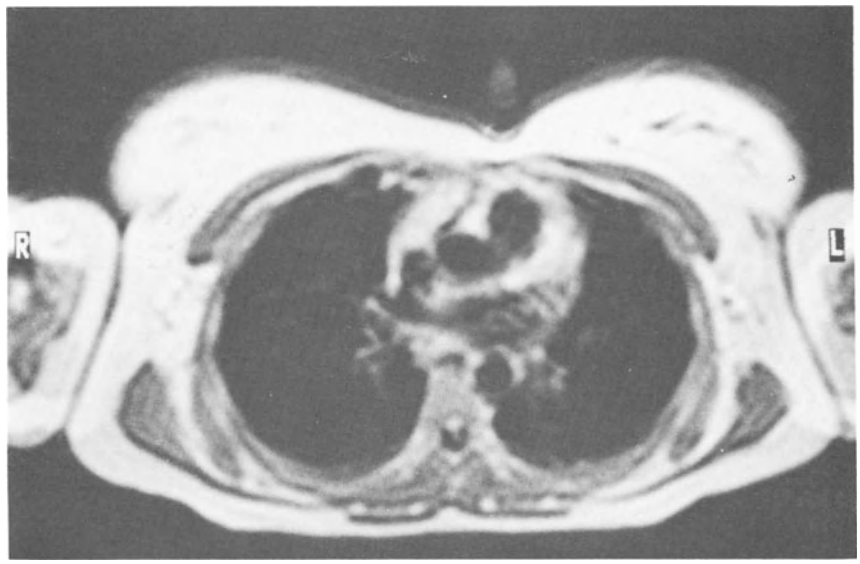

Figure T–19. MR slice.

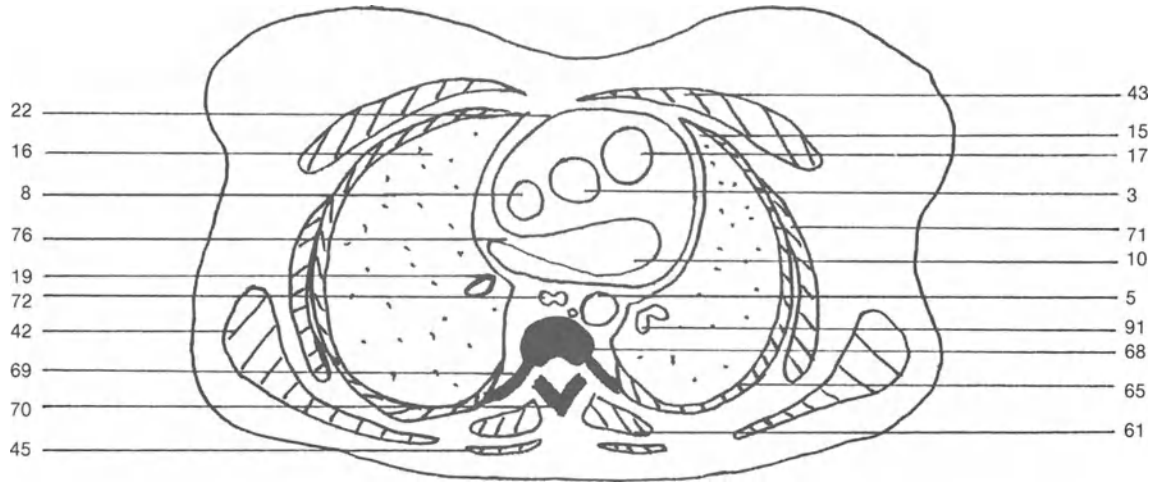

Serratus anterior muscle; (72) Esophagus; (76) Right inferior pulmonary vein; (78) Pectoralis minor muscle; (81) Teres major muscle; (83) Scapula; (84) Transversospinal muscle; (85) Left upper lobe bronchus; (86) Pulmonary valve; (87) Right superior pulmonary vein; (88) Right lower lobe bronchus; (89) Lymph node; (90) Subscapularis muscle; (91) Segmental bronchus.

Transverse slice 7

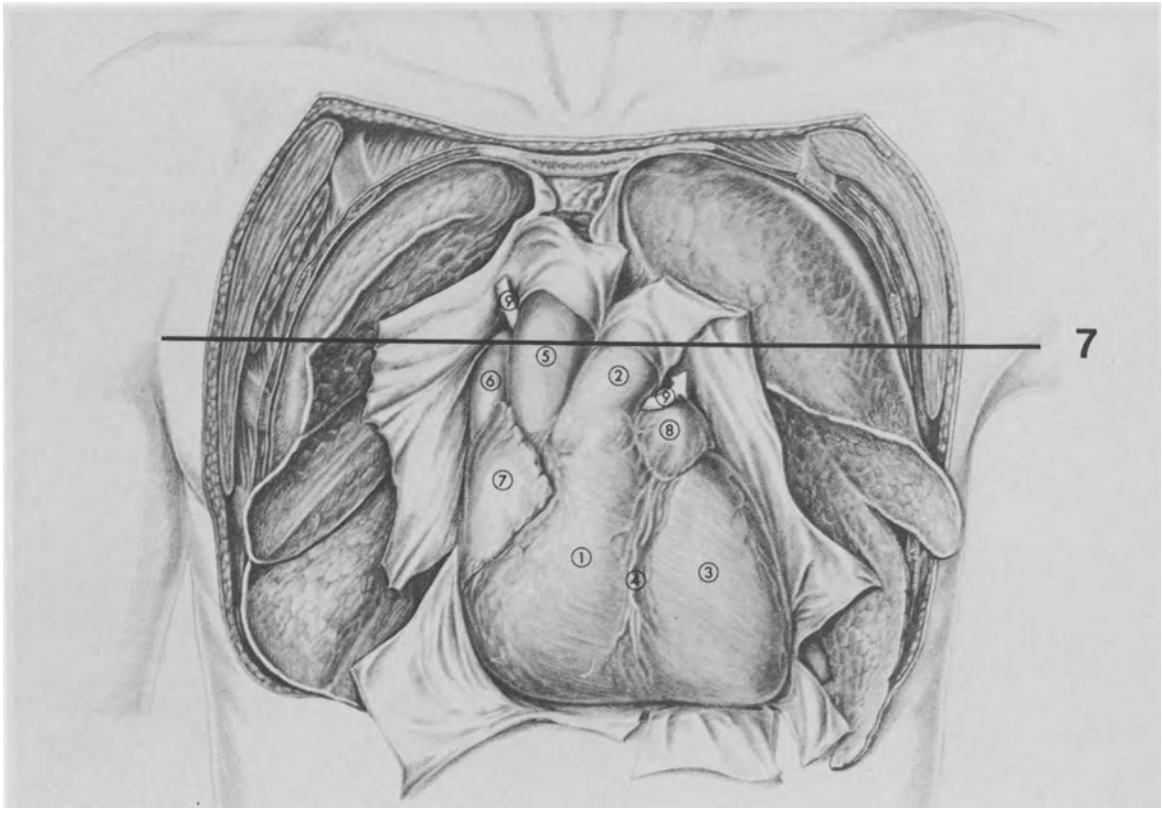

Figure T–20. Plane of section of transverse slice 7.

The two following NMR slices, through the fifth thoracic vertebra, show the right pulmonary artery arising from the pulmonary trunk. The right pulmonary artery is short (approximately 5 cms) and divides into two branches which accompany the corresponding lobar bronchi.

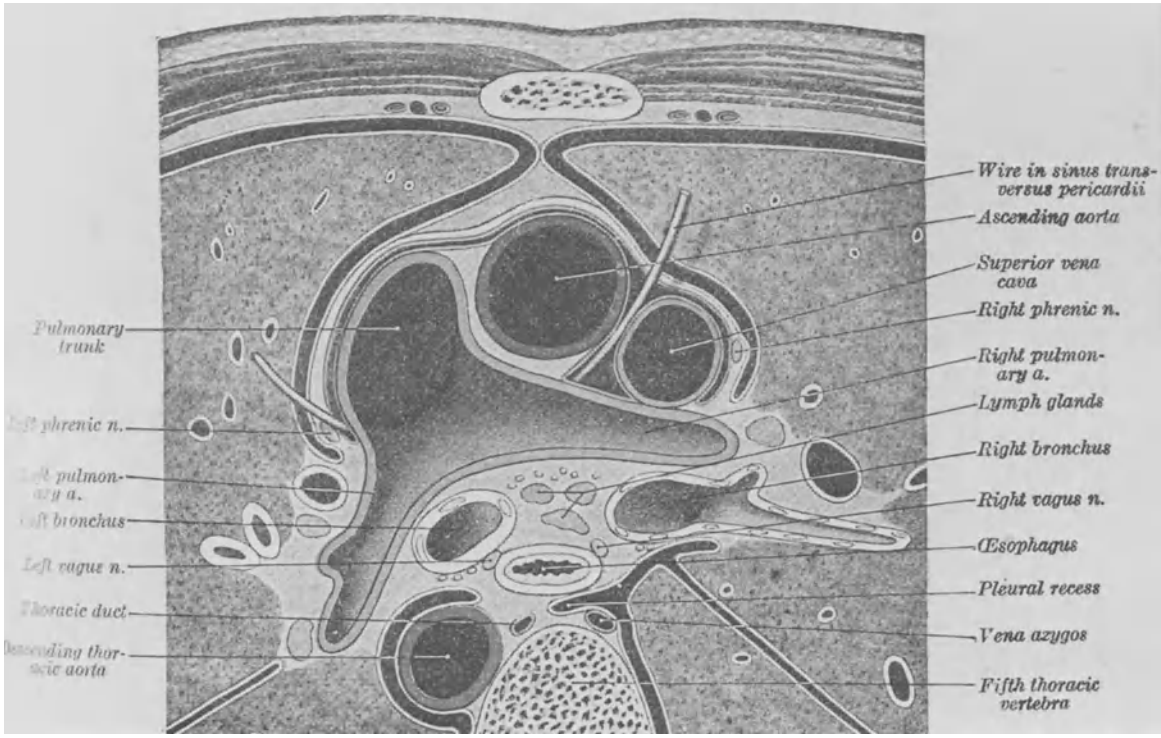

Figure T-21. Anatomical reproduction of transverse slice 7.

This anatomical transverse section shows the different structures of the posterior mediastinum at the level of the division of the pulmonary arteries. The following structures are shown: the esophagus, the azygos vein, the vagus nerves, the thoracic duct and the lymph nodes. These structures are not easily seen on the MR slices.

Please note that an anatomical picture is never inverted, at the opposite of MR slices. The right part of the body is thus represented on the right part of the picture and the left part of the body on the left part of the picture. The MR slices are 'seen' from the bottom of the body and, therefore, the left part of the body is on the right part of the picture and the right part of the body on the left part of the picture.

Transverse slice 7

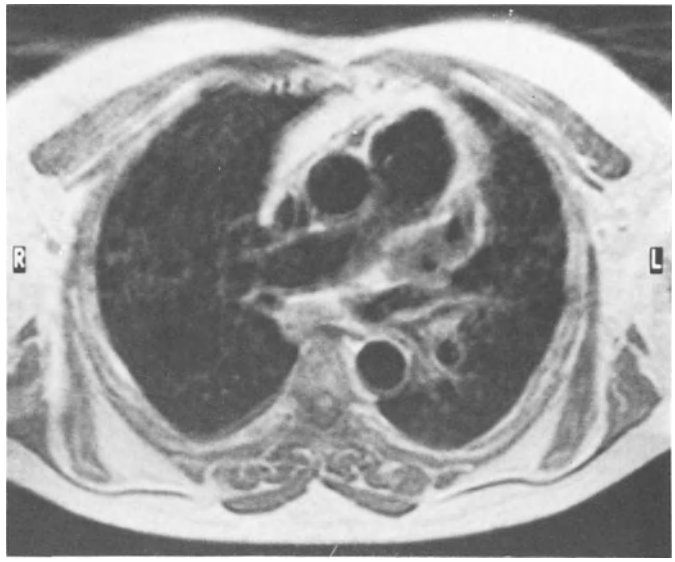

Figure T–22. MR slice.

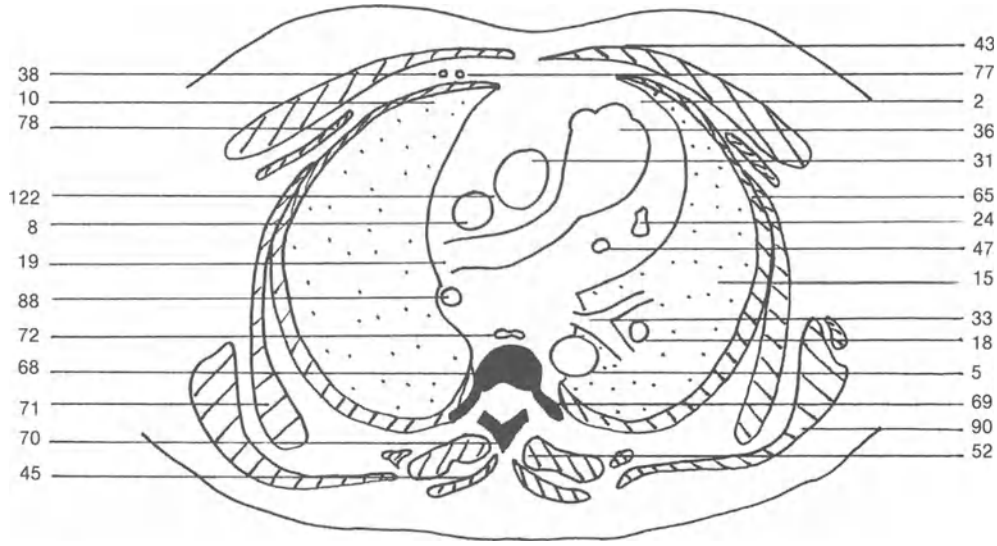

(2) Myocardium; (5) Descending aorta; (8) Superior vena cava; (15) Left lung; (16) Right lung; (18) Left pulmonary artery; (19) Right pulmonary artery; (24) Left atrial appendage; (31) Aortic infundibulum; (33) Left main bronchus; (36) Pulmonary infundibulum; (38) Internal mammary vein; (43) Pectoralis major muscle; (45) Trapezius muscle; (47) Left superior pulmonary vein; (52)

Figure T–23. MR slice.

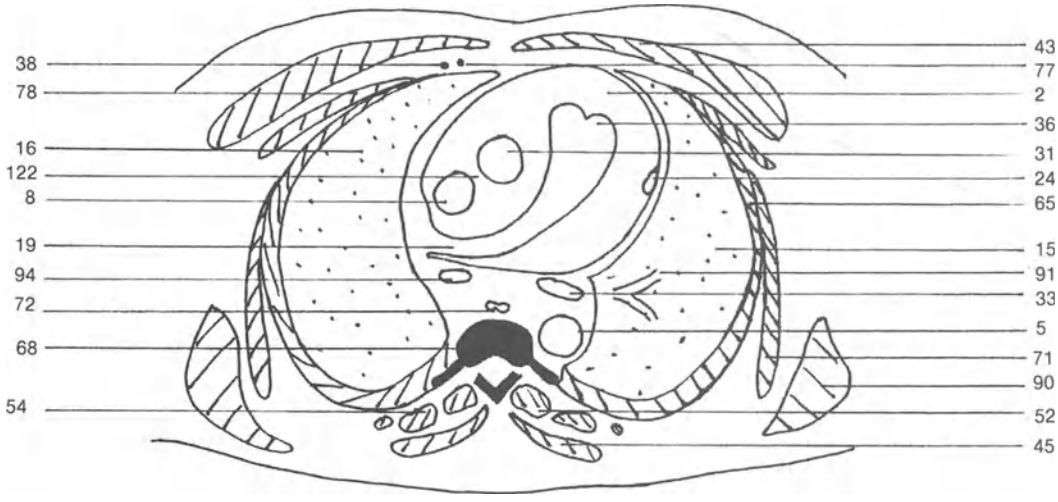

Erector spinae muscle; (54) Rhomboidus muscle; (65) Intercostal muscles; (68) Dorsal vertebra; (69) Rib; (70) Spinous process; (71) Serratus anterior muscle; (72) Esophagus; (77) Internal mammary artery; (78) Pectoralis minor muscle; (88) Right lower lobe bronchus; (90) Subscapularis muscle; (91) Segmental bronchus; (94) Right main bronchus; (122) Transverse sinus of the pericardium.

Transverse slice 8

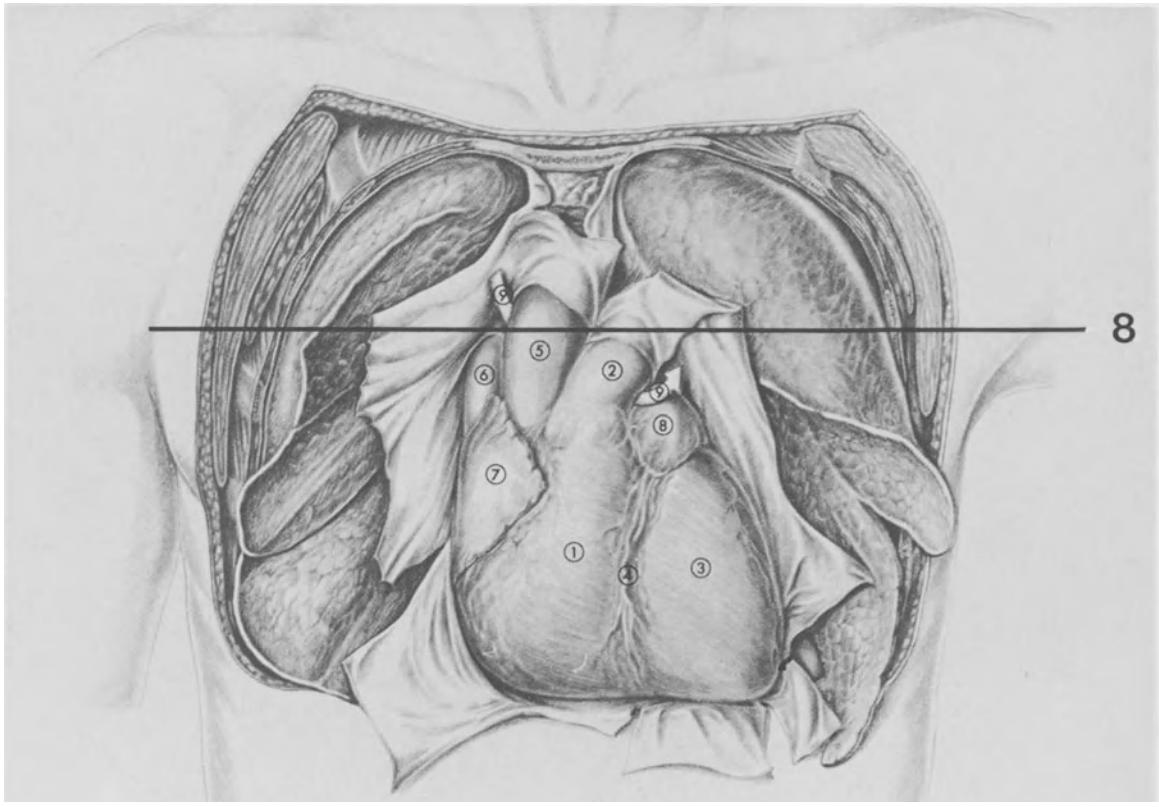

Figure T-24. Plane of section of transverse slice 8.

This slice is very close to the previous one. It shows that the left pulmonary artery rises slightly higher compared to the right pulmonary artery.

The right pulmonary artery is slightly longer and larger than the left. The two pulmonary arteries divide into lobar branches.

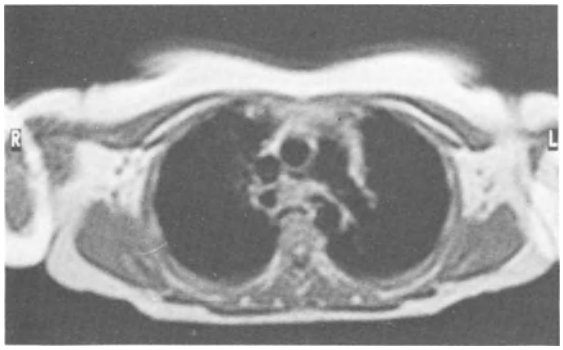

Figure T-25. MR slice.

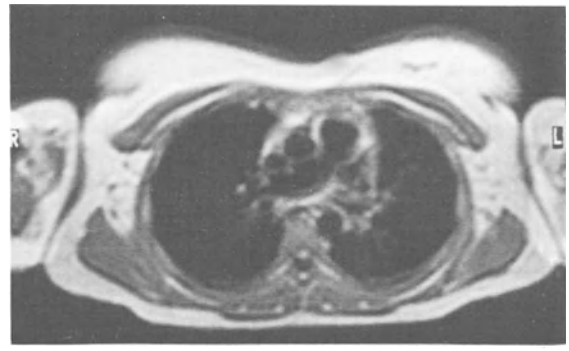

Figure T-26. MR slice.

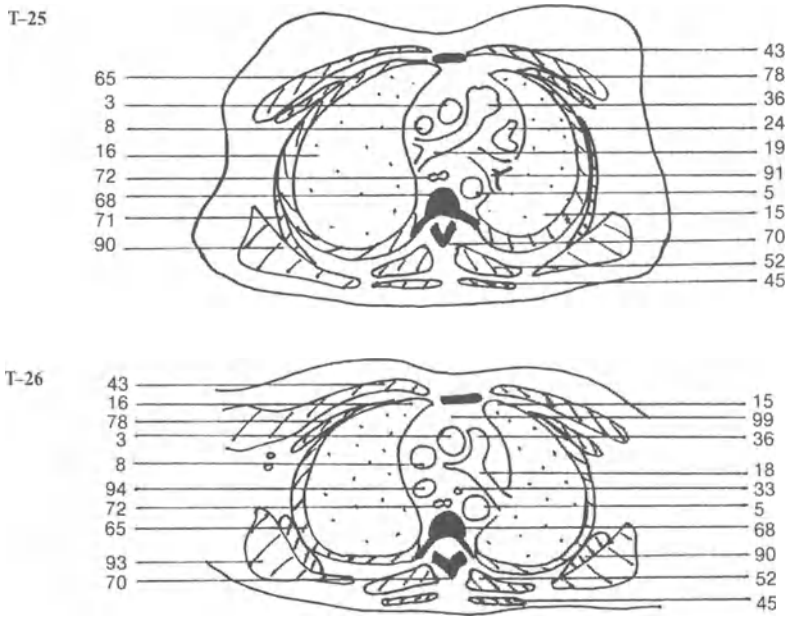

(3) Ascending aorta; (5) Descending aorta; (8) Superior vena cava; (15) Left lung; (16) Right lung; (18) Left pulmonary artery; (19) Right pulmonary artery; (24) Left atrial appendage; (33) Left main bronchus; (36) Pulmonary infundibulum; (43) Pectoralis major muscle; (45) Trapezius muscle; (52) Erector spinae muscle; (65) Intercostal muscles; (68) Dorsal vertebra; (70) Spinous process; (71) Serratus anterior muscle; (72) Esophagus; (78) Pectoralis minor muscle; (90) Subscapularis muscle; (91) Segmental bronchus; (93) Infraspinatus muscle; (94) Right main bronchus; (99) Mediastinum.

Transverse slice 9

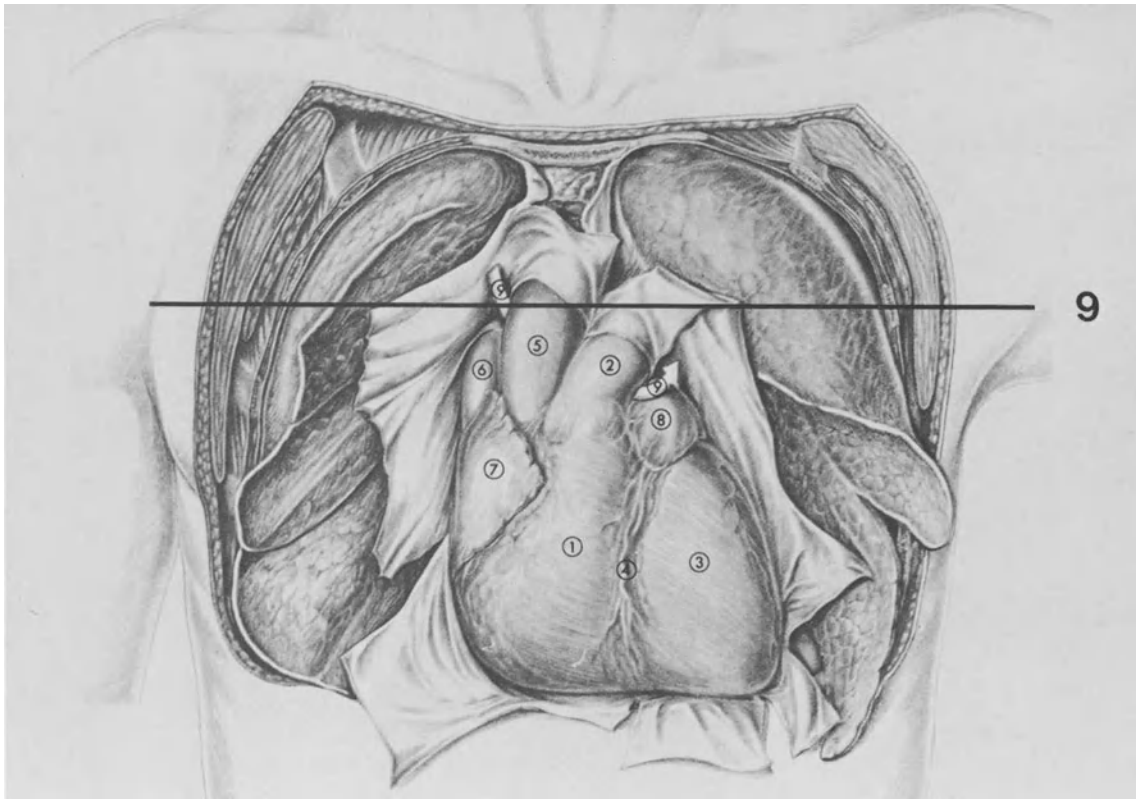

Figure T–27. Plane of section.

This slice is at the level of the division of the trachea into the two main bronchi. At the level of the division the two bronchi are separated by the carina.

The azygos vein is widest on this slice. It passes posterior to the carina, to the right of the esophagus and anterior to the thoracic vertebra. Slightly higher, it will arch forwards to join the posterior part of the superior vena cava.

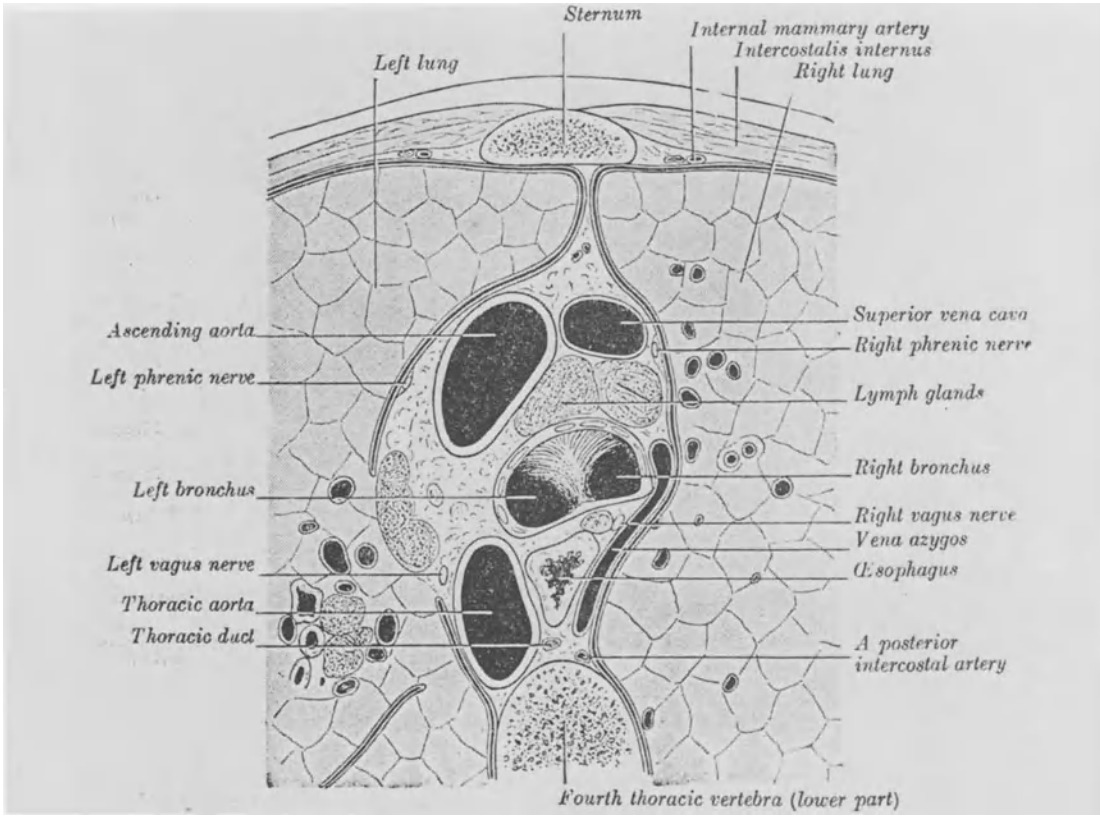

Figure T–28. Anatomical reproduction of transverse slice 9.

This anatomical transverse section shows the relations of the different structures at this level of the mediastinum: the ascending aorta and the superior vena cava are separated from the trachea by lymph nodes (the nomenclature of 'lymph glands' should not be used, because the lymph nodes have no glandular function); posterior to the trachea, the descending aorta, the esophagus and the azygos vein are shown. The orientation of an anatomical slice is the opposite of the orientation of a MR slice. See comment on page 67.

Transverse slice 9

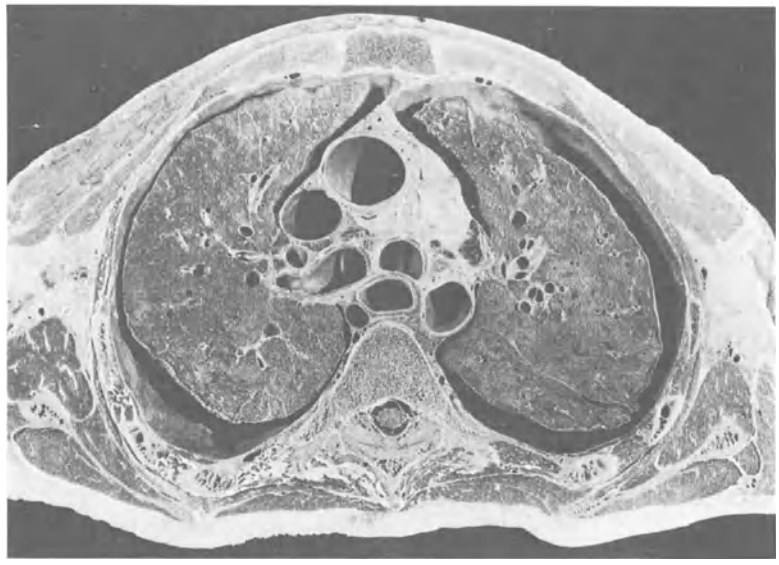

Figure T-29. Anatomical slice.

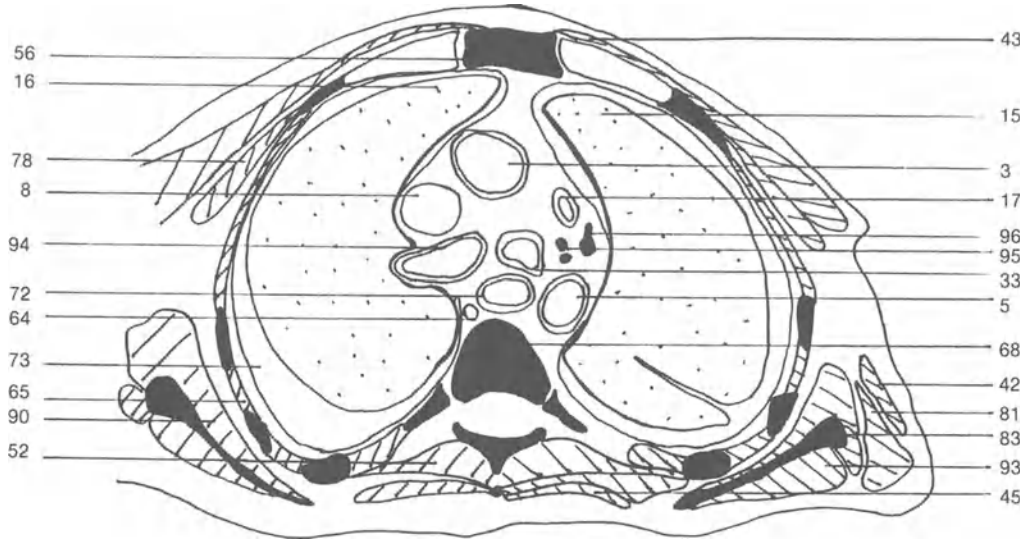

(3) Ascending aorta; (5) Descending aorta; (8) Superior vena cava; (15) Left lung; (16) Right lung; (17) Main pulmonary artery; (18) Left pulmonary artery; (33) Left main bronchus; (42) Latissimus dorsi muscle; (43) Pectoralis major muscle; (44) Carina; (45) Trapezius muscle; (52) Erector spinae muscle; (56) Manubrium; (64) Azygos vein; (65) Intercostal muscles; (68) Dorsal vertebra;

Figure T-30. MR slice.

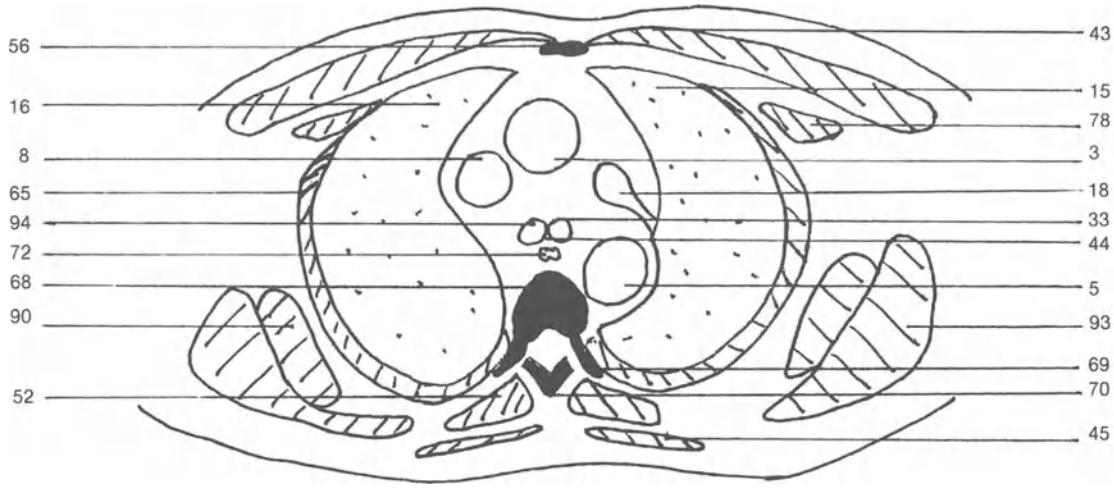

(69) Rib; (70) Spinous process; (72) Esophagus; (73) Pleural cavity; (78) Pectoralis minor muscle; (81) Teres major muscle; (83) Scapula; (90) Subscapularis muscle; (93) Infraspinatus muscle; (94) Right main bronchus; (95) Tracheo-bronchial lymph node; (96) Pulmonary lymph node.

Transverse slice 10

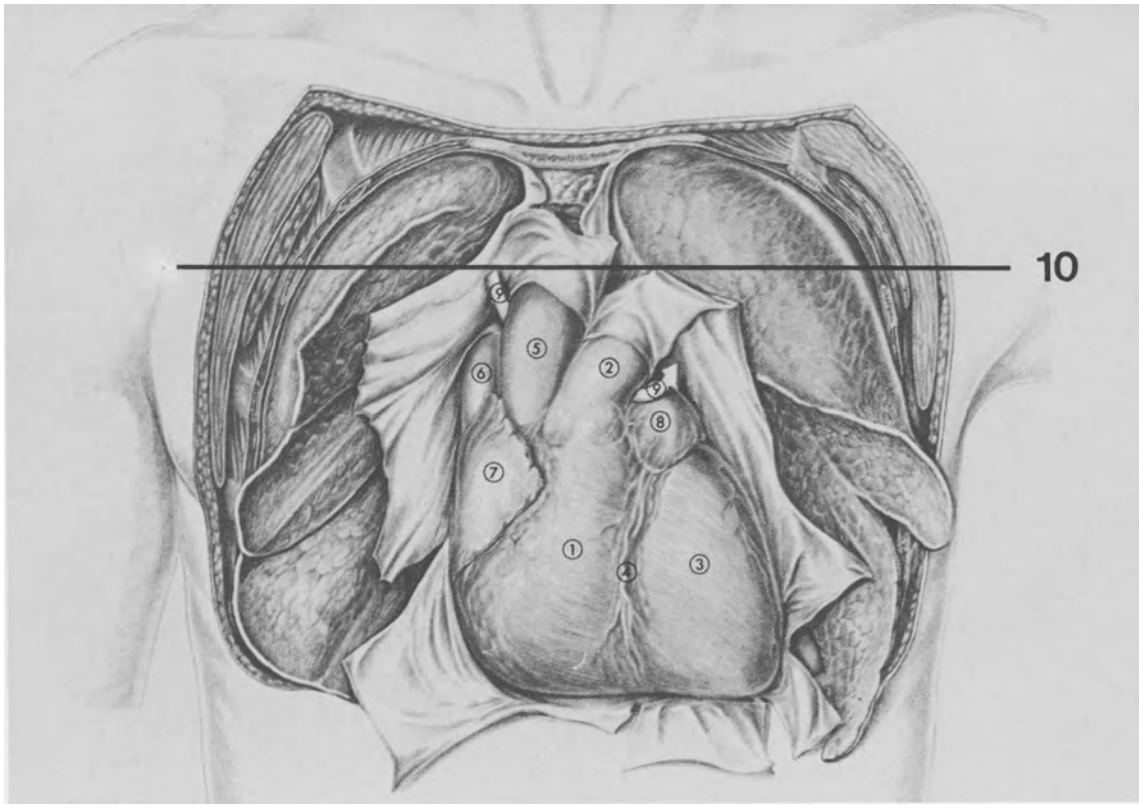

Figure T-31. Plane of section of transverse slice 10.

Slice through the arch of the aorta. The arch of the aorta runs at first backwards and to the left in front of the trachea and finally passes downwards on the left side of the fourth thoracic vertebra, where it is continuous with the descending aorta.

At this level, the azygos vein arches forwards in order to join the posterior part of the superior vena cava.

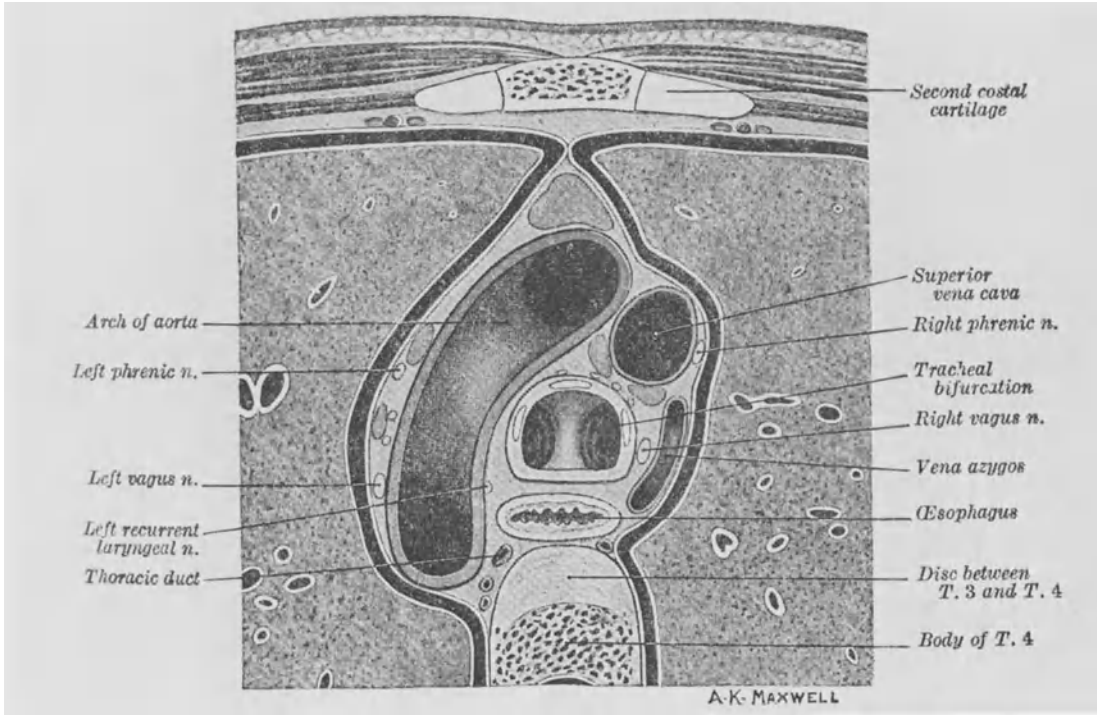

Figure T–32. Anatomical reproduction of transverse slice 10.

This anatomical transverse slice shows the anatomical relations of the arch of the aorta and of the arch of the azygos vein. The trachea is surrounded by two arches. At this level, the superior vena cava is just formed by the reunion of the brachiocephalic veins.

Note: At the opposite of the MR slices, the anatomical slices show the right part of the body on the right part of the picture. The direction of the structures is thus not inverted. See comment on page 67.

Transverse slice 10

Figure T–33. Anatomical slice.

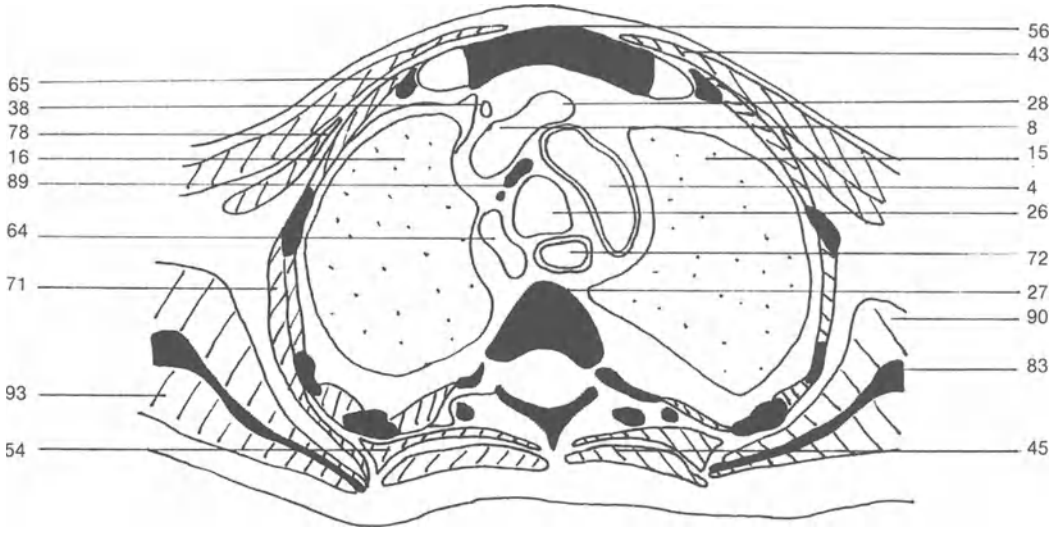

(3) Ascending aorta; (4) Aortic arch; (5) Descending aorta; (8) Superior vena cava; (15) Left lung; (16) Right lung; (26) Trachea; (27) Thoracic vertebra; (28) Left brachiocephalic vein; (29) Left common carotid artery; (38) Internal mammary vein; (43) Pectoralis major muscle; (45) Trapezius muscle; (52) Erector spinae muscle; (54) Rhomboidus muscle; (56) Manubrium; (64) Azygos vein; (65)

Figure T-34. MR slice.

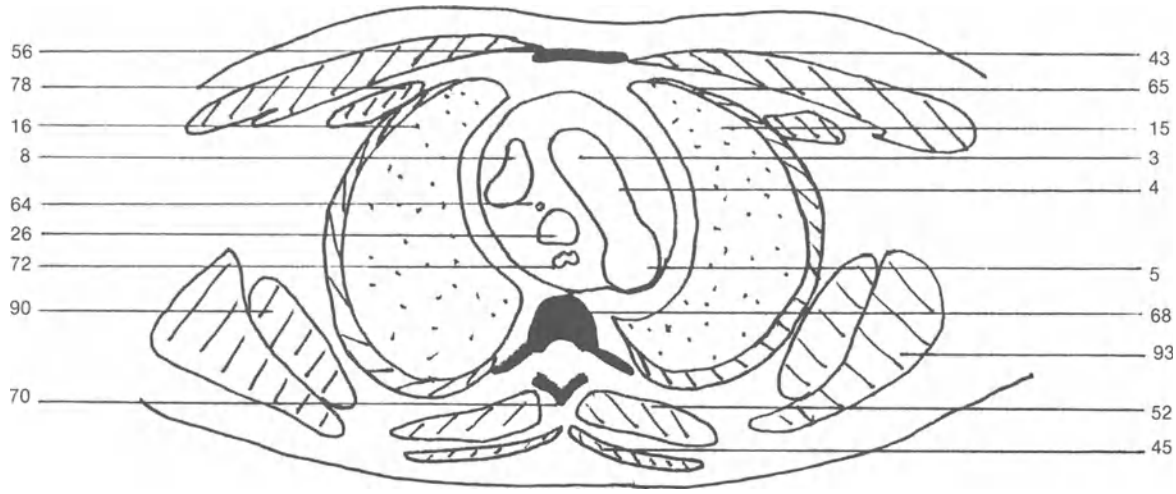

Intercostal muscles; (68) Dorsal vertebra; (70) Spinous process; (71) Serratus anterior muscle; (72) Esophagus; (78) Pectoralis minor muscle; (83) Scapula; (89) Lymph node; (90) Subscapularis muscle; (93) Infraspinatus muscle.

Transverse slice 10

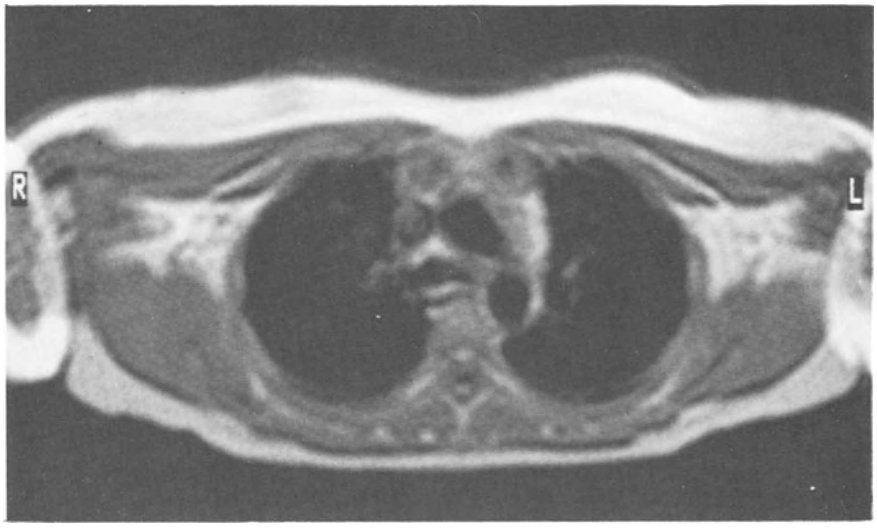

Figure T-35. MR slice.

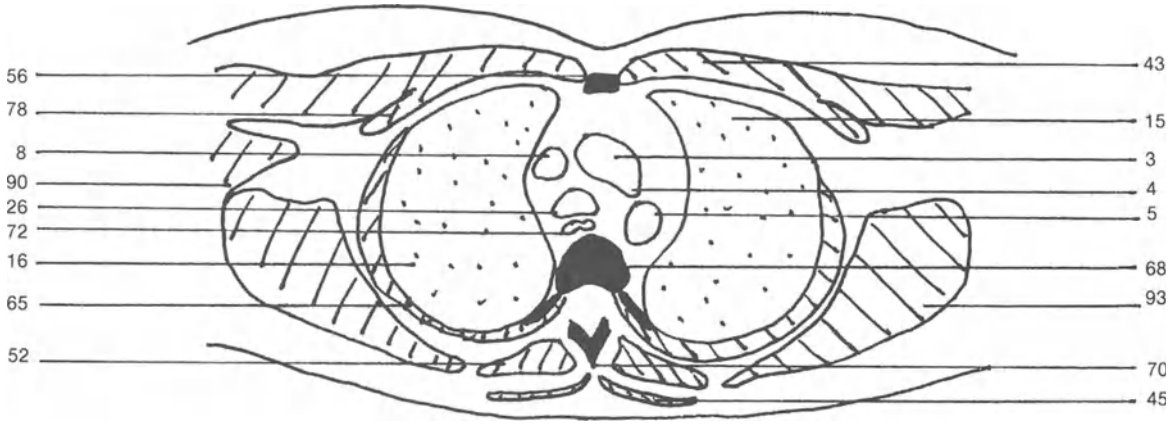

(3) Ascending aorta; (4) Aortic arch; (5) Descending aorta; (8) Superior vena cava; (15) Left lung; (16) Right lung; (26) Trachea; (27) Thoracic vertebra; (43) Pectoralis major muscle; (45) Trapezius muscle; (52) Erector spinae muscle; (54) Rhomboidus muscle; (56)

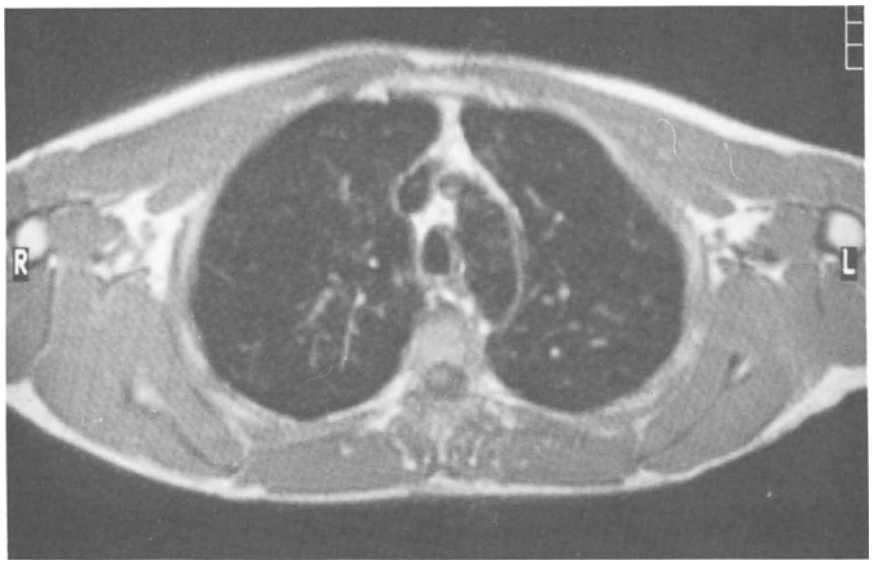

Figure T-36. MR slice.

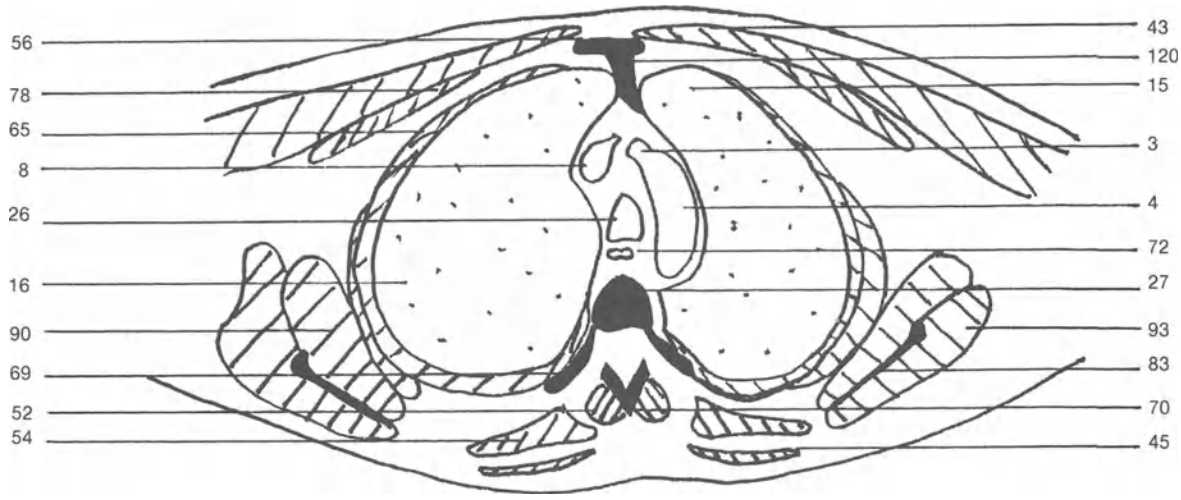

Manubrium; (65) Intercostal muscles; (68) Dorsal vertebra; (69) Rib; (70) Spinous process; (72) Esophagus; (78) Pectoralis minor muscle; (83) Scapula; (90) Subscapularis muscle; (93) Infraspinatus muscle; (120) Pericardosternal ligament.

Transverse slice 11

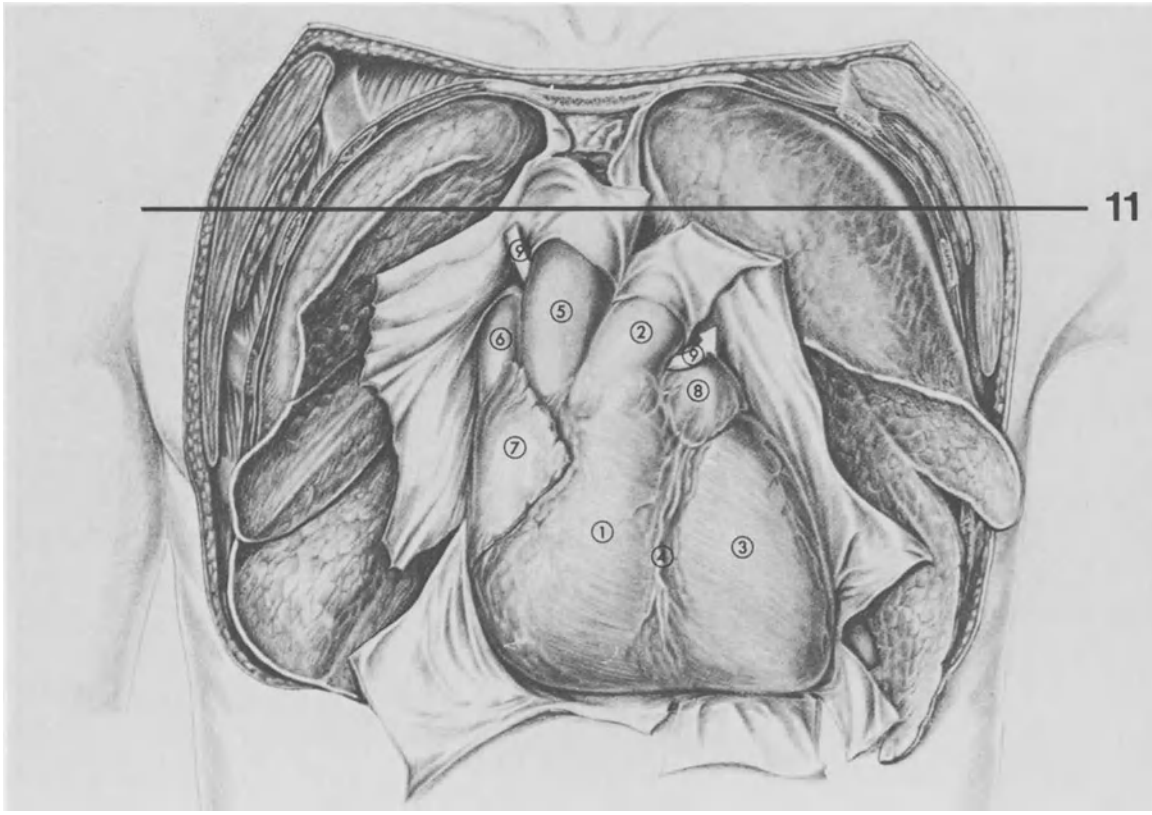

Figure T-37. Plane of section of transverse slice 11.

This slice shows the junction of the two brachiocephalic veins which will form the superior vena cava. Two of the three vessels of the aortic arch are also seen: the brachiocephalic trunk (innominate artery) which accompanies the right brachiocephalic vein and the left common carotid artery accompanying the left brachiocephalic vein. The third vessel of the aortic arch, the left subclavian artery, arises at a superior level.

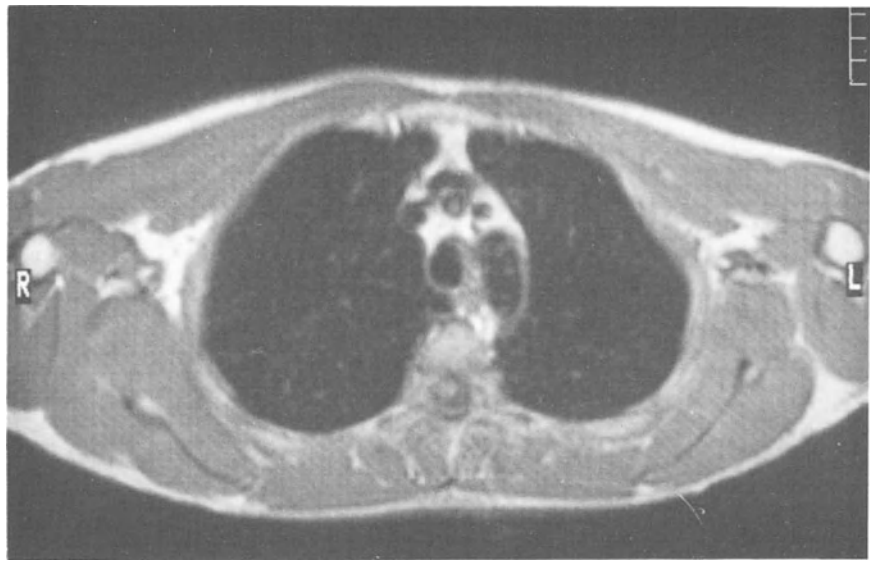

Figure T-38. MR slice.

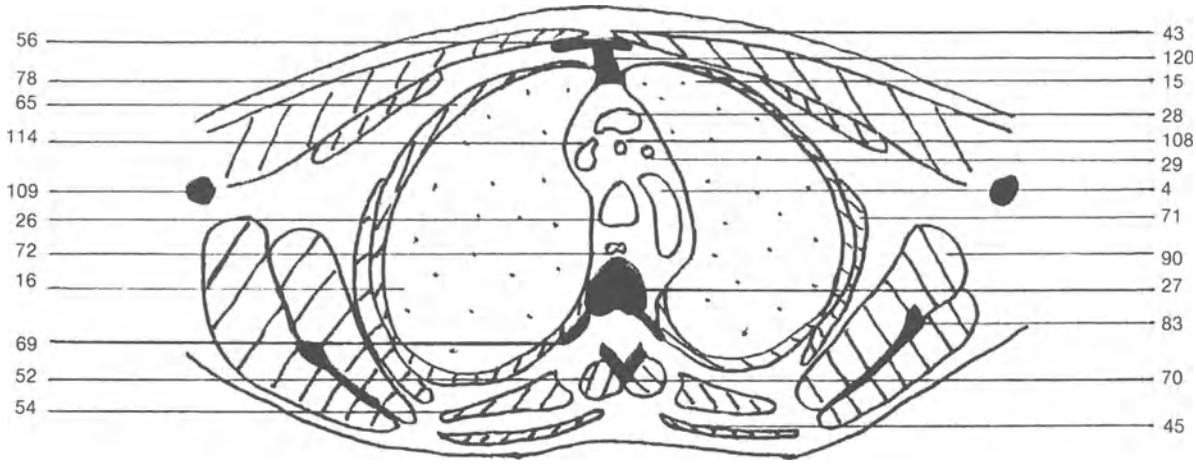

(4) Aortic arch; (15) Left lung; (16) Right lung; (26) Trachea; (27) Thoracic vertebra; (28) Left brachiocephalic vein; (29) Left common carotid artery; (43) Pectoralis major muscle; (45) Trapezius muscle; (52) Erector spinae muscle; (54) Rhomboidus muscle; (56) Manubrium; (65) Intercostal muscles; (69) Rib; (70) Spinous process; (71) Serratus anterior muscle; (72) Esophagus; (78) Pectoralis minor muscle; (83) Scapula; (90) Subscapularis muscle; (108) Brachiocephalic trunk; (109) Humerus; (114) Right brachiocephalic vein; (120) Pericardosternal ligament.

Transverse slice 12

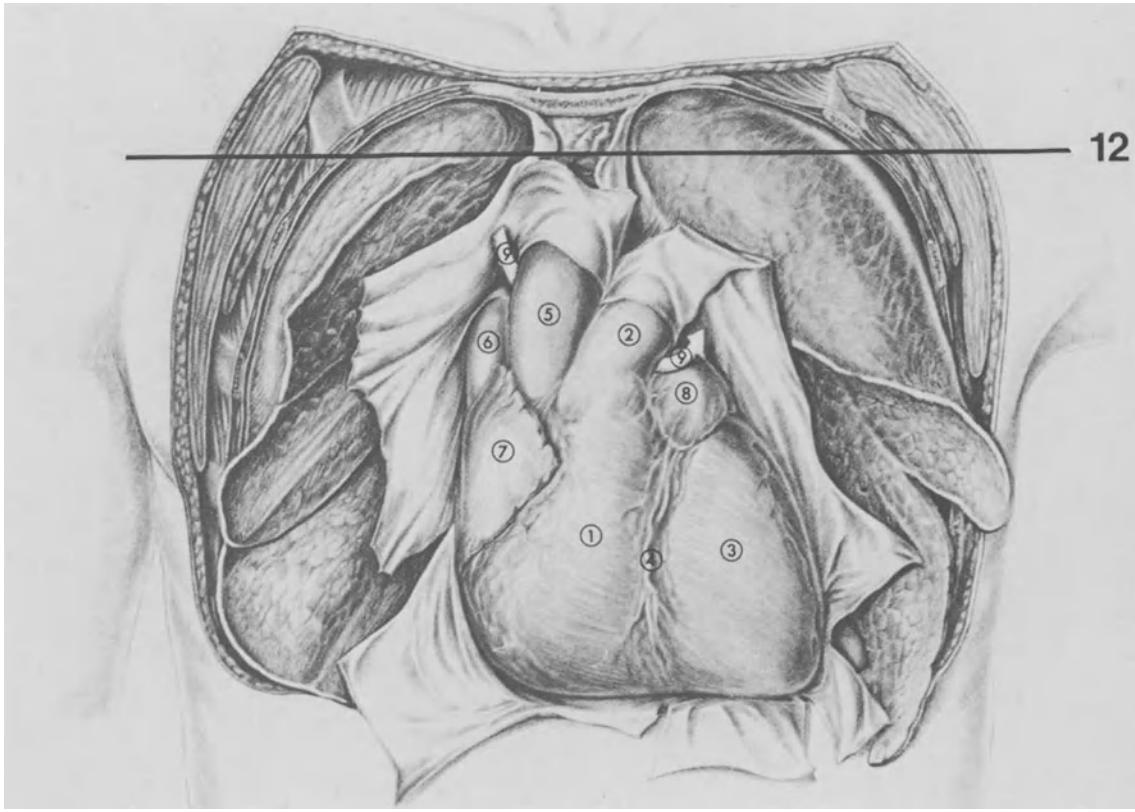

Figure T–39. Plane of section of transverse slice 12.

This slice shows the principal vessels of the neck, i.e. the three branches of the aortic arch (brachiocephalic trunk, left common carotid artery and left subclavian artery) and the two brachiocephalic veins (innominate veins).

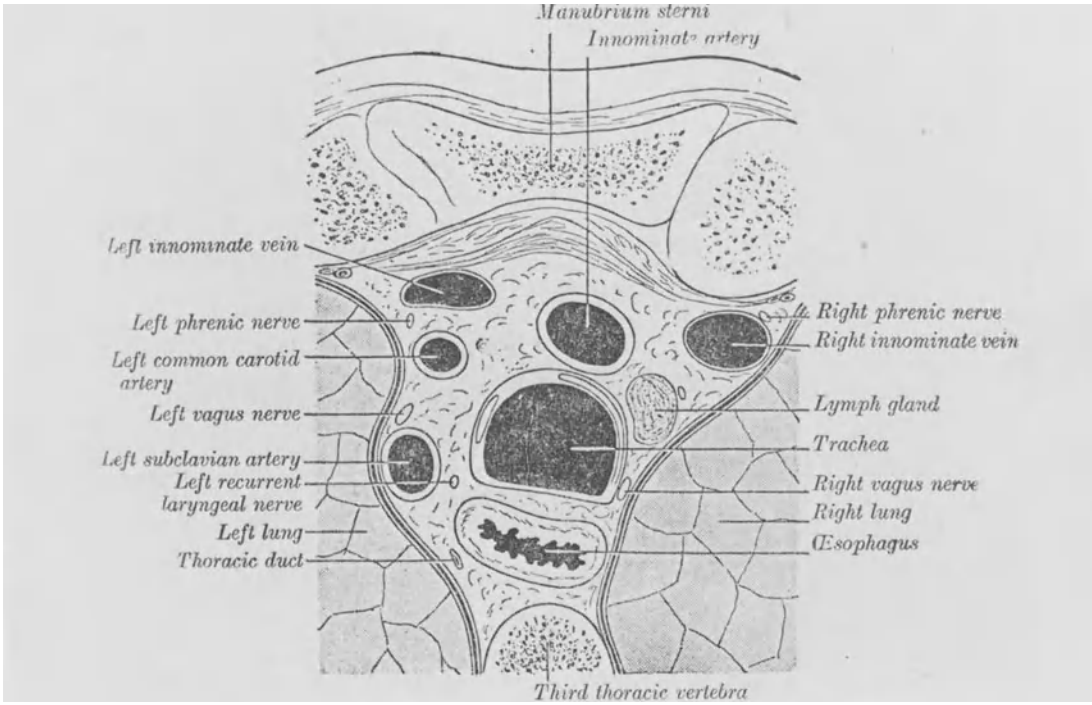

Figure T–40. Anatomical reproduction of transverse slice 12.

This anatomical transverse slice shows the anatomical relations of the principal vessels of the neck. As for Figure T–32, the structures are not inverted on anatomical slices. See comment on page 67.

Transverse slice 12

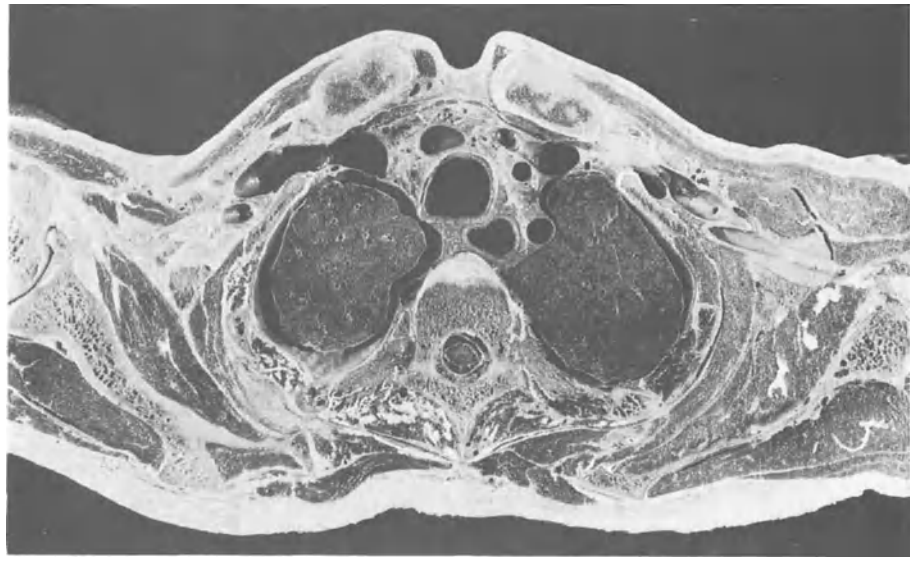

Figure T–41. Anatomical slice.

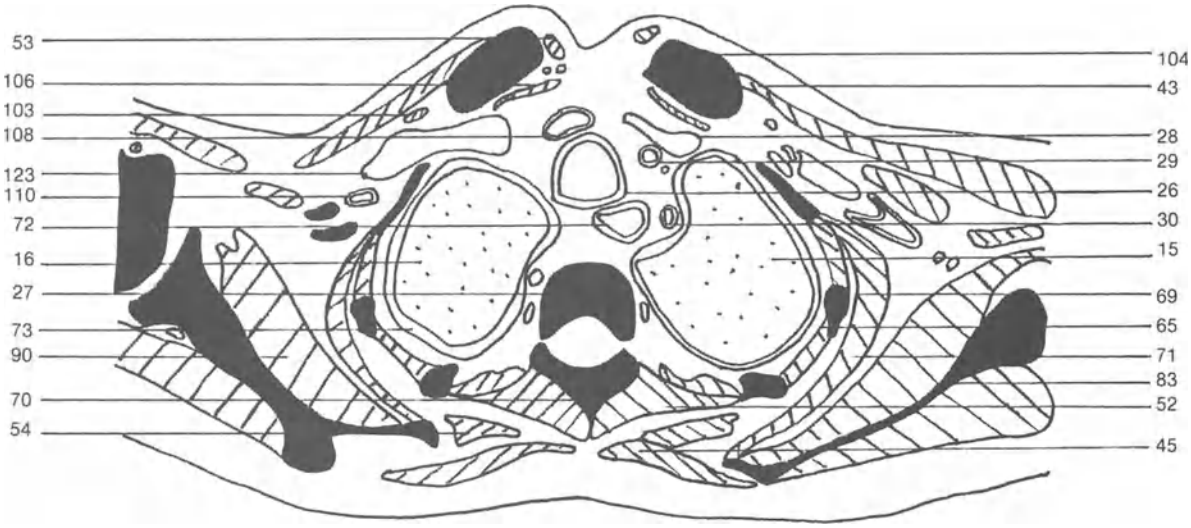

(15) Left lung; (16) Right lung; (26) Trachea; (27) Thoracic vertebra; (28) Left brachiocephalic vein; (29) Left common carotid artery; (30) Left subclavian artery; (43) Pectoralis major muscle; (45) Trapezius muscle; (52) Erector spinae muscle; (53) Sternocleidomastoid muscle; (54) Rhomboidus muscle; (65) Intercostal muscles; (69) Rib; (70) Spinous process; (71) Serratus anterior muscle;

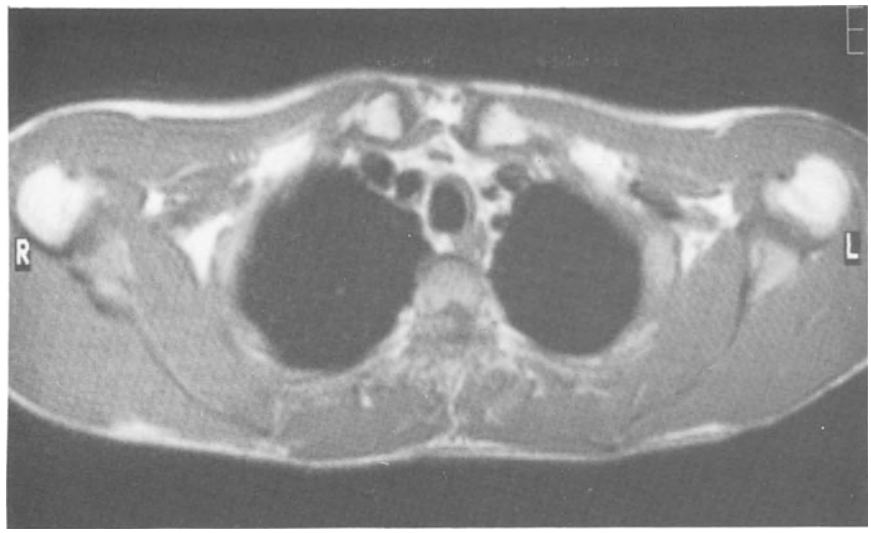

Figure T–42. MR slice.

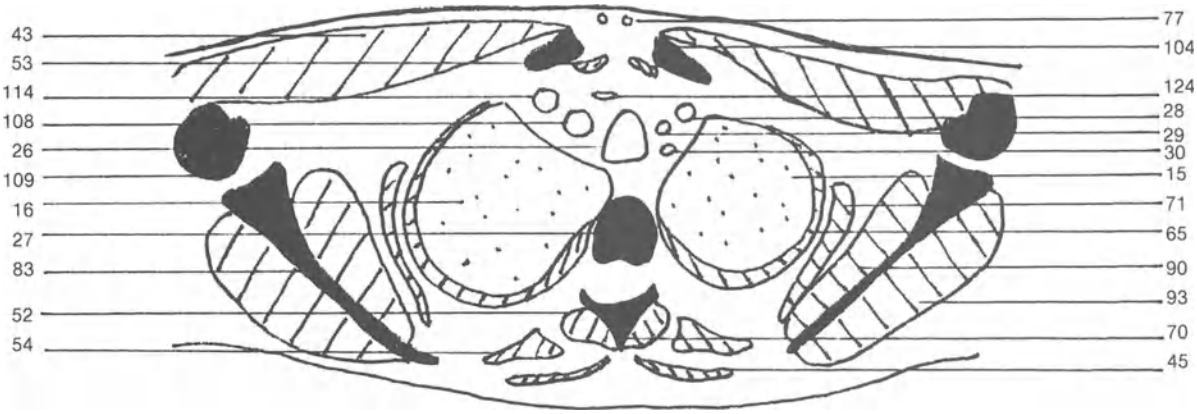

(72) Esophagus; (73) Pleural cavity; (77) Internal mammary artery; (83) Scapula; (90) Subscapularis muscle; (93) Infraspinatus muscle; (103) Subclavius muscle; (104) Clavicle; (106) Sternohyoid muscle; (108) Brachiocephalic trunk; (109) Humerus; (110) Axillary artery; (114) Right brachiocephalic vein; (123) Axillary vein; (124) Jugular arch.

Transverse slice 13

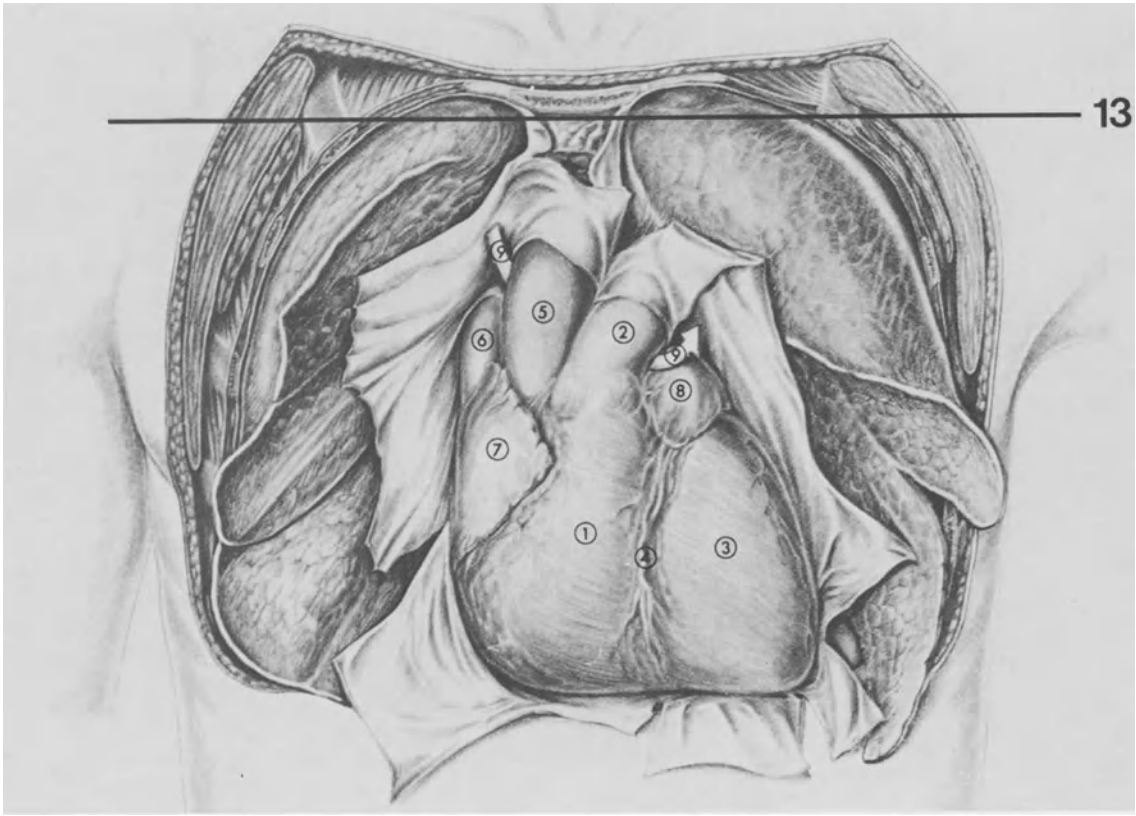

Figure T–43. Plane of section of transverse slice 13.

This level is situated one thoracic vertebra higher than the previous level and shows the division of the brachiocephalic trunk into the right common carotid artery and the right subclavian artery. The left subclavian vein joins the left internal jugular vein to form the left brachiocephalic vein.

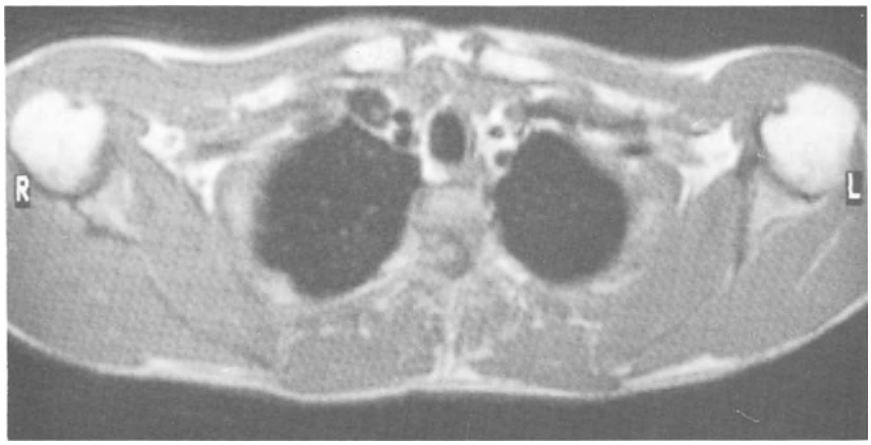

Figure T-44. MR slice.

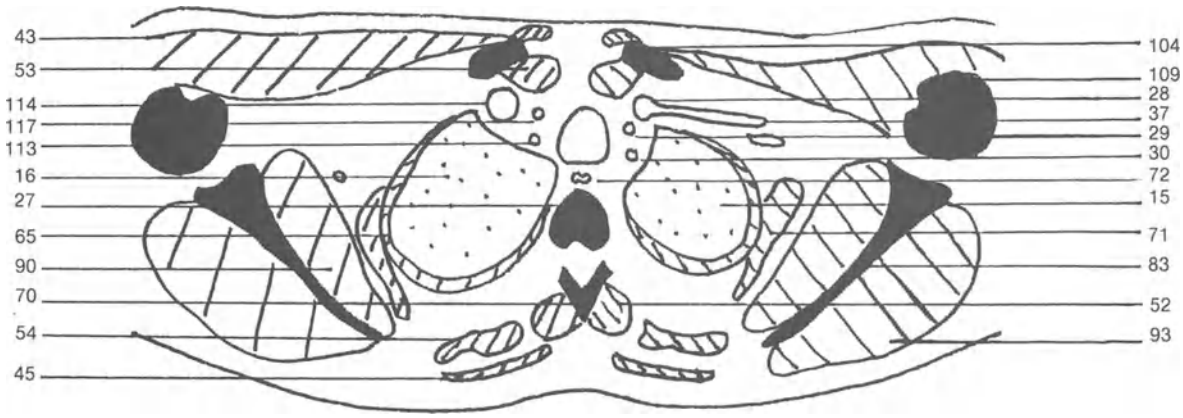

(15) Left lung; (16) Right lung; (27) Thoracic vertebra; (28) Left brachiocephalic vein; (29) Left common carotid artery; (30) Left subclavian artery; (37) Left subclavian vein; (43) Pectoralis major muscle; (45) Trapezius muscle; (52) Erector spinae muscle; (53) Sternocleidomastoid muscle; (54) Rhomboidus muscle; (65) Intercostal muscles; (70) Spinous process; (71) Serratus anterior muscle; (72) Esophagus; (83) Scapula; (90) Subscapularis muscle; (93) Infraspinatus muscle; (104) Clavicle; (109) Humerus; (113) Right subclavian artery; (114) Right brachiocephalic vein; (117) Right common carotid artery.

SAGITTAL SLICES 1-10

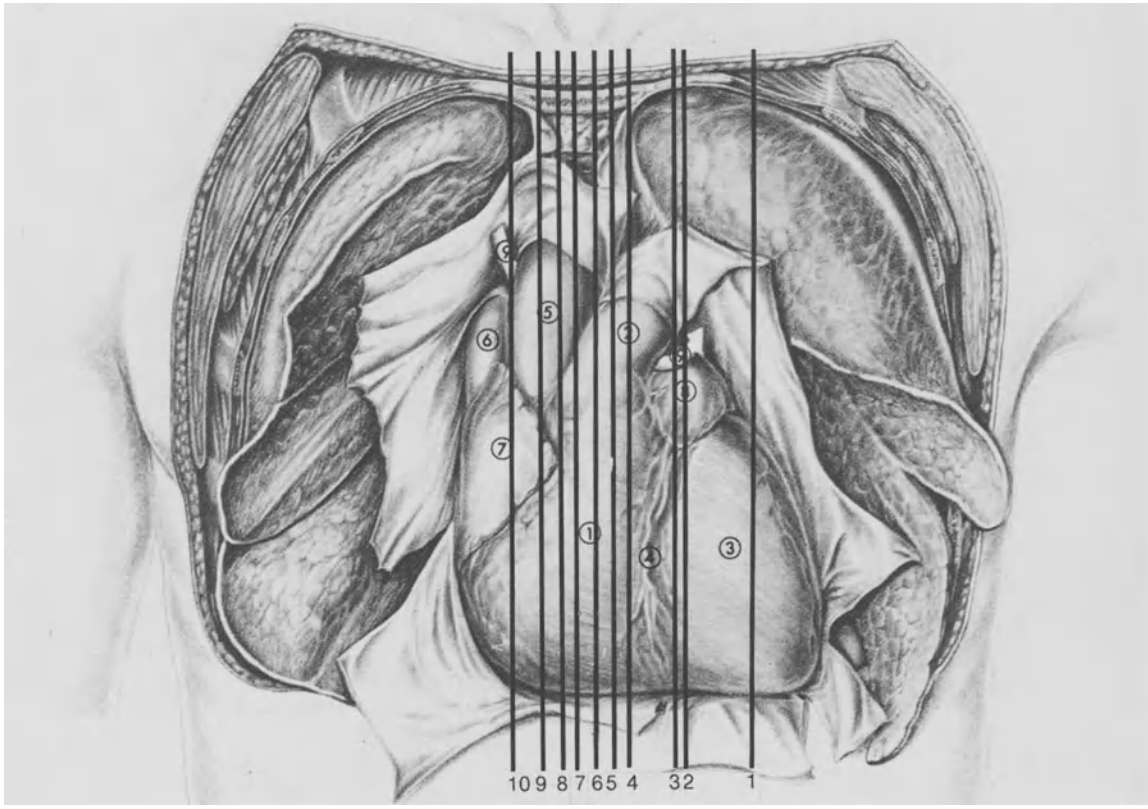

Figure S–0. Plane of section of sagittal slices.

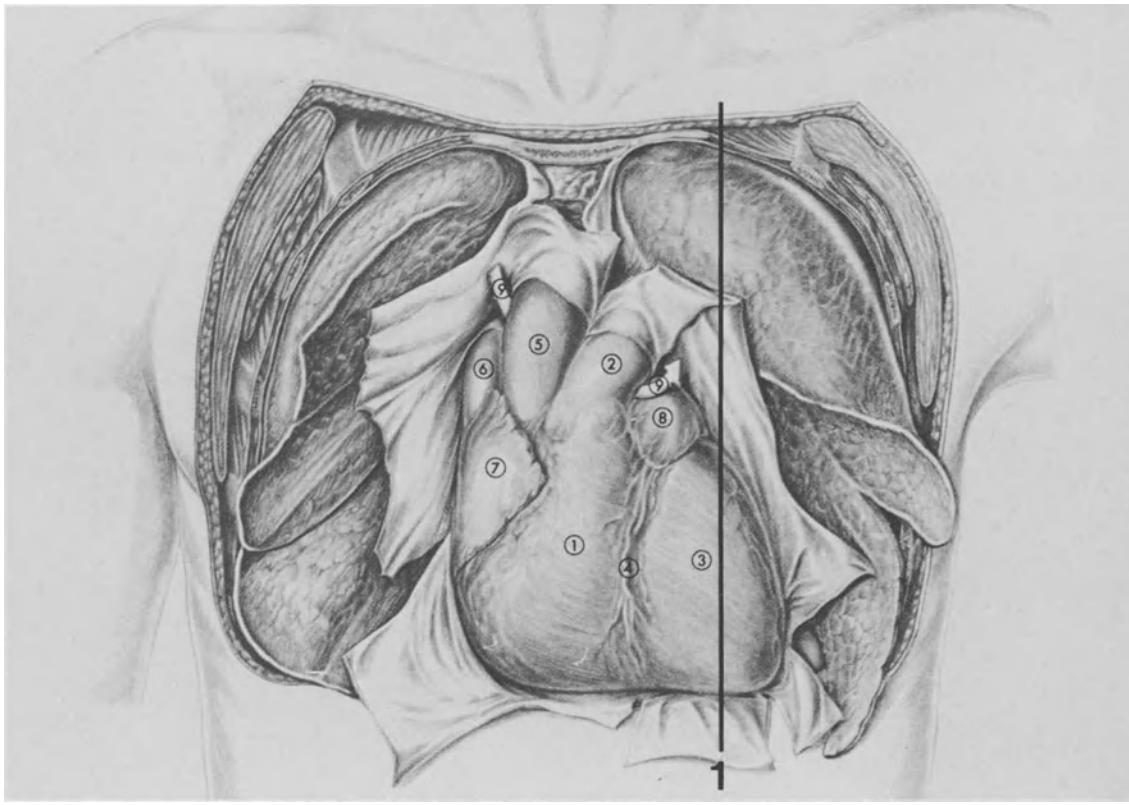

Figure S–1. Plane of section of sagittal slice 1.

This sagittal slice crosses the left part of the heart, represented by the left ventricle.

The subclavian vessels and the branches of the brachial plexus can be seen.

Sagittal slice 1

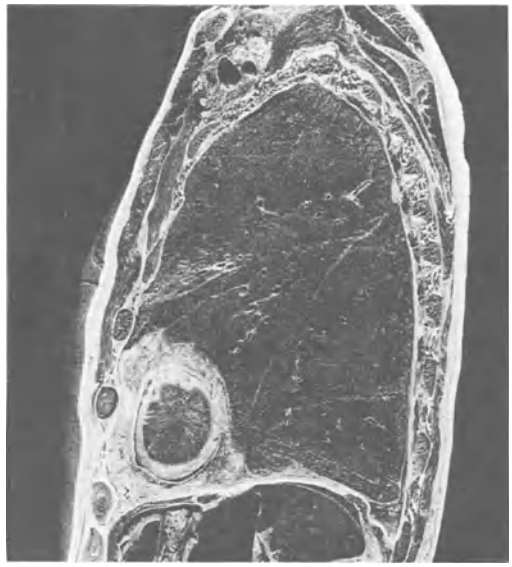

Figure S–2. Anatomical slice.

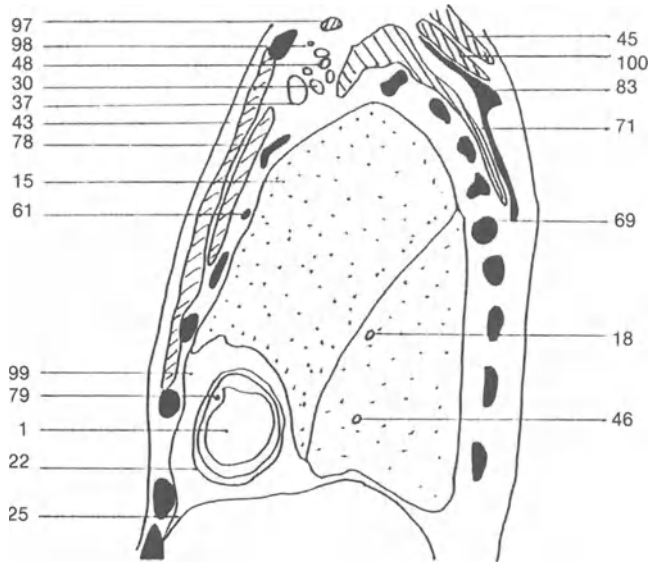

(1) Left ventricular cavity; (2) Myocardium; (15) Left lung; (18) Left pulmonary artery; (22) Pericardium; (25) Diaphragm; (30) Left subclavian artery; (37) Left subclavian vein; (43) Pectoralis major muscle; (45) Trapezius muscle; (46) Left inferior pulmonary vein; (48) Brachial plexus; (69) Rib; (71) Serratus anterior muscle; (78) Pectoralis minor muscle; (79) Left coronary artery; (83) Scapula; (97) Omohyoid muscle; (98) Superficial cervical vein; (99) Mediastinum; (100) Supraspinatus muscle.

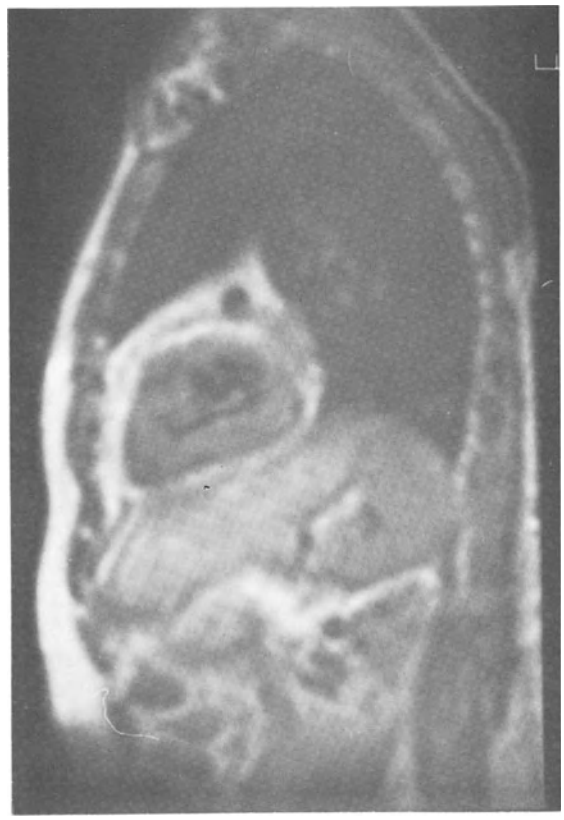

Figure S–3. MR slice.

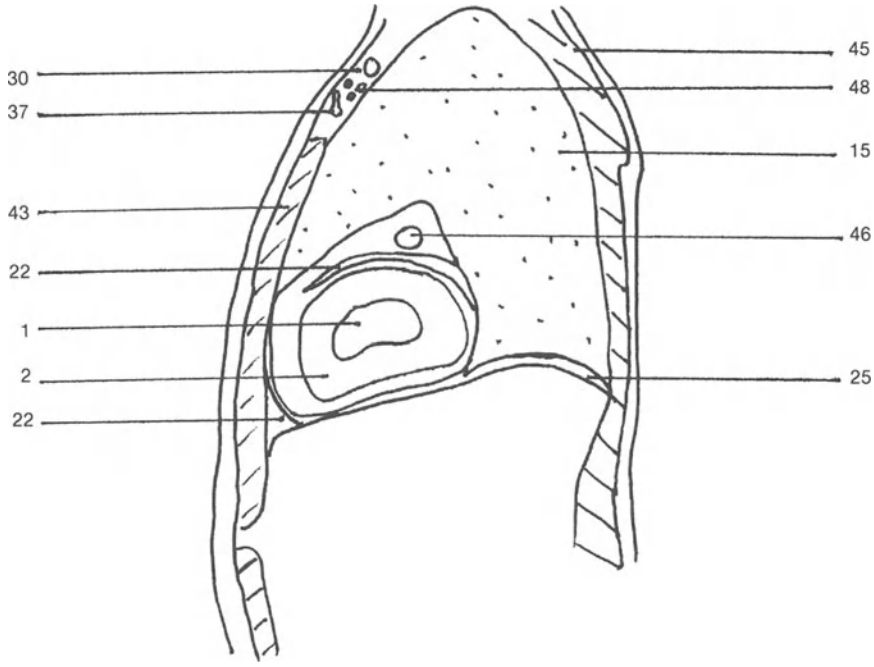

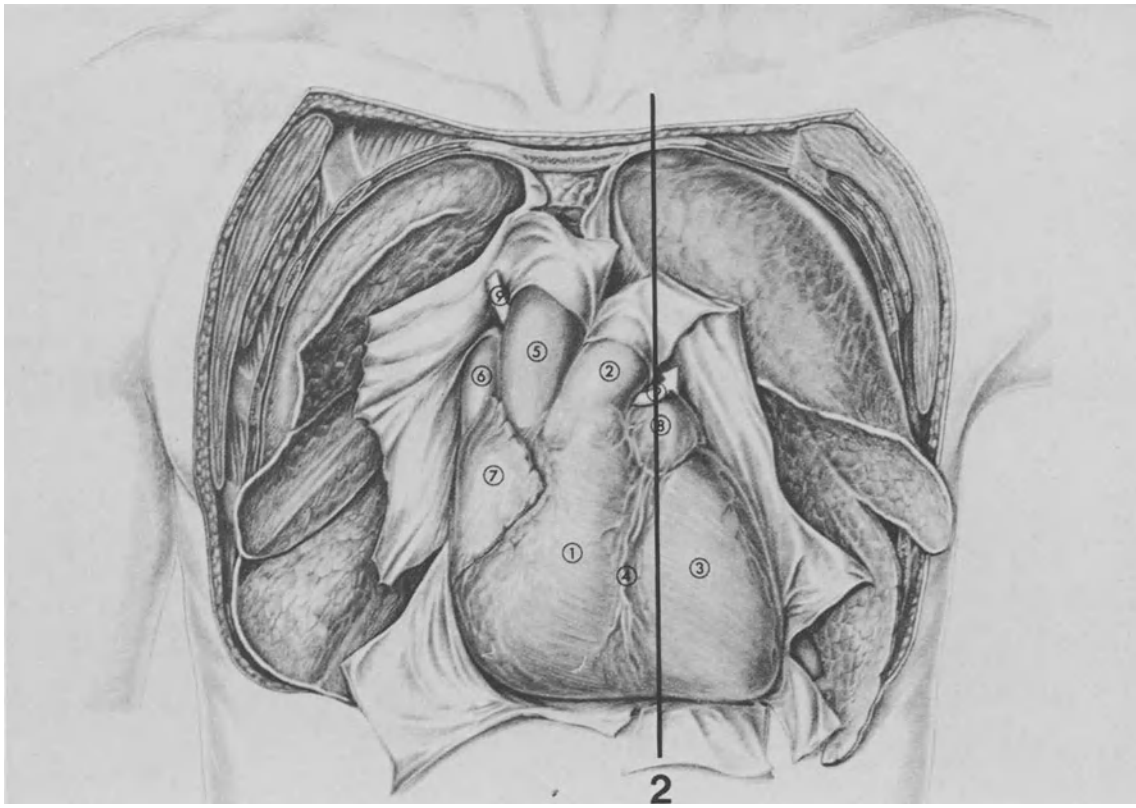

Figure S–4. Plane of section of sagittal slice 2.

This slice crosses the hilum of the left lung. The left pulmonary artery divides into two lobar branches while the pulmonary veins return to the hilum before opening into the left atrium.

The right ventricle is in front of the left ventricle. The left anterior descending coronary artery is situated between the two ventricles.

Sagittal slice 2

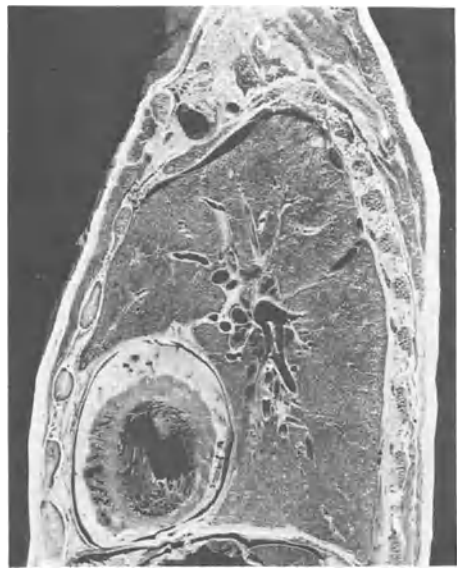

Figure S–5. Anatomical slice.

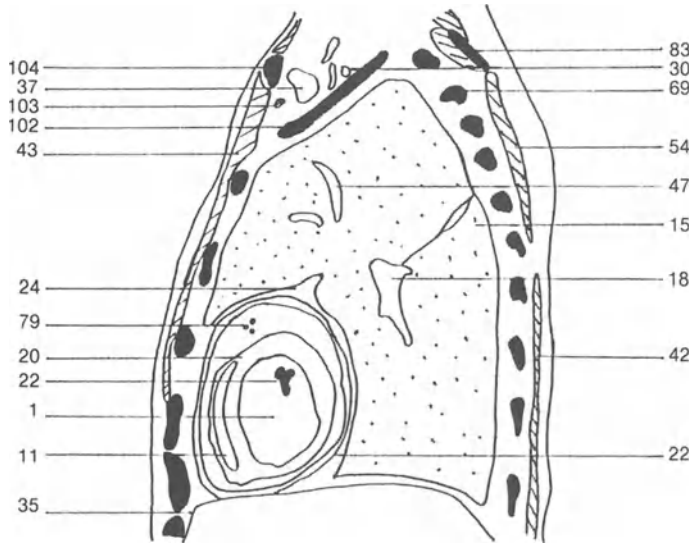

(1) Left ventricular cavity; (11) Right ventricular cavity; (15) Left lung; (18) Left pulmonary artery; (20) Ventricular septum; (21) Papillary muscle; (22) Pericardium; (24) Left atrial appendage; (25) Diaphragm; (30) Left subclavian artery; (37) Left subclavian vein;

Figure S–6. MR slice.

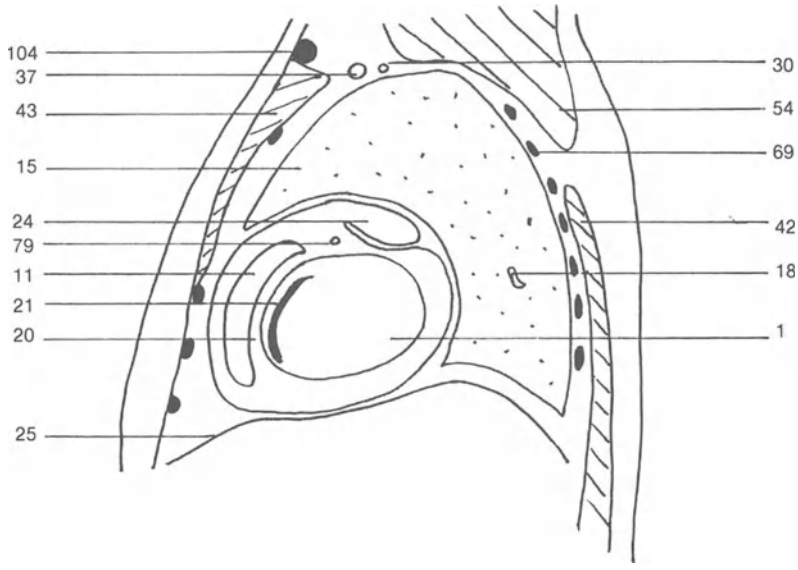

(42) Latissimus dorsi muscle; (43) Pectoralis major muscle; (47) Left superior pulmonary vein; (54) Rhomboidus muscle; (69) Rib; (79) Left coronary artery; (83) Scapula; (102) First rib; (103) Subclavius muscle; (104) Clavicle.

Sagittal slice 3

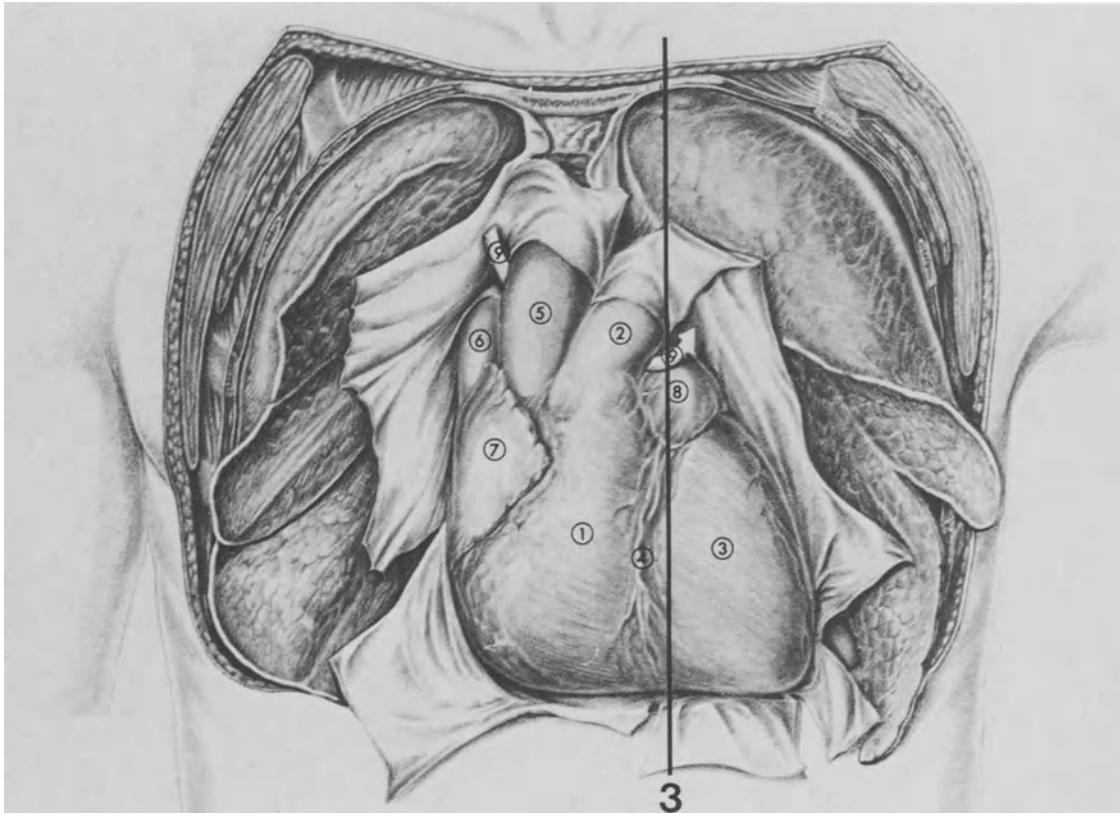

Figure S–7. Plane of section of sagittal slice 3.

This slice is close to the previous one. The junction of the pulmonary veins is seen near the left atrium. The difference of the thickness of the two ventricles is clearly seen. The right ventricle is elongated upwards to form the right ventricular outflow region.

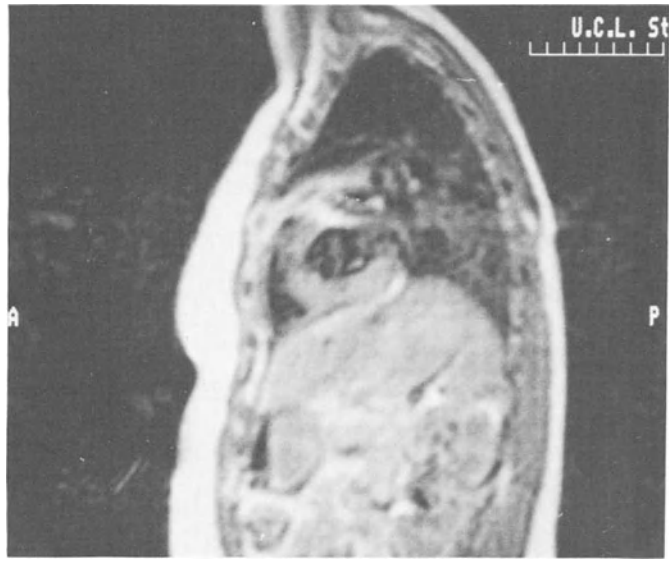

Figure S–8. MR slice.

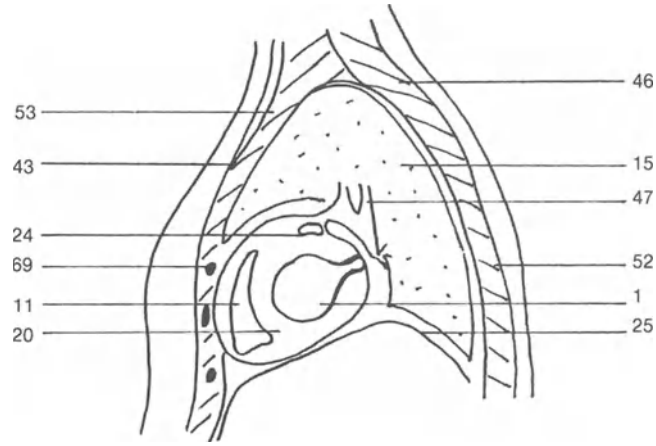

(1) Left ventricular cavity; (11) Right ventricular cavity; (15) Left lung; (20) Ventricular septum; (24) Left atrial appendage; (25) Diaphragm; (43) Pectoralis major muscle; (45) Trapezius muscle; (47) Left superior pulmonary vein; (52) Erector spinae muscle; (53) Sternocleidomastoid muscle; (69) Rib.

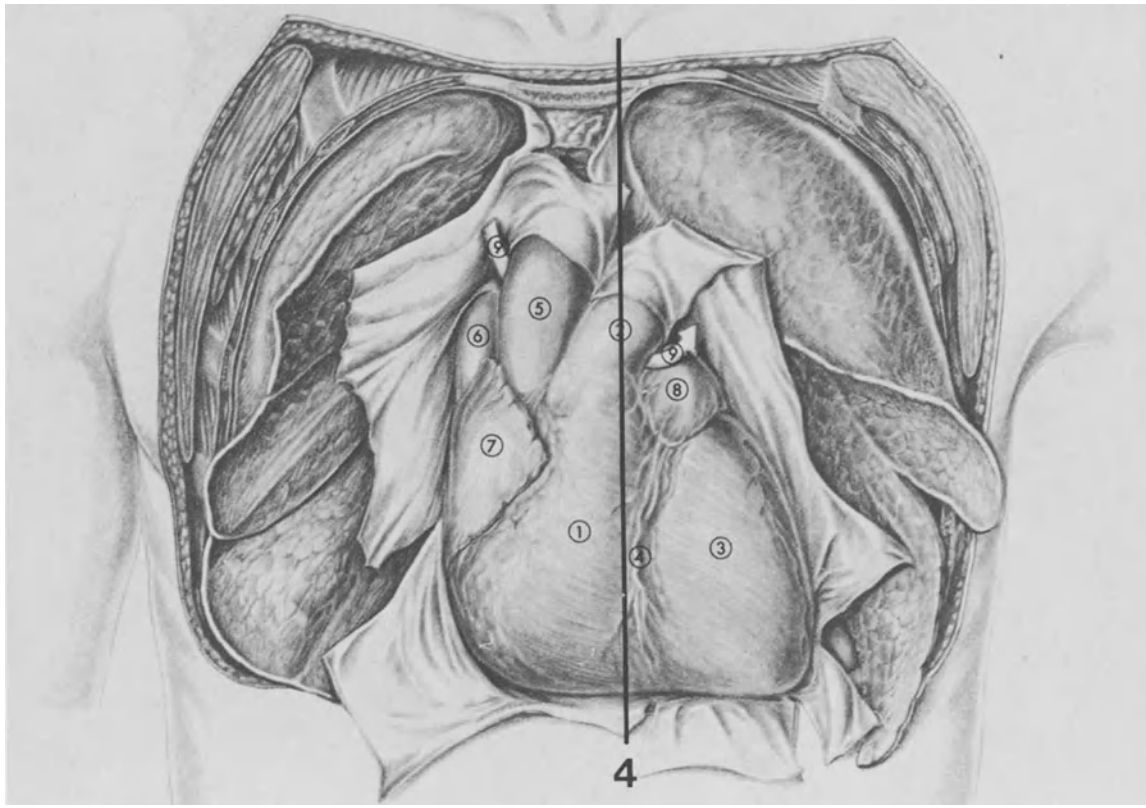

Figure S–9. Plane of section of sagittal slice 4.

Slice through the mitral valvular plane. A double arch is seen: anteriorly, the right ventricle and the infundibulum; posteriorly, the end of the aortic arch and the beginning of the descending aorta.

Additionally, the left lung hilum (with the left bronchus and the left pulmonary artery) and the right pulmonary veins joining the left atrium are seen.

Sagittal slice 4

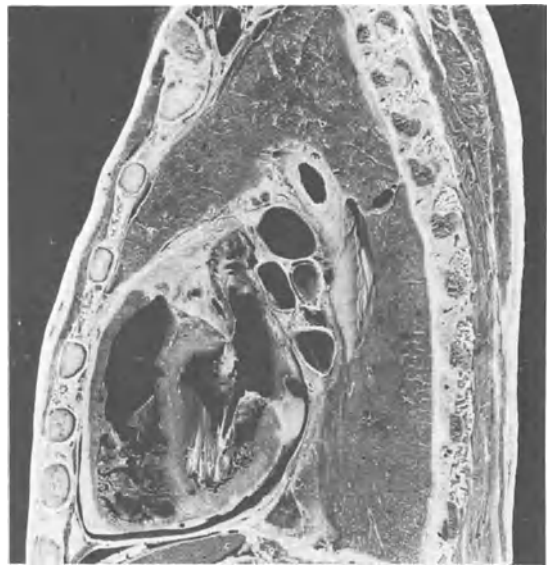

Figure S-10. Anatomical slice.

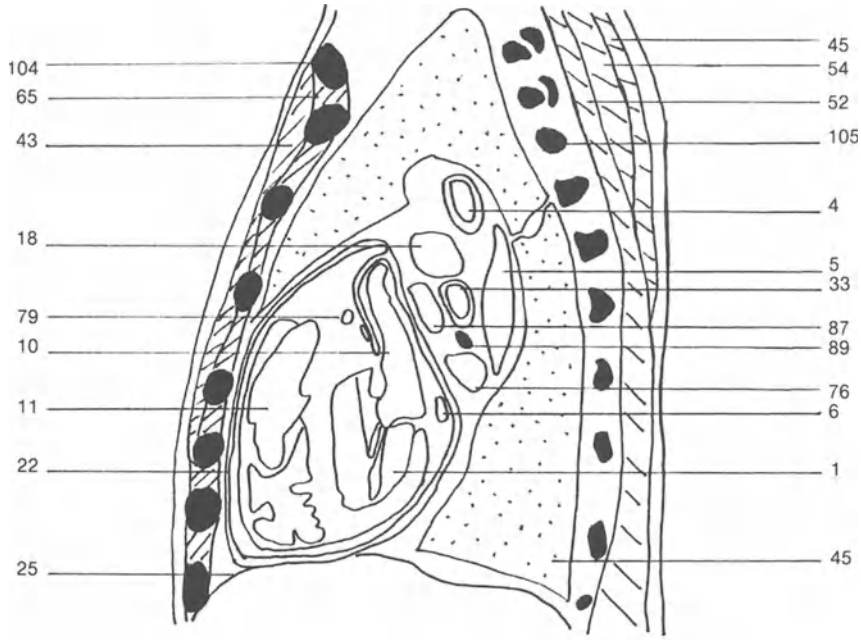

(1) Left ventricular cavity; (2) Myocardium; (4) Aortic arch; (5) Descending aorta; (6) Coronary sinus; (10) Left atrium; (11) Right ventricular cavity; (12) Right ventricular outflow region; (15) Left lung; (18) Left pulmonary artery; (20) Ventricular septum; (22) Pericardium; (25) Diaphragm; (33) Left main bronchus; (36) Pulmonary infundibulum; (43) Pectoralis major muscle; (45) Tra-

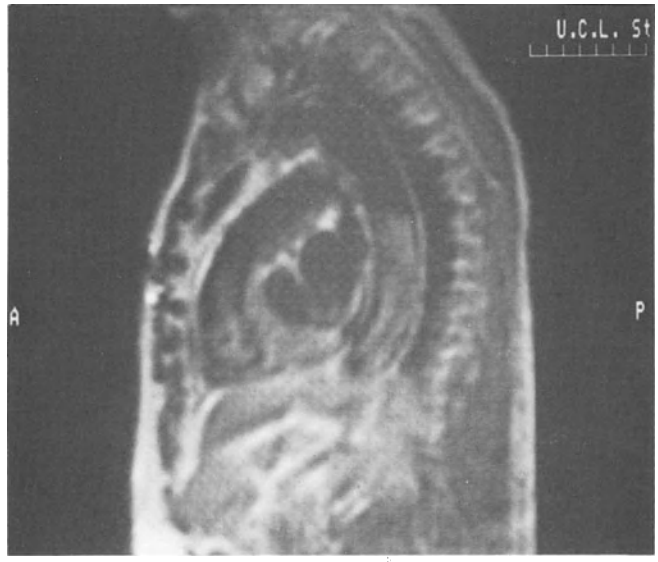

Figure S-11. MR slice.

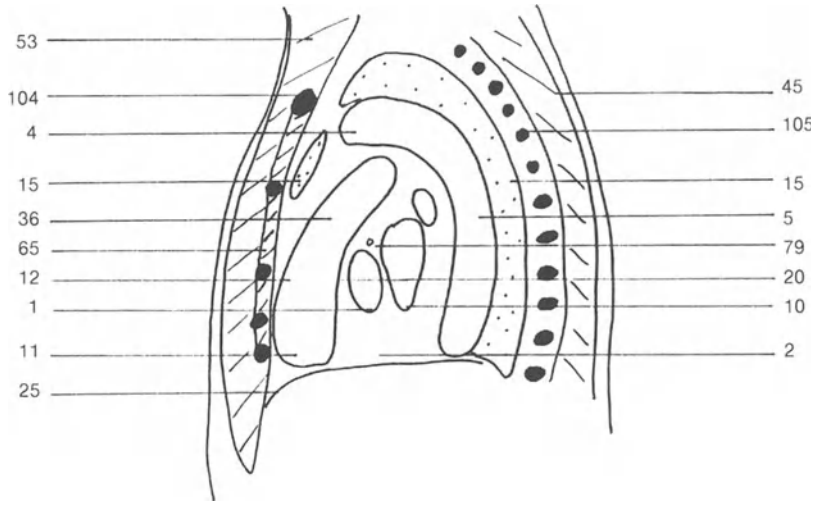

pezius muscle; (52) Erector spinae muscle; (53) Sternocleidomastoid muscle; (54) Rhomboidus muscle; (65) Intercostal muscles; (76) Right inferior pulmonary vein; (79) Left coronary artery; (87) Right superior pulmonary vein; (89) Lymph node; (104) Clavicle; (105) Transverse process.

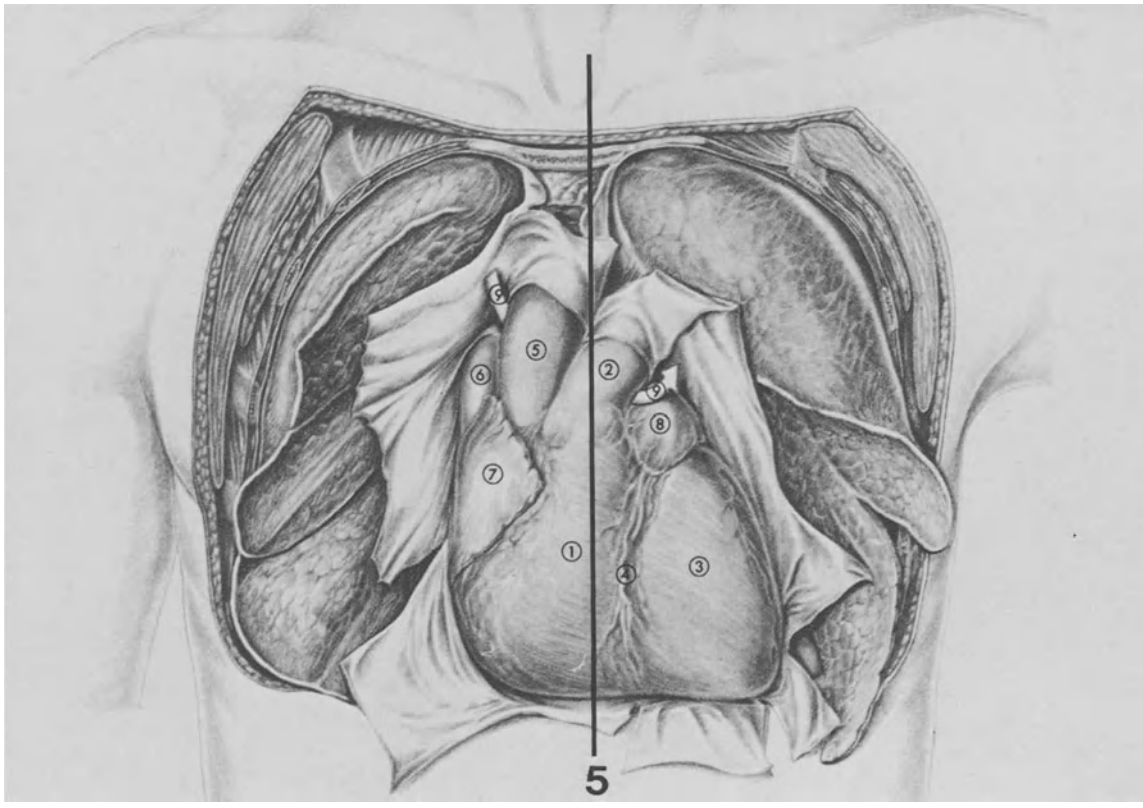

Figure S–12. Plane of section of sagittal slice 5.

The right ventricle, in its upper left angle, forms the right ventricular outflow region followed by the infundibulum (conus arteriosus), from which the pulmonary trunk arises.

The aortic infundibulum is situated behind the beginning of the main pulmonary artery. The ascending aorta arises from the infundibulum at the level of the sagittal median plane (see sagittal slice 7).

The left atrium forms the major part of the posterior cavities.

The aortic arch with the left subclavian artery is seen.

Sagittal slice 5

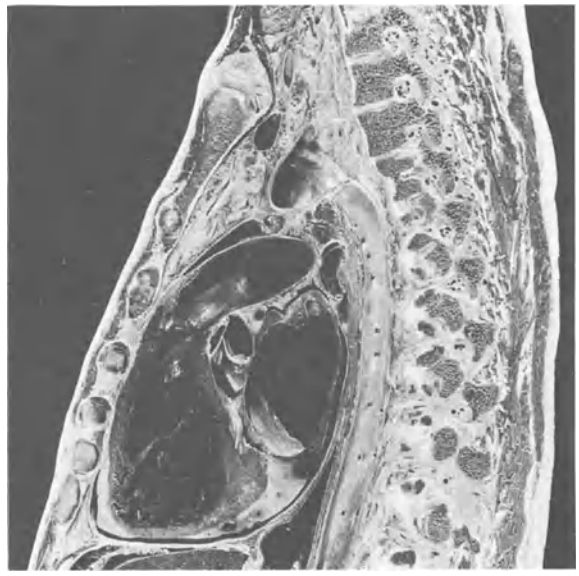

Figure S-13. Anatomical slice.

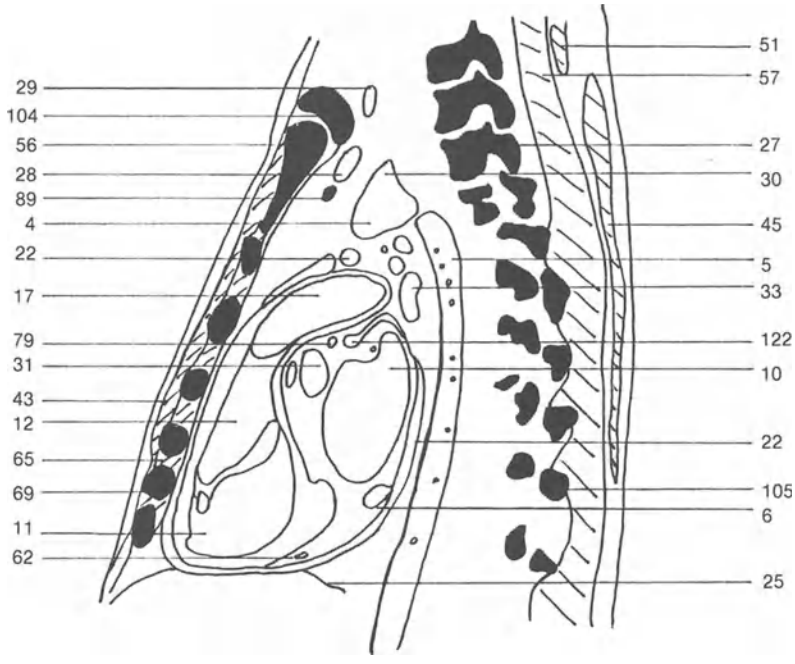

(2) Myocardium; (4) Aortic arch; (5) Descending aorta; (6) Coronary sinus; (10) Left atrium; (11) Right ventricular cavity; (12) Right ventricular outflow region; (15) Left lung; (17) Main pulmonary artery; (22) Pericardium; (25) Diaphragm; (27) Thoracic vertebra; (28) Left brachiocephalic vein; (29) Left common carotid artery; (30) Left subclavian artery; (31) Aortic infundibulum; (33) Left main bronchus; (37) Left subclavian vein; (41) Left internal

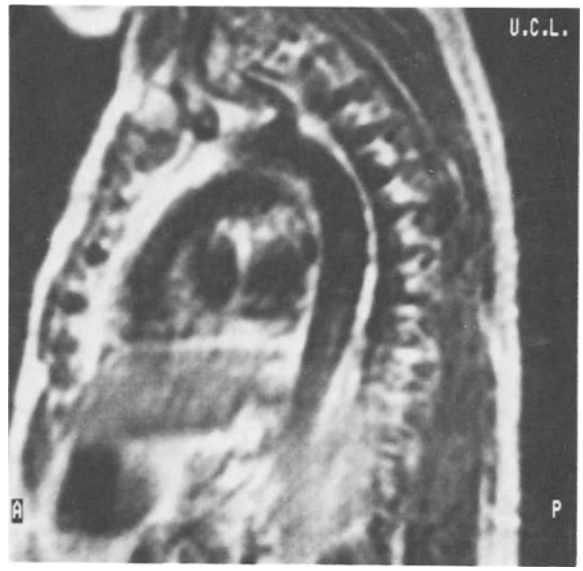

Figure S-14. MR slice.

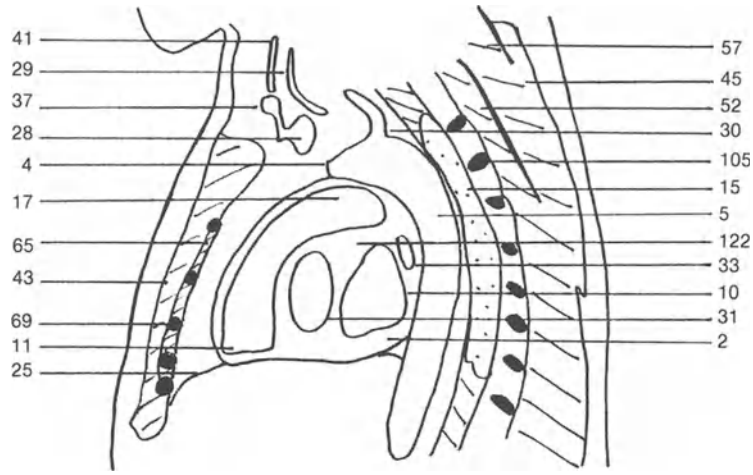

jugular vein; (43) Pectoralis major muscle; (45) Trapezius muscle; (51) Splenius muscle; (52) Erector spinae muscle; (56) Manubrium; (57) Semispinalis capitis muscle; (62) Middle cardiac vein; (65) Intercostal muscles; (69) Rib; (79) Left coronary artery; (89) Lymph node; (104) Clavicle; (105) Transverse process; (122) Transverse sinus of the pericardium.

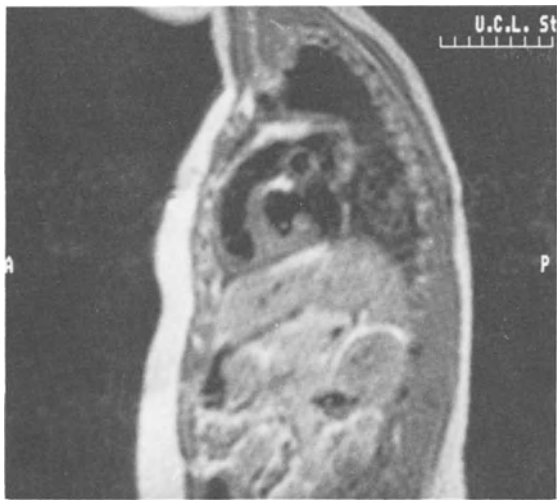

Figure S–15. MR slice.

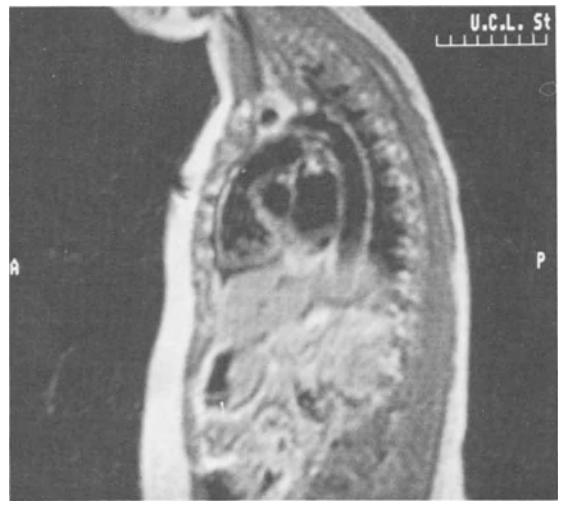

Figure S–16. MR slice.

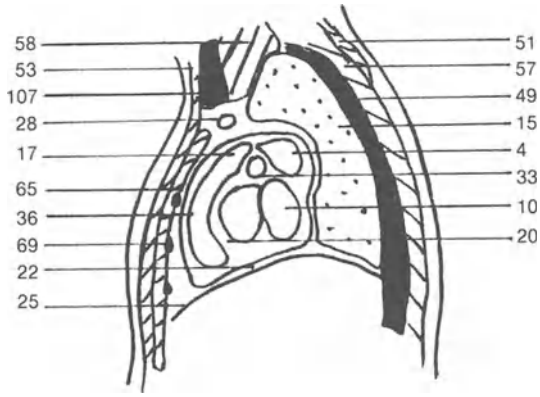

Figures S–15 and S–16 are situated at the same plane of section that Figure S–14 (sagittal slice 5) is. This series of three MR slices allows to see more details of the aortic arch.

(4) Aortic arch; (5) Descending aorta; (6) Coronary sinus; (10) Left atrium; (11) Right ventricular cavity; (15) Left lung; (17) Main pulmonary artery; (20) Ventricular septum; (22) Pericardium; (25) Diaphragm; (28) Left brachiocephalic vein; (29) Left common carotid artery; (31) Aortic infundibulum; (33) Left main bronchus; (36) Pulmonary infundibulum; (43) Pectoralis major muscle; (49) Rachis; (51) Splenius muscle; (53) Sternocleidomastoid muscle; (57) Semispinalis capitis muscle; (58) Laryngeal musculature; (65) Intercostal muscles; (69) Rib; (107) Thyroid gland.

Sagittal slice 6

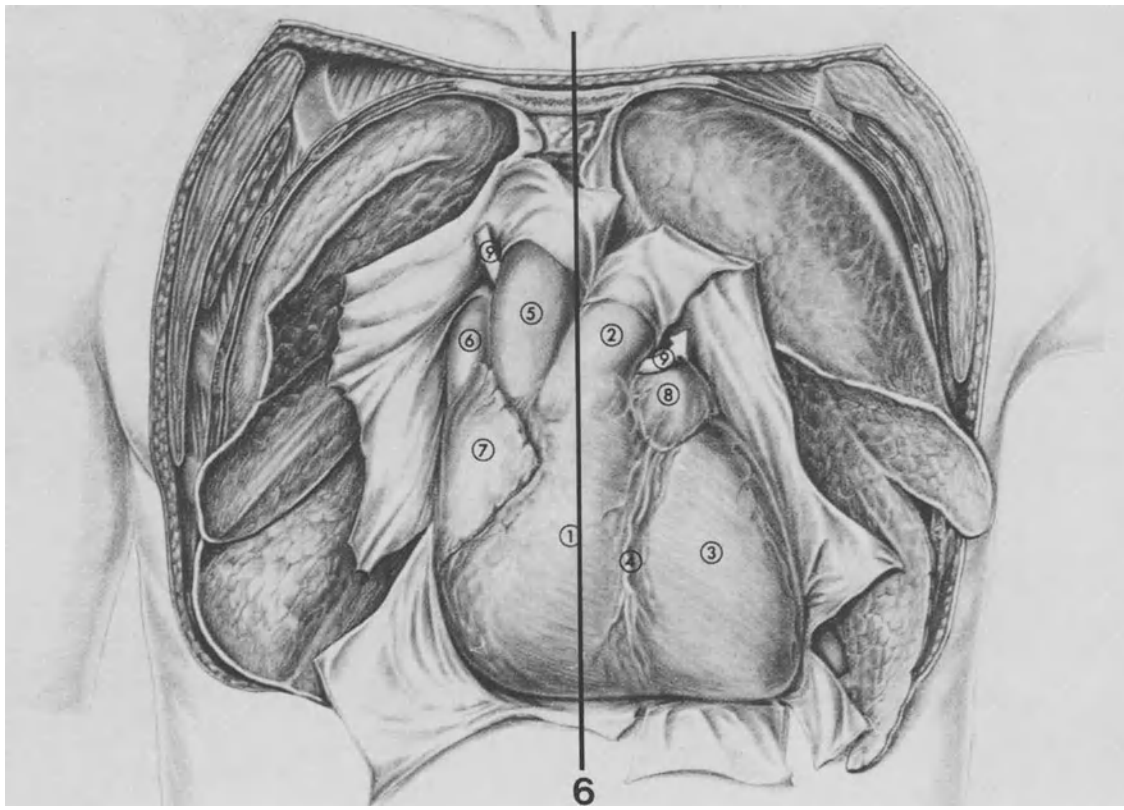

Figure S–17. Plane of section of sagittal slice 6.

This slice is very close to the previous one. The origin of the second vessel of the aortic arch, the left common carotid artery is shown.

The transverse sinus of the pericardium is also seen on this slice.

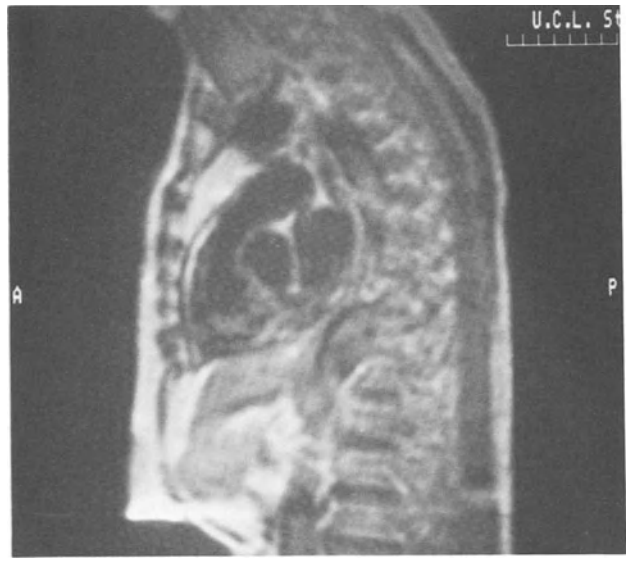

Figure S–18. MR slice.

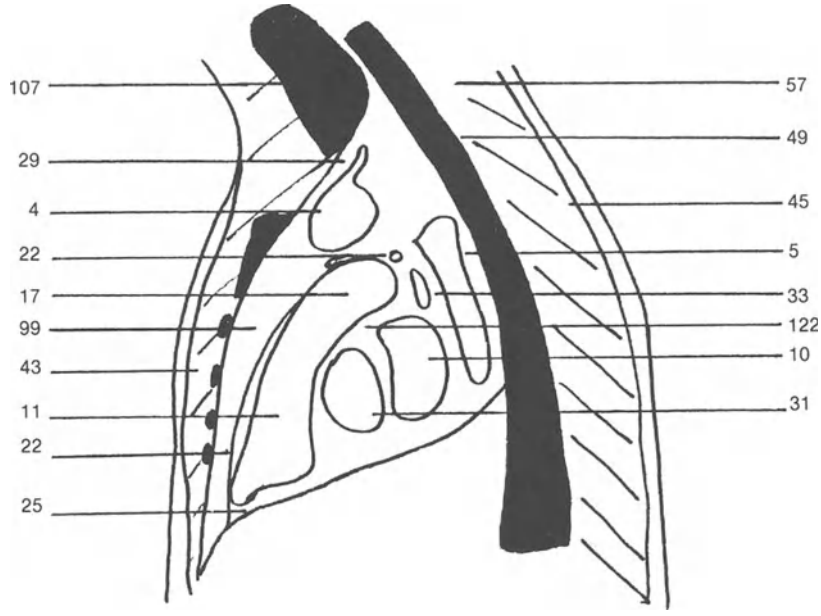

(4) Aortic arch; (5) Descending aorta; (10) Left atrium; (11) Right ventricular cavity; (17) Main pulmonary artery; (22) Pericardium; (25) Diaphragm; (29) Left common carotid artery; (31) Aortic infundibulum; (33) Left main bronchus; (43) Pectoralis major muscle; (45) Trapezius muscle; (49) Rachis; (57) Semispinalis capitis muscle; (99) Mediastinum; (107) Thyroid gland; (122) Transverse sinus of the pericardium.

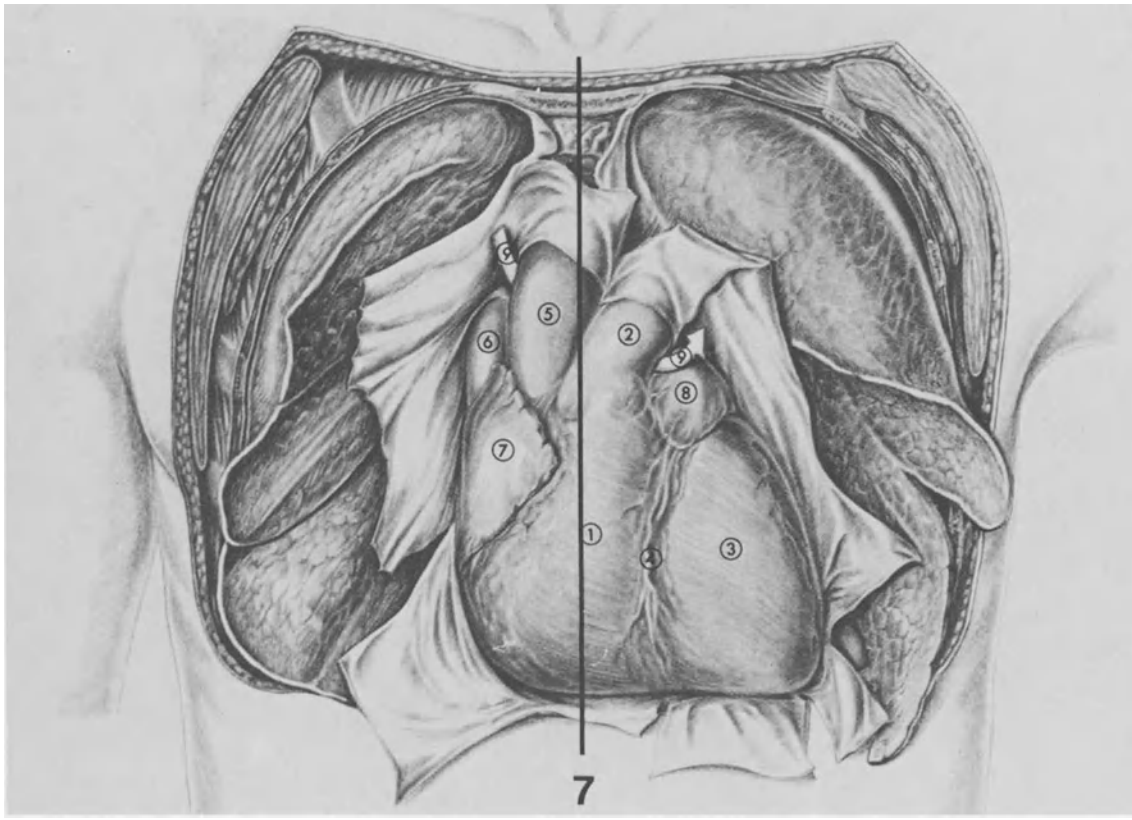

Figure S–19. Plane of section of sagittal slice 7.

Median sagittal slice showing the beginning of the ascending aorta.
The right ventricle disappears progressively while the right atrium appears below the left atrium.
The right pulmonary artery runs between the ascending aorta and the left atrium.
The trachea is well delineated and its rigid structure precludes its collapse, unlike the esophagus.

Sagittal slice 7

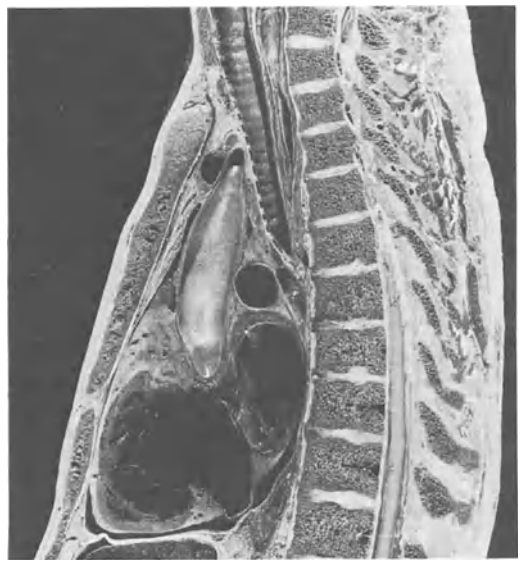

Figure S–20. Anatomical slice.

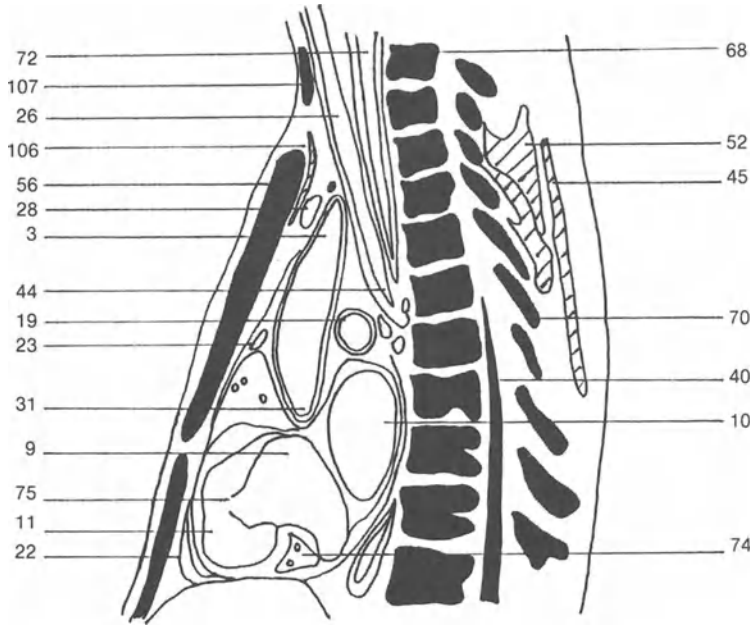

(3) Ascending aorta; (4) Aortic arch; (5) Descending aorta; (9) Right atrium; (10) Left atrium; (11) Right ventricular cavity; (19) Right pulmonary artery; (22) Pericardium; (23) Right atrial appendage; (26) Trachea; (28) Left brachiocephalic vein; (31) Aortic infundibulum; (40) Spinal cord; (43) Pectoralis major muscle; (44)

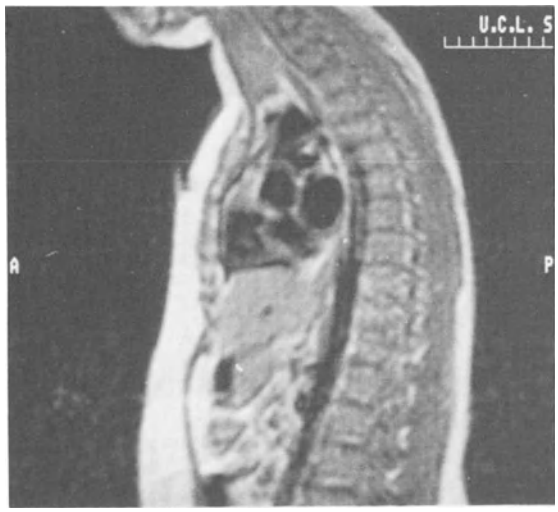

Figure S-21. MR slice.

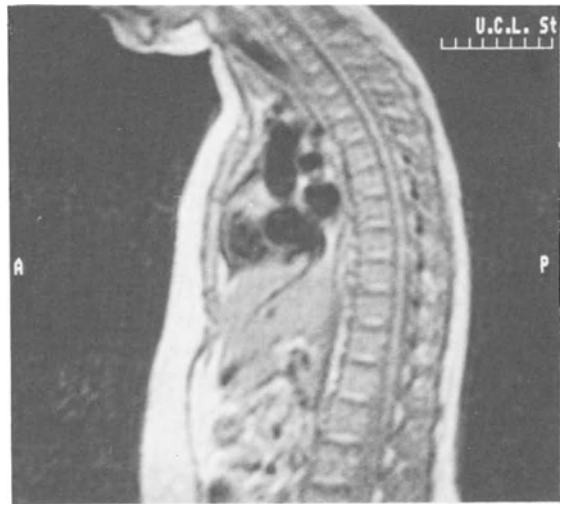

Figure S-22. MR slice.

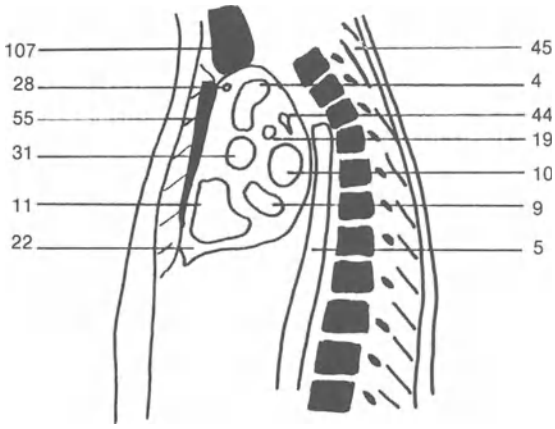

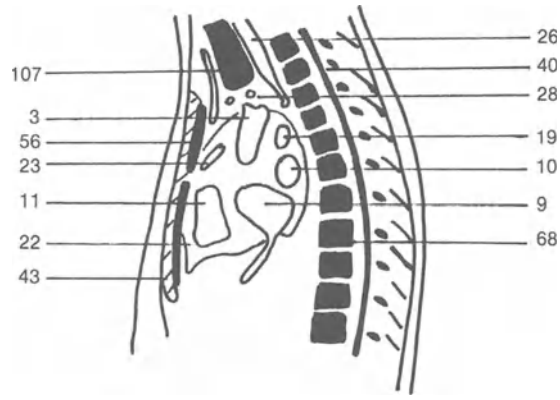

Carina; (45) Trapezius muscle; (52) Erector spinae muscle; (55) Sternum; (56) Manubrium; (68) Dorsal vertebra; (70) Spinous process; (72) Esophagus; (74) Right coronary artery; (75) Tricuspid valve; (106) Sternohyoid muscle; (107) Thyroid gland.

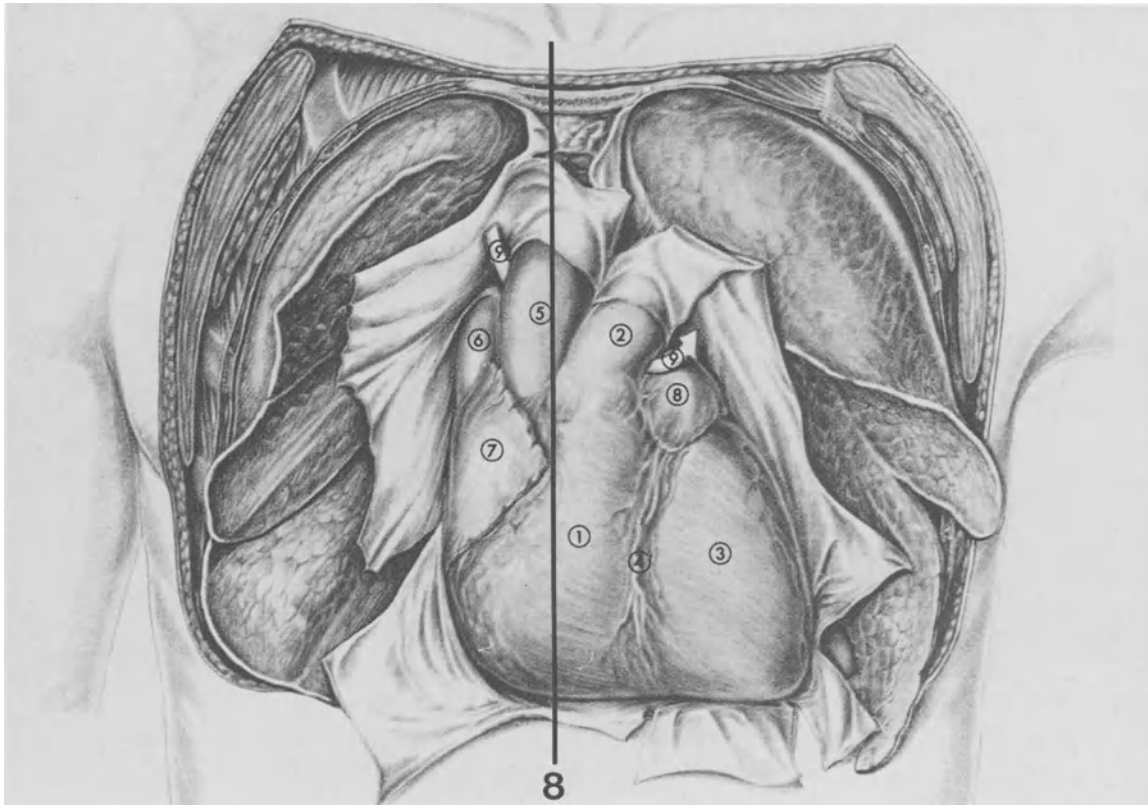

Figure S–23. Plane of section of sagittal slice 8.

This slice is nearly parallel to the right part of the ascending aorta. The relations of the three cardiac cavities at this level are well shown: right ventricle, right atrium and left atrium.

The relations between the ascending aorta, the left brachiocephalic vein, anteriorly, and the right pulmonary artery, posteriorly, are also seen.

The collapsed esophagus lies behind the left atrium.

The brachiocephalic trunk arises at the top of the aortic arch.

Sagittal slice 8

Figure S–24. MR slice.

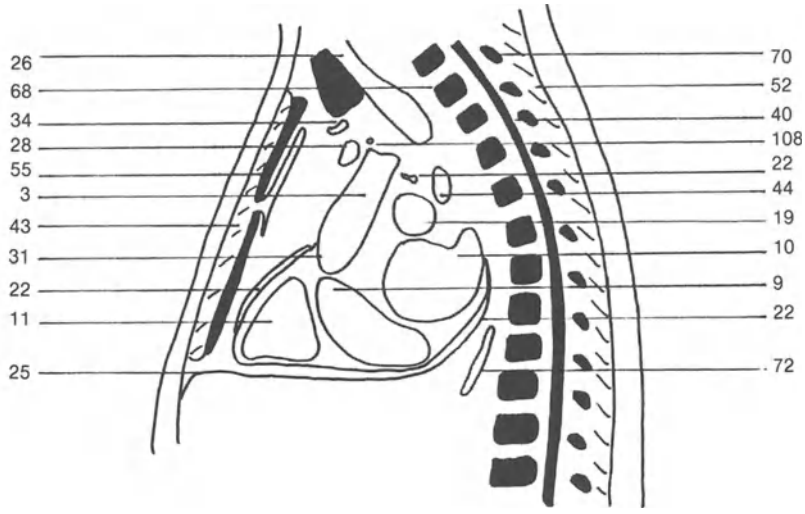

(2) Myocardium; (3) Ascending aorta; (9) Right atrium; (10) Left atrium; (11) Right ventricular cavity; (19) Right pulmonary artery; (22) Pericardium; (25) Diaphragm; (26) Trachea; (28) Left brachiocephalic vein; (31) Aortic infundibulum; (34) Right inferior thyroid vein; (40) Spinal cord; (43) Pectoralis major muscle; (44)

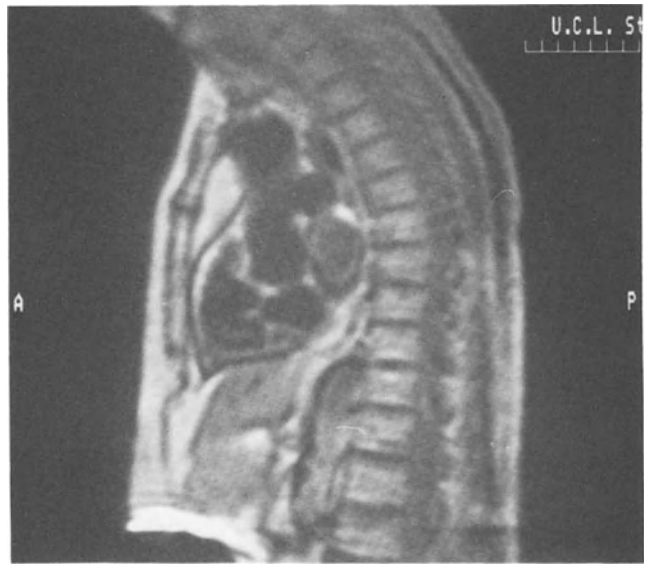

Figure S–25. MR slice.

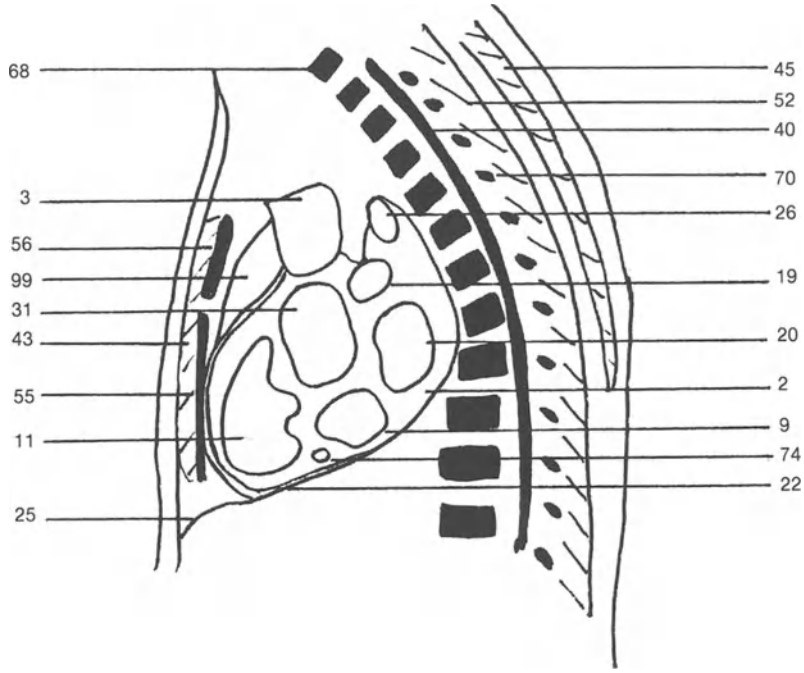

Carina; (45) Trapezius muscle; (52) Erector spinae muscle; (55) Sternum; (56) Manubrium; (68) Dorsal vertebra; (70) Spinous process; (72) Esophagus; (74) Right coronary artery; (99) Mediastinum; (108) Brachiocephalic trunk.

Sagittal slice 9

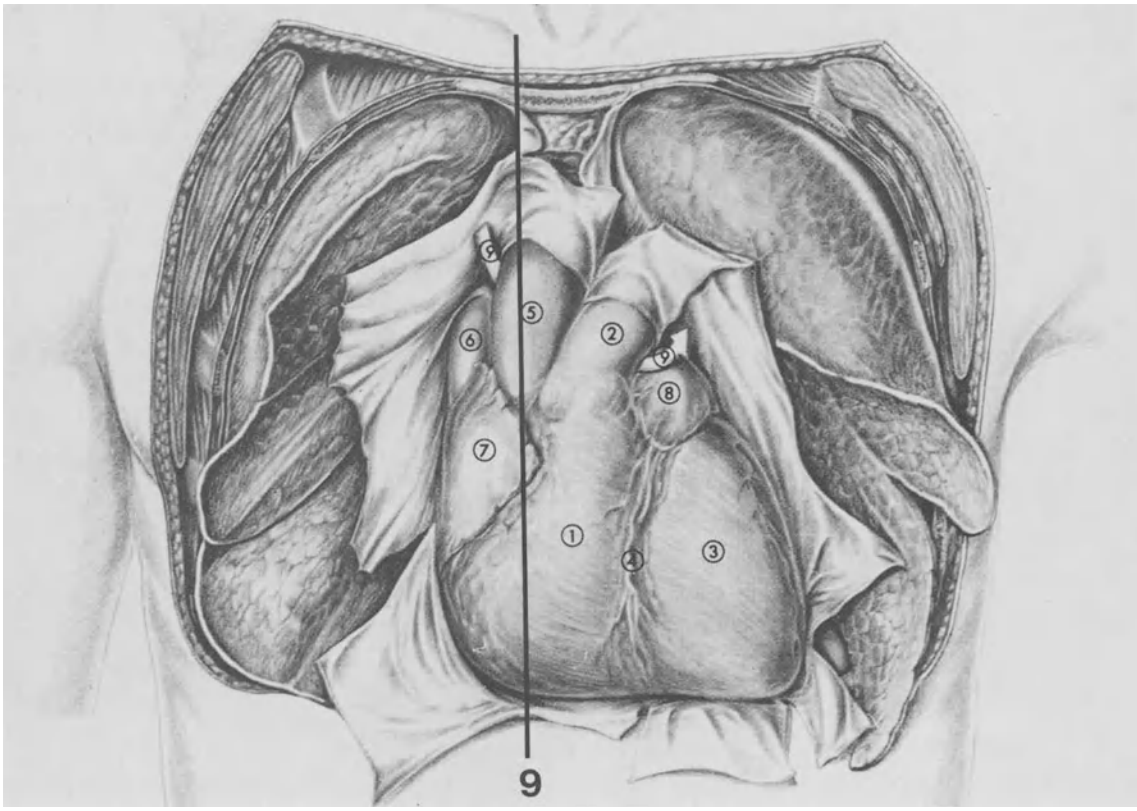

Figure S–26. Plane of section of sagittal slice 9.

The left atrium disappears progressively while the right atrium becomes the predominant cavity.
The left brachiocephalic vein is ending and will join the right brachiocephalic vein to form the superior vena cava.
The right ventricle is still seen anteriorly.

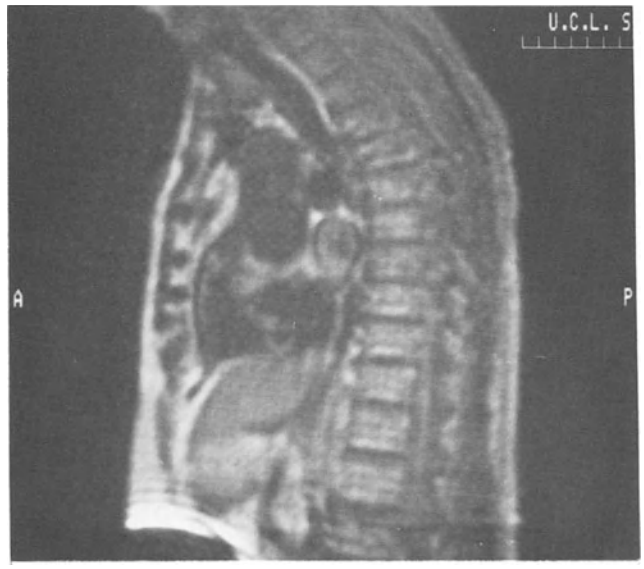

Figure S–27. MR slice.

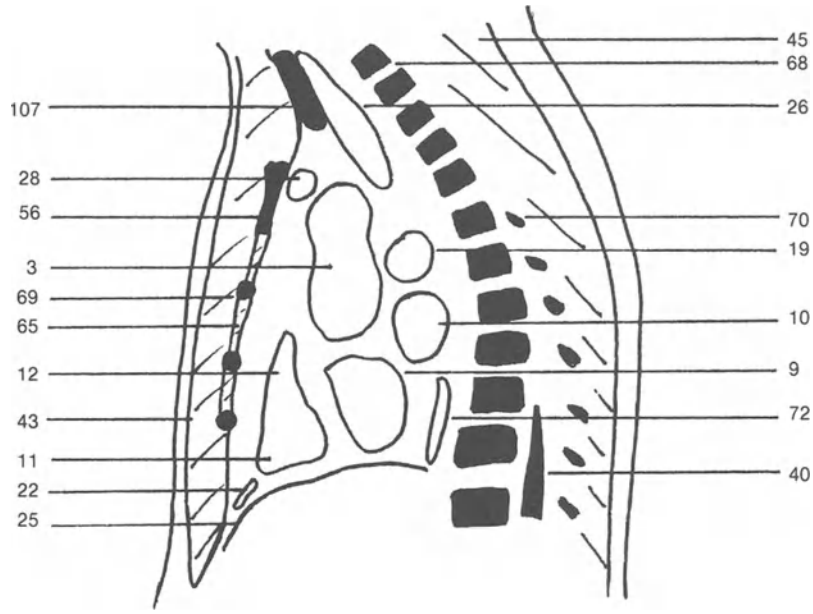

(3) Ascending aorta; (9) Right atrium; (10) Left atrium; (11) Right ventricular cavity; (12) Right ventricular outflow region; (19) Right pulmonary artery; (22) Pericardium; (25) Diaphragm; (26) Trachea; (28) Left brachiocephalic vein; (40) Spinal cord; (43) Pectoralis major muscle; (45) Trapezius muscle; (56) Manubrium; (65) Intercostal muscles; (70) Spinous process; (72) Esophagus; (107) Thyroid gland.

Sagittal slice 10

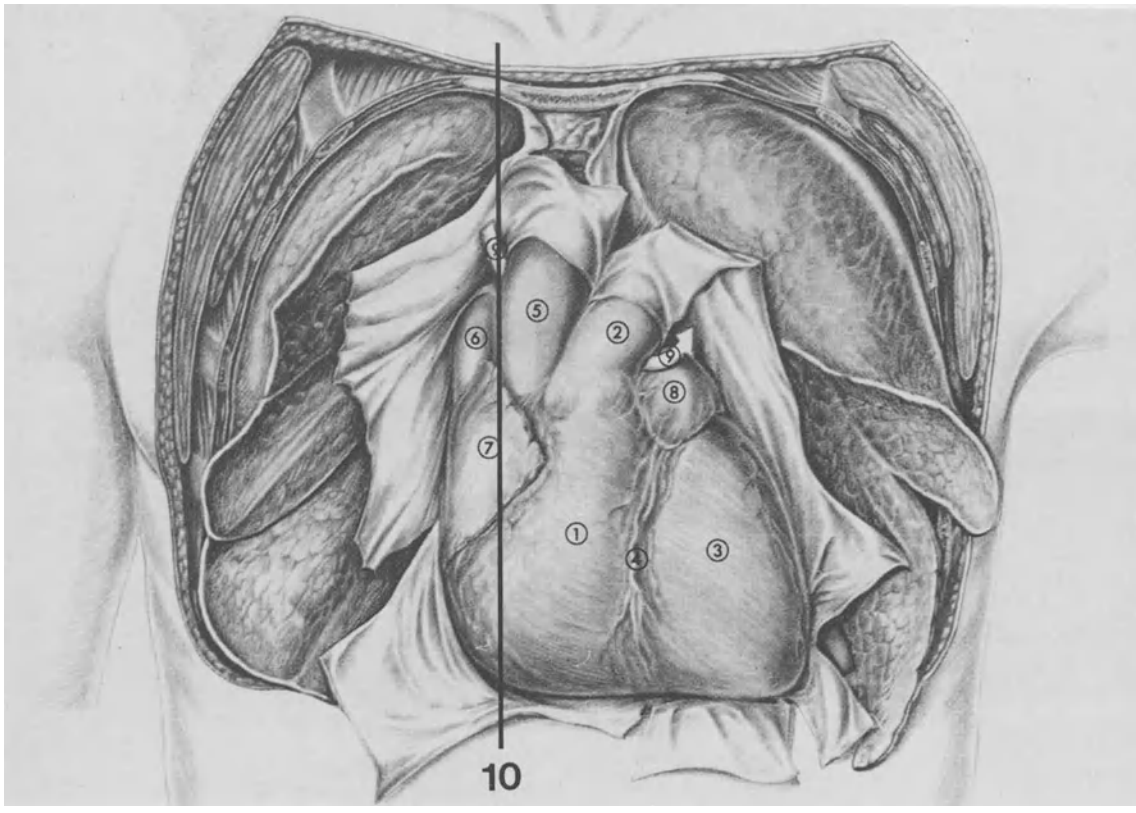

Figure S–28. Plane of section of sagittal slice 10.

This slice crosses the right surface of the heart where the superior vena cava opens into the upper and posterior part of the right atrium. The superior vena cava is formed by the junction of the right and left brachiocephalic veins. The right inferior thyroid vein and the internal mammary vein are seen.

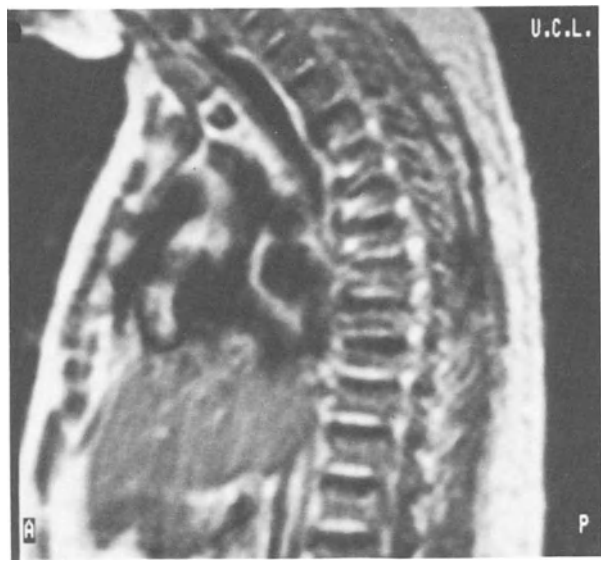

Figure S-29. MR slice.

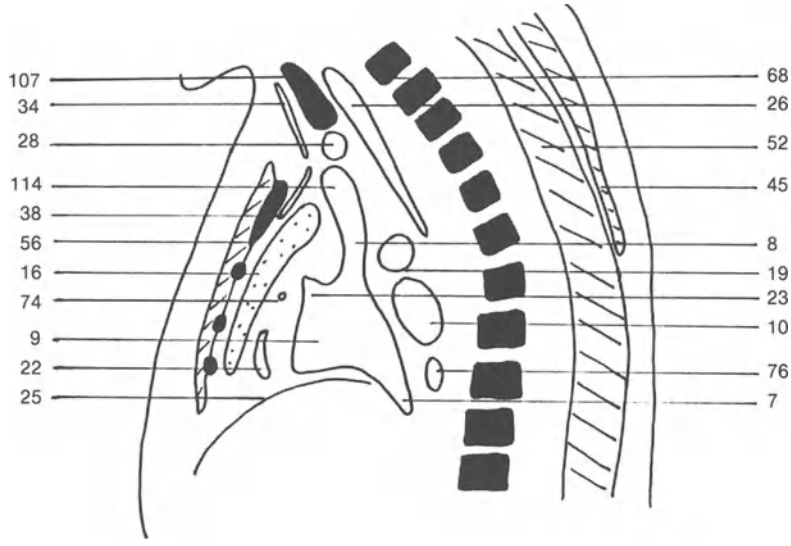

(7) Inferior vena cava; (8) Superior vena cava; (9) Right atrium; (10) Left atrium; (16) Right lung; (19) Right pulmonary artery; (22) Pericardium; (23) Right atrial appendage; (25) Diaphragm; (26) Trachea; (28) Left brachiocephalic vein; (34) Right inferior thyroid vein; (38) Internal mammary vein; (45) Trapezius muscle; (52) Erector spinae muscle; (56) Manubrium; (68) Dorsal vertebra; (74) Right coronary artery; (76) Right inferior pulmonary vein; (107) Thyroid gland; (114) Right brachiocephalic vein.

CORONAL SLICES 1–7

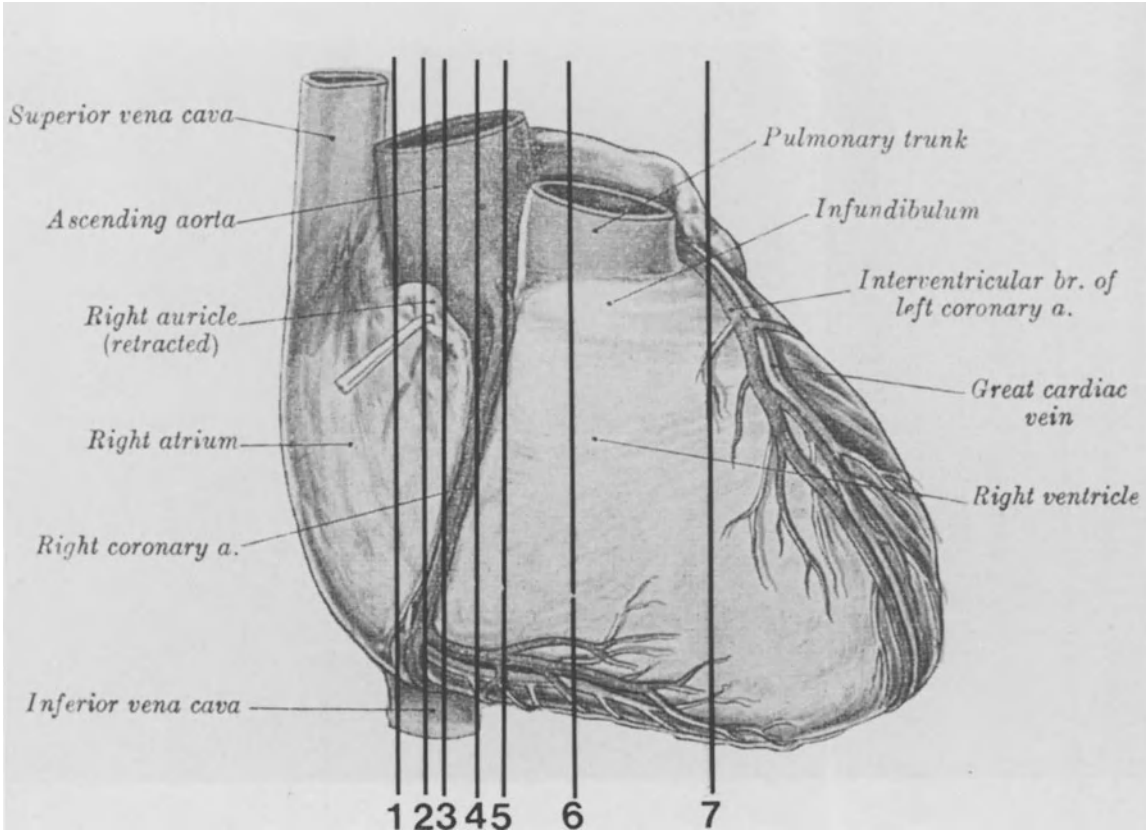

Figure C–0. Plane of section of the coronal slices.

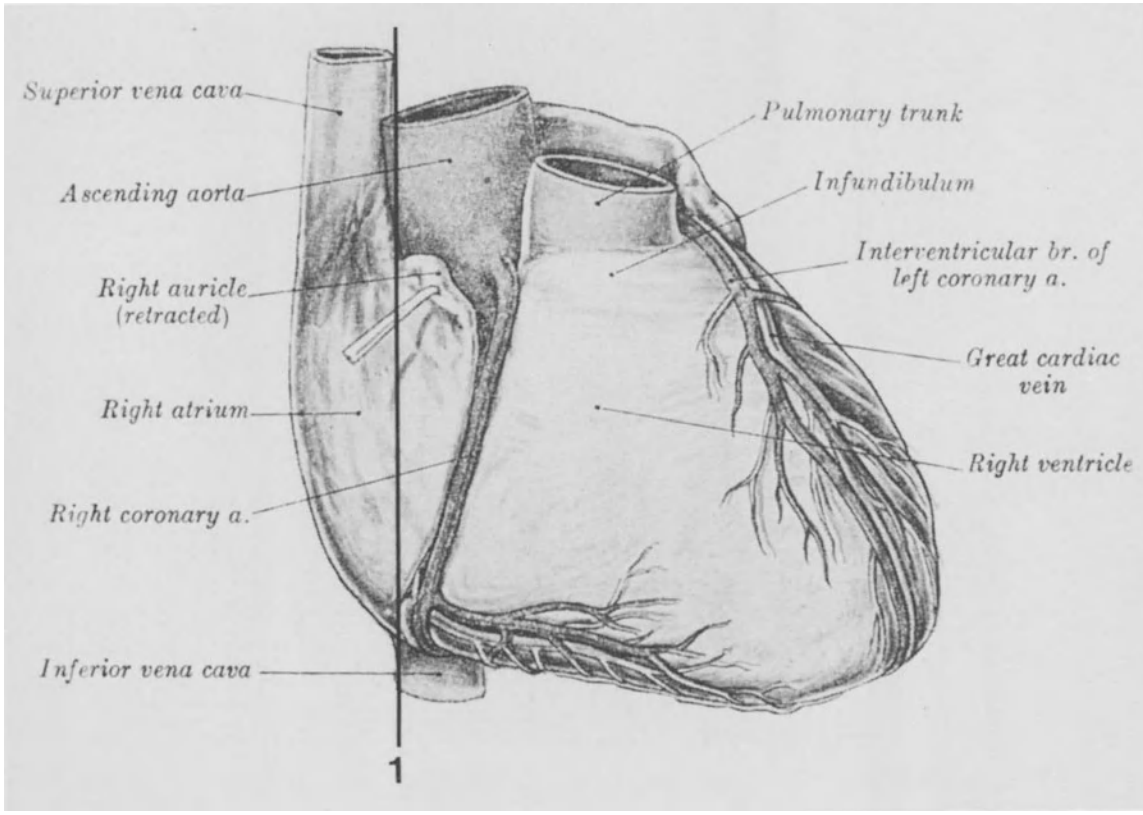

Figure C–1. Plane of section of the coronal slice 1.

This posterior slice is at the level of the division of the trachea into the two main bronchi. The pulmonary arteries, the aortic arch and the posterior part of the left atrium, the most posterior part of the heart, are seen.

Also, the descending aorta crossing the diaphragm is seen.

The inferior vena cava and the right atrium begin to be visible.

Coronal slice 1

Figure C–2. Anatomical slice.

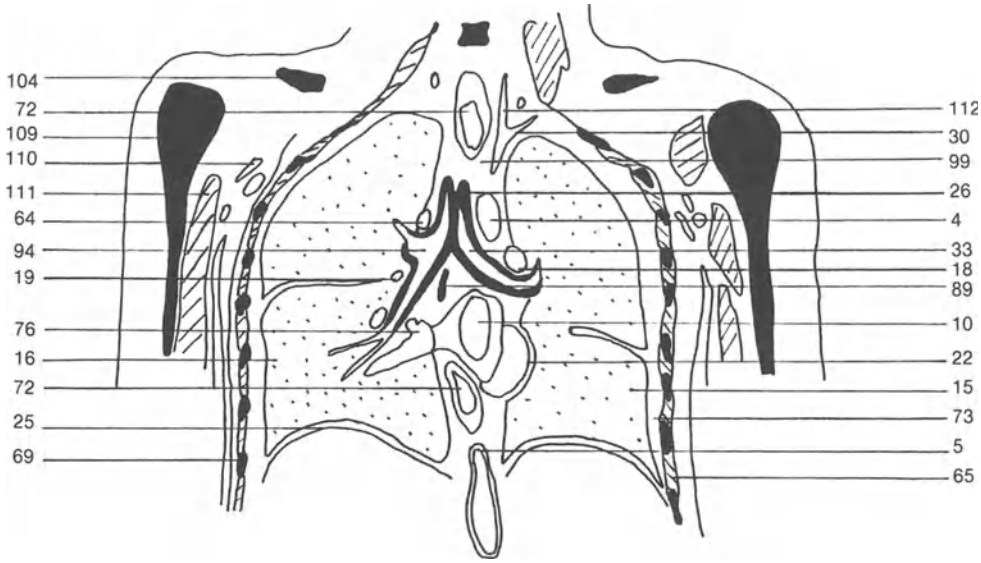

(4) Aortic arch; (5) Descending aorta; (7) Inferior vena cava; (9) Right atrium; (10) Left atrium; (15) Left lung; (16) Right lung; (18) Left pulmonary artery; (19) Right pulmonary artery; (22) Pericardium; (25) Diaphragm; (26) Trachea; (30) Left subclavian artery; (33) Left main bronchus; (44) Carina; (46) Left inferior pulmonary vein; (64) Azygos vein; (65) Intercostal muscles; (69)

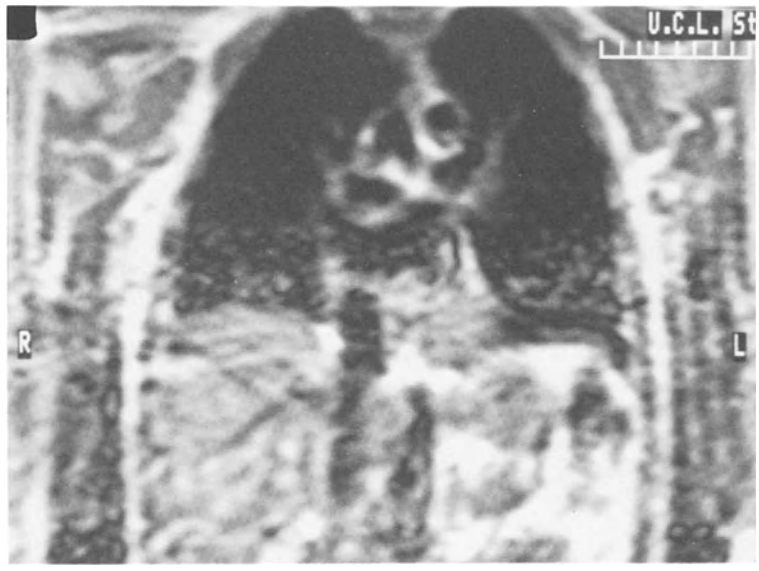

Figure C–3. MR slice.

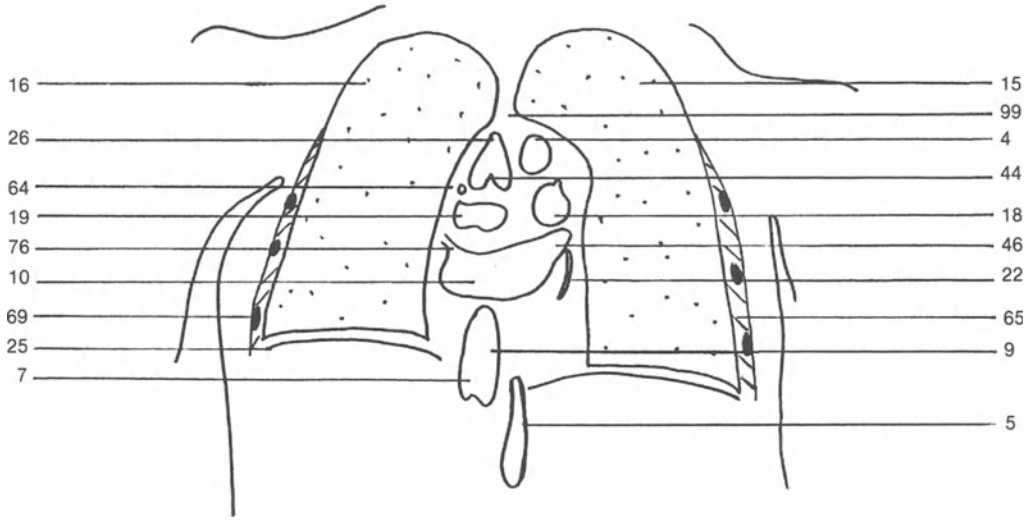

Rib; (72) Esophagus; (73) Pleural cavity; (76) Right inferior pulmonary vein; (89) Lymph node; (94) Right main bronchus; (99) Mediastinum; (104) Clavicle; (109) Humerus; (110) Axillary artery; (111) Coracobrachial muscle; (112) Vertebral artery.

Coronal slice 2

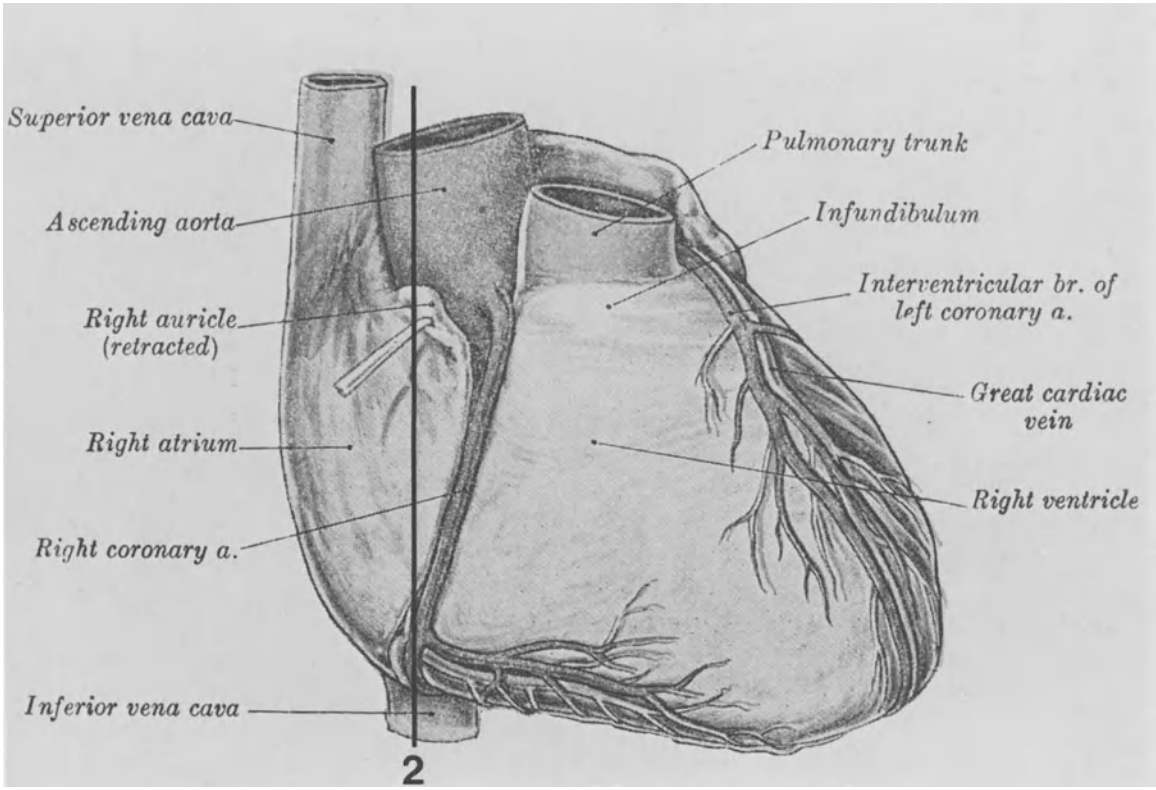

Figure C–4. Plane of section of the coronal slice 2.

The left atrium disappears progressively and the right atrium and the left ventricular wall are now visible. The aortic arch gives off its last branch, the left subclavian artery. The main pulmonary artery divides into the right and left pulmonary arteries. The coronary sinus which runs in the coronary or atrioventricular groove, will open into the inferior part of the right atrium, close to the atrial septum.

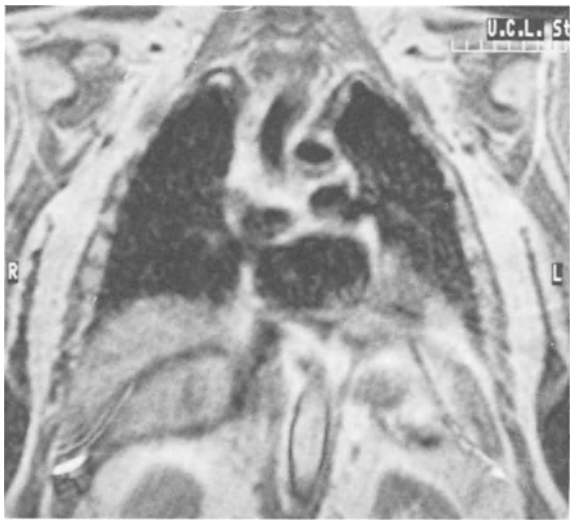

Figure C–5. MR slice.

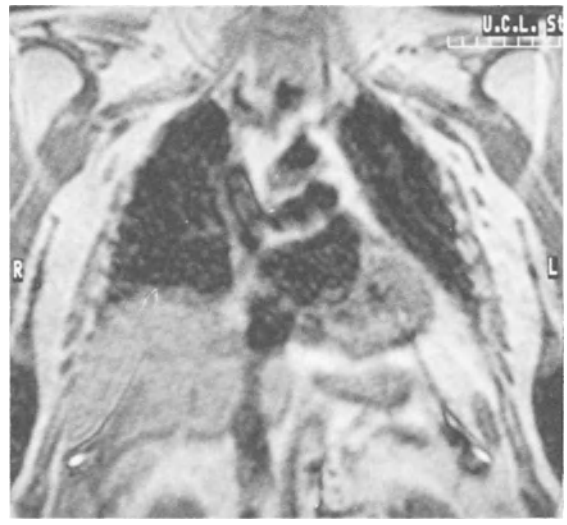

Figure C–6. MR slice.

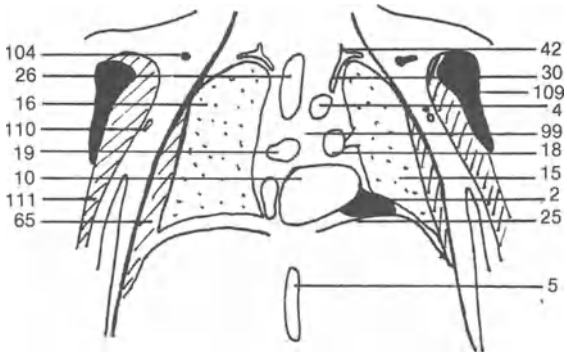

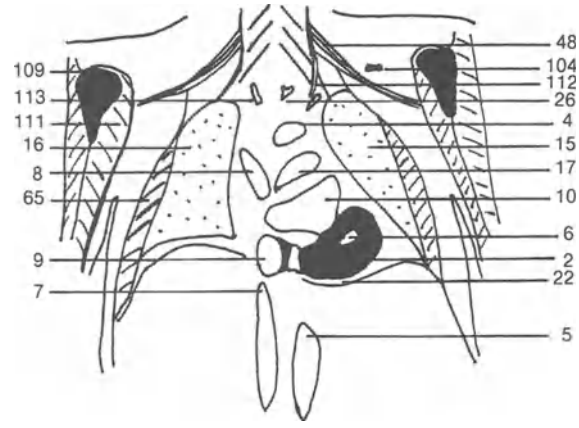

(2) Myocardium; (4) Aortic arch; (5) Descending aorta; (6) Coronary sinus; (7) Inferior vena cava; (8) Superior vena cava; (9) Right atrium; (10) Left atrium; (15) Left lung; (16) Right lung; (17) Main pulmonary artery; (18) Left pulmonary artery; (19) Right pulmonary artery; (22) Pericardium; (25) Diaphragm; (26) Trachea; (30) Left subclavian artery; (48) Brachial plexus; (65) Intercostal muscles; (99) Mediastinum; (104) Clavicle; (109) Humerus; (110) Axillary artery; (111) Coracobrachial muscle; (112) Vertebral artery; (113) Right subclavian artery.

Coronal slice 3

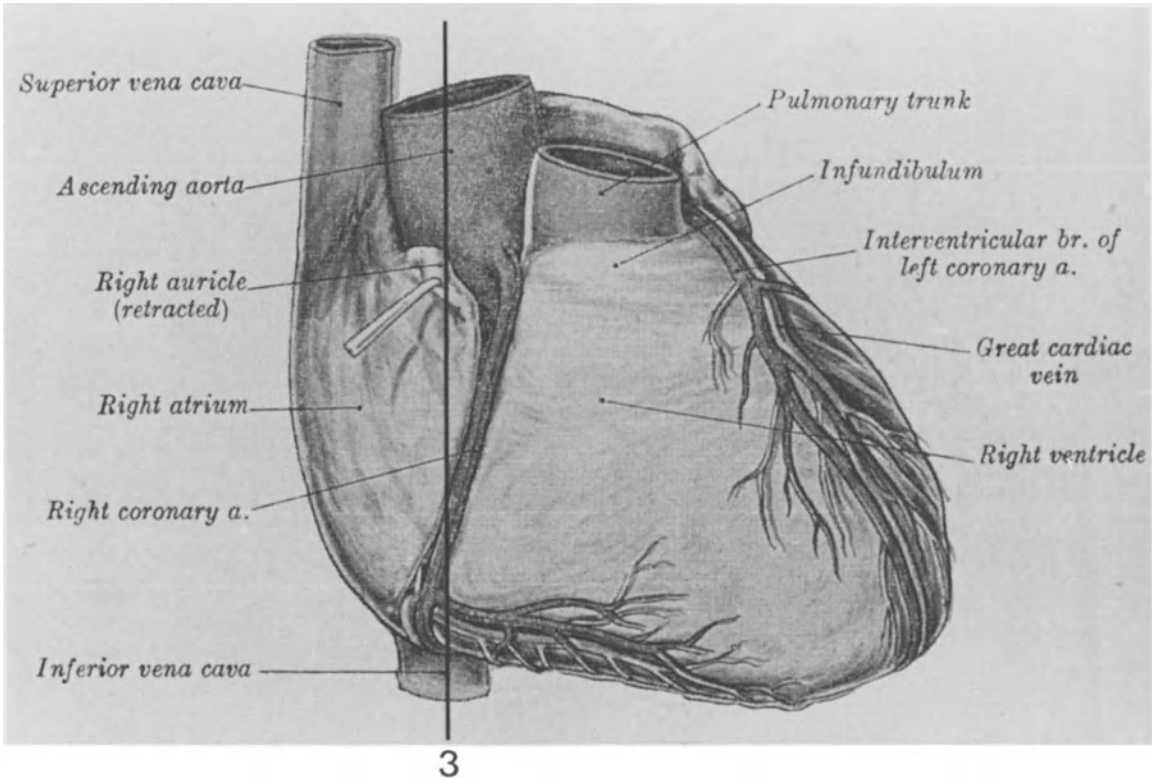

Figure C–7. Plane of section of the coronal slice 3.

This slice shows the opening of the superior vena cava into the right atrium.

The division of the main pulmonary artery into the right and left pulmonary artery is also seen.

The left atrium disappears and only the left atrial appendage, forming its upper left corner, is still visible, lying on the left ventricle.

The right ventricle, anterior to the right atrium, is not seen on this slice.

Figure C–8. MR slice.

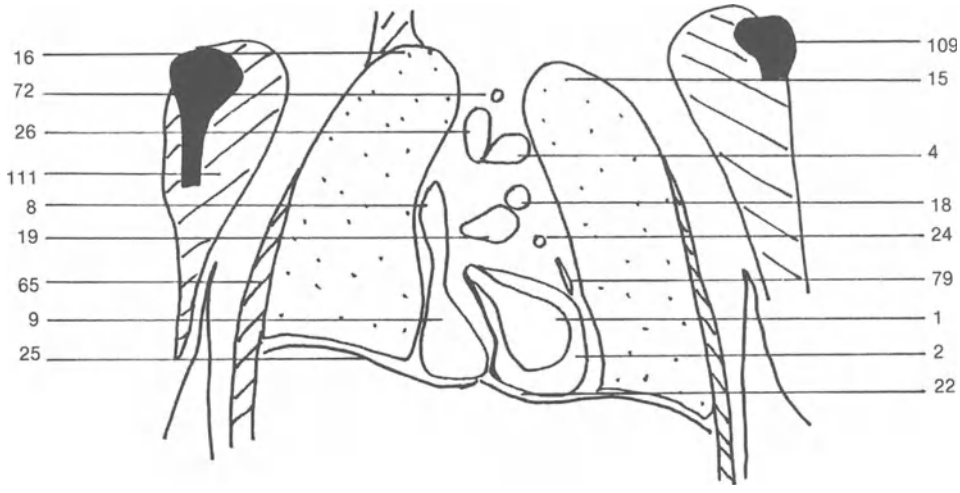

(1) Left ventricular cavity; (2) Myocardium; (4) Aortic arch; (8) Superior vena cava; (9) Right atrium; (15) Left lung; (16) Right lung; (18) Left pulmonary artery; (19) Right pulmonary artery; (22) Pericardium; (24) Left atrial appendage; (25) Diaphragm; (26) Trachea; (65) Intercostal muscles; (72) Esophagus; (79) Left coronary artery; (109) Humerus; (111) Coracobrachial muscle.

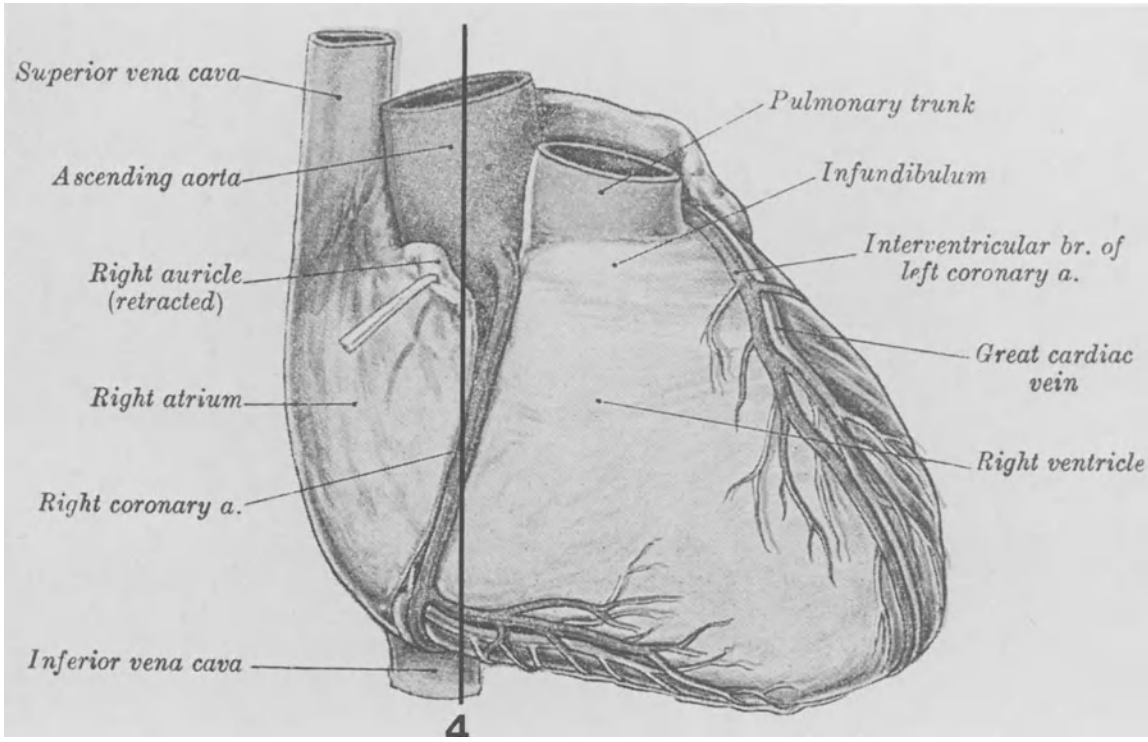

Figure C–9. Plane of section of the coronal slice 4.

On this slice, the right and left brachiocephalic veins are forming the opening of the superior vena cava. This junction is slightly anterior to the opening of the superior vena cava into the right atrium.
The ascending aorta arises from the left ventricle. The aortic arch and the corresponding arteries are also seen. Between the aortic arch and the left ventricle, the main pulmonary artery can be seen, running backwards before its division into the two pulmonary arteries.

Coronal slice 4

Figure C–10. Anatomical slice.

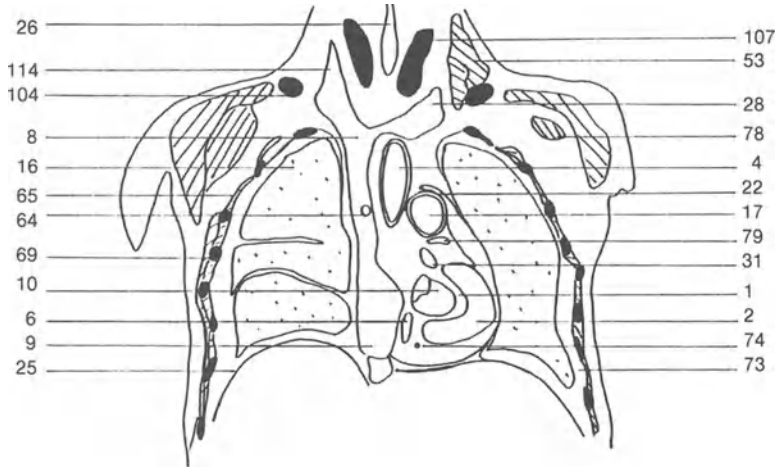

(1) Left ventricular cavity; (2) Myocardium; (3) Ascending aorta; (4) Aortic arch; (6) Coronary sinus; (8) Superior vena cava; (9) Right atrium; (10) Left atrium; (11) Right ventricular cavity; (13) Left ventricular outflow region; (15) Left lung; (16) Right lung; (17) Main pulmonary artery; (22) Pericardium; (23) Right atrial appendage; (24) Left atrial appendage; (25) Diaphragm; (26) Trachea; (28) Left brachiocephalic vein; (29) Left common carotid artery; (31) Aortic infundibulum; (48) Brachial plexus; (53) Sternocleidomastoid muscle; (64) Azygos vein; (65) Intercostal muscles; (69) Rib; (73) Pleural cavity; (74) Right coronary artery; (77) Internal mammary artery; (78) Pectoralis minor muscle; (104) Clavicle; (107) Thyroid gland; (109) Humerus; (114) Right brachiocephalic vein; (115) Right subclavian vein; (116) Deltoid muscle; (117) Right common carotid artery.

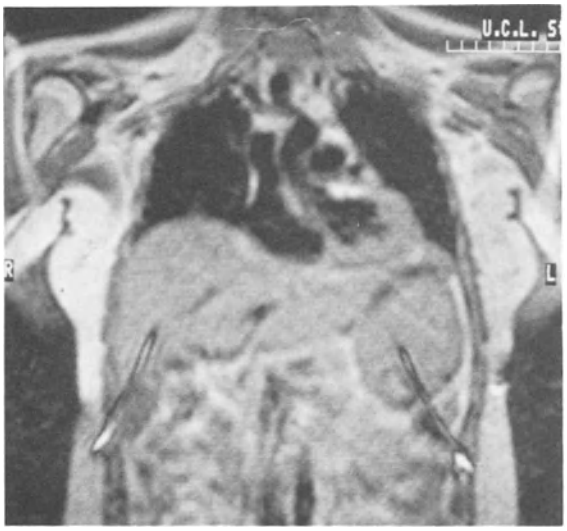

Figure C–11. MR slice.

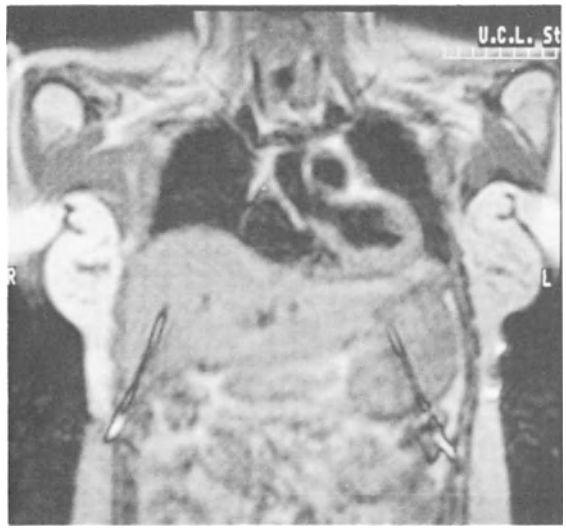

Figure C–12. MR slice.

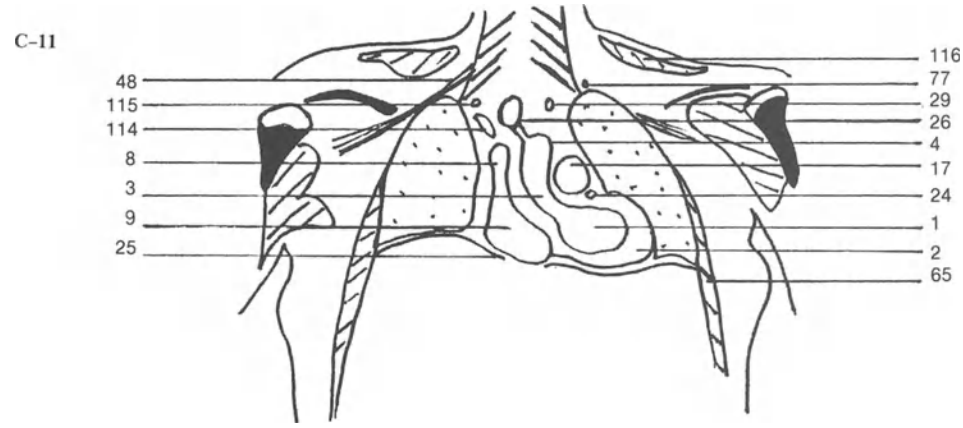

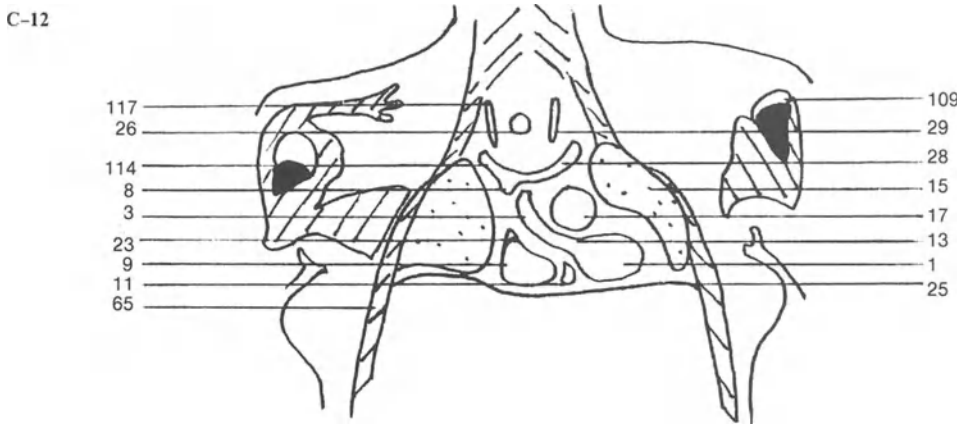

Coronal slice 5

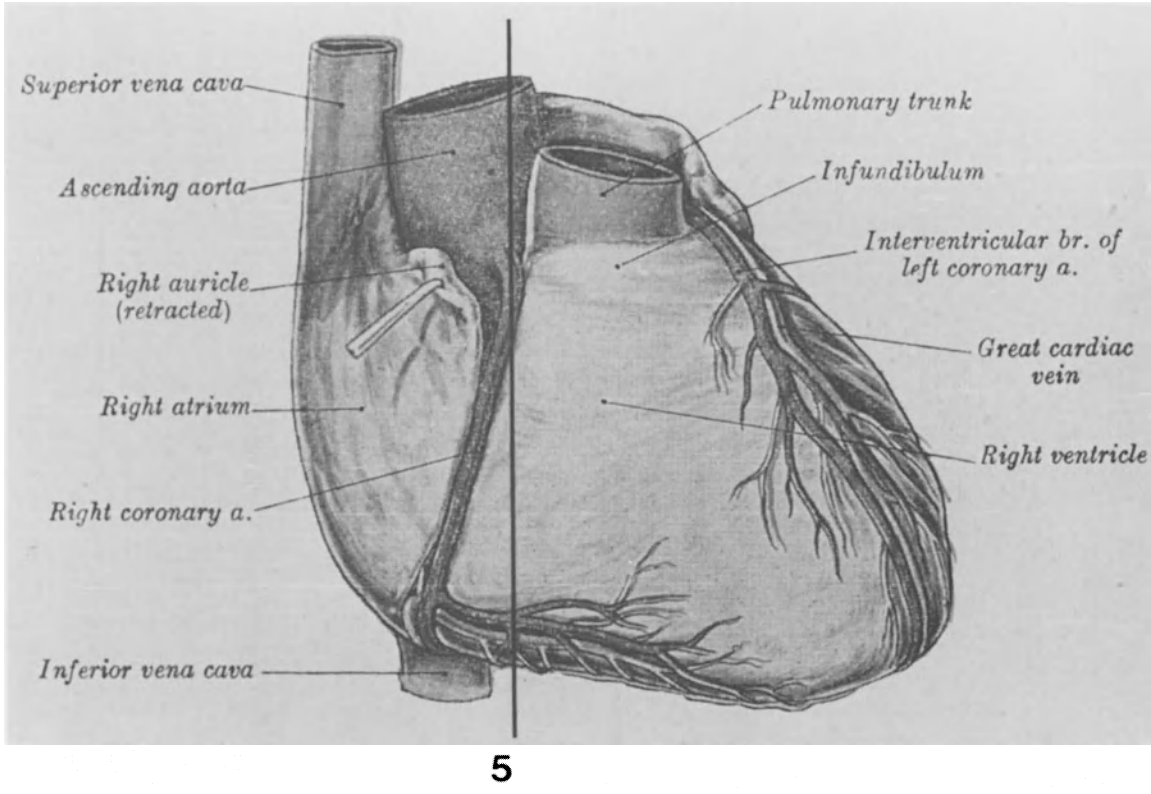

Figure C–13. Plane of section of the coronal slice 5.

This slice, nearly similar to the previous one, shows the ascending aortic relations. Firstly, it passes forwards and to the right; then, it turns backwards and to the left to form the arch of the aorta. The aortic arch gives off two vessels, the brachiocephalic trunk and the left common carotid artery.

On the left side of the ascending aorta, the main pulmonary artery crosses the aorta and immediately after, gives off the two pulmonary arteries.

On the right side, the ascending aorta is related to the superior vena cava.

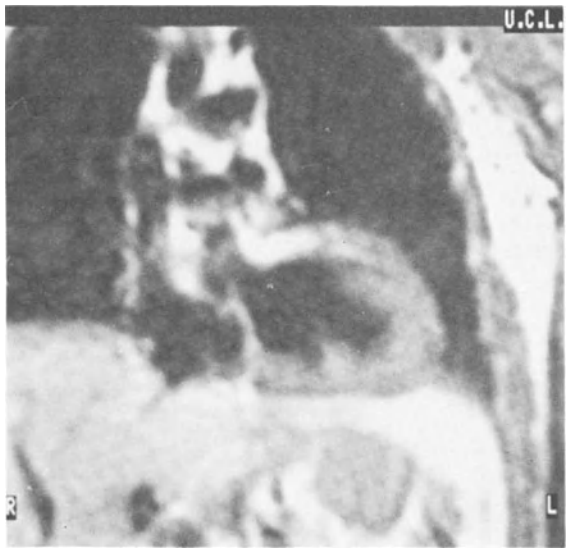

Figure C–14. MR slice.

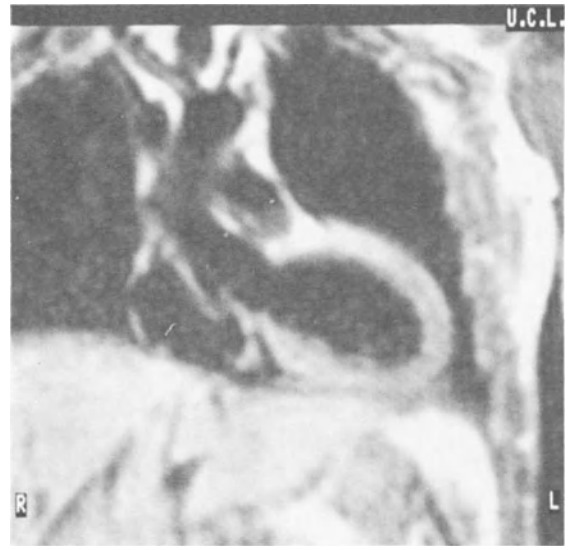

Figure C–15. MR slice.

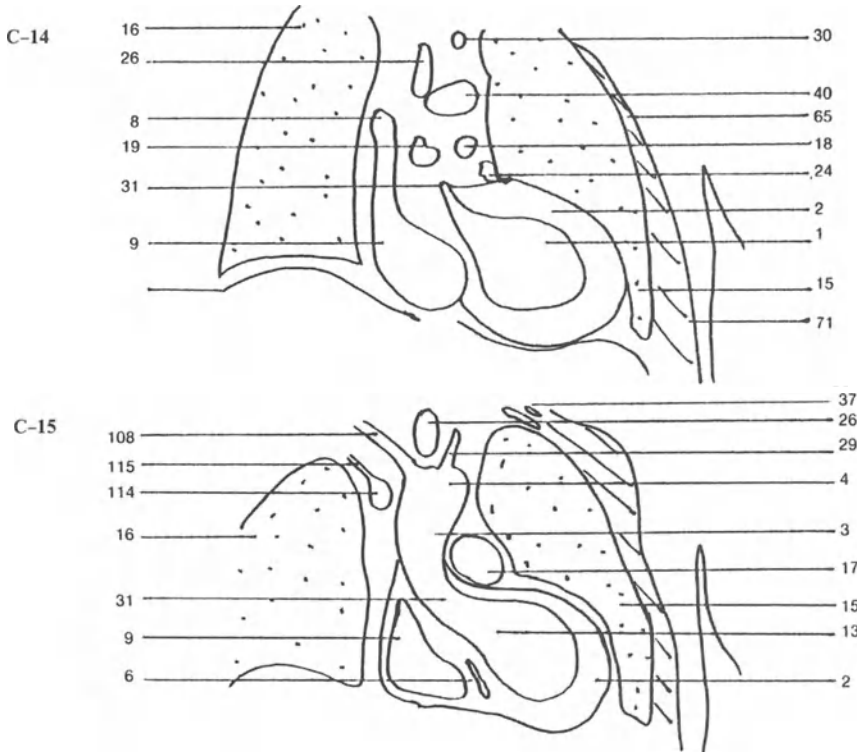

(1) Left ventricular cavity; (2) Myocardium; (3) Ascending aorta; (4) Aortic arch; (6) Coronary sinus; (8) Superior vena cava; (9) Right atrium; (13) Left ventricular outflow region; (15) Left lung; (16) Right lung; (17) Main pulmonary artery; (18) Left pulmonary artery; (19) Right pulmonary artery; (24) Left atrial appendage; (26) Trachea; (29) Left common carotid artery; (30) Left subclavian artery; (31) Aortic infundibulum; (37) Left subclavian vein; (65) Intercostal muscles; (71) Serratus anterior muscle; (108) Brachiocephalic trunk; (114) Right brachiocephalic vein; (115) Right subclavian vein.

Coronal slice 6

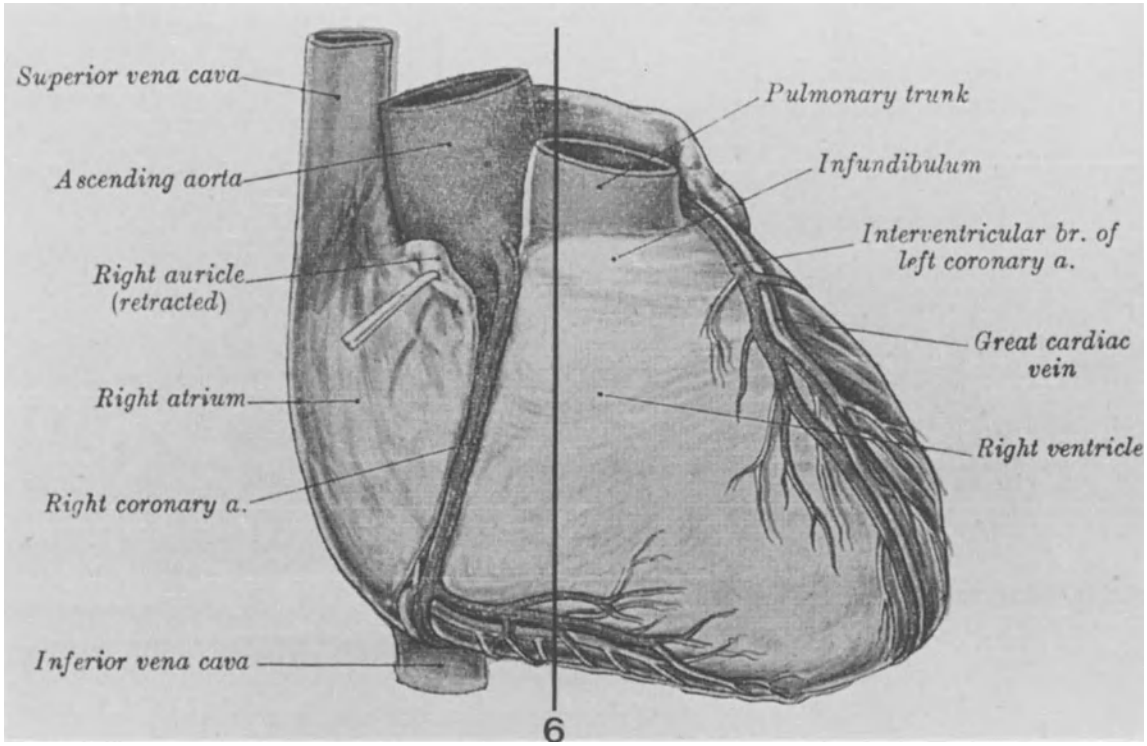

Figure C–16. Plane of section of the coronal slice 6.

This slice shows the right ventricle, the most anterior cavity of the heart, just anterior to the aortic infundibulum.

The right atrium progressively disappears.

At this level, the subclavian vein and the internal jugular vein join to form the brachiocephalic vein.

Figure C–17. MR slice.

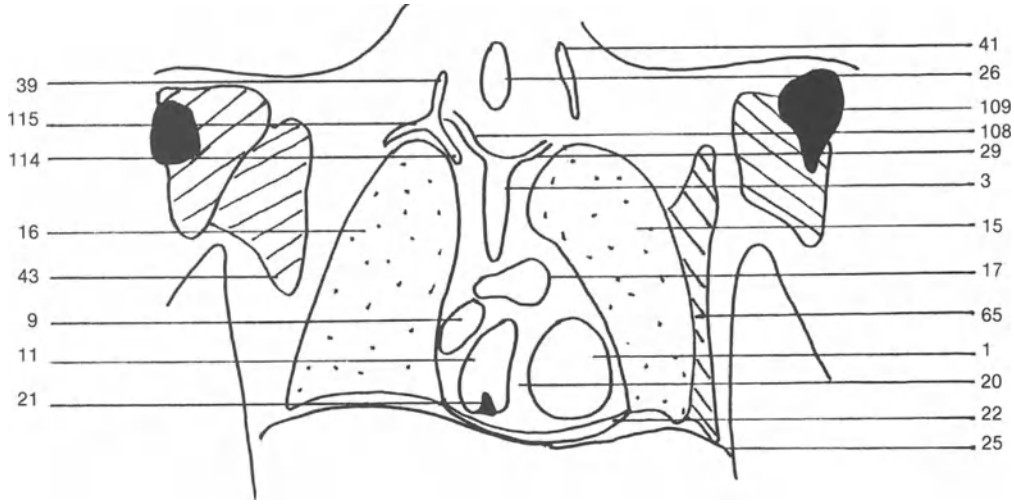

(1) Left ventricular cavity; (3) Ascending aorta; (9) Right atrium; (11) Right ventricular cavity; (15) Left lung; (16) Right lung; (17) Main pulmonary artery; (20) Ventricular septum; (21) Papillary muscle; (22) Pericardium; (25) Diaphragm; (26) Trachea; (29) Left common carotid artery; (39) Right internal jugular vein; (41) Left internal jugular vein; (43) Pectoralis major muscle; (65) Intercostal muscles; (108) Brachiocephalic trunk; (109) Humerus; (114) Right brachiocephalic vein; (115) Right subclavian vein.

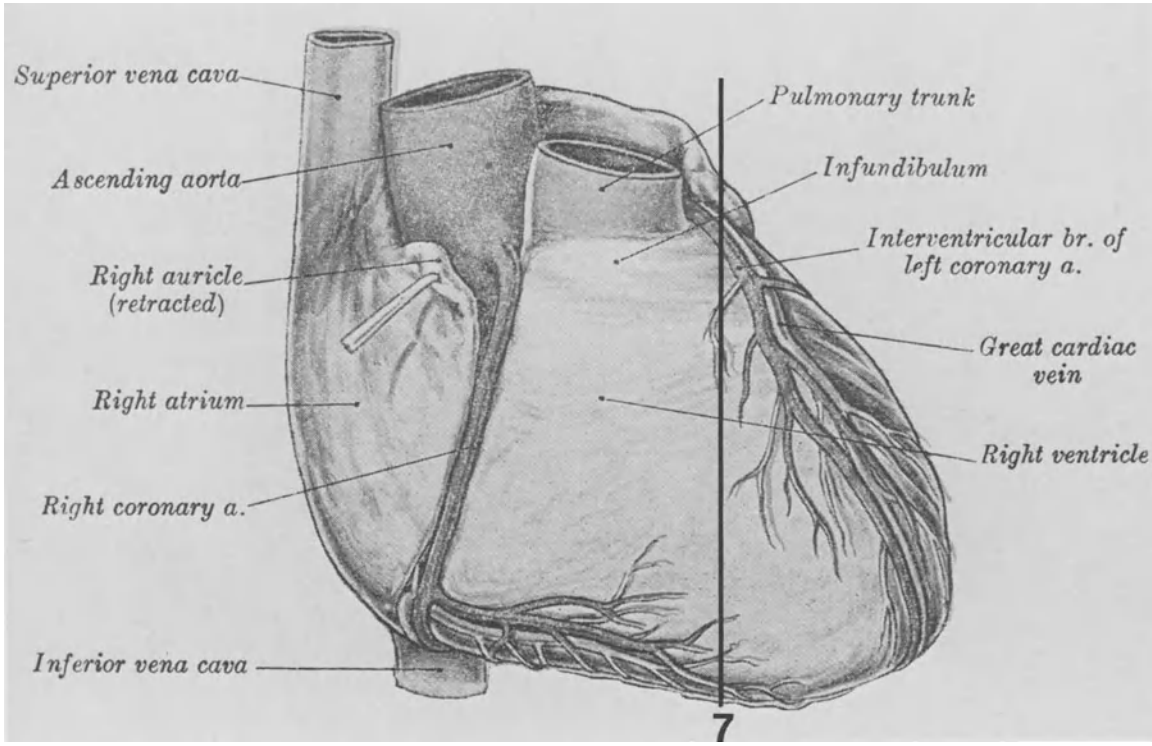

Figure C–18. Plane of section of the coronal slice 7.

This anterior slice shows the tricuspid valvular plane. The right atrium is situated posteriorly and to the right of the right ventricle. The left ventricle is posterior and to the left of the right ventricle. The pericardosternal ligament is seen. The left ventricle becomes smaller anteriorly to form the apex.

Coronal slice 7

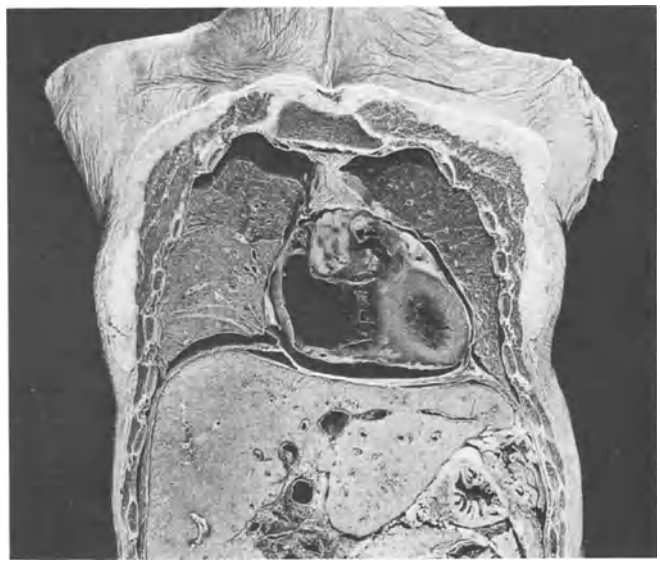

Figure C–19. Anatomical slice.

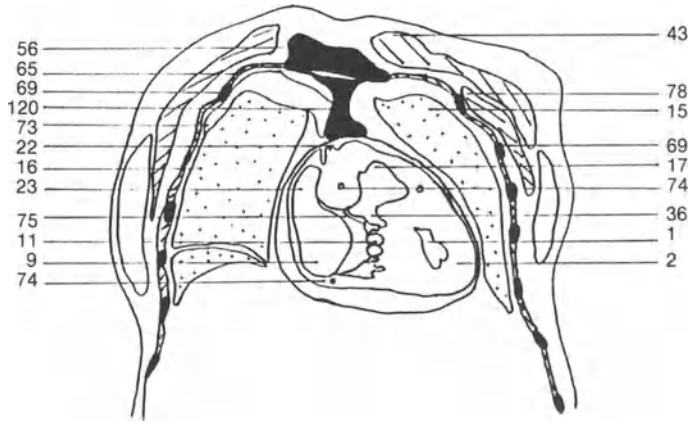

(1) Left ventricular cavity; (2) Myocardium; (9) Right atrium; (11) Right ventricular cavity; (15) Left lung; (16) Right lung; (17) Main pulmonary artery; (20) Ventricular septum; (22) Pericardium; (23) Right atrial appendage; (25) Diaphragm; (26) Trachea; (29) Left common carotid artery; (36) Pulmonary infundibulum; (39) Right internal jugular vein; (41) Left internal jugular vein; (43) Pectoralis major muscle; (56) Manubrium; (65) Intercostal muscles; (69) Rib; (73) Pleural cavity; (74) Right coronary artery; (75) Tricuspid valve; (78) Pectoralis minor muscle; (109) Humerus; (117) Right common carotid artery; (120) Pericardosternal ligament

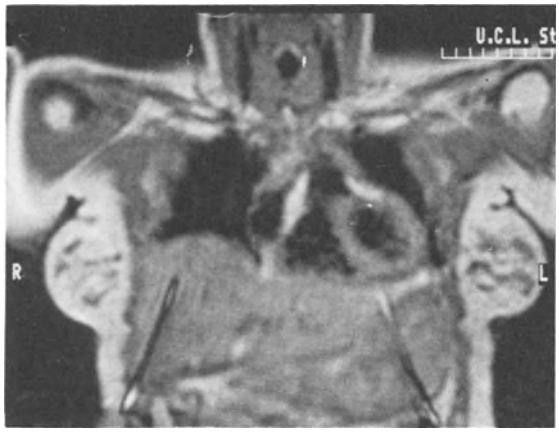

Figure C–20. MR slice.

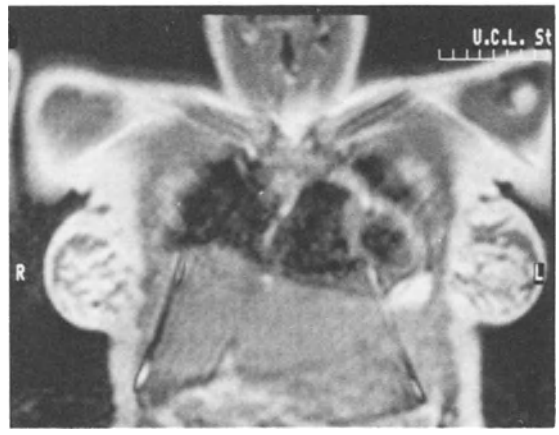

Figure C–21. MR slice.

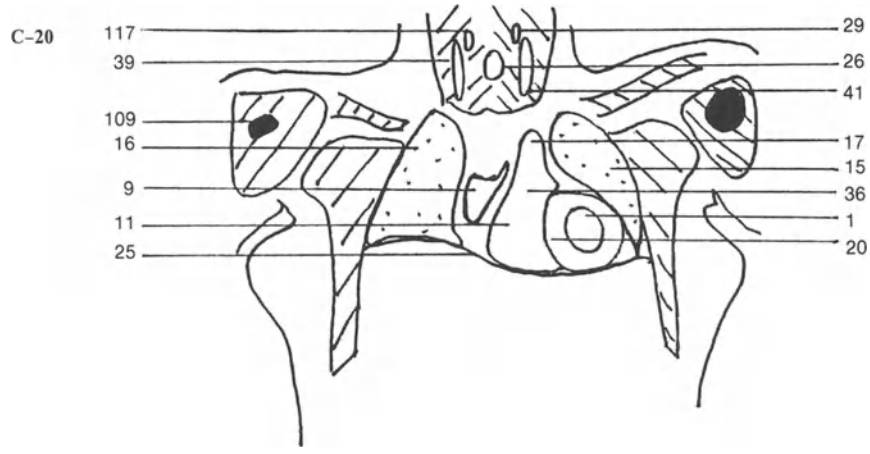

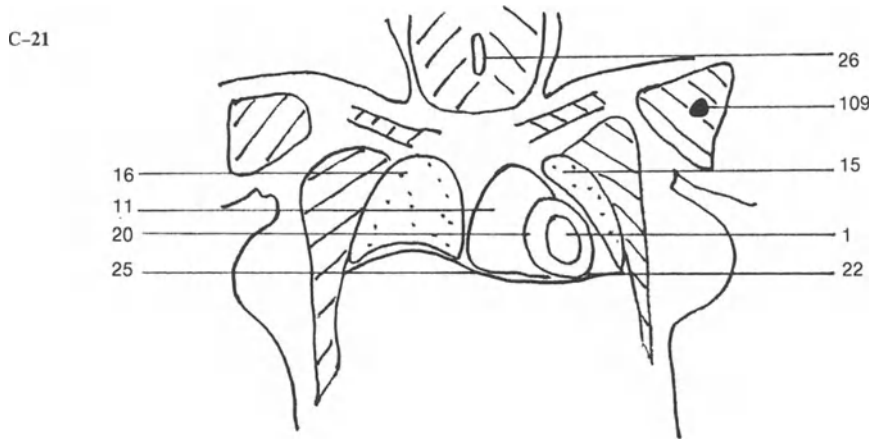

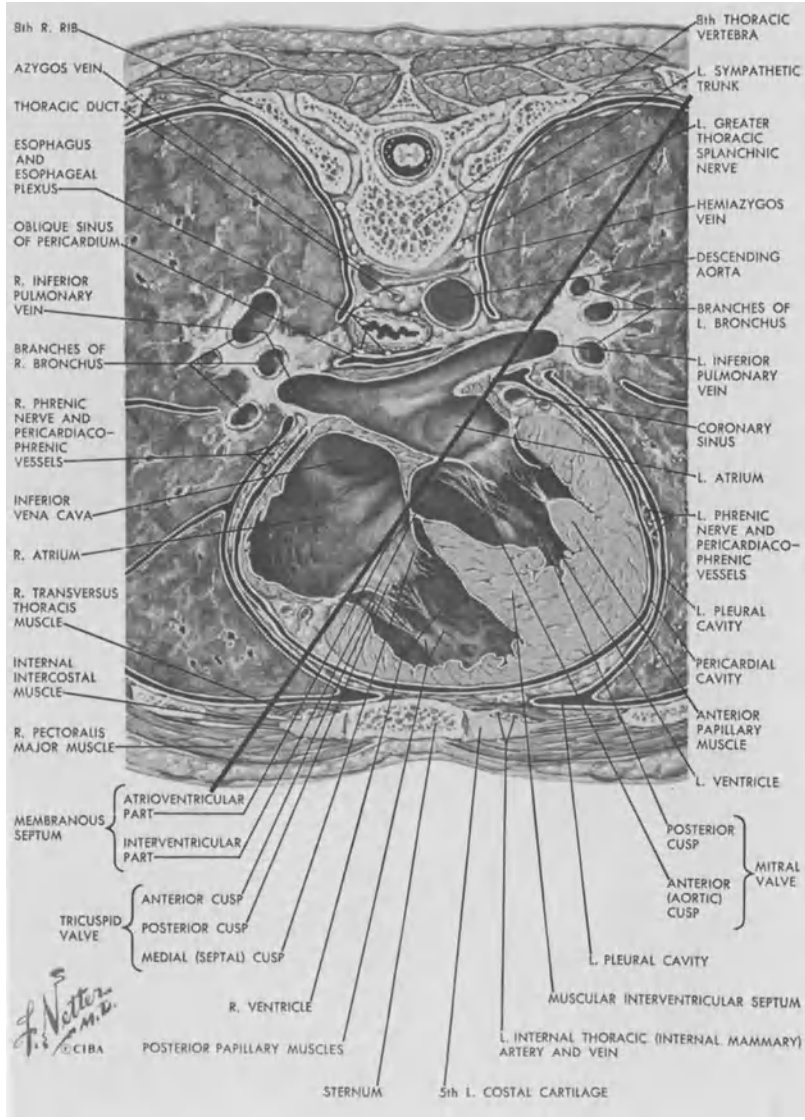

Figure L–0. General plane of section of the LAO slices.

The left anterior oblique (LAO) slices are made as if the observer was on the left anterior part of the patient.

LAO slice 1

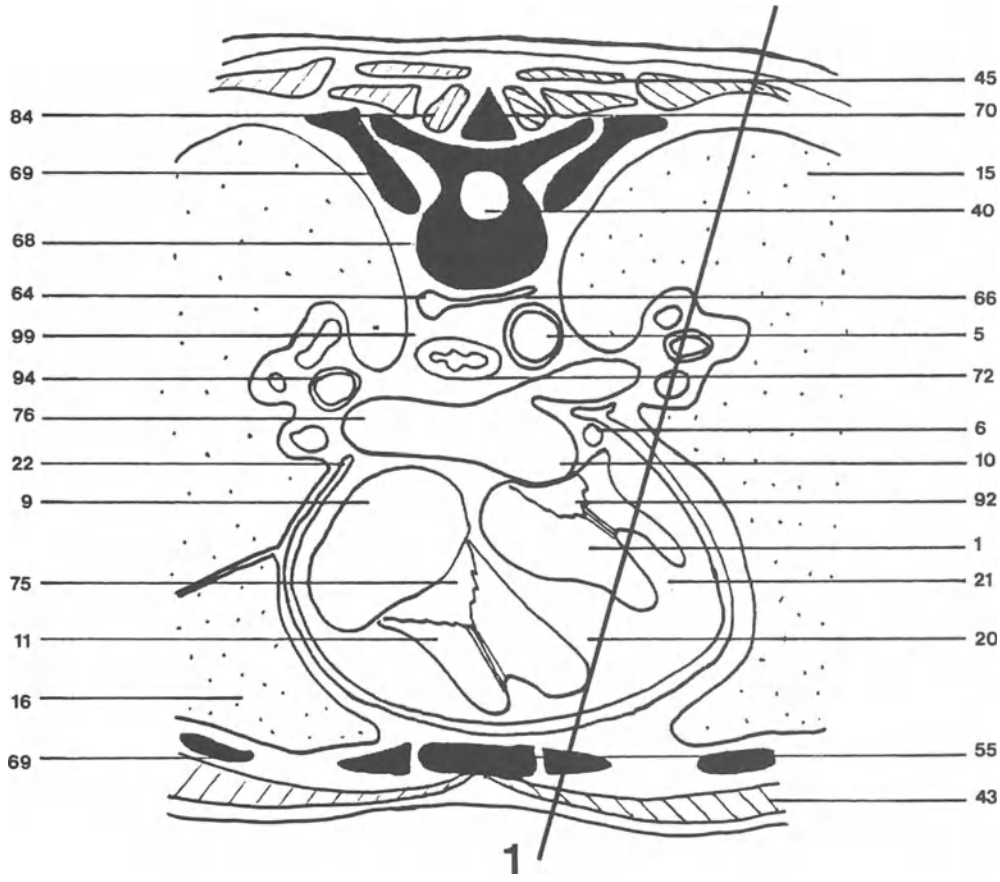

Figure L–1. Plane of section of the LAO slice 1.

This slice is very lateral and shows the left ventricle and only a small part of the right ventricle. The left lung forms the major part of the image. Legends are on the next page.

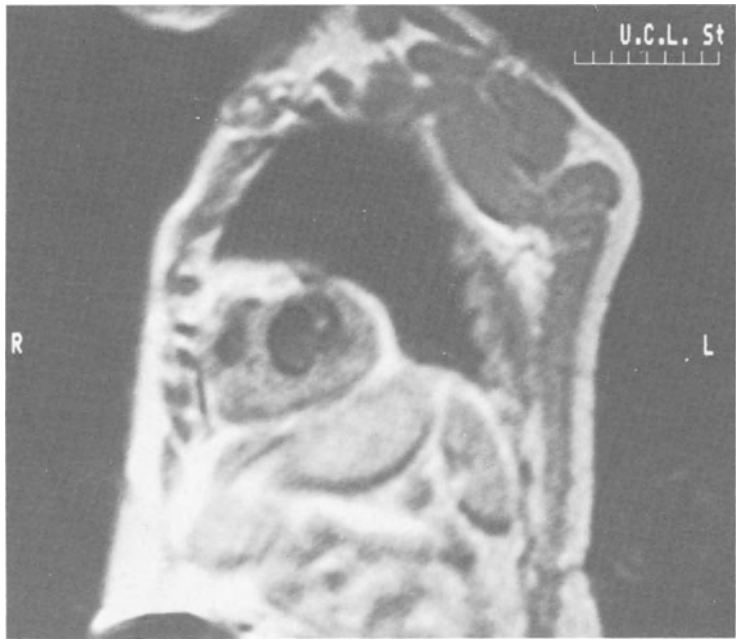

Figure L-2. MR slice.

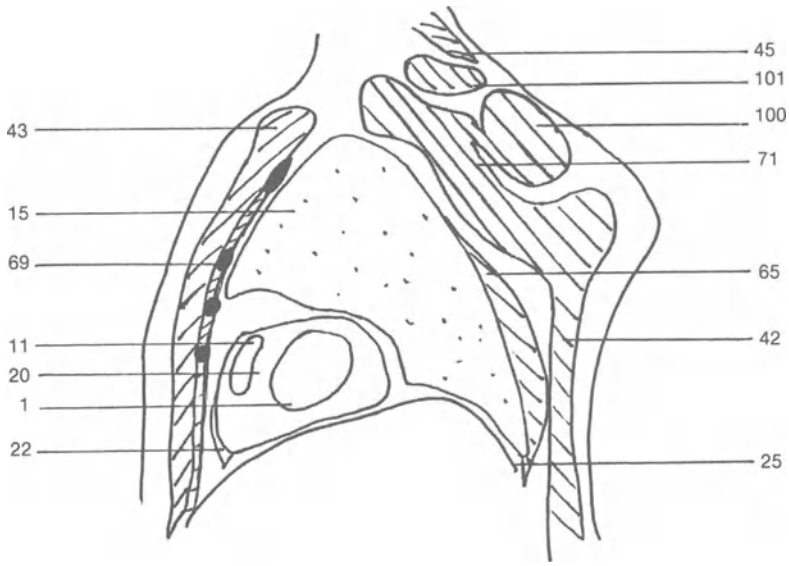

(1) Left ventricular cavity; (5) Descending aorta; (6) Coronary sinus; (9) Right atrium; (10) Left atrium; (11) Right ventricular cavity; (15) Left lung; (16) Right lung; (20) Ventricular septum; (21) Papillary muscle; (22) Pericardium; (25) Diaphragm; (40) Spinal cord; (42) Latissimus dorsi muscle; (43) Pectoralis major muscle; (45) Trapezius muscle; (55) Sternum; (64) Azygos vein; (65) Intercostal muscles; (66) Hemiazygos vein; (68) Dorsal vertebra; (69) Rib; (70) Spinous process; (71) Serratus anterior muscle; (72) Esophagus; (75) Tricuspid valve; (76) Right inferior pulmonary vein; (84) Transversospinal muscle; (92) Mitral valve; (94) Right main bronchus; (99) Mediastinum; (100) Supraspinatus muscle; (101) Levator scapulae muscle.

LAO slice 2

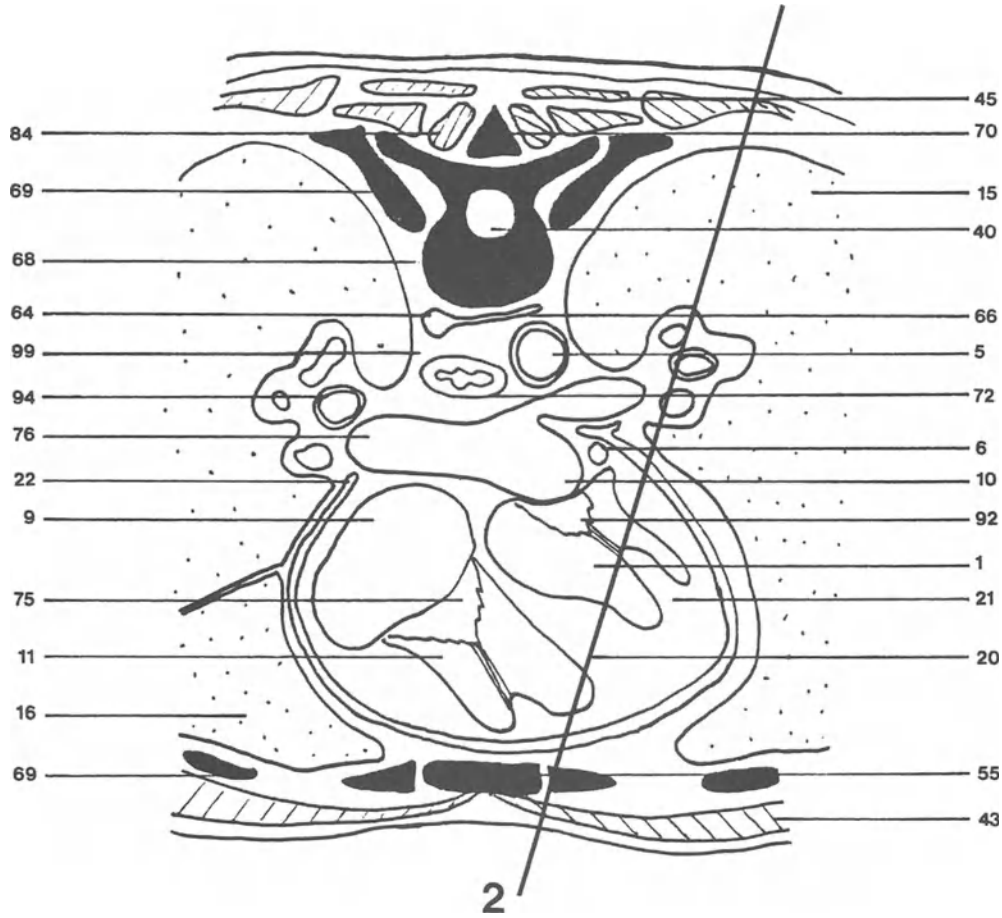

Figure L-3. Plane of section of LAO slice 2.

In its lateral part, the left ventricle is nearly circular while the right ventricle is more elongated and forms, in its upper part, the right ventricular outflow region. The left atrial appendage lies on the upper part of the left ventricle. The left coronary artery runs on the top of the ventricular septum.

Legends are on the next page.

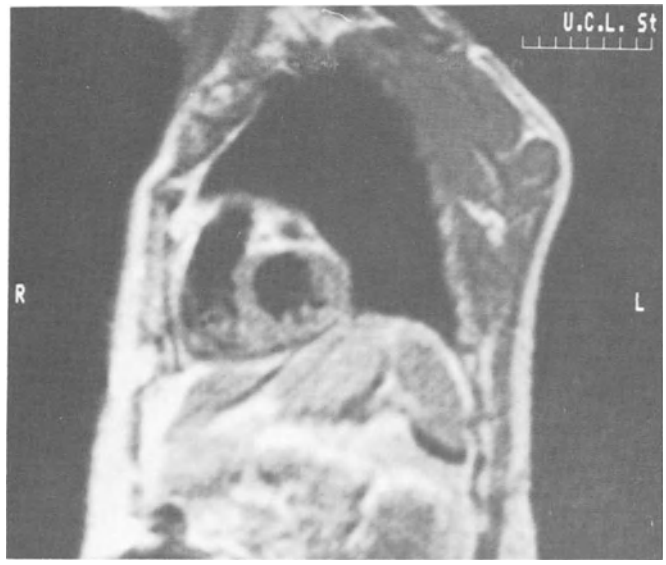

Figure L-4. MR slice.

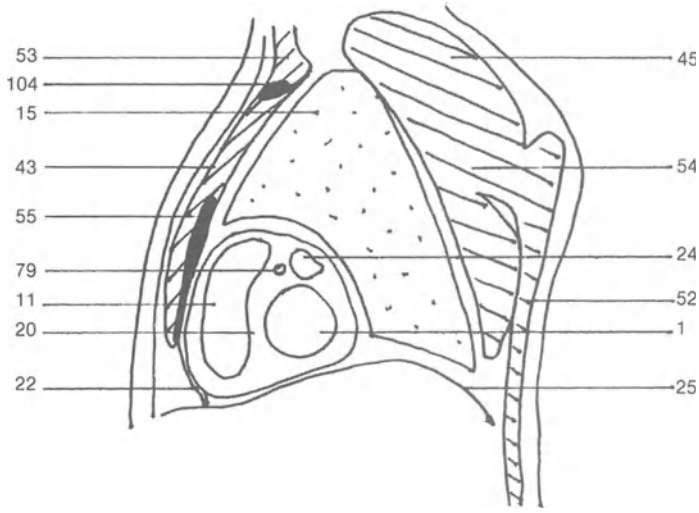

(1) Left ventricular cavity; (5) Descending aorta; (6) Coronary sinus; (9) Right atrium; (10) Left atrium; (11) Right ventricular cavity; (15) Left lung; (16) Right lung; (20) Ventricular septum; (21) Papillary muscle; (22) Pericardium; (24) Left atrial appendage; (25) Diaphragm; (40) Spinal cord; (43) Pectoralis major muscle; (45) Trapezius muscle; (52) Erector spinae muscle; (53) Sternocleidomastoid muscle; (54) Rhomboidus muscle; (55) Sternum; (64) Azygos vein; (66) Hemiazygos vein; (68) Dorsal vertebra; (69) Rib; (70) Spinous process; (72) Esophagus; (75) Tricuspid valve; (76) Right inferior pulmonary vein; (79) Left coronary artery; (84) Transversospinal muscle; (92) Mitral valve; (94) Right main bronchus; (99) Mediastinum; (104) Clavicle.

LAO slice 3

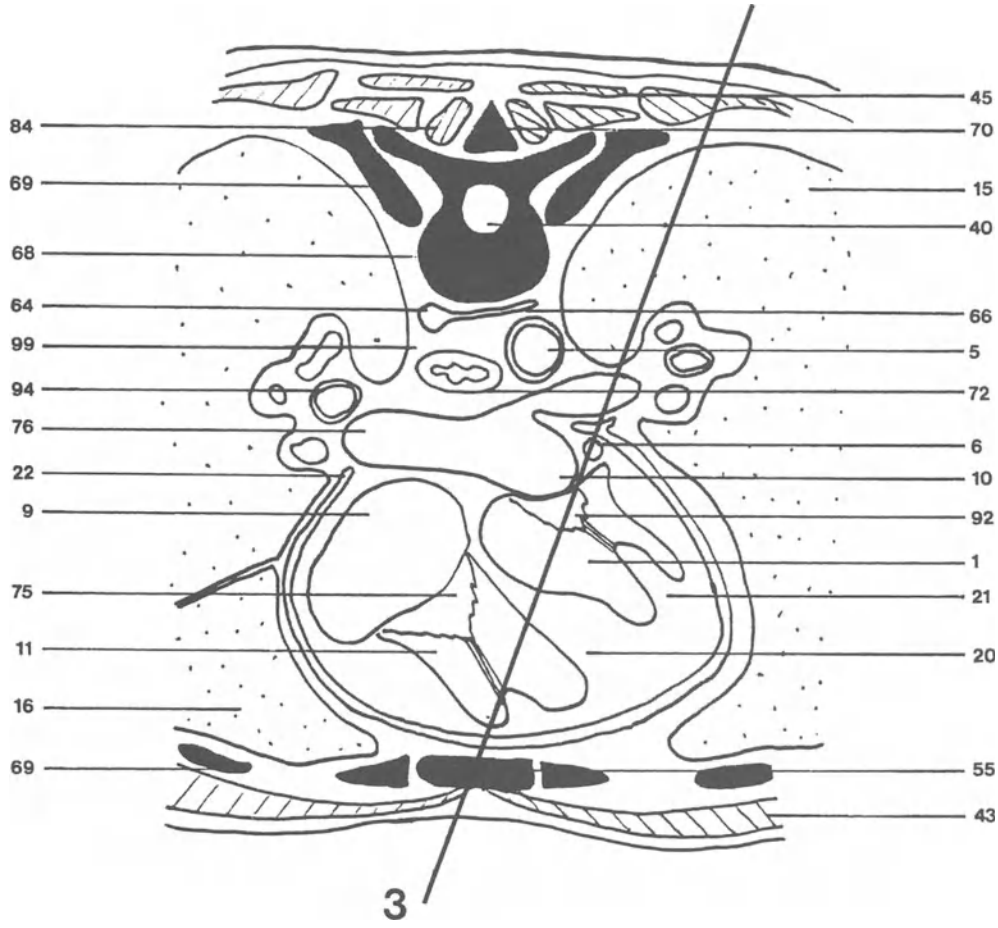

Figure L-5. Plane of section of LAO slice 3.

The slice shows the beginning of the main pulmonary artery.

It runs upwards and backwards, firstly in front of the ascending aorta, and then to its left side. When it becomes posterior to the ascending aorta, the main pulmonary artery divides into right and left pulmonary arteries.

Legends are on the next page.

Figure L-6. MR slice.

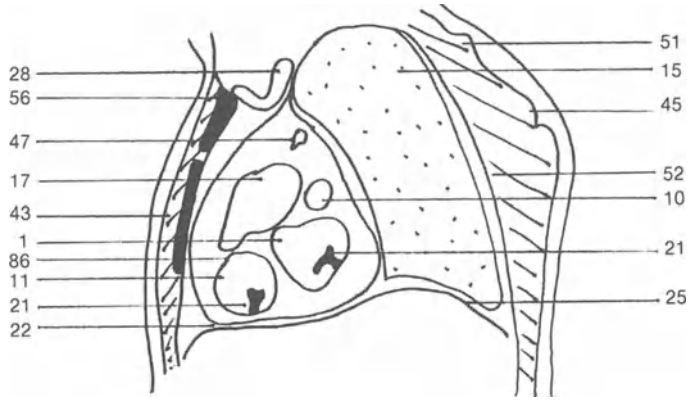

(1) Left ventricular cavity; (5) Descending aorta; (6) Coronary sinus; (9) Right atrium; (10) Left atrium; (11) Right ventricular cavity; (15) Left lung; (16) Right lung; (17) Main pulmonary artery; (20) Ventricular septum; (21) Papillary muscle; (22) Pericardium; (25) Diaphragm; (28) Left brachiocephalic vein; (40) Spinal cord; (43) Pectoralis major muscle; (45) Trapezius muscle; (47) Left superior pulmonary vein; (51) Splenius muscle; (52) Erector spinae muscle; (55) Sternum; (56) Manubrium; (64) Azygos vein; (66) Hemiazygos vein; (68) Dorsal vertebra; (69) Rib; (70) Spinous process; (72) Esophagus; (75) Tricuspid valve; (76) Right inferior pulmonary vein; (84) Transversospinal muscle; (86) Pulmonary valve; (92) Mitral valve; (94) Right main bronchus; (99) Mediastinum.

LAO slice 4

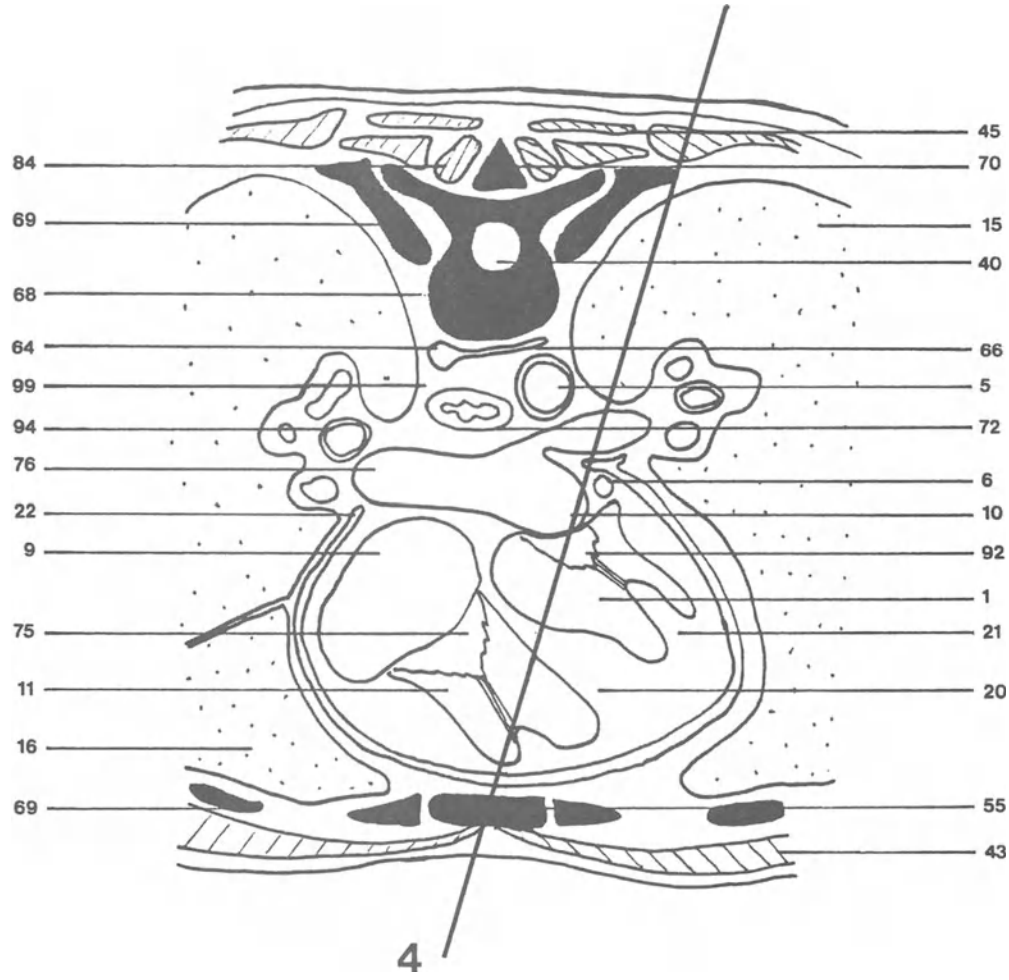

Figure L-7. Plane of section of LAO slice 4.

This slice shows the crossing of the ascending aorta and of the main pulmonary artery. Above the main pulmonary artery, the aortic arch is seen.

The right ventricle is the most anterior part of the heart.

Legends are on the next page.

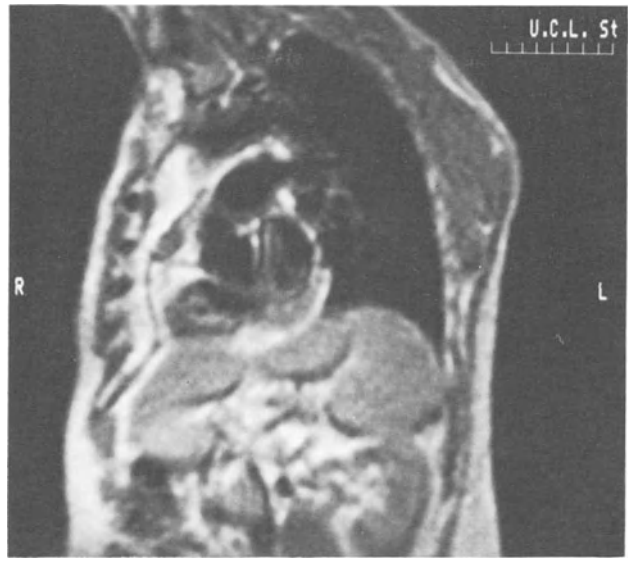

Figure L-8. MR slice.

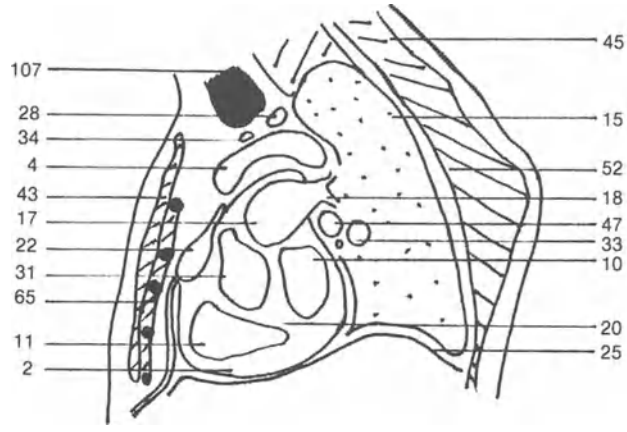

(1) Left ventricular cavity; (2) Myocardium; (4) Aortic arch; (5) Descending aorta; (6) Coronary sinus; (9) Right atrium; (10) Left atrium; (11) Right ventricular cavity; (15) Left lung; (16) Right lung; (17) Main pulmonary artery; (18) Left pulmonary artery; (20) Ventricular septum; (21) Papillary muscle; (22) Pericardium; (25) Diaphragm; (26) Trachea; (28) Left brachiocephalic vein; (31) Aortic infundibulum; (33) Left main bronchus; (34) Right inferior thyroid vein; (40) Spinal cord; (43) Pectoralis major muscle; (45) Trapezius muscle; (47) Left superior pulmonary vein; (52) Erector spinae muscle; (55) Sternum; (64) Azygos vein; (65) Intercostal muscles; (66) Hemiazygos vein; (68) Dorsal vertebra; (69) Rib; (70) Spinous process; (72) Esophagus; (75) Tricuspid valve; (76) Right inferior pulmonary vein; (84) Transversospinal muscle; (92) Mitral valve; (94) Right main bronchus; (99) Mediastinum; (107) Thyroid gland.

LAO slice 5

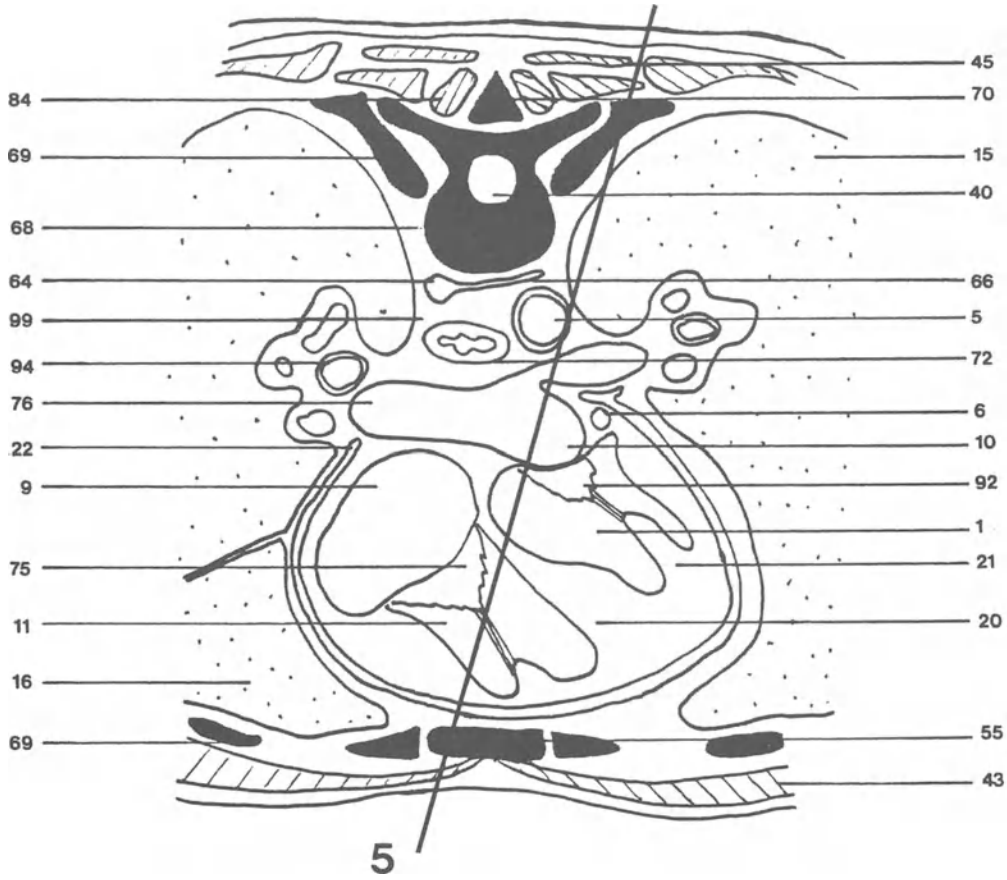

Figure L-9. Plane of section of LAO slice 5.

This slice shows the beginning of the ascending aorta and its prolongation into the aortic arch.
An important feature of the LAO angulation is to follow the thoracic aorta.
The left common carotid artery arises from the aortic arch while the left internal jugular vein will form the left brachiocephalic vein after its junction with the left subclavian vein.
Legends are on the next page.

Figure L-10. MR slice.

Figure L-11. MR slice.

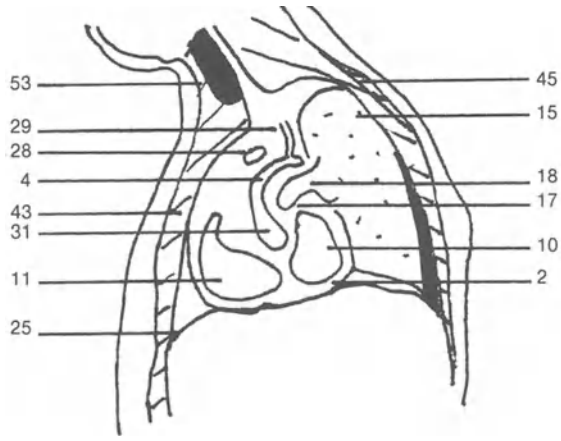

(1) Left ventricular cavity; (2) Myocardium; (4) Aortic arch; (5) Descending aorta; (6) Coronary sinus; (9) Right atrium; (10) Left atrium; (11) Right ventricular cavity; (15) Left lung; (16) Right lung; (17) Main pulmonary artery; (18) Left pulmonary artery; (20) Ventricular septum; (21) Papillary muscle; (22) Pericardium; (25) Diaphragm; (28) Left brachiocephalic vein; (29) Left common carotid artery; (31) Aortic infundibulum; (40) Spinal cord; (41) Left internal jugular vein; (43) Pectoralis major muscle; (45) Trapezius muscle; (47) Left superior pulmonary vein; (49) Rachis; (53) Sternocleidomastoid muscle; (54) Rhomboidus muscle; (55) Sternum; (61) Longissimus thoracis muscle; (64) Azygos vein; (66) Hemiazygos vein; (68) Dorsal vertebra; (69) Rib; (70) Spinous process; (72) Esophagus; (75) Tricuspid valve; (76) Right inferior pulmonary vein; (84) Transversospinal muscle; (92) Mitral valve; (94) Right main bronchus; (99) Mediastinum; (107) Thyroid gland.

LAO slice 6

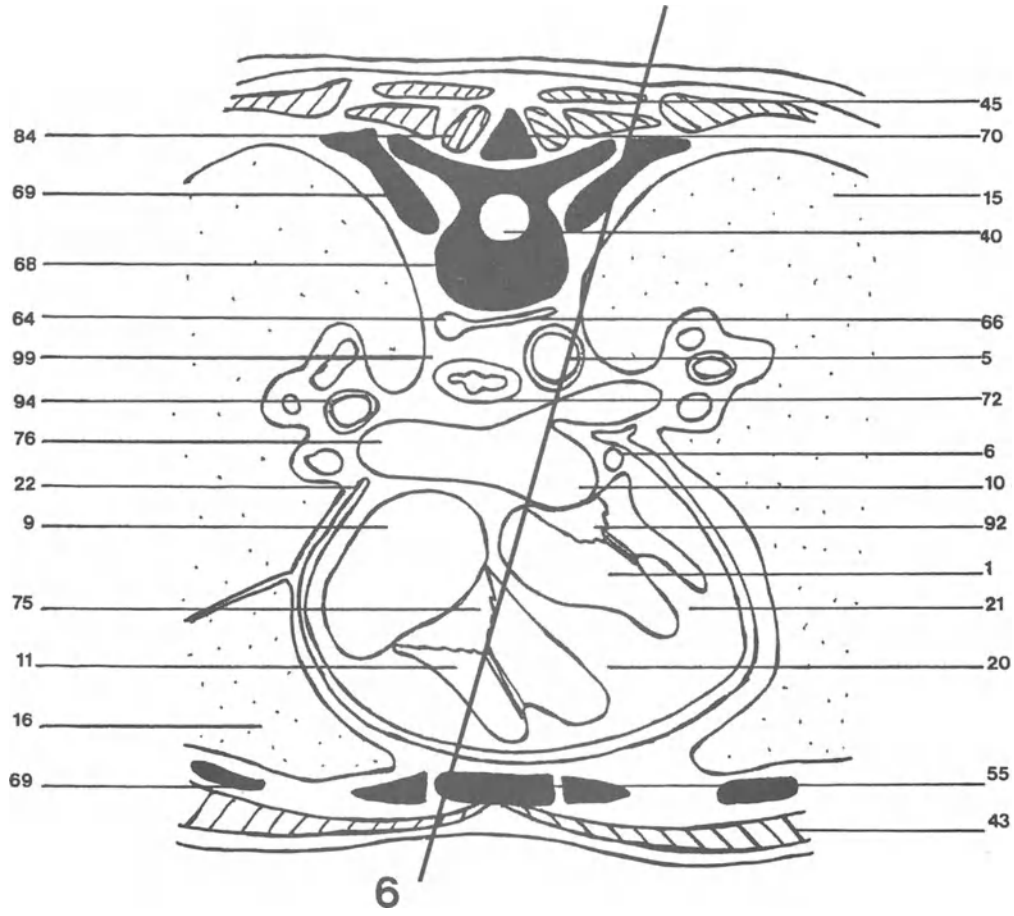

Figure L-12 Plane of section of LAO slice 6.

This slice shows the continuation of the ascending aorta and of the aortic arch. The slice is tangent to the descending aorta of which only a small part is seen.

The left ventricle is no longer be seen. Between the left atrium and the aortic arch the main pulmonary artery is seen at the level of division into left and right pulmonary arteries.

The right lung is seen anteriorly because of the obliquity of the slice, while the left lung volume decreases progressively.

Legends are on the next page.

Figure L-13. MR slice.

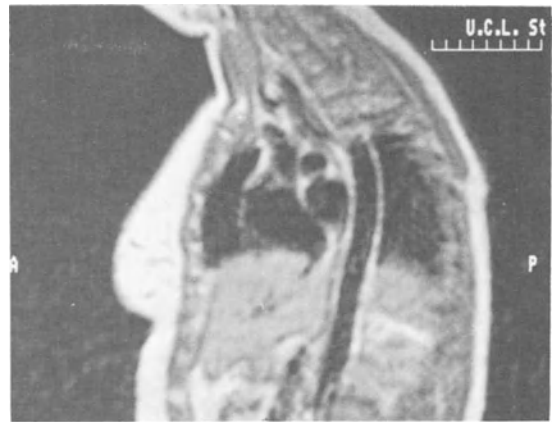

Figure L-14. MR slice.

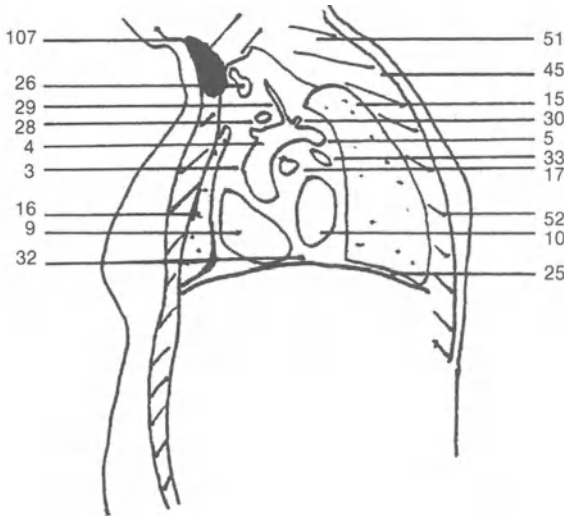

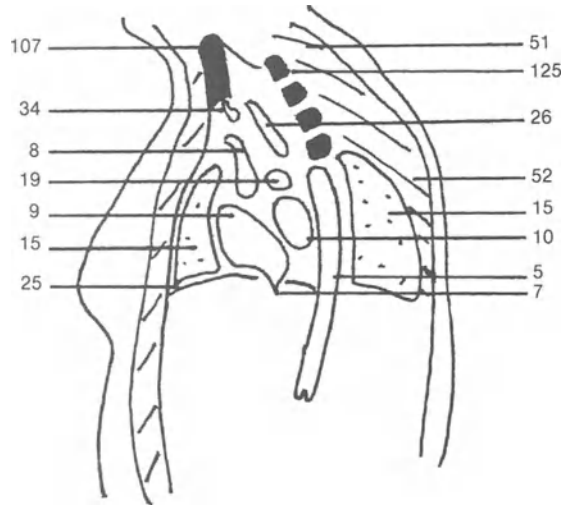

(1) Left ventricular cavity; (3) Ascending aorta; (4) Aortic arch; (5) Descending aorta; (6) Coronary sinus; (7) Inferior vena cava; (8) Superior vena cava; (9) Right atrium; (10) Left atrium; (11) Right ventricular cavity; (15) Left lung; (16) Right lung; (17) Main pulmonary artery; (19) Right pulmonary artery; (20) Ventricular septum; (21) Papillary muscle; (22) Pericardium; (25) Diaphragm; (26) Trachea; (28) Left brachiocephalic vein; (29) Left common carotid artery; (30) Left subclavian artery; (32) Atrial septum; (33) Left main bronchus; (34) Right inferior thyroid vein; (40) Spinal cord; (43) Pectoralis major muscle; (45) Trapezius muscle; (51) Splenius muscle; (52) Erector spinae muscle; (55) Sternum; (64) Azygos vein; (66) Hemiazygos vein; (68) Dorsal vertebra; (69) Rib; (70) Spinous process; (72) Esophagus; (75) Tricuspid valve; (76) Right inferior pulmonary vein; (84) Transversospinal muscle; (92) Mitral valve; (94) Right main bronchus; (99) Mediastinum; (107) Thyroid gland; (125) Cervical vertebra.

LAO slice 7

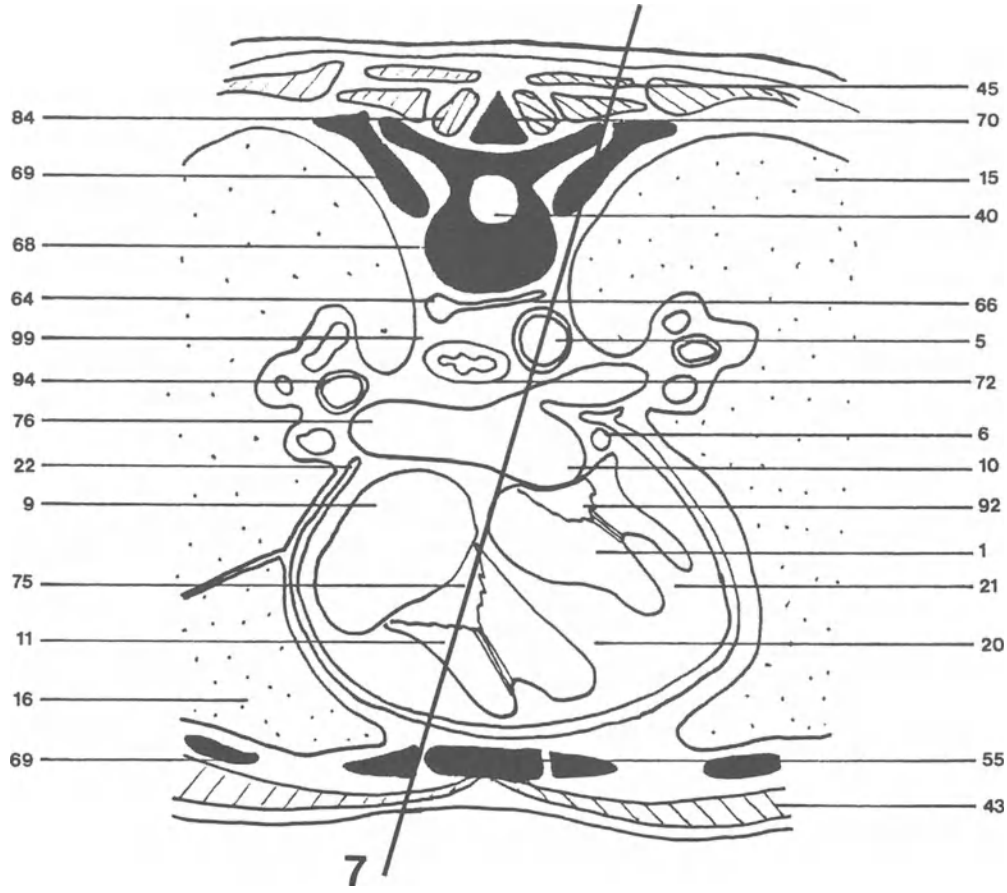

Figure L-15. Plane of section of LAO slice 7.

The slice allows us to see the thoracic aorta; it is one of the advantages of the LAO slices.
The cavities of the heart depicted here are only the left atrium and the right atrium.
The main pulmonary artery divides into left and right pulmonary arteries.
Legends are on the next page.

Figure L-16. MR slice.

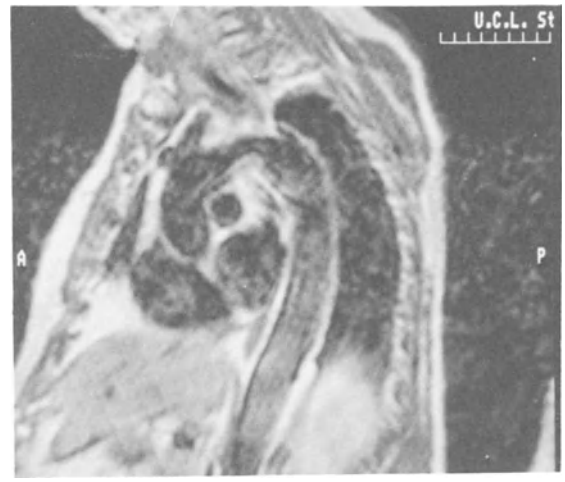

Figure L-17. MR slice.

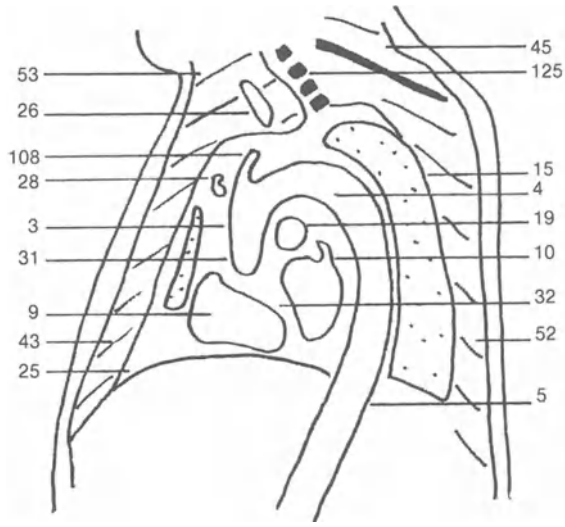

(1) Left ventricular cavity; (3) Ascending aorta; (4) Aortic arch; (5) Descending aorta; (6) Coronary sinus; (9) Right atrium; (10) Left atrium; (11) Right ventricular cavity; (15) Left lung; (16) Right lung; (17) Main pulmonary artery; (18) Left pulmonary artery; (19) Right pulmonary artery; (20) Ventricular septum; (21) Papillary muscle; (22) Pericardium; (23) Right atrial appendage; (25) Diaphragm; (26) Trachea; (28) Left brachiocephalic vein; (31) Aortic infundibulum; (32) Atrial septum; (35) Larynx; (40) Spinal cord; (42) Latissimus dorsi muscle; (43) Pectoralis major muscle; (45) Trapezius muscle; (52) Erector spinae muscle; (53) Sternocleidomastoid muscle; (54) Rhomboidus muscle; (55) Sternum; (64) Azygos vein; (66) Hemiazygos vein; (68) Dorsal vertebra; (69) Rib; (70) Spinous process; (72) Esophagus; (75) Tricuspid valve; (76) Right inferior pulmonary vein; (84) Transversospinal muscle; (92) Mitral valve; (94) Right main bronchus; (99) Mediastinum; (108) Brachiocephalic trunk; (125) Cervical vertebra.

LAO slice 8

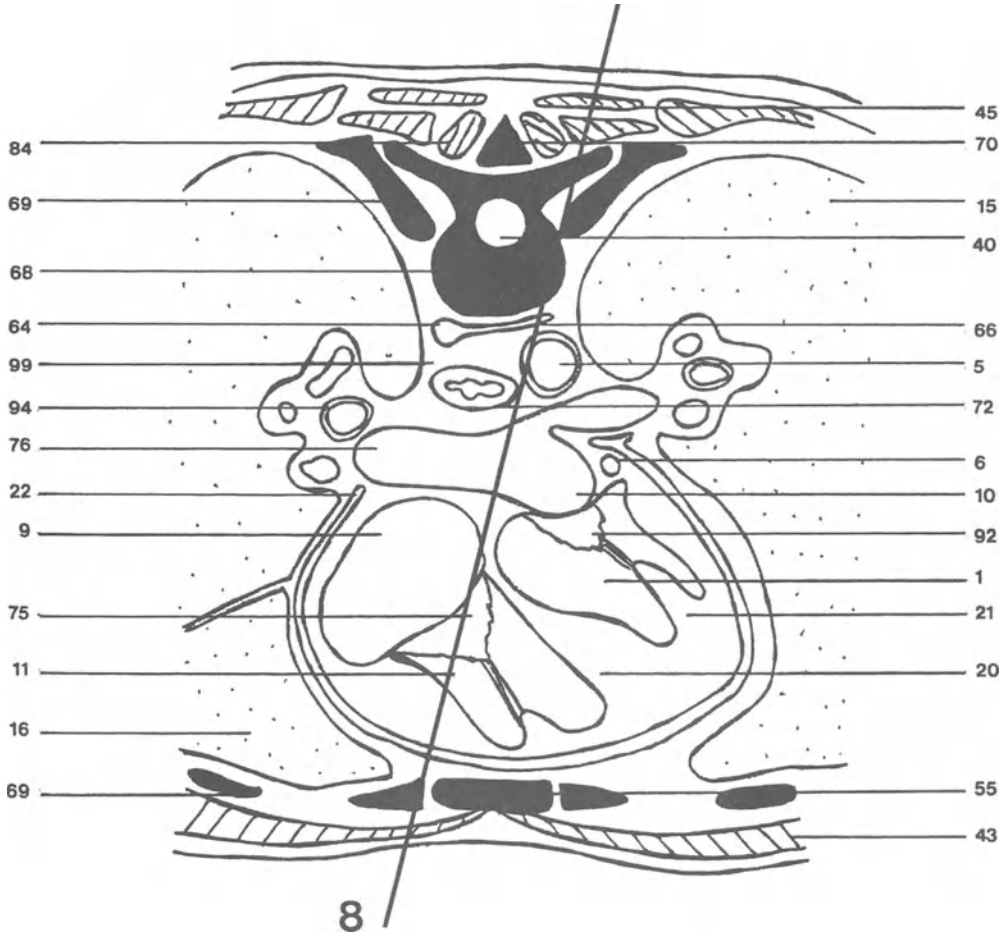

Figure L-18 Plane of section of LAO slice 8.

This slice close to the previous one shows the thoracic aorta and the beginning of the left common carotid artery and the left subclavian artery arising from the aortic arch.

The right pulmonary artery runs behind the ascending aorta. The cardiac cavities visualized are the left atrium and the right atrium.

Legends are on the next page.

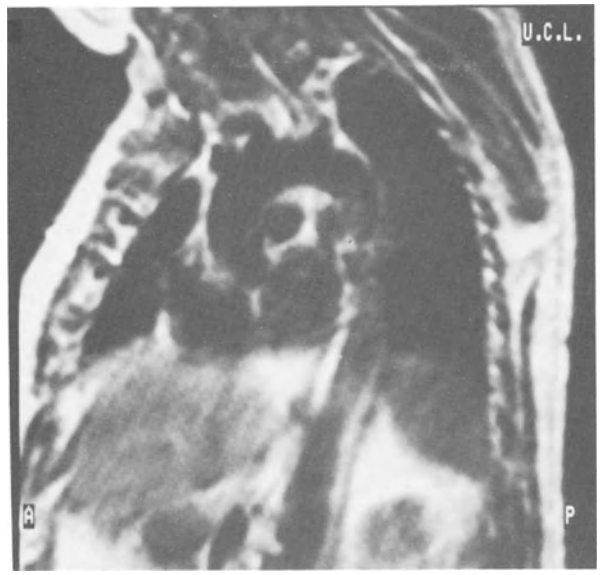

Figure L-19. MR slice.

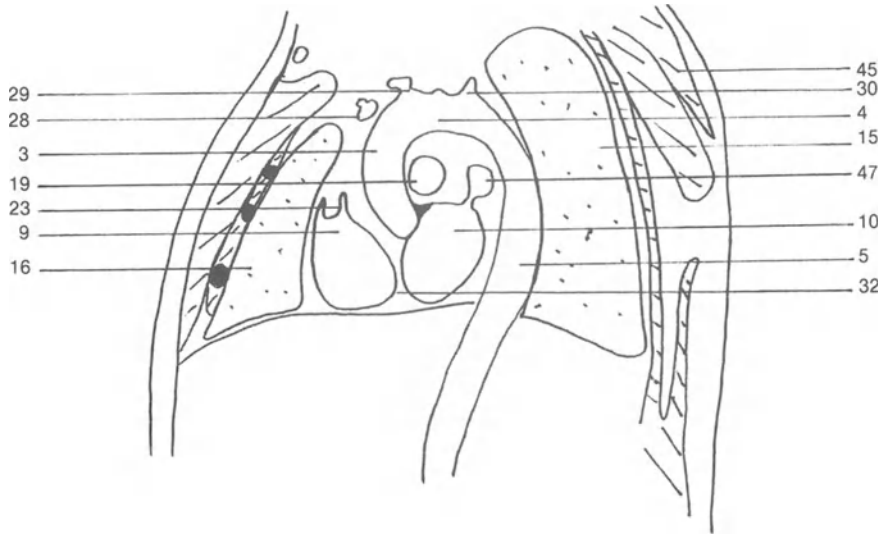

(1) Left ventricular cavity; (3) Ascending aorta; (4) Aortic arch; (5) Descending aorta; (6) Coronary sinus; (9) Right atrium; (10) Left atrium; (11) Right ventricular cavity; (15) Left lung; (16) Right lung; (19) Right pulmonary artery; (20) Ventricular septum; (21) Papillary muscle; (22) Pericardium; (23) Right atrial appendage; (28) Left brachiocephalic vein; (29) Left common carotid artery; (30) Left subclavian artery; (32) Atrial septum; (40) Spinal cord; (43) Pectoralis major muscle; (45) Trapezius muscle; (47) Left superior pulmonary vein; (55) Sternum; (64) Azygos vein; (66) Hemiazygos vein; (68) Dorsal vertebra; (69) Rib; (70) Spinous process; (72) Esophagus; (75) Tricuspid valve; (76) Right inferior pulmonary vein; (84) Transversospinal muscle; (92) Mitral valve; (94) Right main bronchus; (99) Mediastinum.

LAO slice 9

Figure L-20. Plane of section of LAO slice 9.

This slice is behind the aortic arch and shows the superior vena cava and its opening into the right atrium. Only a part of the decending aorta is still seen. The right lung becomes larger.

Behind the superior vena cava, the right pulmonary artery is seen. The left main bronchus lies behind this artery.

Legends are on the next page.

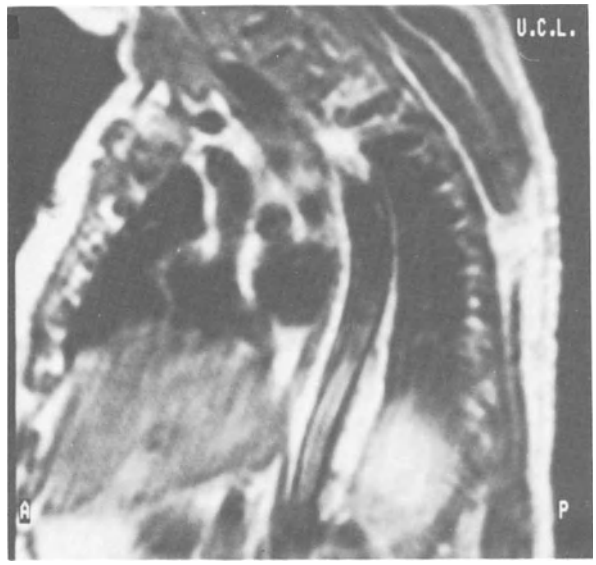

Figure L-21. MR slice.

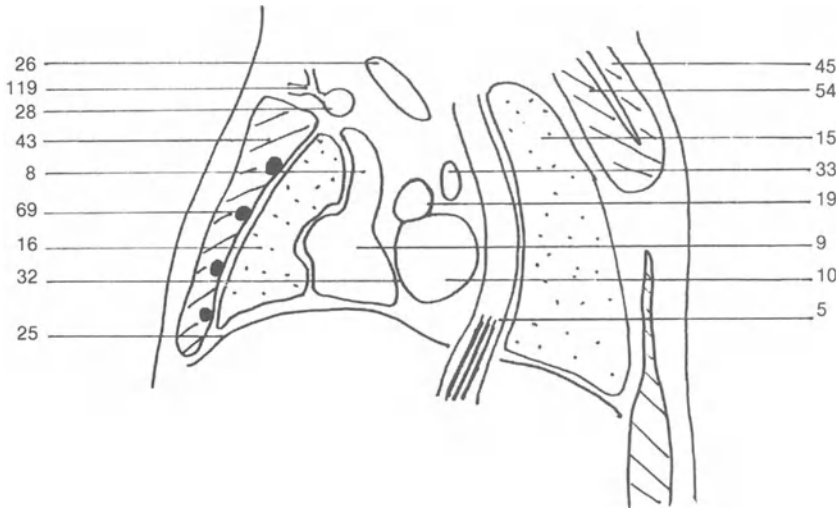

(1) Left ventricular cavity; (5) Descending aorta; (6) Coronary sinus; (8) Superior vena cava; (9) Right atrium; (10) Left atrium; (11) Right ventricular cavity; (15) Left lung; (16) Right lung; (19) Right pulmonary artery; (20) Ventricular septum; (21) Papillary muscle; (22) Pericardium; (25) Diaphragm; (26) Trachea; (28) Left brachiocephalic vein; (32) Atrial septum; (33) Left main bronchus; (40) Spinal cord; (43) Pectoralis major muscle; (45) Trapezius muscle; (54) Rhomboidus muscle; (55) Sternum; (64) Azygos vein; (66) Hemiazygos vein; (68) Dorsal vertebra; (69) Rib; (70) Spinous process; (72) Esophagus; (75) Tricuspid valve; (76) Right inferior pulmonary vein; (84) Transversospinal muscle; (92) Mitral valve; (94) Right main bronchus; (99) Mediastinum; (119) External jugular vein.

LAO slice 10

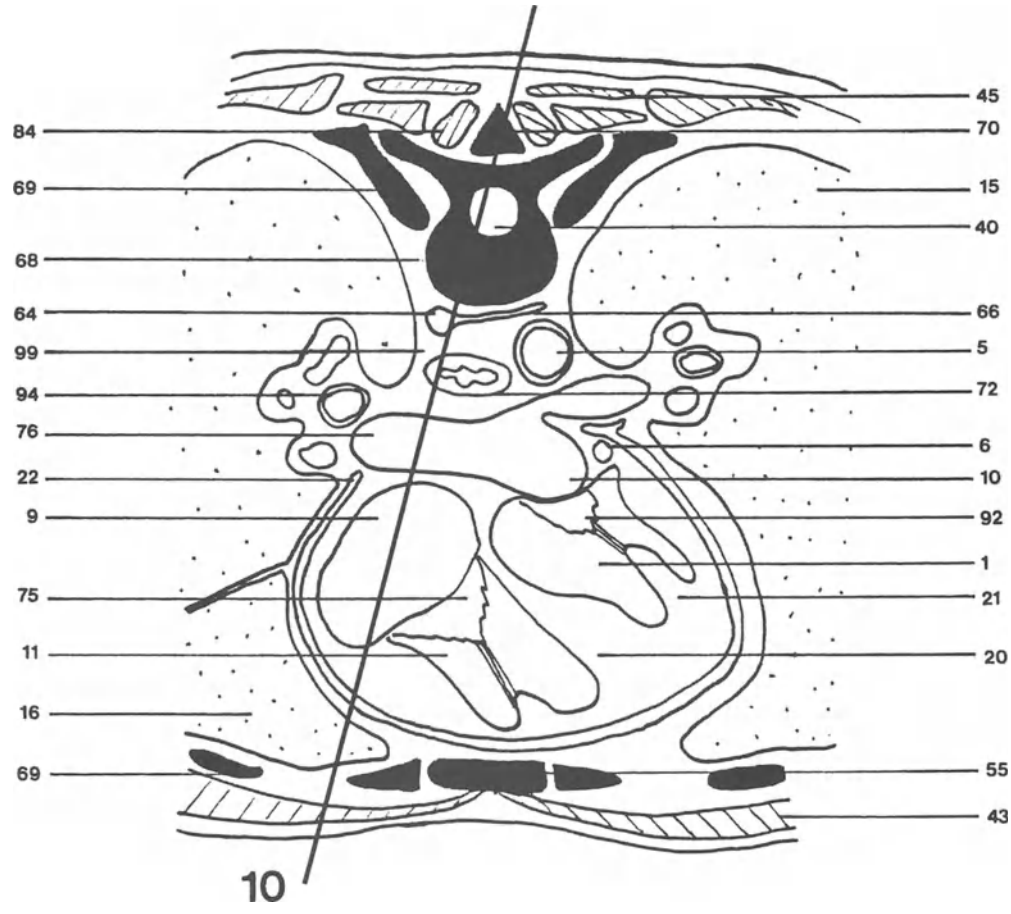

Figure L-22. Plane of section of LAO slice 10.

Slice through the right lateral part of the heart. The opening of the superior vena cava into the right atrium is shown. The left brachiocephalic vein ends at the top of the superior vena cava in a slice perpendicular to this one (see previous images). The right brachiocephalic vein, shorter than the left one, is parallel to this slice. It is formed by the junction of the right subclavian vein and of the right internal jugular vein. The middle of the slice shows the trachea, the esophagus and the initial part of the descending aorta. The right and left lungs are here of the same size. Legends are on the next page.

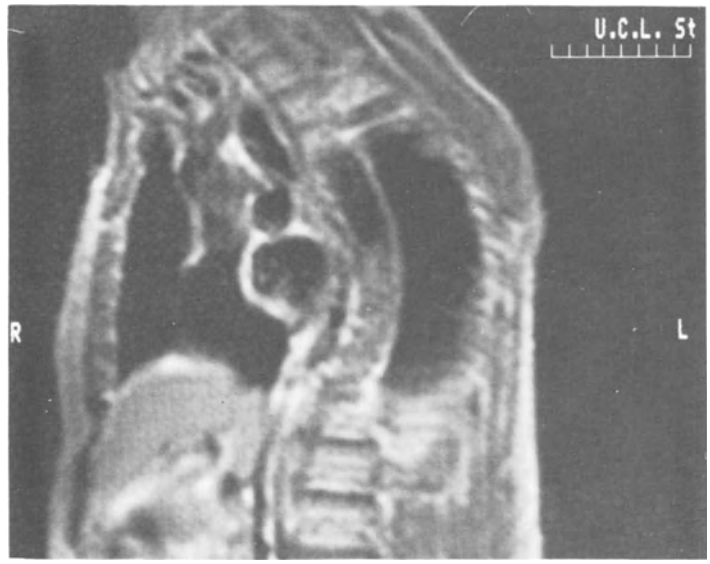

Figure L-23. MR slice.

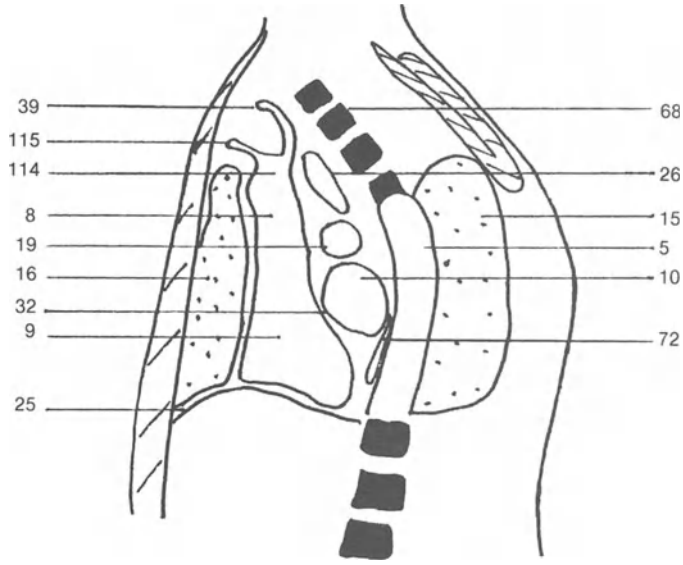

(1) Left ventricular cavity; (5) Descending aorta; (6) Coronary sinus; (8) Superior vena cava; (9) Right atrium; (10) Left atrium; (11) Right ventricular cavity; (15) Left lung; (16) Right lung; (19) Right pulmonary artery; (20) Ventricular septum; (21) Papillary muscle; (22) Pericardium; (25) Diaphragm; (26) Trachea; (32) Atrial septum; (39) Right internal jugular vein; (40) Spinal cord; (43) Pectoralis major muscle; (45) Trapezius muscle; (55) Sternum; (64) Azygos vein; (66) Hemiazygos vein; (68) Dorsal vertebra; (69) Rib; (70) Spinous process; (72) Esophagus; (75) Tricuspid valve; (76) Right inferior pulmonary vein; (84) Transversospinal muscle; (92) Mitral valve; (94) Right main bronchus; (99) Mediastinum; (114) Right brachiocephalic vein; (115) Right subclavian vein.

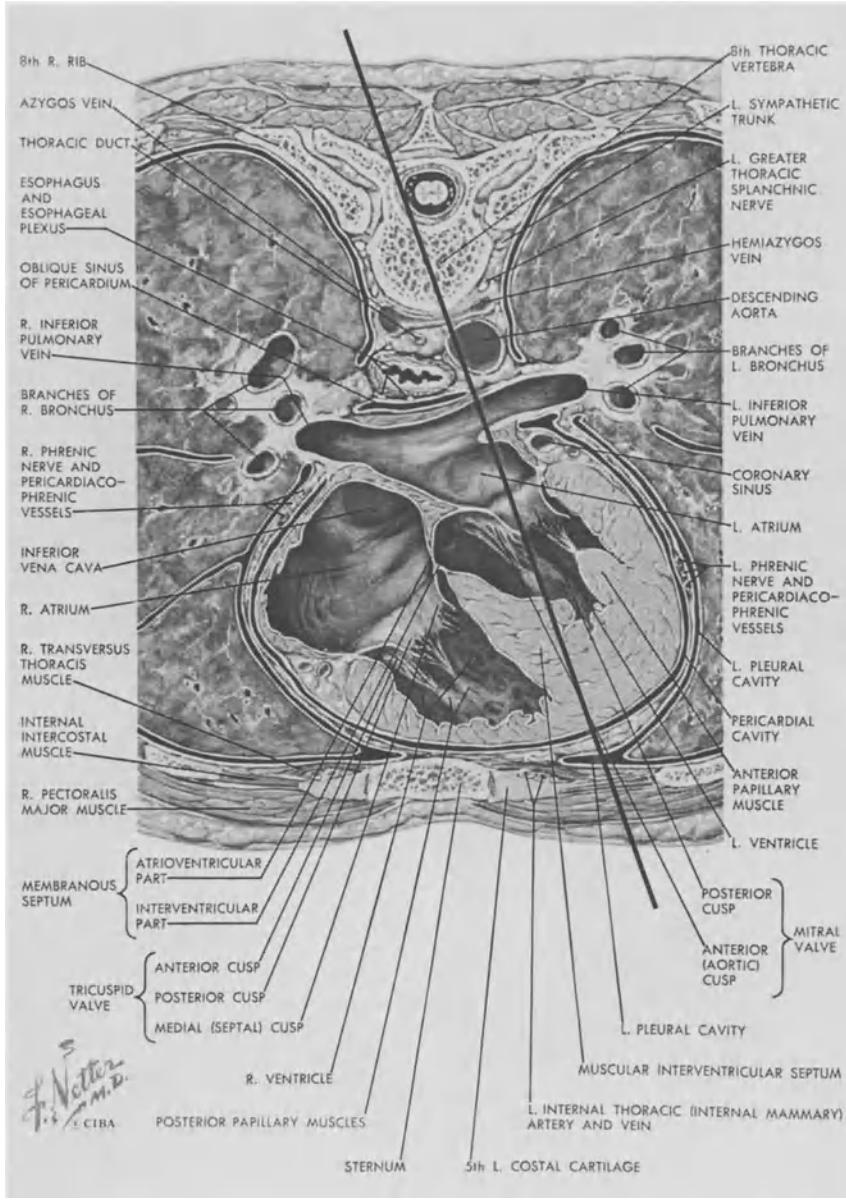

Figure R–0. General plane of section of the RAO slices.

The right anterior oblique (RAO) slices are made as if the observer was on the right anterior part of the patient.

RAO slice 1

Figure R-1. Plane of section of RAO slice 1.

This slice is close to the left lung hilum and its major structures are seen: the left main bronchus, the left pulmonary artery and the left pulmonary veins.
The long axis of the left ventricle is shown and the apex is well seen. The obliquity of the slice increases the true depth of pectoralis major muscle.
Legends are on the next page.

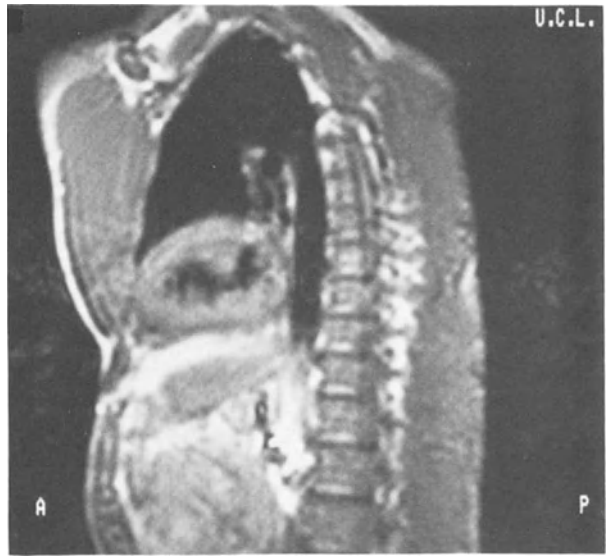

Figure R-2. MR slice.

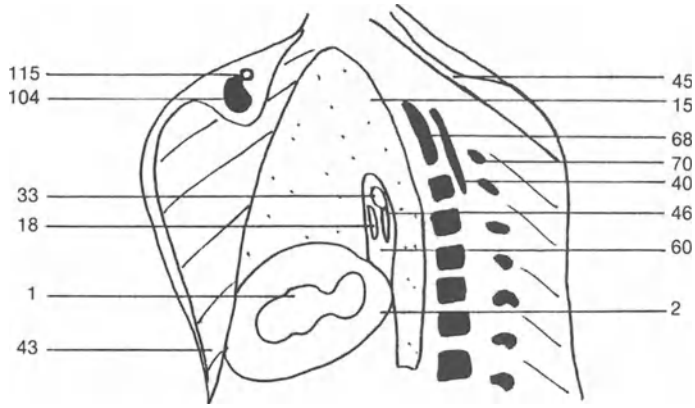

(1) Left ventricular cavity; (2) Myocardium; (5) Descending aorta; (6) Coronary sinus; (9) Right atrium; (10) Left atrium; (11) Right ventricular cavity; (15) Left lung; (16) Right lung; (18) Left pulmonary artery; (20) Ventricular septum; (21) Papillary muscle; (22) Pericardium; (33) Left main bronchus; (40) Spinal cord; (43) Pectoralis major muscle; (45) Trapezius muscle; (46) Left inferior pulmonary vein; (55) Sternum; (60) Left lung hilum; (64) Azygos vein; (66) Hemiazygos vein; (68) Dorsal vertebra; (69) Rib; (70) Spinous process; (72) Esophagus; (75) Tricuspid valve; (76) Right inferior pulmonary vein; (84) Transversospinal muscle; (92) Mitral valve; (94) Right main bronchus; (99) Mediastinum; (104) Clavicle; (115) Right subclavian vein.

RAO slice 2

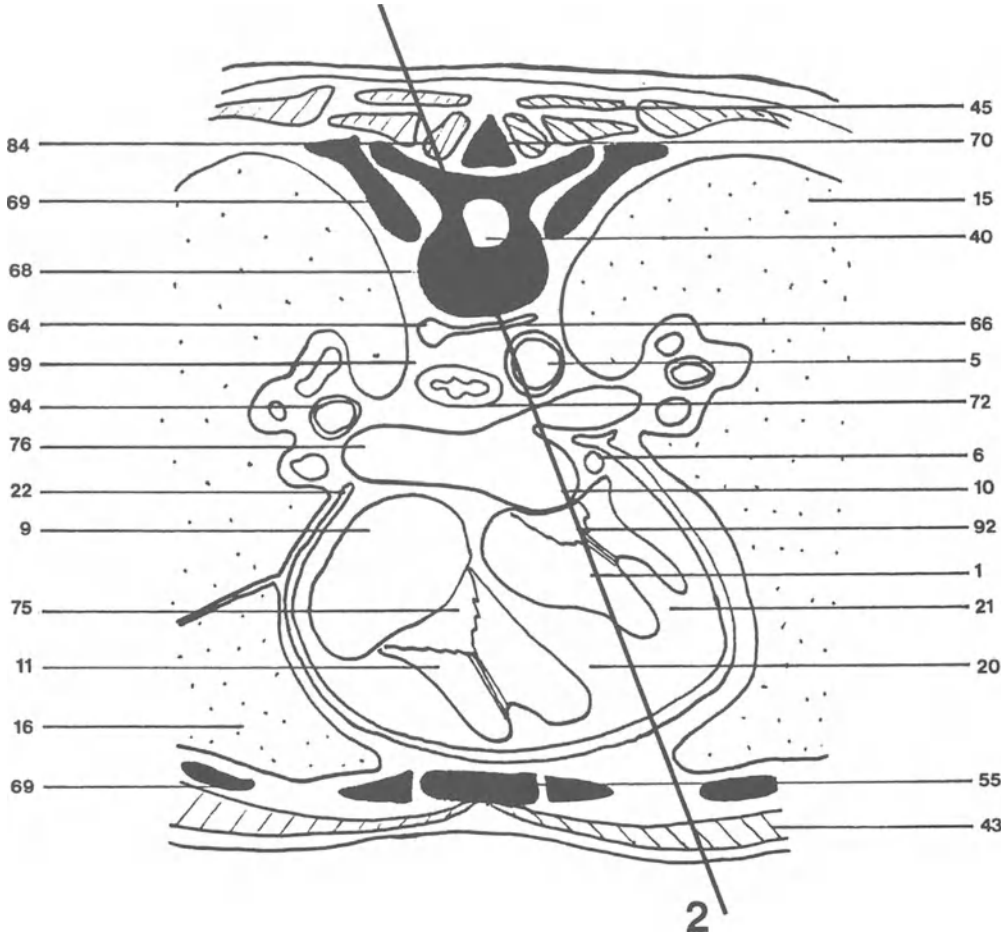

Figure R-3. Plane of section of RAO slice 2.

Slice through the middle of the left ventricular cavity. The walls are thus thinner than on the previous slice. The beginning of the left atrium, behind the left ventricle, is seen.

The aorta becomes visible, i.e., the aortic arch and the descending aorta.

Legends are on the next page.

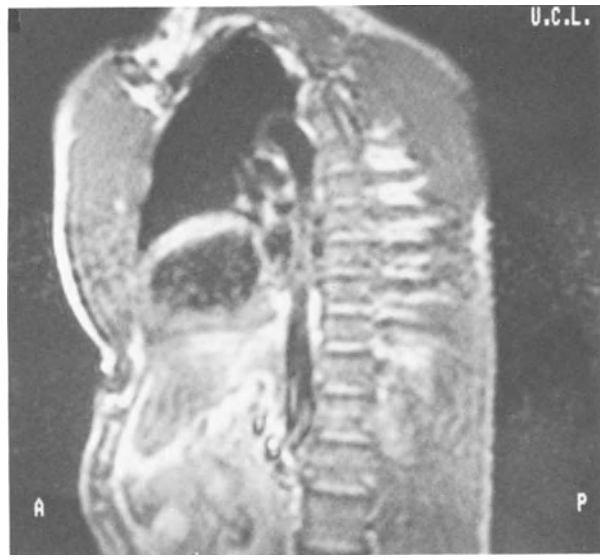

Figure R-4. MR slice.

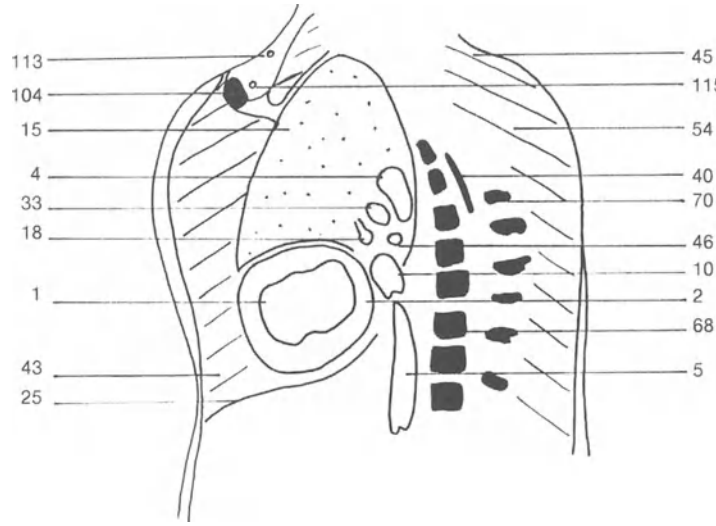

(1) Left ventricular cavity; (2) Myocardium; (4) Aortic arch; (5) Descending aorta; (6) Coronary sinus; (9) Right atrium; (10) Left atrium; (11) Right ventricular cavity; (15) Left lung; (16) Right lung; (18) Left pulmonary artery; (20) Ventricular septum; (21) Papillary muscle; (22) Pericardium; (25) Diaphragm; (33) Left main bronchus; (40) Spinal cord; (43) Pectoralis major muscle; (45) Trapezius muscle; (46) Left inferior pulmonary vein; (54) Rhomboidus muscle; (55) Sternum; (64) Azygos vein; (66) Hemiazygos vein; (68) Dorsal vertebra; (69) Rib; (70) Spinous process; (72) Esophagus; (75) Tricuspid valve; (76) Right inferior pulmonary vein; (84) Transversospinal muscle; (92) Mitral valve; (94) Right main bronchus; (99) Mediastinum; (104) Clavicle; (113) Right subclavian artery; (115) Right subclavian vein.

RAO slice 3

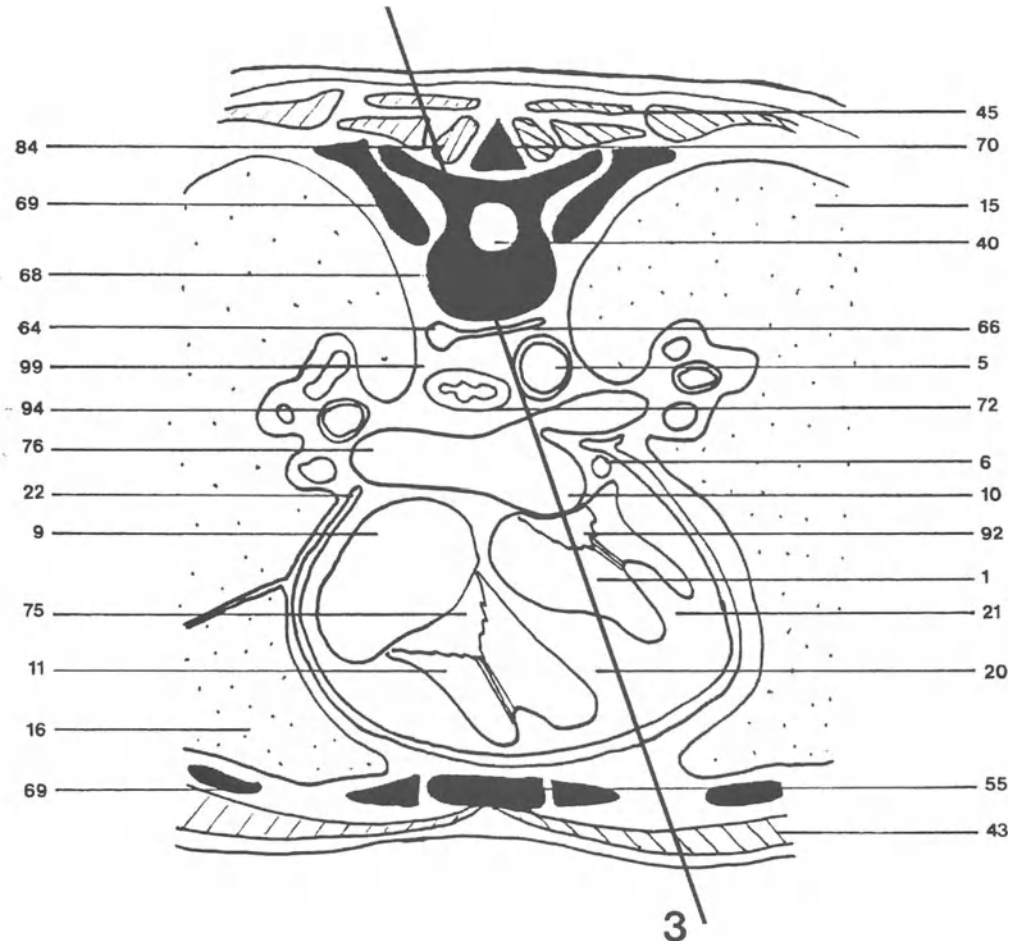

Figure R–5. Plane of section of RAO slice 3.

Slice through the mitral valve. The left lung hilum and, superiorly, the aortic arch are seen. The left lung becomes smaller and the right lung is seen. Legends are on the next page.

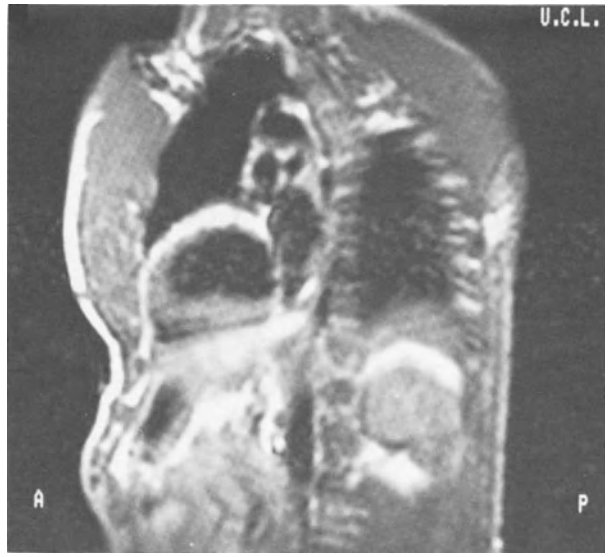

Figure R–6. MR slice.

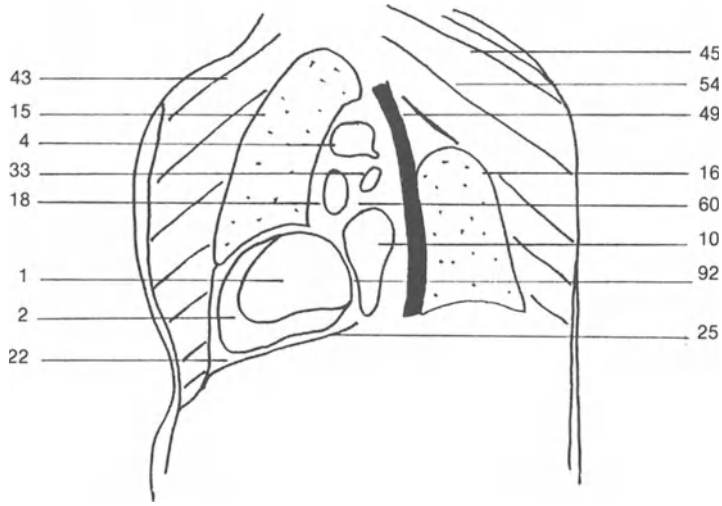

(1) Left ventricular cavity; (2) Myocardium; (4) Aortic arch; (5) Descending aorta; (6) Coronary sinus; (9) Right atrium; (10) Left atrium; (11) Right ventricular cavity; (15) Left lung; (16) Right lung; (18) Left pulmonary artery; (20) Ventricular septum; (21) Papillary muscle; (22) Pericardium; (25) Diaphragm; (33) Left main bronchus; (40) Spinal cord; (43) Pectoralis major muscle; (49) Rachis; (54) Rhomboidus muscle; (55) Sternum; (60) Left lung hilum; (64) Azygos vein; (66) Hemiazygos vein; (68) Dorsal vertebra; (69) Rib; (70) Spinous process; (72) Esophagus; (75) Tricuspid valve; (76) Right inferior pulmonary vein; (84) Transversospinal muscle; (92) Mitral valve; (94) Right main bronchus; (99) Mediastinum.

RAO slice 4

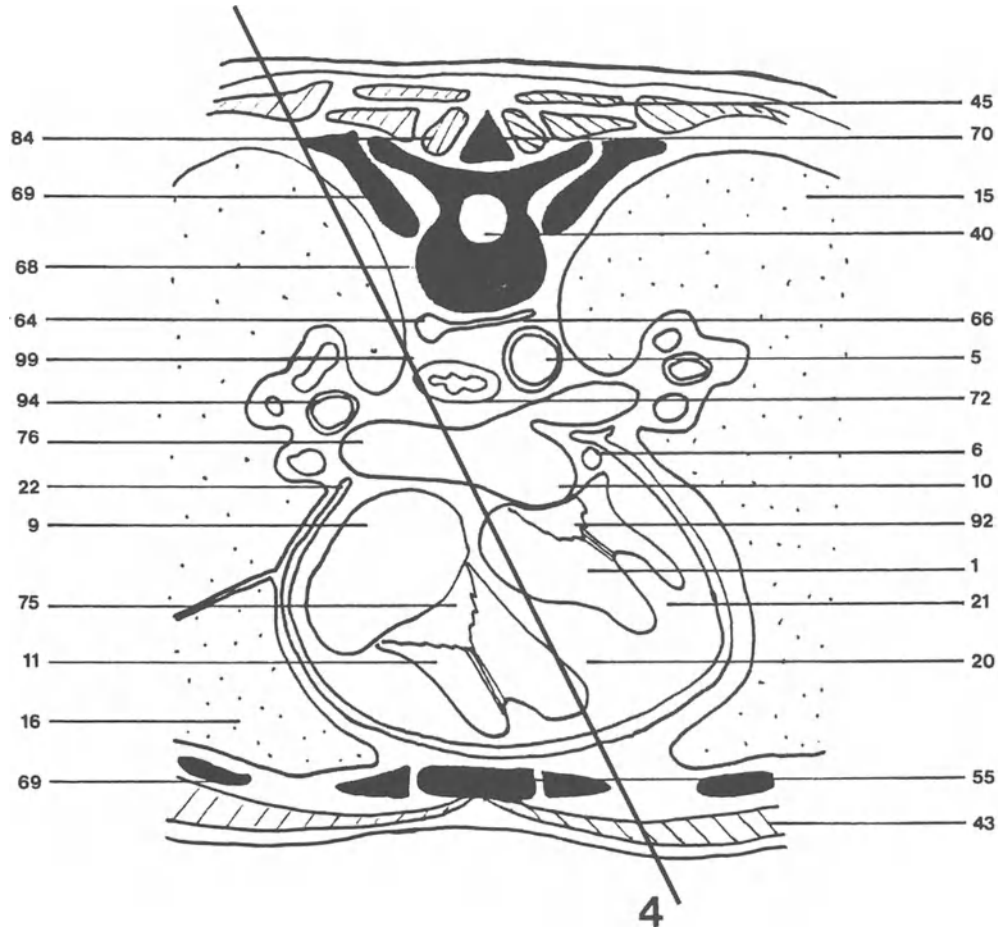

Figure R–7. Plane of section of RAO slice 4.

The slice is tangent to the ventricular septum which seems to be thick. The left ventricular cavity volume decreases and only a small part of the aorta is still seen. Legends are on the next page.

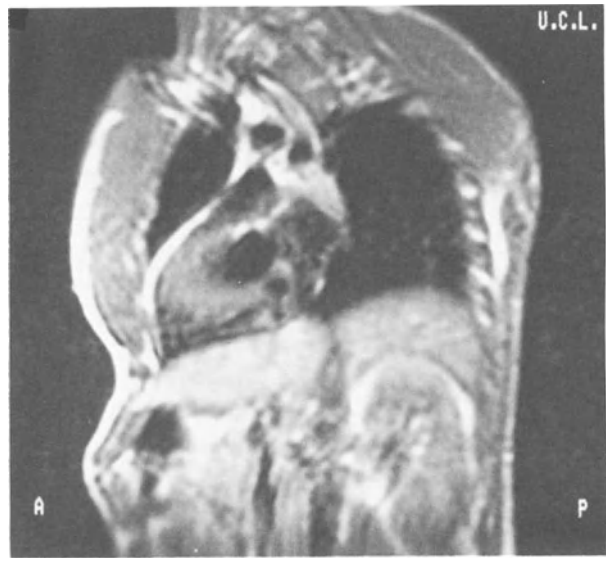

Figure R-8. MR slice.

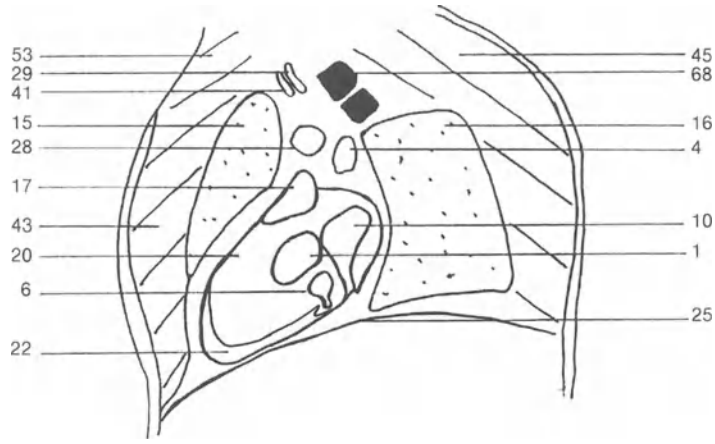

(1) Left ventricular cavity; (4) Aortic arch; (5) Descending aorta; (6) Coronary sinus; (9) Right atrium; (10) Left atrium; (11) Right ventricular cavity; (15) Left lung; (16) Right lung; (17) Main pulmonary artery; (20) Ventricular septum; (21) Papillary muscle; (22) Pericardium; (25) Diaphragm; (28) Left brachiocephalic vein; (29) Left common carotid artery; (40) Spinal cord; (41) Left internal jugular vein; (43) Pectoralis major muscle; (45) Trapezius muscle; (53) Sternocleidomastoid muscle; (55) Sternum; (64) Azygos vein; (66) Hemiazygos vein; (68) Dorsal vertebra; (69) Rib; (70) Spinous process; (72) Esophagus; (75) Tricuspid valve; (76) Right inferior pulmonary vein; (84) Transversospinal muscle; (92) Mitral valve; (94) Right main bronchus; (99) Mediastinum.

RAO slice 5

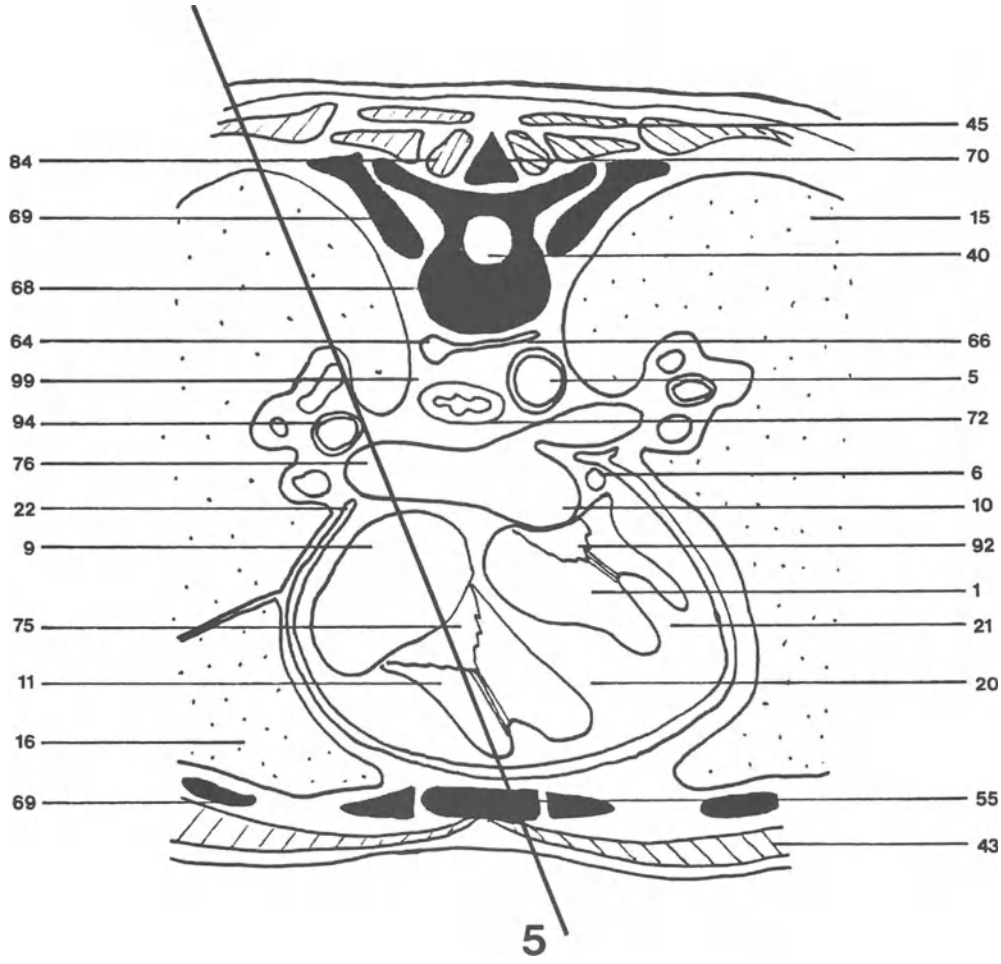

Figure R–9. Plane of section of RAO slice 5.

This slice shows the right ventricle and the beginning of the main pulmonary artery. The right atrium appears behind the right ventricle and the superior vena cava opens into the right atrium. The left atrium becomes very small.

The trachea and the right main bronchus are seen. The right main bronchus accompanies the right pulmonary vessels in the right lung.
The left lung is very small.
Legends are on the next page.

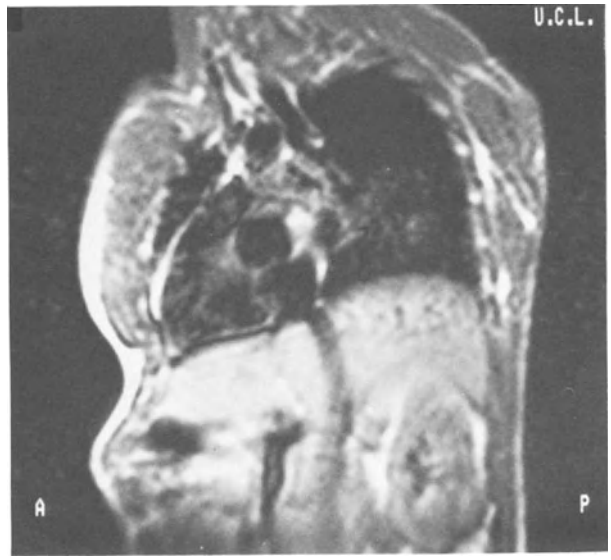

Figure R-10. MR slice.

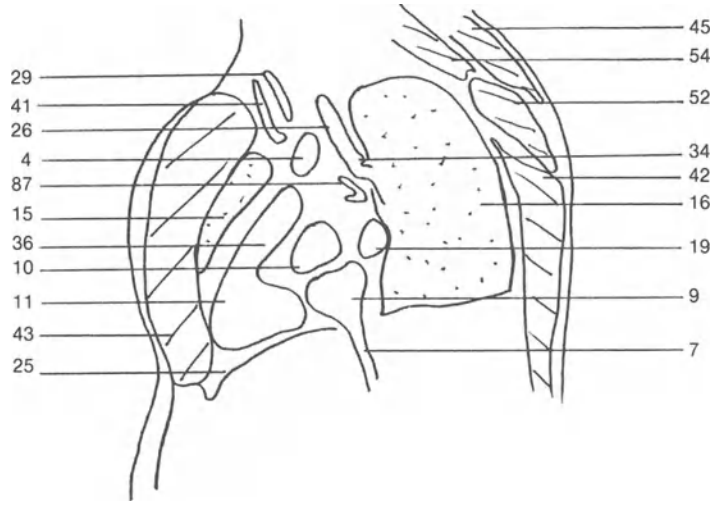

(1) Left ventricular cavity; (5) Descending aorta; (6) Coronary sinus; (7) Inferior vena cava; (9) Right atrium; (10) Left atrium; (11) Right ventricular cavity; (15) Left lung; (16) Right lung; (19) Right pulmonary artery; (20) Ventricular septum; (21) Papillary muscle; (22) Pericardium; (25) Diaphragm; (26) Trachea; (29) Left common carotid artery; (36) Pulmonary infundibulum; (40) Spinal cord; (41) Left internal jugular vein; (42) Latissimus dorsi muscle; (43) Pectoralis major muscle; (45) Trapezius muscle; (52) Erector spinae muscle; (54) Rhomboidus muscle; (55) Sternum; (64) Azygos vein; (66) Hemiazygos vein; (68) Dorsal vertebra; (69) Rib; (70) Spinous process; (72) Esophagus; (75) Tricuspid valve; (76) Right inferior pulmonary vein; (84) Transversospinal muscle; (87) Right superior pulmonary vein; (92) Mitral valve; (94) Right main bronchus; (99) Mediastinum.

RAO slice 6

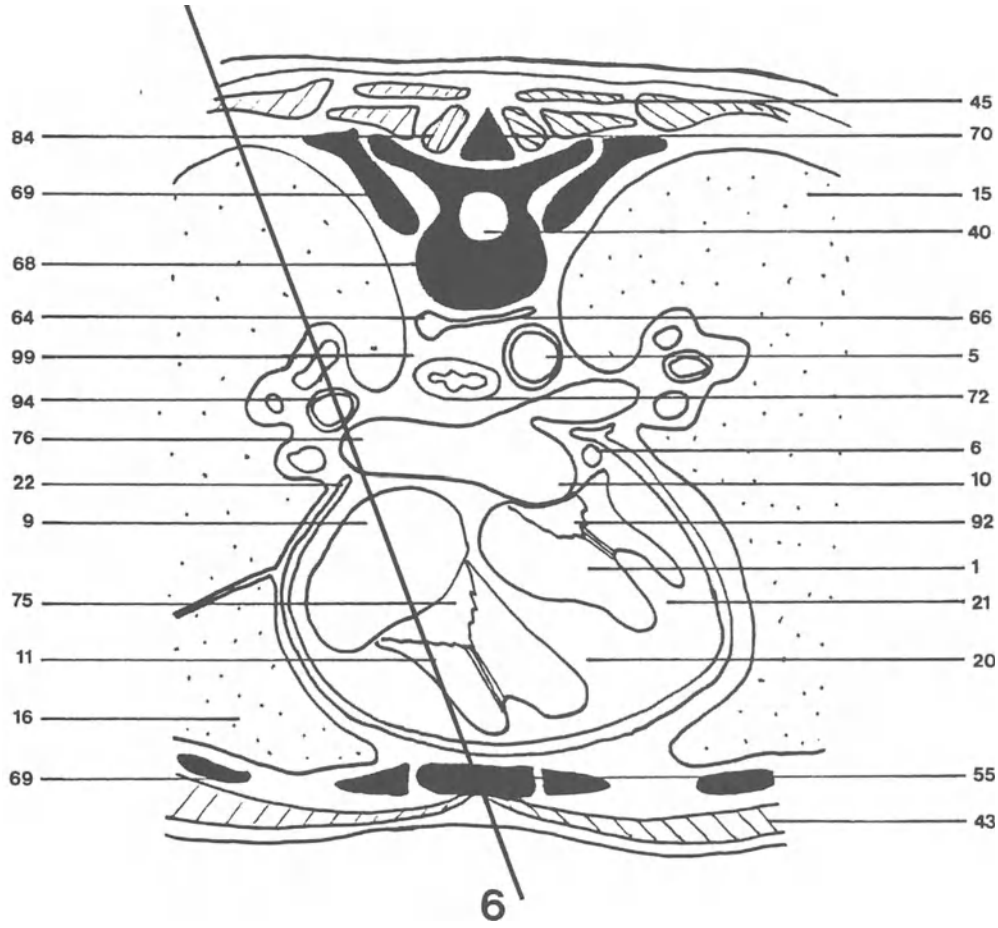

Figure R-11. Plane of section of RAO slice 6.

The obliquity of this slice allows us to see, respectively from behind, the superior vena cava, the ascending aorta, the right atrium and the left ventricle. The vena cava is situated on the right of the ascending aorta and the two vessels are well seen only on this kind of slice.

Also this slice shows that the inflow tract of the right ventricle is nearly perpendicular to the right ventricular outflow region, while these two chambers are nearly parallel in the left ventricle, as shown on the previous images.

Legends are on the next page.

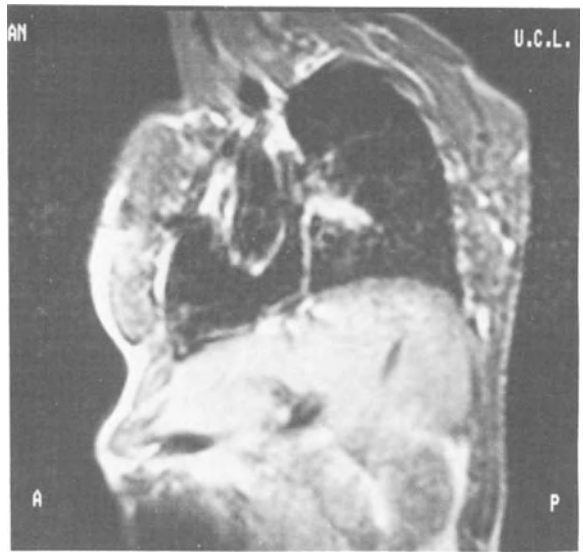

Figure R–12. MR slice.

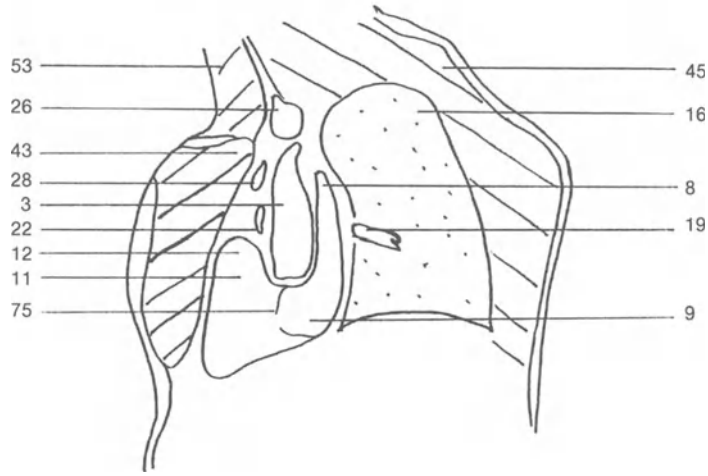

(1) Left ventricular cavity; (3) Ascending aorta; (5) Descending aorta; (6) Coronary sinus; (8) Superior vena cava; (9) Right atrium; (10) Left atrium; (11) Right ventricular cavity; (12) Right ventricular outflow region; (15) Left lung; (16) Right lung; (19) Right pulmonary artery; (20) Ventricular septum; (21) Papillary muscle; (22) Pericardium; (26) Trachea; (28) Left brachiocephalic vein; (40) Spinal cord; (43) Pectoralis major muscle; (45) Trapezius muscle; (53) Sternocleidomastoid muscle; (55) Sternum; (64) Azygos vein; (66) Hemiazygos vein; (68) Dorsal vertebra; (69) Rib; (70) Spinous process; (72) Esophagus; (75) Tricuspid valve; (76) Right inferior pulmonary vein; (84) Transversospinal muscle; (92) Mitral valve; (94) Right main bronchus; (99) Mediastinum.

CHAPTER TWO

Dynamic and functional studies

Long axis views
Short axis views
Double angulation views
End systole and end diastole

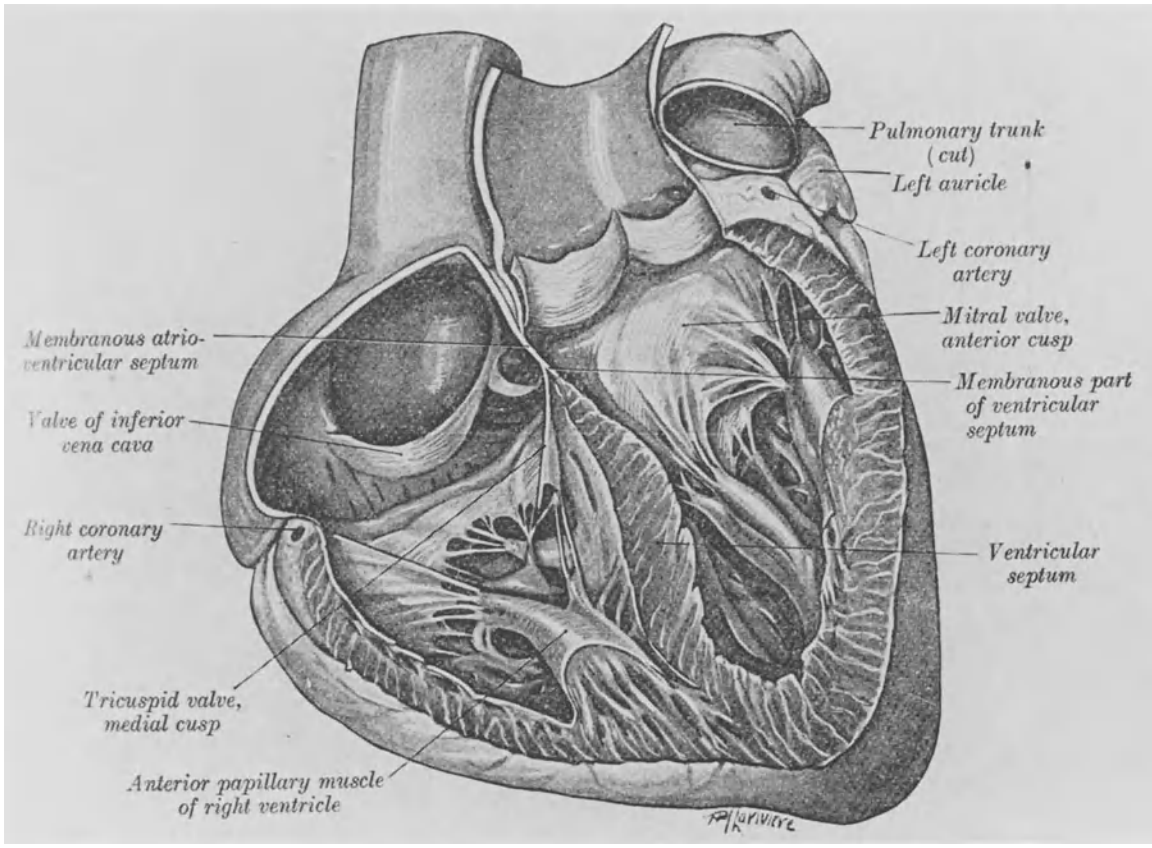

This Cine MR imaging study is situated at the level of the left ventricle and the left atrium. The images are divided into 12 separate frames and illustrate the different phases of the ventricular contraction and filling. The chamber blood has a high signal intensity. The relaxed ventricle is first filled by the atrium (images 1 and 2). When the increase of ventricular pressure makes this filling more difficult, the atrium contracts (image 3).

After this contraction, the mitral valve closes (images 4 and 5) while the left ventricle contracts. The left ventricular volume is smallest at end systole (images 6 and 7). The left atrium fills progressively (images 8 and 9) while the left ventricle relaxes. These two phenomena make the mitral valve protrude into the ventricle (images 10 and 11). This valve then opens (image 12) and the left atrium can again fill the left ventricle (image 1).

Long axis views

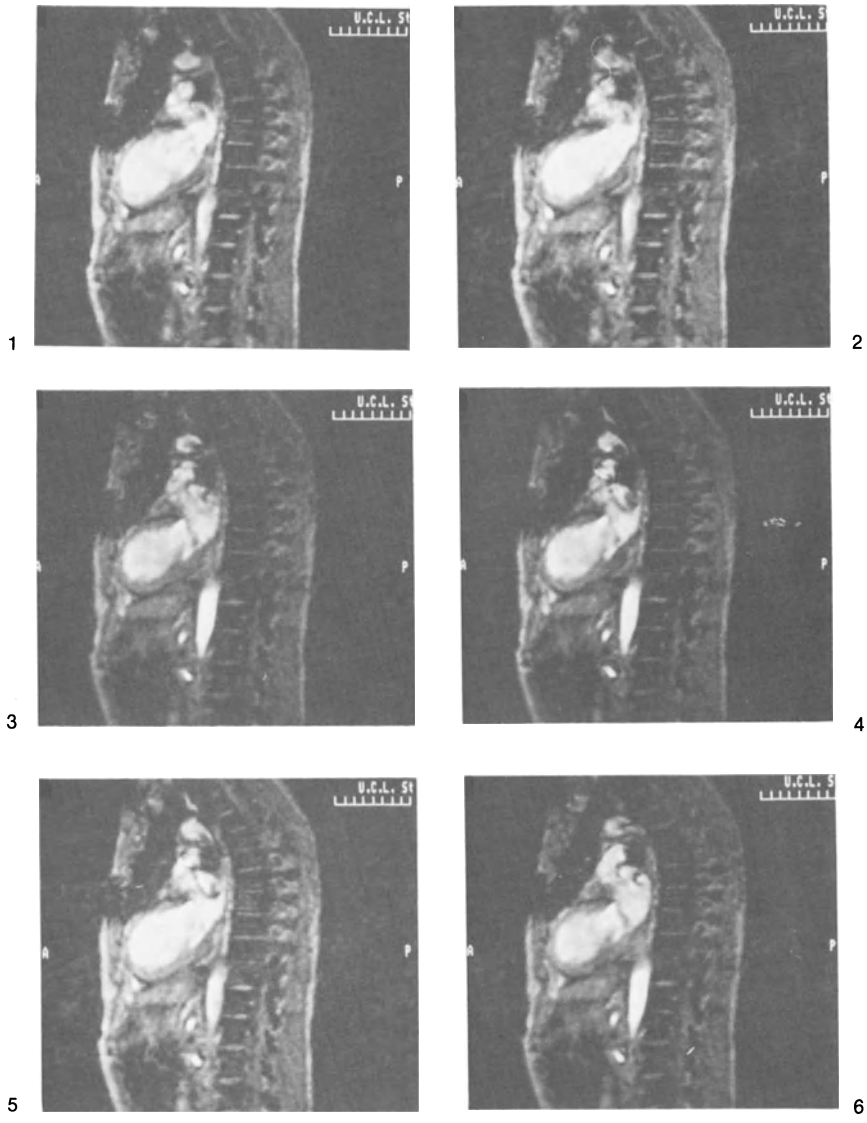

Figure D–1. Images 1–6.

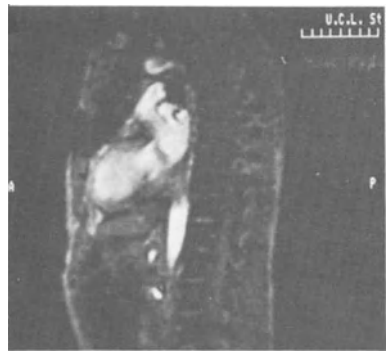

7

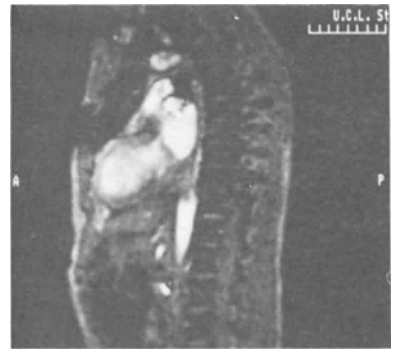

8

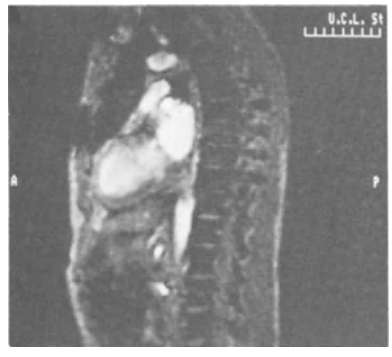

9

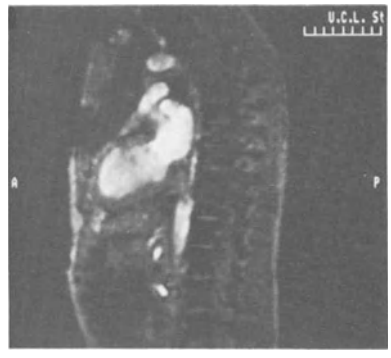

10

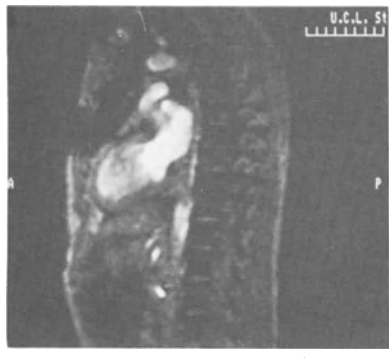

11

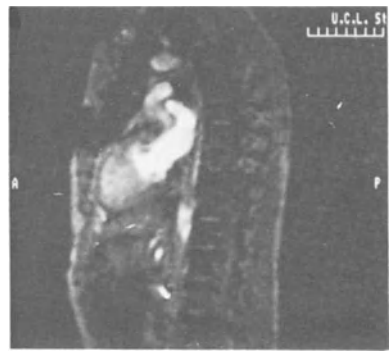

12

Figure D–1. Images 7–12.

Long axis views

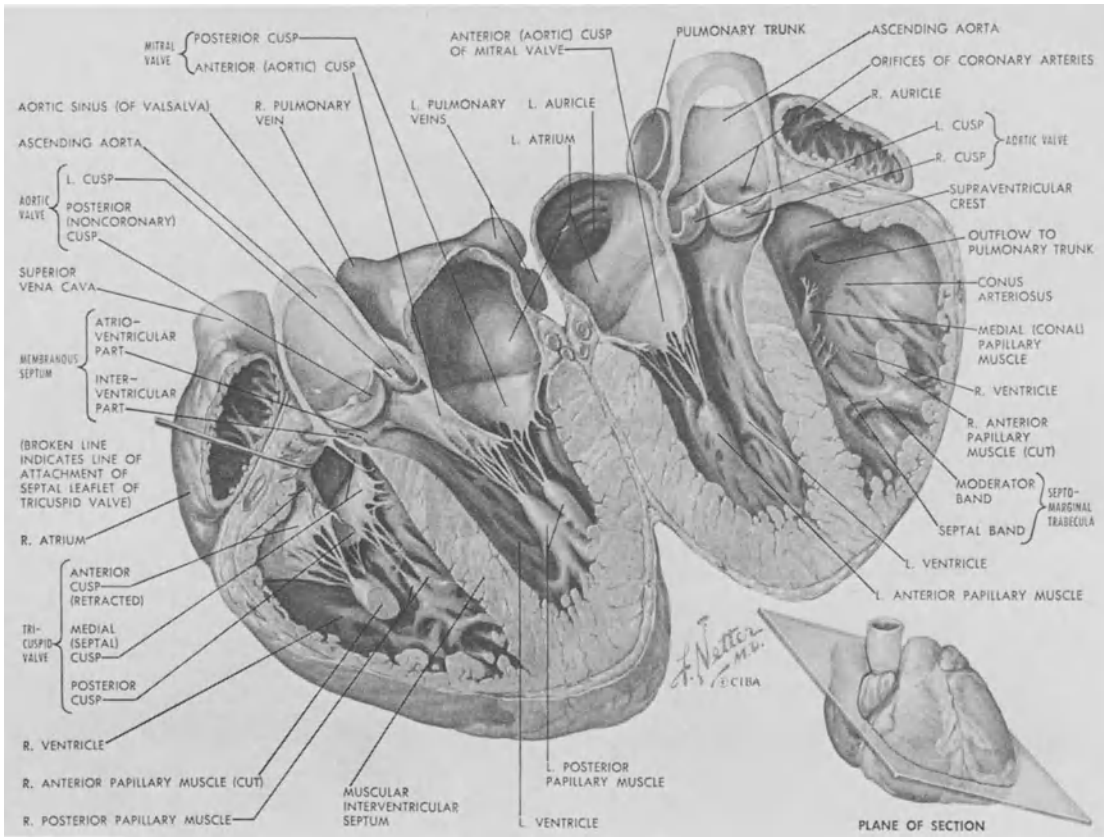

This slice illustrates the thickening of the left ventricular wall during systole in a patient with left ventricular hypertrophy. The left ventricle is relaxed in image 1 and progressively thickens until the end of systole (image 6).

The left atrium is not seen very well on these images; the aortic flow is shown by the high signal intensity (images 4 to 6).

The transverse images of the same patient are shown in Figure D–6 (p. 195).

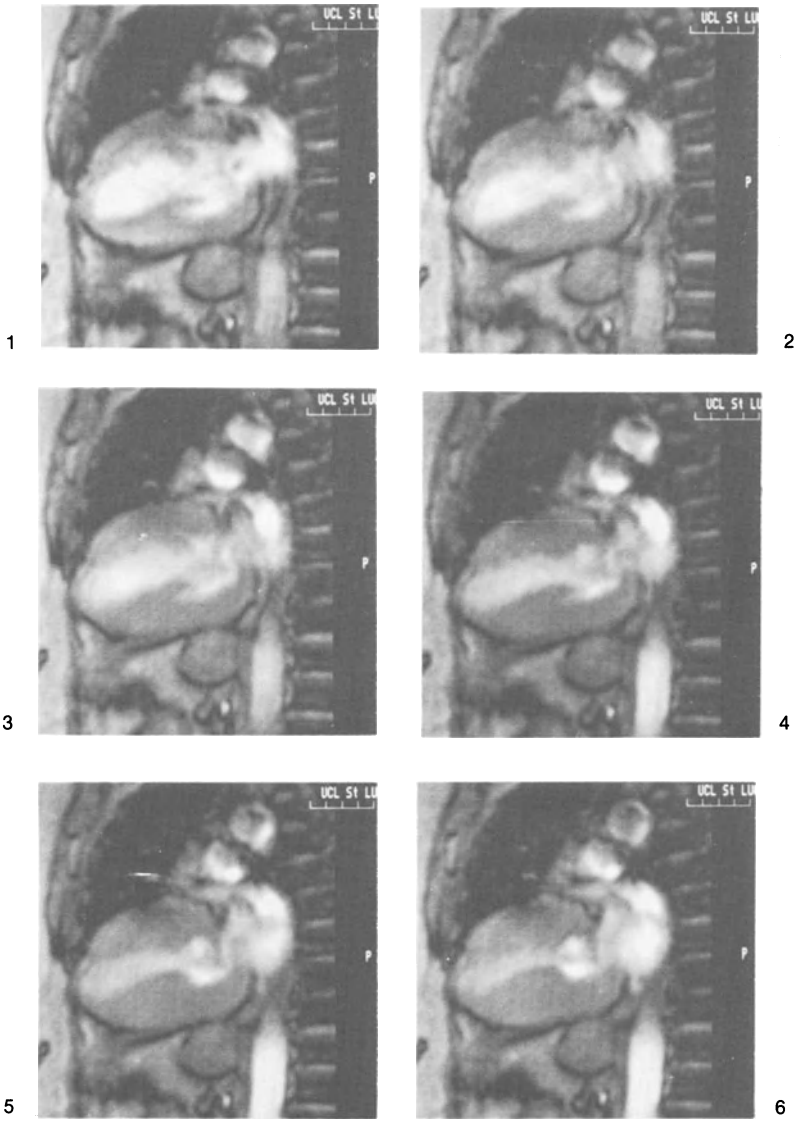

Figure D–2. Images 1–6.

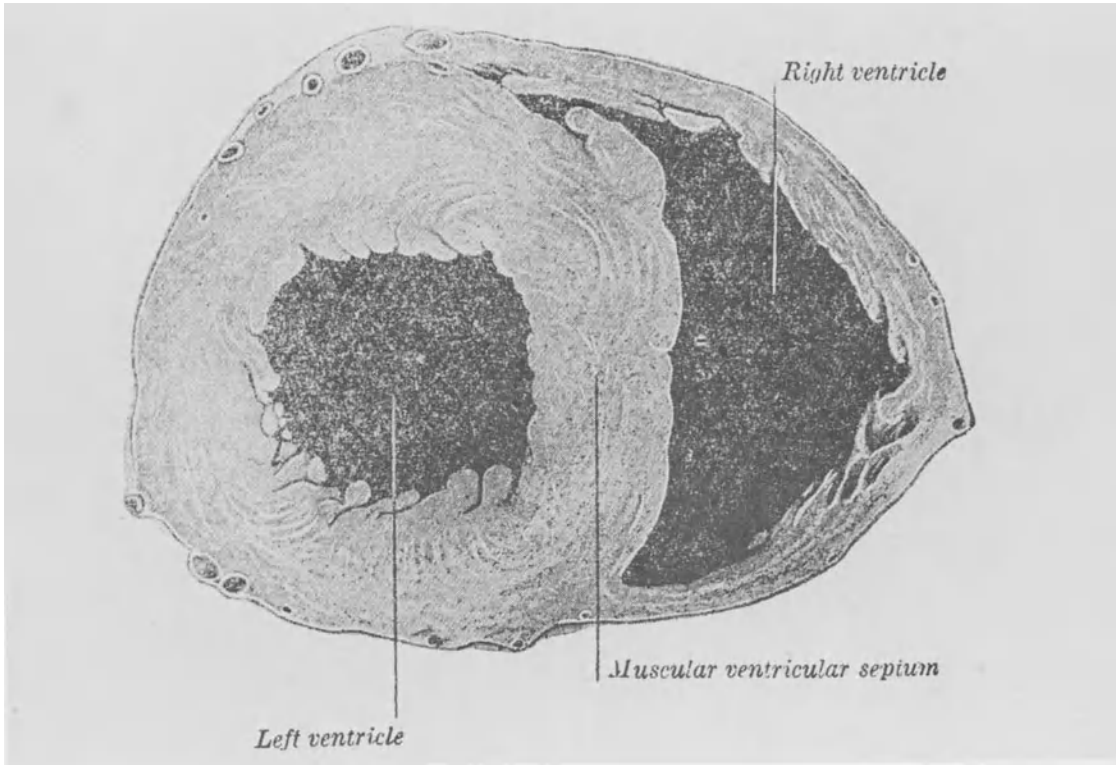

Short axis views of right and left ventricles. The axis is perpendicular to the long axis shown on the previous slices (Fig. D1 and D2).

The myocardial wall systolic thickening and the papillary muscles can be seen.

The right ventricle is elongated and situated in front of the spherical left ventricle.

The end systole occurs at image 6.

Remember that anatomical slices, as the slice shown on this page, are not inverted, at the opposite of the MR slices. The left ventricle is on the left part of this slice, though it is situated on the right side of the MR images.

Short axis views

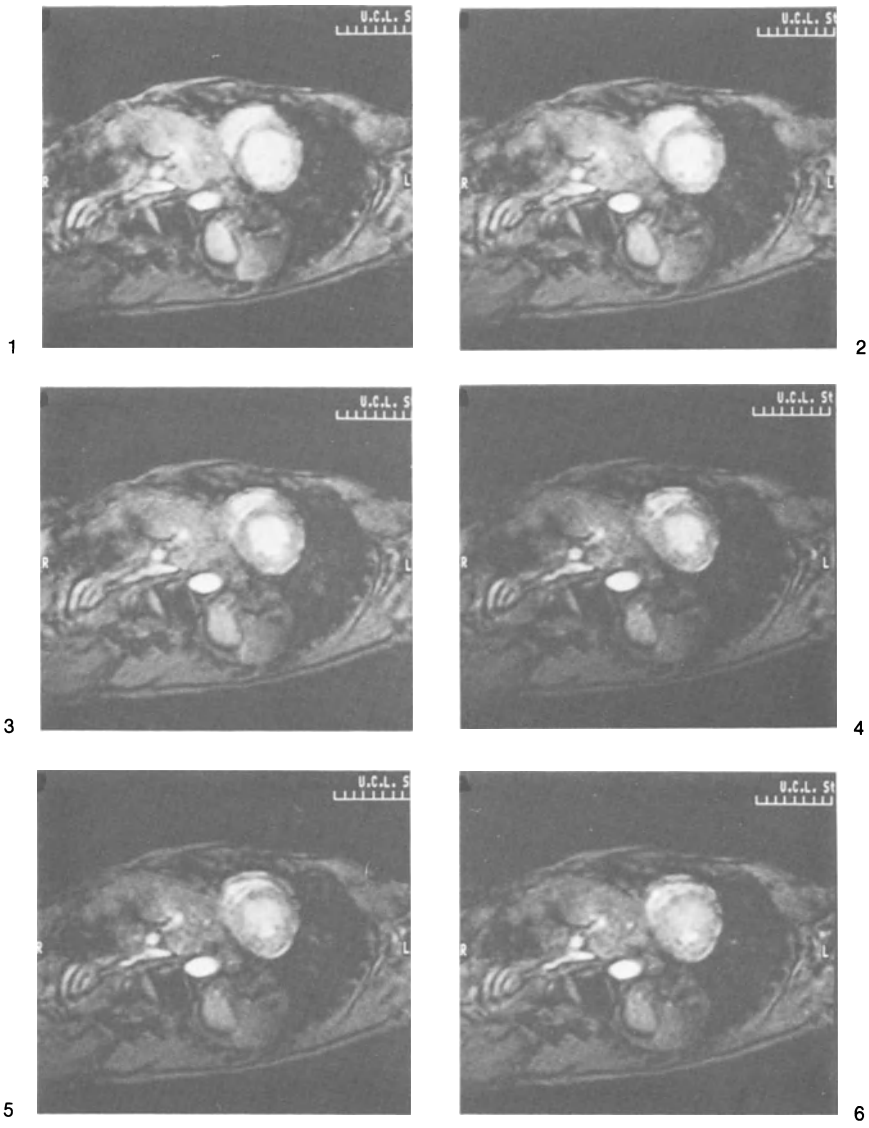

Figure D–3. Images 1–6.

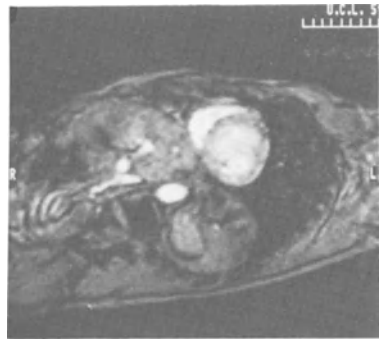
7

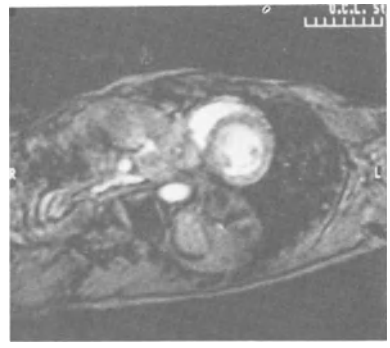
8

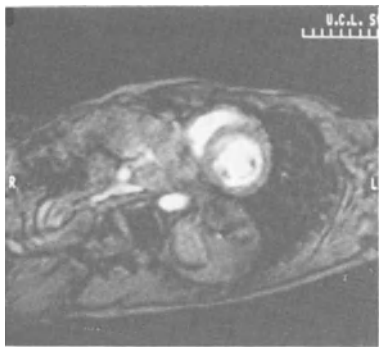
9


10


11

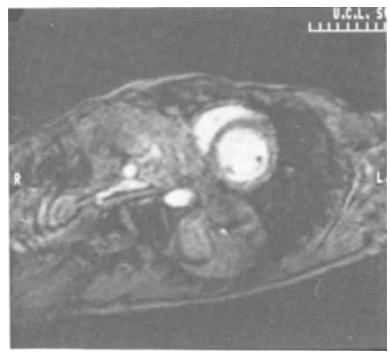
12

Figure D–3. Images 7–12.

Short axis views

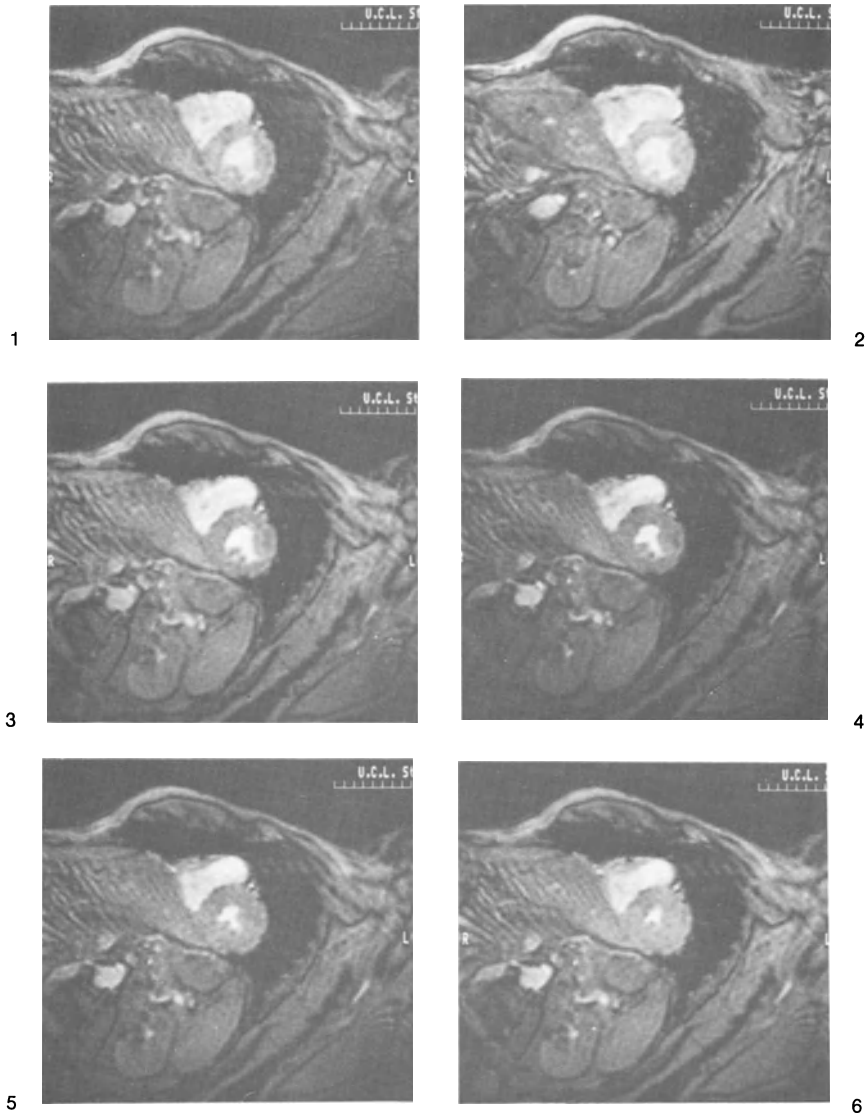

Figure D–4. Images 1–6.

Short axis views of right and left ventricles at a superior level of the same patient as on Figure D–3.

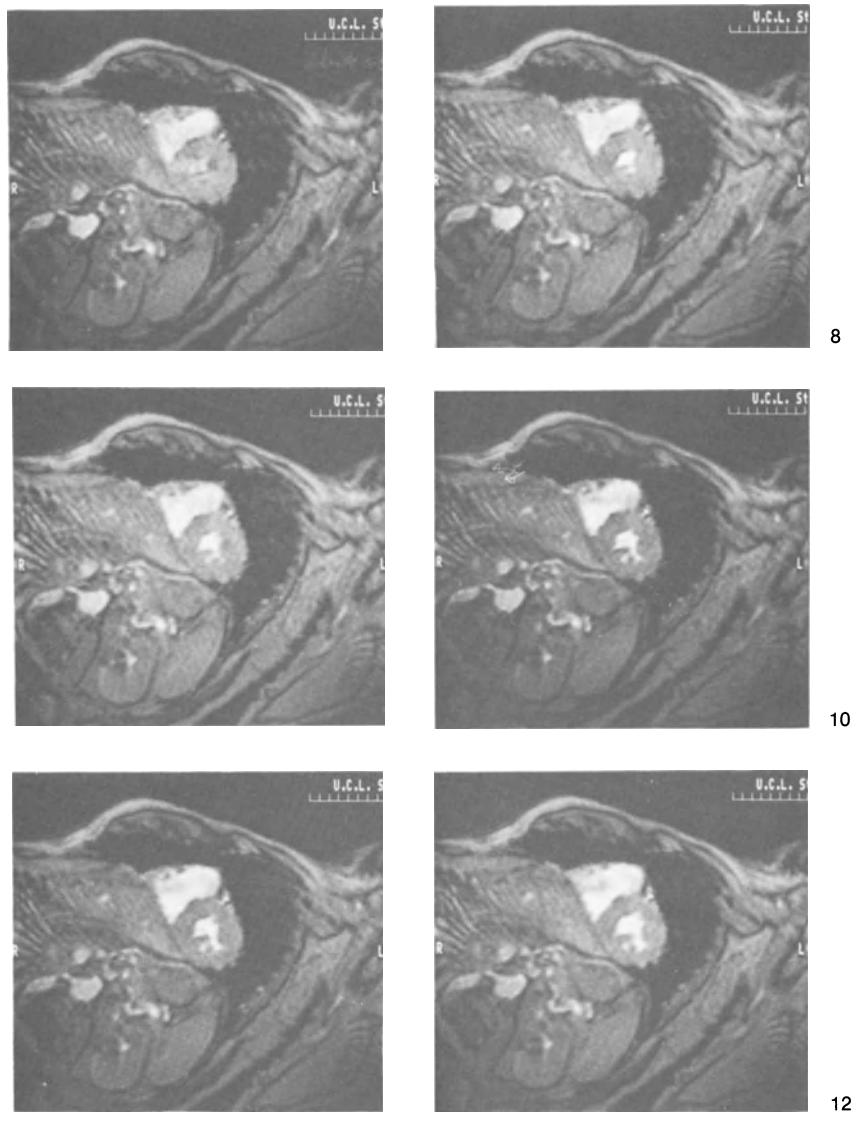

Figure D–4. Images 7–12.

Short axis views

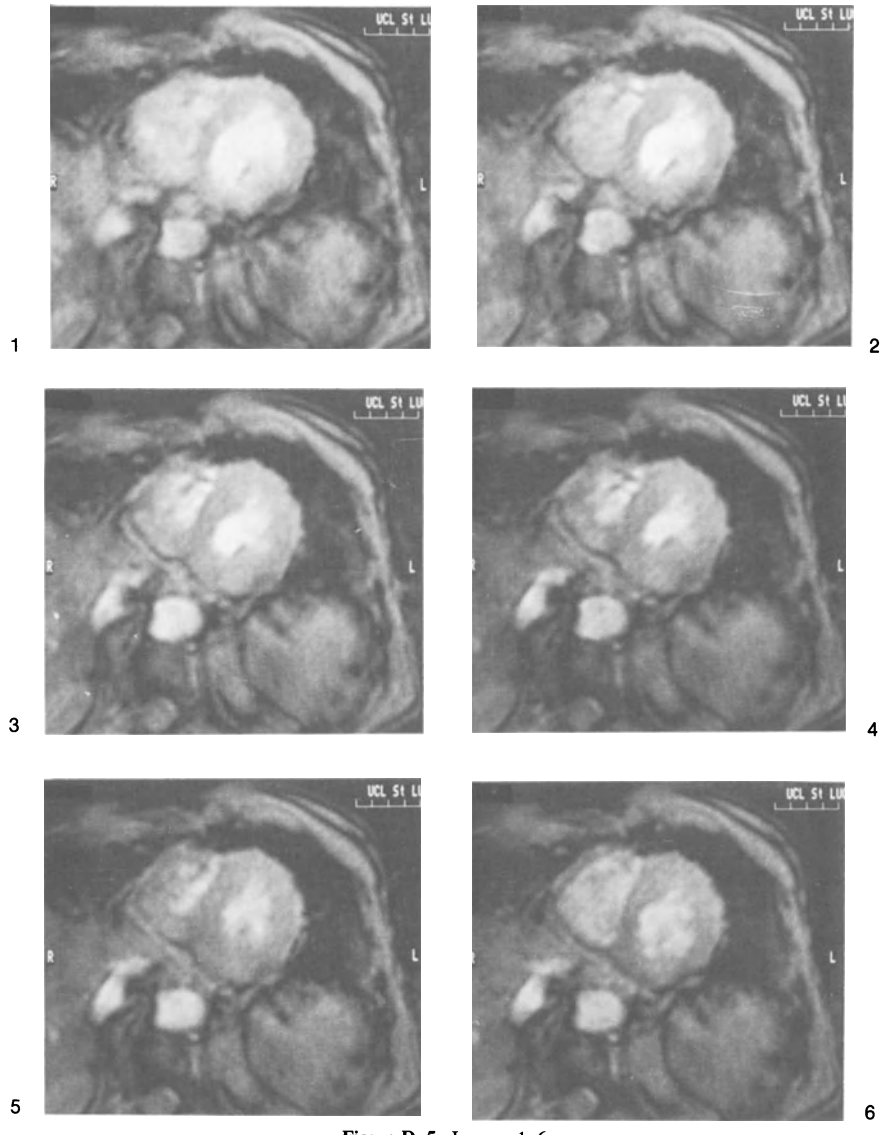

Figure D-5. Images 1–6.

Short axis views of right and left ventricles. The end-diastolic image with thinner walls is on the upper left panel and the end systolic image with thicker wall is on the lower right panel.

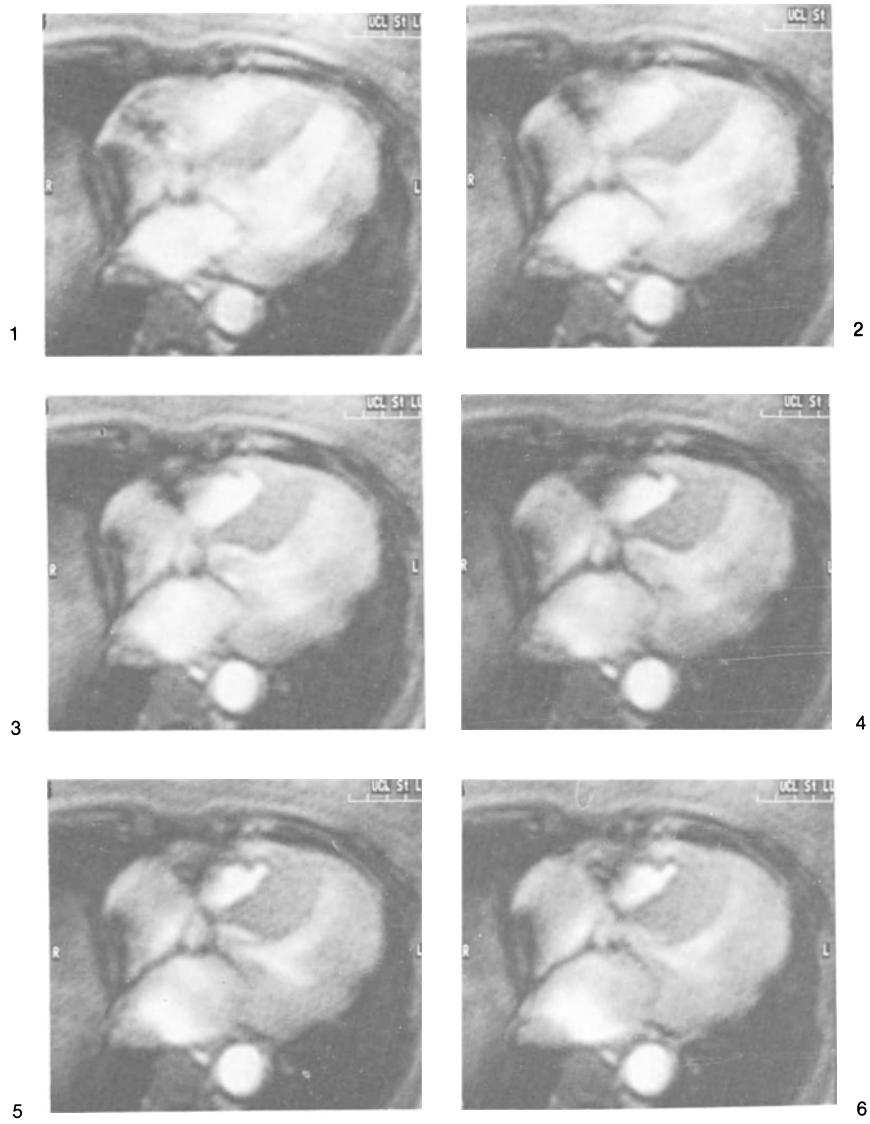

Figure D–6. Images 1–6.

Transverse images through the four cardiac cavities. The end dialostic image is on the upper left panel and the end systolic image is on the lower right panel. The left ventricle is hypertrophied. This patient is the same as in Figure D–2.

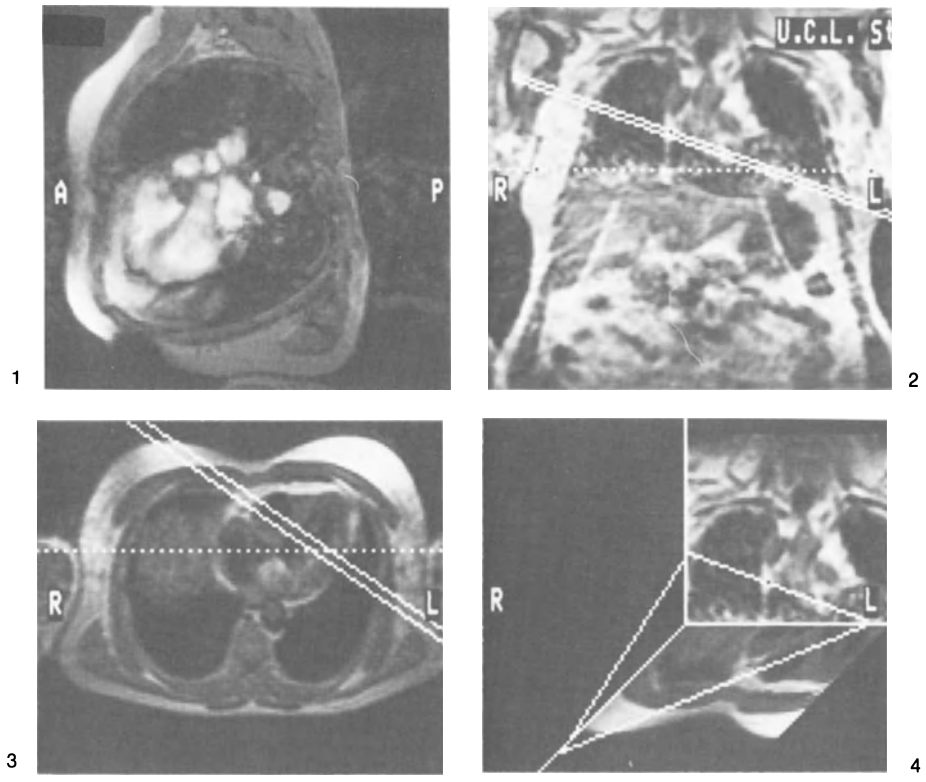

Figure DA–1.

Imaging section (upper left panel) resulting from a double angulation procedure. The spatial orientation of the heart is defined using a coronal and a transversal scan. The coronal angulation is directed to the left ventricle and the aortic infundibulum (upper right panel). The transversal angulation follows the short axis of the heart (lower left panel). The upper left panel resulting image shows the left ventricle and the aorta.

The schematics of the upper left panel is drawn.
The lower right panel shows the planes of section of the two angulations.

(1) Left ventricular cavity;
(5) Descending aorta;
(10) Left atrium;
(11) Right ventricular cavity;
(31) Aortic infundibulum.

Double angulation views

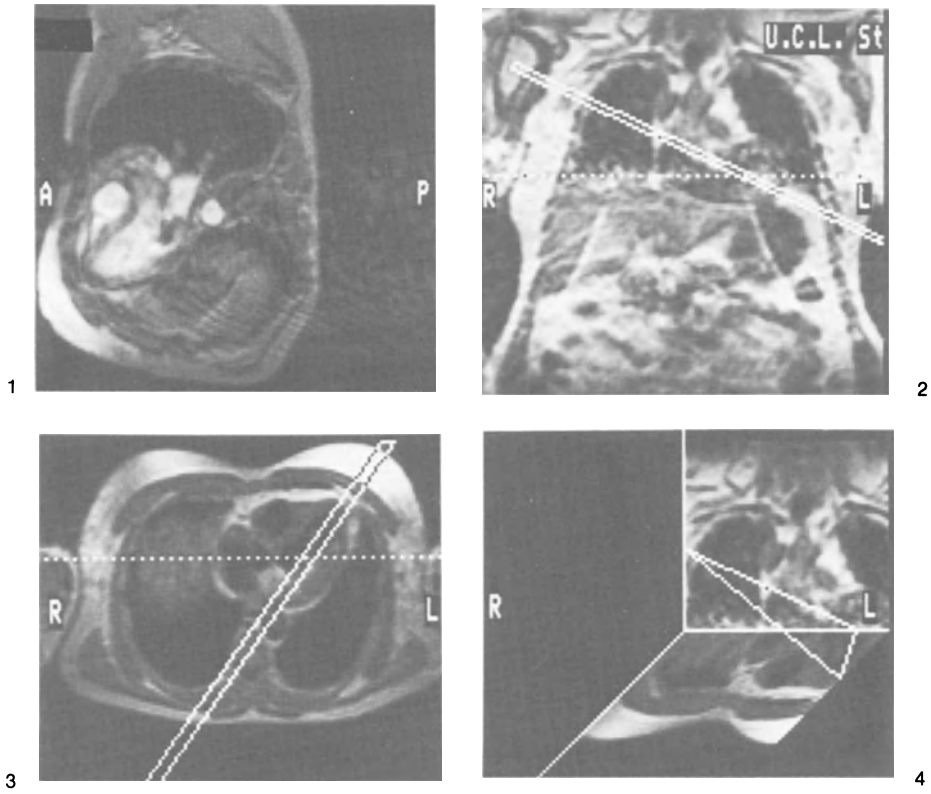

Figure DA-2.

Imaging section (upper left panel) resulting from a double angulation procedure. The coronal angulation is the same as on Figure DA-1.
The transversal angulation follows the long axis of the heart (lower left panel). The upper left panel resulting image shows the left atrium, the left ventricle and the aortic infundibulum.

The schematics of the upper left panel is drawn.
The lower right panel shows the planes of section of the two angulations.

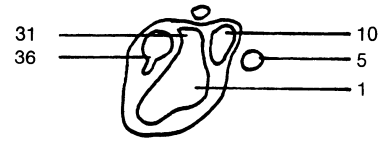

(1) Left ventricular cavity;
(5) Descending aorta;
(10) Left atrium;
(31) Aortic infundibulum.
(36) Pulmonary infundibulum.

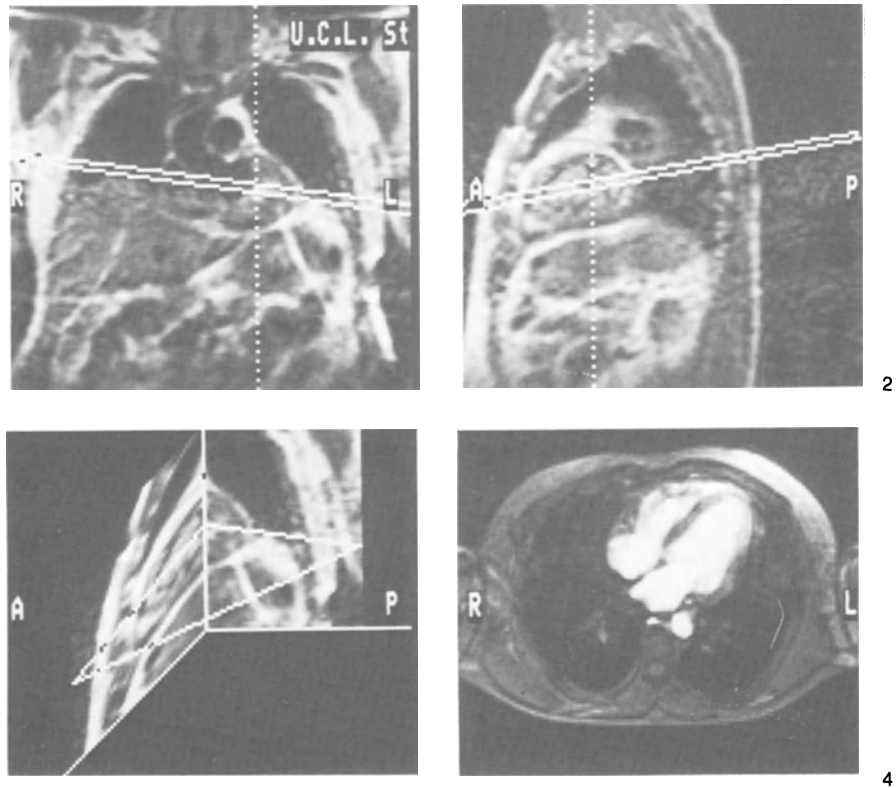

Figure DA-3.

The same coronal angulation as in Figure DA-1 and 2 is used (upper left panel) and the second angulation follows the long axis of the sagittal plane (upper right panel). The resulting image shows the four cavities of the heart (lower right panel).

The schematics of the lower right panel is drawn. The lower left panel shows the planes of section of the two angulations.

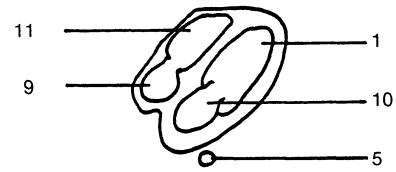

(1) Left ventricular cavity;
(5) Descending aorta;
(9) Right atrium;
(10) Left atrium;
(11) Right ventricular cavity;

Double angulation views

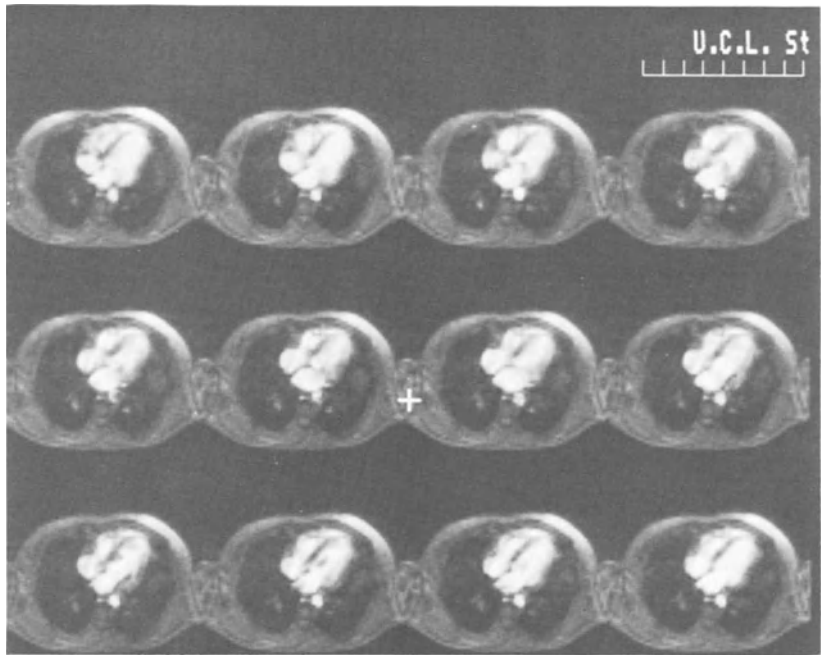

Figure DA–4.

Four cavities view in 12 consecutive time frames. The four cavities view was obtained from the double angulation procedure illustrated in Figure DA–3.

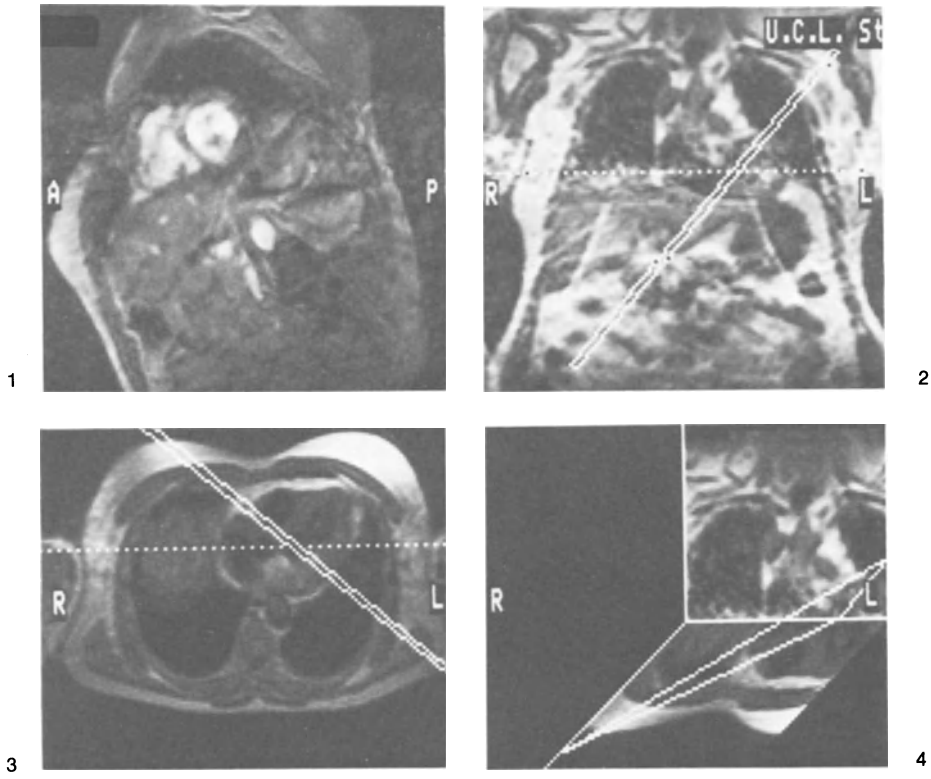

Figure DA-5.

This double angulation resulting image is the short axis view (upper left panel). The image results from a coronal angulation along the short axis of the left ventricle (upper right panel) and from a transversal angulation perpendicular to the ventricular septum (lower left panel).

The schematic of the upper left panel is drawn.
The lower right panel shows the planes of sections of the two angulations.

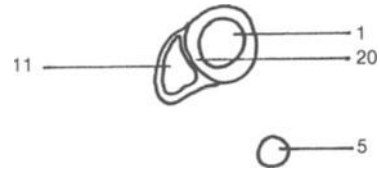

(1) Left ventricular cavity;
(5) Descending aorta;
(11) Right ventricular cavity;
(20) Ventricular septum.

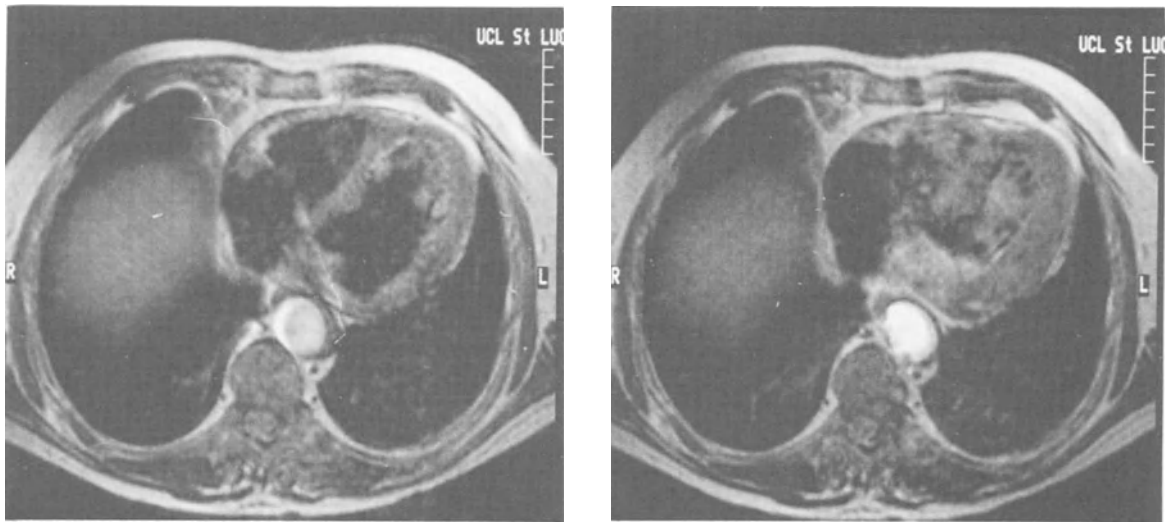

1 **Figure ES–1.** 2

Two ECG-triggered transverse images through the heart at end diastole and end systole. The regional wall thickening is clearly demonstrated on these spin-echo images.

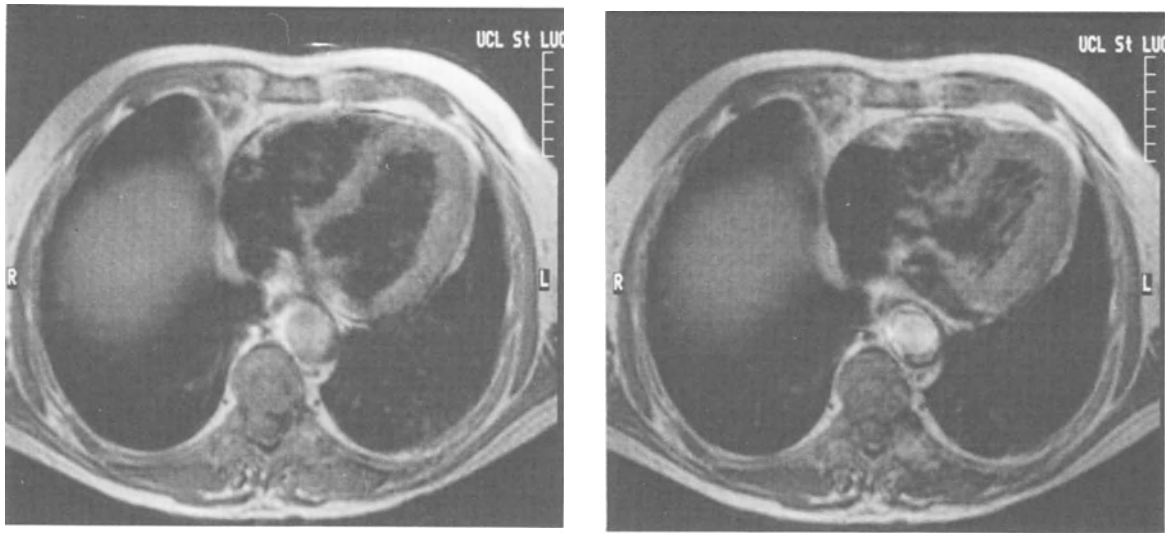

1 **Figure ES–2.** 2

Another example of two ECG-triggered transverse spin-echo images through the heart at end diastole and end systole.

End systole and end diastole

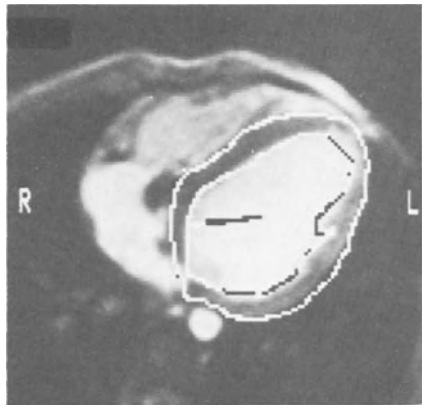

1

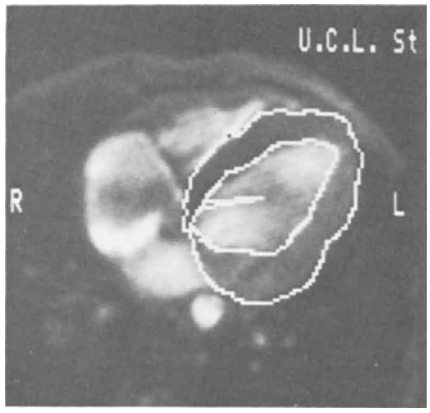

2

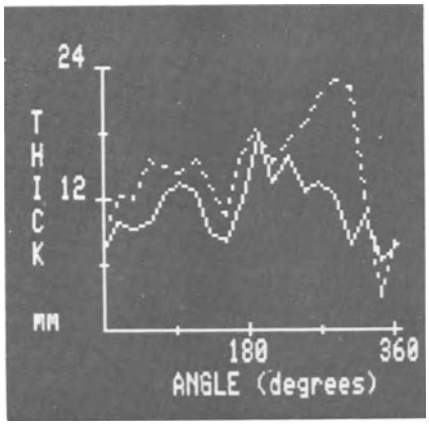

3

Figure ES–3.

Transverse cine MR images using the gradient-echo technique.

The endocardial and epicardial borders of the end-diastolic image and of the end systolic image have been outlined.

Measurements of regional wall thickening can be made to quantify systolic regional wall thickening.

The continued line of panel 3 represents the end diastolic wall thickness. The dotted line represents the end systolic wall thickness. The 0-degree point is situated on the line crossing the left ventricular cavity (panels 1 and 2). The degree progression is clockwise.

APPENDIX

Comprehensive bibliography

1. Books

Brown JJ, Higgins CB: *Pocket Atlas of Cardiac and Thoracic MRI*. Raven Press, 1989

Higgins CB, Silverman NH, Kersting-Sommerhoff BA, Schmidt K: *Congenital Heart Disease*, Echocardiography and Magnetic Resonance Imaging. Raven Press, 1991

Higgins CB, Hricak H: *Magnetic Resonance Imaging of the Body*. Raven Press, 1987

Marcus ML, Schelbert HR, Skorton DJ, Wolf GL: *Cardiac Imaging*. A companion to Braunwald's Heart Disease, Part VII: Cardiac Nuclear Magnetic Resonance Imaging. pp 732–976. WB Saunders Company, 1991

Pohost GM, O'Rourke RA: *Principles and Practice of Cardiovascular Imaging*. Little, Brown and Company, 1991

Stark DD, Bradley Jr WG: *Magnetic Resonance Imaging*. The CV Mosby Company, 1988

Underwood R, Firmin D: *An Introduction to Magnetic Resonance of the Cardiovascular System*. Current Medical Literature Ltd, 1988

Vanderwall EE, de Roos A: *Magnetic Resonance Imaging in Coronary artery Disease*. Kluwer Acad. Publ., 1991

von Schulthess GK: *Morphology and Function in MRI*. Cardiovascular and renal systems. Springer Verlag, 1989

2. Books chapters

Canby, RC, Evanochko WT, Pohost GM: NMR imaging of the cardiovascular system, in: Fozzard HA, ed. *The Heart and Cardiovascular System*. Raven Press: 331–349, 1986

Drucker EA, Dinsmore RE: Magnetic resonance imaging of congenital heart disease, in: Miller DD, ed. *Clinical Cardiac Imaging*. McGraw-Hill: 585–589, 1988

Higgins CB: Newer cardiac imaging techniques: digital subtraction angiography; computed tomography; magnetic resonance imaging, in: Braunwald E, ed. *Heart Disease: A Textbook of Cardiovascular Medicine*. Saunders: 356–382, 1988

Higgins CB: Cardiovascular anatomy, in: Budinger TF, ed. *Medical Magnetic Resonance. A Primer-1988*. Margulis AR. Society of Magnetic Resonance in Medicine: 187–200, 1988

Johnston DL, Rokey R, Okada RD: Principles of cardiovascular magnetic resonance imaging, in: Miller DD, ed. *Clinical Cardiac Imaging*. McGraw-Hill: 103–125, 1988

Pohost GM: Applications of NMR imaging to the cardiovascular system: physiologic, pathologic, and angiographic studies, in: Ed Budinger TF, Margulis AR, ed. *Medical Magnetic Resonance, A Primer–1988*. Society of Magnetic Resonance in Medicine: 175–186, 1988

3. Review articles

Bittner V, Cranney GB, Lotan CS, Pohost GM: Overview of cardiovascular nuclear magnetic resonance imaging. *Cardiol Clin* 7: 631–649, 1989

Bouchard A, et al: Uses of magnetic resonance imaging in cardiovascular disease. *Am J Cardiac Imaging* 3: 75–87, 1989

Choyke PL et al: Nongated cardiac magnetic resonance imaging: preliminary experience at 0.12 T. *AJR* 143: 1143–1150, 1984

Council of scientific affairs, American medical association: Magnetic resonance imaging of the cardiovascular system. Present state of the art and future potential. *JAMA* 259: 253–259, 1988

Grist TM et al: Gated cardiac MR imaging and P-31 MR spectroscopy in humans at 1.5T. Work in progress. *Radiology* 170: 357–361, 1989

Hartnell G.: Cardiovascular MRI. *Bristol Med Chir J* 103: 23–24, 1988

Heidelberger E et al: Aspects of cardiac diagnosis using synchronized NMR imaging. *Eur J Radiol* 3: 281–285, 1983

Herfkens R: Nuclear magnetic resonance imaging of the cardiovascular system: normal and pathologic findings. *Radiology* 147: 749–759, 1983

Higgins CB et al: Cardiovascular imaging with nuclear magnetic resonance. *Cardiol Clin* 1: 527–539, 1983

Higgins CB et al: Magnetic resonance imaging of the cardiovascular system. *Am Heart J* 109: 136–152, 1985

Higgins CB et al: Magnetic resonance imaging of the heart: a review of the experience in 172 subjects. *Radiology* 155: 671–679, 1985

Higgins CB: Overview of MR of the heart. *AJR* 146: 907–918, 1986

Bibliography

Higgins CB: MR of the heart: anatomy, physiology, and metabolism. *AJR* 151: 239–248, 1988

Higgins CB: Nuclear magnetic resonance (NMR) imaging in ischemic heart disease. *J Am Coll Cardiol* 15: 150–151, 1990

Johnston DL et al: The role of magnetic resonance imaging in the examination of the cardiovascular system. *Acta Clin Belg* 43: 282–290, 1988

Lanzer P et al: Cardiac imaging using gated magnetic resonance. *Radiology* 150: 121–127, 1984

Lanzer P et al: ECG-synchronized cardiac MR imaging: method and evaluation. *Radiology* 155: 681–686, 1985

Lieberman JM et al: Gated magnetic resonance imaging of the heart. *Radiol Clin North AM* 22: 847–858, 1984

Lim, TH, Saloner D, Anderson CM: Current applications of magnetic resonance vascular imaging. *Cardiol Clin* 7: 661–683, 1989

McNamara MT et al: Cardiovascular applications of magnetic resonance imaging. *Magn Reson Imaging* 2: 167–183, 1984

Miller SW et al: Cardiac magnetic resonance imaging: the Massachusetts General Hospital experience. *Radiol Clin North Am* 23: 745–764, 1985

Nishikawa J et al: ECG-gated NMR-CT for cardiovascular disease. *Radiat Med* 1: 274–280, 1983

Nishikawa J et al: Effectiveness of ECG-gated magnetic resonance imaging in diagnosing cardiovascular diseases. *J Cardiogr* 15: 1187–1198, 1985

Osbakken M et al: Nuclear magnetic resonance: theory and review of cardiac applications. *Am Heart J* 108: 574–590, 1984

Pflugfelder PW et al: Cardiovascular applications of magnetic resonance imaging. *Can Med Assoc J* 133: 1121–1125, 1985

Pohost GM et al: Nuclear magnetic resonance. New methods for the assessment of cardiac structure and function. *Cardiology* 71: 162–172, 1984

Pohost GM et al: Nuclear magnetic resonance: potential clinical relevance to the cardiovascular system. *Circulation* 72: 111–121, 1985

Pohost GM, Canby RC: Nuclear magnetic resonance imaging: current applications and future prospects. *Circulation* 75: 88–95, 1987

Radda GK: Potential and limitations of nuclear magnetic resonance for the cardiologist. *Br Heart J* 50: 197–201, 1983

Ratner AV et al: Nuclear magnetic resonance imaging of the heart. *Semin Nucl Med* 13: 339–346, 1983

Reed JD et al: Cardiovascular MRI: current role in patient management. *Radiol Clin North AM* 26: 589–606, 1988

Reeves RC et al: NMR evaluation of the cardiovascular system. *Ala J Med Sci* 22: 288–297, 1985

Reeves RC et al: Potential approaches to evaluating the cardiovascular system using NMR. *Prog Cardiovasc Dis* 29: 53–64, 1986

Smolorz J et al: Nuclear magnetic resonance imaging of the heart. *Eur J Nucl Med* 13: 653–660, 1988

Steiner RE et al: Nuclear magnetic resonance imaging of the heart. Current status and future prospects. *Br Heart J* 50: 202–208, 1983

Steiner RE: Nuclear magnetic resonance imaging of the heart and mediastinum. *Br Med Bull* 40: 191–193, 1984

Steiner RE: Nuclear magnetic resonance imaging of the heart. *Cardiovasc Intervent Radiol* 8: 314–320, 1986

Tscholakoff D et al: Magnetic resonance imaging of the heart. *Int J Card Imaging* 1: 73–85, 1985

Wagner S, Buser P, Auffermann W, Holt WW, Wolfe CL, Higgins CB: Cine magnetic resonance imaging: tomographic analysis of left ventricular function. *Cardiol Clin* 7: 651–659, 1989

Waterton JC et al: Magnetic resonance (MR) cine imaging of the human heart. *Br J Radiol* 58: 711–716, 1985

Willis RJ et al: Cardiac imaging: new technologies and clinical applications. *Cardiovasc Clin* 17: 1–454, 1986

Wolf GZ: MRI and the future of cardiac imaging. *Am J Cardiol* 64: 60E–63E, 1989

Wolfe CL: Assessment of myocardial ischemia and infection by contrast enhanced magnetic resonance imaging. *Cardiol Clin* 7: 685–696, 1989

Yoffie RL et al: Three-dimensional magnetic resonance imaging of the heart. *Radiol Technol* 60: 305–309, 1989

Zeitler E et al: Diagnosis of cardiovascular diseases with NMR imaging. *Prog Nucl Med* 8: 100–111, 1984

4. Technical considerations

Bendel P: T2-weighted contrasts in rapid low flip-angle imaging. *Magn Reson Med* 5: 366–370, 1987

Chapman B et al: Real-time movie imaging from a single cardiac cycle by NMR. *Mag Reson Med* 5: 246–254, 1987

Dimick RN et al: Optimizing electrocardiograph electrode placement for cardiac-gated magnetic resonance imaging. *Invest Radiol* 22: 17–22, 1987

Doherty JU et al: Changes in cardiac excitability and vulnerability in NMR fields. *Invest Radiol* 20: 129–135, 1985

Eiho S et al: Left ventricular image processing. *Med Prog Technol* 12: 101–115, 1987

Evans AJ et al: A cardiac phantom and pulsatile flow pump for magnetic resonance imaging studies. *Invest Radiol* 23: 579–583, 1988

Evans AJ et al: Effects of turbulence on signal intensity in gradient echo images. *Invest Radiol* 23: 512–518, 1988

Klipstein RH et al: Colour display of quantitative blood flow and cardiac anatomy in a single magnetic resonance cine loop. *Br J Radiol* 60: 105–111, 1987

Lenz G, Haacke E, White RD: Retrospective cardiac gating: a review of technical aspects and future directions. Magn Reson Imaging 7: 445–455, 1989

Lund G et al: serial myocardial T2 relaxation time measurements in normal subjects and heart transplant recipients. *J Heart Transplant* 7: 274–279, 1988
Norris S et al: Comparison of computer and non-computer assisted technologies in noninvasive cardiac imaging. *Am J Hypertens* 1: 96S–99S, 1988
Prato FS et al: Cardiac T1 calculations from MR spin-echo images. *Magn Reson Med* 4: 227–243, 1987
Randall PA et al: Magnetic resonance imaging of prosthetic cardiac valves in vitro and in vivo. *Am J Cardiol* 1: 973–976, 1988
Rzedzian RR et al: Instant images of the human heart using a new, whole body MR imaging system. *AJR* 149: 245–250, 1987
Soulen RL et al: Magnetic resonance imaging of prosthetic heart valves. *Radiology* 154: 705–707, 1985
Schneiders NJ et al: Accurate T2 NMR images. *Med Phys* 10: 642–645, 1983
Thickman D et al: Effect of phase-encoding direction upon magnetic image quality of the heart. *Magn Reson Med* 6: 390–396, 1988
Valk PE et al: MR imaging of the aorta with three-dimensional vessel reconstruction: validation by angiography. *Radiology* 157: 721–725, 1985
van Dijk P: ECG-triggered NMR imaging of the heart. *Diagn Imag Clin Med* 53: 29–37, 1984
Wendt RE 3d et al: Electrocardiographic gating and monitoring in NMR imaging. *Magn Reson Imaging* 6: 89–95, 1988
Zimmermann BH et al: Artifacts and hazards in NMR imaging due to metal implants and cardiac pacemakers. *Diagn Clin Med* 53: 53–56, 1984

5. Normal anatomy and MR-imaging planes of the heart

Akins EW et al: Importance of imaging plane for magnetic resonance imaging of the normal left ventricle. *Am J Cardiol* 56: 366–372, 1985
Bernstein MA et al: Pulse sequence generated oblique magnetic resonance imaging: applications to cardiac imaging. *Med Phys* 13: 648–657, 1986
Buchalter M et al: Noninvasive quantification of left ventricular rotational deformation in normal humans using magnetic resonance imaging myocardial tagging. *Circulation* 81: 1236–1244, 1990
Burbank F et al: Echocardiographic-like angled views of the heart by MR imaging. *J. Comput Assist Tomogr* 12: 181–195, 1988
Byrd BF et al: Normal cardiac dimensions by magnetic resonance imaging. *Am J Cardiol* 55: 1440–1442, 1985
Crooks LE et al: Magnetic resonance imaging strategies for heart studies. *Radiology* 153: 459–465, 1984
De Brux JL et al: Magnetic resonance imaging of the heart compared with anatomic and ultrasonographic data. *Surg Radiol Anat* 9: 303–314, 1987
Dinsmore RE et al: Magnetic resonance imaging of the heart: positioning and gradient angle selection for optimal imaging planes. *AJR* 143: 1135–1142, 1984
Dinsmore RE et al: Magnetic resonance imaging of the heart using image planes oriented to cardiac axes: experience with 100 cases. *AJR* 145: 1177–1183, 1985
Feiglin DH et al: Gated cardiac magnetic resonance structural imaging: optimization by electronic axial rotation. *Radiology* 154: 129–132, 1985
Friedman BJ et al: Comparison of magnetic resonance imaging and echocardiography in determination of cardiac dimensions in normal subjects. *J Am Coll Cardiol* 5: 1369–1376, 1985
Go RT et al: Volume and planar gated cardiac magnetic resonance imaging: a correlative study of normal anatomy with thallium-201 SPECT and cadaver sections. *Radiology* 150: 129–135, 1984
Grivegnee AR et al: Magnetic resonance imaging of the heart: comparison with two dimensional echocardiography. *Ann Radiol* (Paris) 30: 105–109, 1987
Higgins CB et al: Assessment of cardiac anatomy using nuclear magnetic resonance imaging. *J Am Coll Cardiol* 5: 77S–81S, 1985
Kaul S et al: Measurement of normal left heart dimensions using optimally oriented MR images. *AJR* 146: 75–79, 1986
Link KM et al: Reconstruction of the four basic cardiac projections from magnetic resonance images: a new aspect. *Radiographics* 8: 1109–1136, 1988
Longmore DB, Underwood SR, Bland C et al: Dimensional accuracy of magnetic resonance in studies of the heart. *Lancet* i: 1360, 1985
Murphy WA et al: Obliques views of the heart by magnetic resonance imaging. *Radiology* 154: 225–226, 1985
Nazarian GK et al: Correlation between magnetic resonance imaging of the heart and cardiac anatomy. *Mayo clin Proc* 62: 573–583, 1987
O'Donovan PB et al: Magnetic resonance imaging of the thorax: the advantages of coronal and sagittal planes. *AJR* 143: 1183–1188, 1984
Rholl KS et al: Oblique magnetic resonance imaging of the cardiovascular system. *Radiographics* 6: 177–188, 1986
Van Rossum AC et al: Oblique views in magnetic resonance imaging of the heart by combined axial rotations. *Acta Radiol* 28: 497–503, 1987
Van Rossum AC et al: Magnetic resonance imaging of the heart by combined axial rotations. *Acta Radiol* 28: 497–503, 1987
Van Rossum AC et al: Magnetic resonance imaging of cardiac anatomy. A standad procedure. *Eur J Radiol* 7: 23–27, 1987
Webb WR et al: Coronal magnetic resonance imaging of

Bibliography

the chest: normal and abnormal. *Radiology* 153: 729–735, 1984

Wechsler RJ et al: Cross-sectional imaging of the chest wall. *J Thorac Imaging* 4: 29–40, 1989

Wenink AC et al: Correlation of morphology of the left ventricular outflow tract with two-dimensional Doppler echocardiography and magnetic resonance imaging in atrioventricular septal defect. *Am J Cardiol* 63: 1137–1140, 1989

6. **Ventricular function** (ejection fraction, wall motion analysis, myocardial mass)

Akins EW et al: Assessment of left ventricular wall thickness in healed myocardial infraction by magnetic resonance imaging. *Am J Cardiol* 59: 24–26, 1987

Askenase AD et al: Cine MRI evaluation of regional asynergy after experimental coronary occlusion. *Am J Cardiac Imaging* 3: 91–99, 1989

Axel L et al: Heart wall motion: improved method of spatial modulation of magnetization for MR imaging. *Radiology* 172: 349–350, 1989

Beyar R et al: Quantification and validation of left ventricular wall thickening by a three-dimensional volume element MRI approach. *Circulation* 81: 297–307, 1990

Buchalter MB et al: Noninvasive quantification of left ventricular rotational deformation in normal humans using magnetic resonance imaging myocardial tagging. *Circulation* 81: 1236–1244, 1990

Buckwalter KA et al: Gated cardiac MRI: ejection-fraction determination using the right anterior oblique view. *AJR* 147: 33–37, 1986

Buschsieweke U et al: Hemodynamic parameters of the left ventricle with nuclear magnetic resonance imaging. *Ann Radiol* (Paris) 29: 464–466, 1986

Buser PT et al: Noninvasive evaluation of global left ventricular function with use of cine nuclear magnetic resonance. *J Am Coll Cardiol* 13: 1294–1300, 1989

Caputo GR et al: Measurement of canine left ventricular mass by using MR imaging. *AJR* 148: 33–38, 1987

Cranney GB et al: Left ventricular volume measurement using cardiac axis nuclear magnetic resonance imaging. Validation by calibrated ventricular angiography. *Circulation* 82: 154–163, 1990

Culham JA et al: Cardiac output by MR imaging: an experimental study comparing right ventricle and left ventricle with thermodilution. *Can Assoc Radiol J* 39: 247–249, 1988

Deutsch HJ et al: Cardiac function by magnetic resonance imaging. *Int J Card Imaging* J: 3–11, 1988

Dilworth LR, Aisen AM, Mancini J et al: Determination of left ventricular volumes and ejection fraction by nuclear magnetic resonance imaging. *Am Heart* J 113: 24, 1987

Dinsmore RE: Quantitation of cardiac dimensions from ECG-synchronized MRI studies. *Cardiovasc Intervent Radiol* 10: 356–364, 1987

Doyle M et al: Dynamic NMR cardiac imaging in a piglet. *Br J Radiol* 56: 925–930, 1983

Edelman RR et al: Cardiac function: evaluation with fastecho MR imaging. *Radiology* 162: 611–615, 1987

Fisher MR et al: Multiphasic cardiac magnetic resonance imaging: normal regional left ventricular wall thickening. *AJR* 145: 27–30, 1985

Florentine MS et al: Measurement of left ventricular mass in vivo using gated nuclear magnetic resonance imaging. *J Am Coll Cardiol* 8: 107–112, 1986

Higgins CB et al: Cine MR: evaluation of cardiac ventricular function and valvular function. *Int J Card Imaging* 3: 21–28, 1988

Higgins CB et al: Functional evaluation of the heart with magnetic resonance imaging. *Magn Reson Med* 6: 121–139, 1988

Just H et al: Estimation of left ventricular volume and mass by magnetic resonance imaging: comparison with quantitative biplane angiocardiography. *Cardiovasc Intervent Radiol* 10: 1–4, 1987

Keller AM et al: In vivo measurement of myocardial mass using nuclear magnetic resonance imaging. *J Am Coll Cardiol* 8: 113–117, 1986

Le Page R et al: A brief evaluation of cardiac gated MRI in left ventricular ejection fraction determination: a comparison with standard left ventriculography DSA and nuclear medicine. *Ann Radiol* (Paris) 29: 87–90, 1986

Lotan CS et al: The value of cine nuclear magnetic resonance imaging for assessing regional ventricular function. *J Am Coll Cardiol* 14: 1721–1729, 1989

Maddahi J et al: Noninvasive quantification of left ventricular myocardial mass by gated proton nuclear magnetic resonance imaging. *J Am Coll Cardiol* 10: 682–692, 1987

Markiewicz W et al: Evaluation of the right ventricle by magnetic resonance imaging. *Am Heart J* 113: 8–15, 1987

Markiewicz W, Sechtem U, Kerby R et al: Measurement of ventricular volumes in the dog by magnetic resonance imaging. *J Am Coll Cardiol* 106: 365, 1987

Milliken MC et al: Left ventricular mass as determined by magnetic resonance imaging in male endurance athletes. *Am J Cardiol* 62: 301–305, 1988

Mogelvang J et al: Evaluation of left ventricular volumes measured by magnetic resonance imaging. *Eur Heart J* 7: 1016–1021, 1986

Mogelvang J et al: Evaluation of right ventricular volumes measured by magnetic resonance imaging. *Eur Heart J* 9: 529–533, 1988

Ostrzega E et al: Quantification of left ventricular myocardial mass in humans by nuclear magnetic resonance imaging. *Am Heart J* 117: 444–452, 1989

Osbakken M et al: Evaluation of ventricular function with gated cardiac magnetic resonance imaging. *Cathet Cardiovasc Diagn* 12: 156–160, 1986

Peshock RM et al: Assessment of myocardial systolic wall thickening using nuclear magnetic resonance imaging. *J Am Coll Cardiol* 14: 653–659, 1989

Pflugfelder PW et al: Quantification of regional myocardial function by rapid cine MR imaging. *AJR* 150: 523–529, 1988

Rehr RB et al: Left ventricular volumes measured by MR imaging. *Radiology* 156: 717–719, 1985

Sechtem U, Pflugfelder P, Higgins CB: Quantification of cardiac function by conventional and cine magnetic resonance imaging. *Cardiovasc Intervent Radiol* 106: 365, 1987

Sechtem U et al: Regional left ventricular wall thickening by magnetic resonance imaging: evaluation in normal persons and in patients with global and regional dysfunction. *Am J Cardiol* 59: 145–151, 1987

Sechtem U et al: Measurement of right and left ventricular volumes in healthy individuals with cine MR imaging. *Radiology* 163: 697–702, 1987

Semelka R, Tomei E, Wagner S, Mayo J, Kondo CH, Suzuki J, Caputo G, Higgins CB: Normal left ventricular dimensions and function: interstudy reproducibility of measurements with cine-MR imaging. *Radiology* 174: 763–768, 1990

Shapiro EP et al: Determination of left ventricular mass by magnetic resonance imaging in hearts deformed by acute infarction. *Circulation* 79: 706–711, 1989

Stratemeir RJ, Thompson R, Brady TJ et al: Ejection fraction determination by MR imaging: comparison with left ventricular angiography. *Radiology* 158: 775, 1986

Tscholakoff D et al: Gated magnetic resonance imaging for assessment of cardiac function and myocardial infarction. *Radiol Clin North Am* 23: 449–457, 1985

Underwood SR et al: Assessment of regional left ventricular function by magnetic resonance. *Br Heart J* 56: 334–340, 1986

Underwood SR et al: Left ventricular volume measured rapidly by oblique magnetic resonance imaging. *Br Heart J* 60: 188–195, 1988

Utz JA et al: Cine MR determination of left ventricular ejection fraction. *AJR* 148: 839–843, 1987

Van Dijk P: Direct cardiac NMR imaging of heart wall and blood flow velocity. *J Comput Assist Tomogr* 8: 429–436, 1984

Van Rossum AC et al: Evaluation of magnetic resonance imaging for determination of left ventricular ejection fraction and comparison with angiography. *Am J Cardiol* 62: 628–633, 1988

Van Rossum AC et al: Magnetic resonance imaging of the heart for determination of ejection fraction. *Int J Cardiol* 18: 53–63, 1988

White RD et al: Segmental evaluation of left ventricular wall motion after myocardial infarction: magnetic resonance imaging versus echocardiography. *Am Heart J* 115: 166–175, 1988

White RD et al: Estimation of the functional and anatomic extent of myocardial infarction using magnetic resonance imaging. *Am Heart J* 115: 740–748, 1988

Zerhouni EA et al: Human heart: tagging with MR imaging – a method for noninvasive assessment of myocardial motion. *Radiology* 169: 59–63, 1988

7. Congenital heart disease

Amparo EG et al: Demonstration of coarctation of the aorta by magnetic resonance imaging. *AJR* 143: 1192–1194, 1984

Baker EJ: MRI of coarctation of the aorta in infants: use of a high field strength. *Br Heart J* 62: 97–101, 1989

Baker EJ: MRI at a high field strength of ventricular septal defects in infants. *Br Heart* 62: 305–310, 1989

Bank ER et al: CT and MR of congenital heart disease. *Radiol Clin North Am* 26: 241–262, 1988

Bisset GS et al: Vascular rings: MR imaging. *AJR* 149: 251–256, 1987

Casolo GC et al: ECG-gated magnetic resonance imaging in right ventricular dysplasia. *Am Heart J* 113: 1245–1248, 1987

Chrispin A et al: Echo planar imaging of normal and abnormal connections of the heart and great arteries. *Pediatr Radiol* 16: 289–292, 1986

Chrispin A et al: Transectional echo planar imaging of the heart in cyanotic congenital heart disease. *Pediatr Radiol* 16: 293–297, 1986

Chung KJ et al: Cine magnetic resonance imaging after surgical repair in patients with transposition of the great arteries. *Circulation* 77: 104–109, 1988

Coscina WF et al: MR imaging of double aortic arch. *J Comput Assist Tomogr* 10: 673–675, 1986

Didier D et al: Identification and localization of ventricular septal defect by gated magnetic resonance imaging. *Am J Cardiol* 57: 1363–1368, 1986

Didier D et al: Estimation of pulmonary vascular resistance by MRI in patients with congenital cardiovascular shunt lesions. *AJR* 146: 919–924, 1986

Didier D et al: Congenital heart disease; gated MR imaging in 72 patients. *Radiology* 158: 227–235, 1986

Diethelm L et al: Atrial-level shunts; sensitivity and specificity of MR in diagnosis. *Radiology* 162: 181–186, 1987

Dinsmore RE et al: Magnetic resonance imaging of the interatrial septum and atrial septum defects. *AJR* 145: 697–703, 1985

Fisher MR et al: Magnetic resonance imaging and computed tomography in congenital heart disease. *Semin Roentgenol* 20: 272–282, 1985

Fletcher BD et al: Gated magnetic resonance imaging of

Bibliography

congenital cardiac malformations. *Radiology* 150: 137–140, 1984

Fletcher BD et al: MRI of congenital abnormalities of the great arteries. *AJR* 146: 941–948, 1986

Fletcher BD et al: Right atrioventricular valve atresia: anatomic evaluation with MR imaging. *AJR* 148: 671–674, 1987

Formanek AG et al: MR imaging of the central pulmonary arterial tree in conotruncal malformation. *AJR* 147: 1127–1131, 1986

Higgins CB et al: Magnetic resonance imaging in patients with congenital heart disease. *Circulation* 70: 851–860, 1984

Gomes AS et al: Congenital abnormalities of the aortic arch: MR imaging. *Radiology* 165: 691–695, 1987

Humes RA et al: Aortico-left ventricular tunnel: diagnosis based on two-dimensional echocardiography, color flow Doppler imaging, and magnetic resonance imaging. *Mayo Clin Proc* 61: 901–907, 1986

Jacobstein MD et al: Evaluation of atrioventricular septal defect by magnetic resonance imaging. *Am J Cardiol* 55: 1158–1161, 1985

Jacobstein MD et al: Magnetic resonance imaging in patients with hypoplastic right heart syndrome. *Am Heart J* 110: 154–158, 1985

Julsrud PR et al: Extracardiac vasculature in candidates for Fontan surgery: MR imaging. *Radiology* 173: 503–506, 1989

Link KM et al: MR imaging of Ebstein anomaly; results in four cases. *AJR* 150: 363–367, 1988

Link KM et al: MR imaging of the crisis-cross heart. *AJR* 152: 809–812, 1989

Lowell DG et al: The detection of atrial and ventricular septal defects with electrocardiographically synchronized magnetic resonance imaging. *Circulation* 73: 89–94, 1986

Mayo J et al: Magnetic resonance imaging in pediatric vascular disease. *J Can Assoc Radiol* 38: 165–169, 1987

Mirowitz SA et al: Tetralogy of Fallot: MR findings. *Radiology* 171: 207–212, 1989

Nishimura T et al: Double-chambered right ventricle demonstrated by magnetic resonance imaging before cardiac catheterization-case report. *Angiography* 39: 259–262, 1988

Park JH: Pictorial essay. MR imaging of congenitally corrected transposition of the great vessels in adults. *AJR* 153: 491–494, 1989

Park LH et al: MR imaging of congenitally corrected transposition of the great vessels in adults. *AJR* 153: 491–494, 1989

Rees S et al: Magnetic resonance imaging of the pulmonary arteries and their systematic connections in pulmonary atresia: comparison with angiographic and surgical findings. *Br Heart J* 58: 621–626, 1987

Rees S et al: Comparison of magnetic resonance imaging with echocardiography and radionuclide angiography in assessing cardiac function and anatomy following Mustard's operation for transposition of the great arteries. *Am J Cardiol* 61: 1316–1322, 1988

Rees S: Applications of flow measurements by velocity mapping to congenital heart disease. *Am J Cardiol* 64: 953–956, 1989

Rees S et al: Coarctation of the aorta; MR-imaging in late postoperative assessment. *Radiology* 173: 499–502, 1989

Ross RD et al: Magnetic resonance imaging for diagnosis of pulmonary vein stenosis after 'correction' of total anomalous pulmonary venous connection. *Am J Cardiol* 60: 1199–1201, 1987

Sechtem U et al: Ventricular septal defect: visualization of shunt flow and determination of shunt size by cine MR imaging. *AJR* 149: 689–692, 1987

Simpson IA et al: Cine magnetic resonance imaging for evaluation of anatomy and flow relations in infants and children with coarctation of the aorta. *Circulation* 78: 142–148, 1988

Smith MA et al: Magnetic resonance imaging of the infant heart at 1.5 T. *Br J Radiol* 62: 367–370, 1989

Soulen RL et al: Advances in noninvasive evaluation of congenital anomalies of the thoracic aorta. *Radiol Clin North Am* 23: 727–736, 1985

Soulen RL et al: Evaluation of balloon angioplasty of coarctation restenosis by magnetic resonance imaging. *Am J Cardiol* 60: 343–345, 1987

Vannier MW et al: Three-dimensional magnetic resonance imaging of congenital heart disease. *Radiographics* 8: 857–871, 1988

von Schulthess GK et al: Coarctation of the aorta: MR imaging. *Radiology* 158: 469–474, 1986

8. Valvular heart diseases

de Roos A et al: Cine MR imaging in aortic stenosis. *J Comput Assist Tomogr* 13: 421–425, 1989

Germain, P: Value of cine-MRI in the diagnosis and quantification of valvular regurgitation. Comparison with angiography and doppler-echocardiography. *Arch Mal coeur* 82: 1659–1668, 1989

Glogar D et al: Assessment of mitral regurgitation by magnetic resonance imaging. *Magn Reson Imaging* 7: 611–617, 1989

Hill JA et al: Mitral stenosis; imaging by nuclear magnetic resonance. *Am J Cardiol* 1: 352–354, 1986

Nishimura T et al: Cine-MR imaging in mitral regurgitation: comparison with color Doppler flow imaging. *AJR* 153: 721–724, 1989

Pflugfelder PW et al: Noninvasive evaluation of mitral regurgitation by analysis of left atrial signal loss in cine magnetic resonance. *Am Heart J* 117: 1113–1119, 1989

Pflugfelder PW et al: Comparison of cine MR imaging with Doppler echocardiography for the evaluation of aortic regurgitation. *AJR* 152: 729–735, 1989

Schiebler M, Axel L, Reichek N, Aurigemma G, Yeager B, Douglas, Bogin K, Kressel H: Correlation of cine MR imaging with two-dimensional pulsed Doppler echocardiography in valvular insufficiency. *J Comp Assist Tomography* 11: 627–632, 1987

Sechtem U et al: Noninvasive assessment of aortic and mitral valve insufficiencies with dynamic magnetic resonance tomography. *Z Kardiol* 77: 145–151, 1988

Sechtem U et al: Mitral or aortic regurgitation: quantification of regurgitant volumes with cine MR imaging. *Radiology* 167: 425–430, 1988

Slone RM et al: Magnetic resonance imaging late after tricuspid valvectomy. *Am J Cardiol* 59: 1426–1427, 1987

Underwood SR et al: Magnetic resonance assessment of aortic and mitral regurgitation. *Br Heart J* 56: 455–462, 1986

Underwood SR, Firmin DN, Mohiaddin RH, Klipstein RH, Bogren H, Rees RSO, Longmore DB: Cine magnetic resonance imaging of valvular heart disease. *Radiology* 165: 723–727, 1987

Utz JA et al: Valvular regurgitation: dynamic MR imaging. *Radiology* 168: 91–94, 1988

Wagner S et al: Diagnostic accuracy and estimation of the severity of valvular regurgitation form the signal void cine magnetic resonance imaging. *Am Heart J* 118: 760–767, 1989

Winkler ML et al: MRI of perivavular infectious pseudoaneurysms. *AJR* 147: 253–256, 1986

9. Chest, mediastinum and pulmonary hila

Aronberg DJ et al: MRI and CT of the mediastinum: comparisons, controversies and pitfalls. *Radiol Clin North Am* 23: 439–448, 1985

Axel L et al: NMR imaging of the chest at 0.12 T: initial clinical experience with a resistive magnet. *AJR* 141: 1157–1162, 1983

Batra P et al: MR imaging of the thorax: a comparison of axial, coronal and sagittal imaging planes. *J Comput Assist Tomogr* 12: 75–81, 1988

Bisset GS 3d: Pediatric thoracic applications of magnetic resonance imaging. *J Thorac Imaging* 4: 51–57, 1989

Berquist TH et al: Magnetic resonance of the chest: a diagnostic comparison with computed tomography and hilar tomography. *Magn Reson Imaging* 2: 315–327, 1984

Boisserie-Lacroix M et al: A pleuropericardial cyst in an unusual location: the value of magnetic resonance. *Comput Med Imaging Graph* 12: 277–280, 1988

Brasch RC et al: Magnetic resonance imaging of the thorax in childhood. Work in progress. *Radiology* 150: 463–467, 1984

Cohen AM: Magnetic resonance imaging of the thorax. *Radiol Clin North Am* 22: 829–846, 1984

Epstein DM et al: MR imaging of the mediastinum: a retrospective comparison with computed tomography. *J Comput Assist Tomogr* 8: 670–676, 1984

Fisher MR: Magnetic resonance for evaluation of the thorax. *Chest* 95: 166–173, 1989

Fisher MR et al: Central thrombi in pulmonary arterial hypertension detected by MR imaging. *Radiology* 158: 223–226, 1986

Gamsu G et al: Magnetic resonance imaging of the thorax. *Am Rev Respir Dis* 139: 254–274, 1989

Gefter WB: Chest applications of magnetic resonance imaging: an update. *Radiol Clin North Am* 26: 573–588, 1988

Guttierrez FR et al: NMR imaging of pulmonary arteriovenous fistulae. *J Comput Assist Tomogr* 8: 750–752, 1984

Heelan RT et al: Carcinomatous involvement of the hilum and mediastinum: computed tomographic and magnetic resonance evaluation. *Radiology* 156: 111–115, 1985

Kangarloo H: Chest MRI in children. *Radiol Clin North Am* 26: 263–275, 1988

Katz ME et al: Mediastinal vessels: postoperative evaluation with MR imaging. *Radiology* 161: 647–651, 1986

Kundel HL et al: The potential role of NMR imaging in thoracic disease. *Radiol Clin North Am* 21: 801–808, 1983

Laissy JP et al: MR appearance of the normal chest after pneumonectomy. *J Comput Assist Tomogr* 13: 248–252, 1989

Levitt RG et al: Magnetic resonance imaging of mediastinal and hilar masses: comparisons with CT. *AJR* 145: 9–14, 1985

Mark AS et al: Gated acquisition of MR images of the thorax: advantages for the study of the hila and mediastinum. *Magn Reson Imaging* 5: 57–63, 1987

Newhouse JH: Nuclear magnetic resonance studies of the chest. *Clin Chest Med* 5: 307–312, 1984

Poon PY: MR imaging of the thorax. *Chest* 92: 1–2, 1987

Posteraro RH et al: Cine-gradient-refocused MR imaging of central pulmonary emboli. *AJR* 152: 465–568, 1989

Rholl KS et al: Magnetic resonance imaging of fibrosing mediastinitis. *AJR* 145–255–259, 1985

Rokey R et al: Lipomatous encasement and compression of the heart: antemortem diagnosis by cardiac nuclear magnetic resonance imaging and catheterization. *Am Heart J* 117: 952–953, 1989

Ross JS et al: Magnetic resonance of the chest: initial experience with imaging and in vivo Tl and T2 calculations. *Radiology* 152: 95–101, 1984

Ross JS et al: Magnetic resonance imaging of the chest. Initial experience. *Cleve Clin Q* 52: 533–539, 1985

Sarrazin R et al: The mediastinum in sagittal sectioning. Anatomy and magnetic resonance imaging (MRI). *Surg Radiol Anat* 9: 95–105, 1987

Shirkhoda A et al: MR imaging of mediastinal thymolipoma. *J Comput Assist Tomogr* 11: 364–365, 1987

Bibliography

Spritzer C et al: Magnetic resonance imaging of the thorax: techniques, current applications, and future directions. *J Thorac Imaging* 4: 1–18, 1989

Stein MG et al: MR imaging of pulmonary emboli: an experimental study in dogs. *AFR* 147: 1133–1137, 1986

Swensen SJ et al: Magnetic resonance imaging of the thorax. *J Thorac Imaging* 4: 19–33, 1989

Thickman D et al: Demonstration of pulmonary embolism by magnetic resonance imaging. *AJR* 142: 921–922, 1984

von Schulthess GK et al: Mediastinal masses: MR imaging. *Radiology* 158: 289–296, 1986

Webb WR et al: Evaluation of magnetic resonance sequences in imaging mediastinal tumors. *AJR* 143: 723–727, 1984

Webb WR et al: Clinical NMR imaging of the chest and mediastinum. *Diagn Imag Clin Med* 53: 22–28, 1984

Webb WR: Magnetic resonance imaging of the hila and mediastinum. *Cardiovasc Intervent Radiol* 8: 306–313, 1986

Webb WR et al: Sagittal MR imaging of the chest: normal and abnormal. *J Comput Assist Tomogr* 9: 471–479, 1985

Webb WR: Magnetic resonance imaging of the mediastinum, hila, and lungs. *J Thorac Imaging* 1: 65–73, 1985

Webb WR et al: Multisection sagittal and coronal magnetic resonance imaging of the mediastinum and hila. Work in progress. *Radiology* 150: 475–478, 1984

Webb WR et al: Magnetic resonance imaging of the normal and abnormal pulmonary hila. *Radiology* 152: 89–94, 1984

Westcott JL et al: MR imaging of the hilum and mediastinum: effects of cardiac gating. *J Comput Assist Tomogr* 9: 1073–1078, 1985

White RD et al: MR imaging of pulmonary arterial hypertension and pulmonary emboli. *AJR* 149: 15–21, 1987

10. Myocardial ischemia and infarction

Aisen AM et al: Visualization of myocardial infarction and subsequent coronary reperfusion with MRI using a dog model. *Magn reson Imaging* 5: 399–404, 1987

Akins EW et al: Improved detection of healed myocardial infarction by Fourier amplitude and phase imaging in two projections validation with MRI. *Radiographics* 9: 323–339, 1989

Atkinson D, Burstein D, Edelman R: First-pass cardiac perfusion: evaluation with ultrafast MR imaging. *Radiology* 174: 752–762

Azhari H et al: Three dimensional mapping of acute ischemic regions using MRI: wall thickening versus motion analysis. *Am J Physiol* 259: H1492–H1503, 1990

Been M et al: Characterization of acute myocardial infarction by gated magnetic resonance imaging. *Lancet* 1985 1: 348–350

Brown JJ et al: Nuclear magnetic resonance analysis of acute and chronic myocardial infarction in dogs: alterations in spin-lattice relaxation times. *Am Heart J* 108: 1292–1297

Brown JJ et al: Nuclear magnetic resonance analysis of acute myocardial infarction in dogs: the effects of transient coronary ischemia in varying duration and reperfusion on spin lattice relaxation times. *Am Heart J* 109: 486–490, 1985

Brown JJ et al: Regional myocardial blood flow, edema formation, and magnetic relaxation times during acute myocardial ischemia in the canine. *Invest Radiol* 20: 465–471, 1985

Buda AJ et al: Detection and sizing of myocardial ischemia and infarction by nuclear magnetic resonance imaging in the canine heart. *Am Heart J* 110: 1284–1290, 1985

Canby RC et al: Proton nuclear magnetic resonance relaxation times in severe myocardial ischemia. *J Am Coll Cardiol* 10: 412–420, 1987

Caputo GR et al: Measurement of myocardial infarct size at early and late time intervals using MR imaging: an experimental study in dogs. *AJR* 149: 237–243, 1987

Checkley et al: Detection of myocardial infarction in the mini-pig using NMR imaging. *Magn Reson Med* 5: 201–216, 1987

de Roos A et al: MR imaging of acute myocardial infarction: value of Gd-DTPA. *AJR* 150: 531–534, 1988

de Roos A et al: Myocardial infarct size after reperfusion therapy: assessment with Gd-DTPA-enhanced MR imaging. *Radiology* 176: 517–521, 1990

Dilworth LR et al: Serial nuclear magnetic resonance imaging in acute myocardial infarction. *Am J Cardiol* 59: 1203–1205, 1987

Eichstaedt HW et al: Magnetic resonance imaging (MRI) in different stages of myocardial infarction using the contrast agent gadolinium-DTPA. *Clin Cardiol* 9: 527–535, 1986

Filipchuk NG et al: Detection and localization of recent myocardial infarction by magnetic resonance imaging. *Am J Cardiol* 58: 214–219, 1986

Fisher MR et al: Acute myocardial infarction: MR evaluation in 29 patients. *AJR* 148: 247–251, 1987

Higgins CB et al: Magnetic resonance imaging of ischemic heart disease. *Prog Cardiovasc Dis* 28: 257–266, 1986

Higgins CB et al: Nuclear magnetic resonance imaging of acute myocardial infarction in dogs: alterations in magnetic relaxation times. *Am J Cardiol* 52: 184–188, 1983

Johns JA et al: Quantitation of acute myocardial infarct size by nuclear magnetic resonance imaging. *J Am Coll Cardiol* 15: 143–149, 1990

Johnston DL et al: Evaluation of myocardial ischemia and infarction by nuclear magnetic resonance techniques. *Can J Cardiol* 4: 116–129, 1988

Johnston DL et al: In vivo detection of reperfused myocardium by nuclear magnetic resonance imaging. *J Am Coll Cardiol* 9: 127–135, 1987

Johnston DL et al: Magnetic resonance imaging during acute myocardial infarction. *Am J Cardiol* 57: 1059–1065, 1986

Johnston DL et al: Assessment of myocardial ischemia with proton magnetic resonance: effects of a three hour coronary occlusion with and without reperfusion. *Circulation* 71: 595–601, 1985

Johnston DL et al: Nuclear magnetic resonance imaging of the acute myocardial infarction within 24 hours of chest pain onset. *Am J Cardiol* 64: 172–179, 1989

McNamara MT et al: Magnetic resonance imaging of chronic myocardial infarcts in man. *AJR* 146: 315–320, 1986

McNamara MT et al: Detection and characterization of acute myocardial infarction in man with use of gated magnetic resonance. *Circulation* 71: 717–724, 1985

McNamara MT et al: Acute myocardial ischemia: magnetic resonance contrast enhancement with gadolinium-DTPA. *Radiology* 153- 157–163, 1984

Nishimura T et al: Value and limitation of gadolinium-DTPA contrast enhancement in the early detection of acute canine myocardial infarction. *Am J Physiol Imaging* 2: 181–185, 1987

Nishimura T et al: Serial assessment of myocardial infarction by using gated MRI and gadolinium-DTPA. *AJR* 153: 715–720, 1989

Nomura M et al: Magnetocardiographic studies of ventricular repolarization in old inferior myocardial infarction. *Eur Heart J* 10: 8–15, 1989

Peshock RM et al: Magnetic resonance imaging of acute myocardial infarction: gadolinium diethylenetriamine pentaacetic acid as a marker of reperfusion. *Circulation* 74: 1434–1440, 1986

Pflugfelder PW et al: Early detection of canine myocardial infarction by magnetic resonance imaging in vivo. *Circulation* 71: 587–594, 1985

Pomeroy OH et al: Magnetic resonance imaging of acute myocardial ischemia using a manganese chelate, Mn-DPDP. *Invest Radiol* 24: 531–536, 1989

Revel D et al: Magnetic resonance imaging of ischemic heart disease. *Radiol Clin North Am* 23: 719–726, 1985

Rokey R et al: Myocardial infarct quantification by MR imaging early after coronary occlusion in dogs. *Radiology* 158: 771–774, 1986

Runge VM et al: Gated magnetic resonance imaging of acute myocardial ischemia in dogs: application of multiecho techniques and contrast enhancement with GD DTPA. *Magn Reson Imaging* 3: 255–266, 1985

Ryan T et al: Distinguishing viable from infarcted myocardium after experimental ischemia and reperfusion by using nuclear magnetic resonance imaging. *J Am Coll Cardiol* 15: 1355–64, 1990

Saeed M et al: Demarcation of myocardial ischemia: magnetic susceptibility effect of contrast medium in MR imaging. Radiology 173: 763–767, 1989

Saeed M et al: Occlusive and reperfused myocardial infarcts: differentiation with Mn-DPDP-enhanced MR imaging. *Radiology* 172: 59–64, 1989

Schmiedl U et al: Magnetic resonance imaging of myocardial infarction using albumin-(GD-DTPA), a macromolecular bloodvolume contrast agent in a rat model. *Invest radiol* 22: 713–721, 1987

Schmiedl U et al: Acute myocardial ischemia and reperfusion: MR imaging with albuumin-GD-DTPA. *Radiology* 170: 351–356, 1989

Schouman-Claeys E et al: Canine acute myocardial infarction. In vivo detection by MRI with gradient echo technique and contribution of GD-DOTA. *Invest Kadiol* 23: S254–S257, 1988

Slutsky RA et al: Effects of transient coronary ischemia and reperfusion on myocardial edema formation and in vitro magnetic relaxation times. *J Am Coll Cardiol* 3: 1454–1460, 1984

Tscholakoff D et al: MRI of reperfused myocardial infarct in dogs. *AJR* 146: 925–930, 1986

Tscholakoff D et al: Early-phase myocardial infarction: evaluation by MR imaging. *Radiology* 159: 667–672, 1986

Tscholakoff D et al: Occlusive and reperfused myocardial infarcts: effect of GD-DTPA on ECG-gated MR imaging. Radiology 160: 515–519, 1986

Van Rossum AC et al: Value of gadolinium-diethylenetriamine pentaacetic acid dynamics in magnetic resonance imaging of acute myocardial infarction with occluded and reperfused coronary arteries after thrombolysis. *Am J Cardiol* 65: 845–851, 1990

Wesbey G et al: Imaging and characterization of acute myocardial infarction in vivo by gated nuclear magnetic resonance. *Circulation* 69: 125–130, 1984

Williams ES et al: Prolongation of proton spin-lattice relaxation times in regionally ischemic tissue from dog hearts. *J Nucl Med* 21: 449–453, 1980

Wisenberg G et al: Nuclear magnetic resonance and radionuclide angiographic assessment of acute myocardial infarction in a randomized trial of intravenous streptokinase. *Am J Cardiol* 62: 1011–1016, 1988

Wisenberg G et al: Serial nuclear magnetic resonance imaging of acute myocardial infarction with and without reperfusion. *Am Heart J* 115: 510–518, 1988

11. Cardiomyopathies

Been M et al: Nuclear magnetic resonance in hypertrophic cardiomyopathy. *Br Heart J* 54: 48–52, 1985

Casolo GC et al: Detection of apical hypertrophic cardiomyopathy by magnetic resonance imaging. *Am Heart J* 117: 468–472, 1989

Higgins CB et al: Magnetic resonance imaging in hypertrophic cardiomyopathy. *Am J Cardiol* 55: 1121–1126, 1985

Bibliography

Mochizuki S et al: Clinical application of NMR-CT for idiopathic cardiomyopathy. *Heart Vessels* 1: 54–57, 1985

Nishimura T et al: Magnetic resonance imaging in familial hypertrophic cardiomyopathy associated with abnormal thallium perfusion and cardiac enzymes. *Jpn Circ J* 52: 395–400, 1988

Sechtem U et al: Magnetic resonance imaging of restrictive cardiomyopathy. *Am J Cardiol* 59: 480–482, 1987

12. Contrast agents

Boudreau RJ et al: The preliminary evaluation of Mn-DTPA as a potential contrast agent for nuclear magnetic resonance imaging. *Am J Physiol Imaging* 1: 19–25, 1986

Brasch RC et al: Contrast-enhanced NMR imaging: animal studies using gadolinium-DTPA complex. *AJR* 142: 625–630, 1984

Brown JJ et al: Myocardial paramagnetic contrast agents for MR imaging. *AJR* 151: 865–871, 1988

Caillé JM et al: Gadolinium as a contrast agent for NMR. *AJNR* 4: 1041–1042, 1983

Carr DH et al: Gadolinium-DTPA as a contrast agent in MRI: initial clinical experience in 20 patients. *AJR* 143: 215–224, 1984

Carr DH: Paramagnetic contrast media for magnetic resonance imaging of the mediastinum and lungs. *J Thorac Imaging* 1: 74–78, 1985

Desreux JF et al: Highly stable lanthanide macrocyclic complexes: in search of new contrast agents for NMR imaging. *Int J Rad Appl Instrum* 15: 9–15, 1988

Gibby WA: MR contrasts agents: an overview. *Radiol Clin North Am* 26: 1047–1058, 1988

Helpern JA et al: The development of a pH-sensitive contrast agent for NMR 1H imaging. *Magn Reson Med* 5: 302–305, 1987

Hopkins AL et al: Oxygen-17 contrast agents. Fast imaging techniques. *Invest Radiol* 23: S240–S242, 1988

Paramagnetic metal complexes as MRI contrast agents. *Int J Rad Appl Instrum* 15: 1–49, 1988

Johnston DL et al: Use of gadolinium-DTPA as a myocardial perfusion agent: potential applications and limitations for magnetic resonance imaging. *J Nucl Med* 28: 871–877, 1987

Keana JF et al: Nitroxides as potential contrast enhancing agents for MRI application: influence of structure on the rate of reduction by rat hepatocytes, whole liver homogenate, subcellular fractions, and ascorbate. *Magn Reson Med* 5: 525–536, 1987

Mendonnça-Dias MH et al: Paramagnetic contrast agents in nuclear magnetic resonance medical imaging. *Semin Nucl Med* 13: 364–376, 1983

Meyer D et al: Gd-DOTA, a potential MRI contrast agent. Current status of physicochemical knowledge. *Invest radiol* 23: S232–S235, 1988

Ogan MD et al: Albumin labeled with Gd-DTPA. An intravascular contrast-enhancing agent for magnetic resonance blood pool imaging: preparation and characterization. *Invest Radiol* 22: 665–671, 1987

Roux E et al: Contrast agents in magnetic resonance imaging. *J Belge Radiol* 71: 31–36, 1988

Runge VM et al: Paramagnetic agents for contrast-enhanced NMR imaging: a review. *AJR* 14: 1209–1215, 1983

Runge VM: Gd-DTPA: an i.v. contrast agent for clinical MRI. *Int J Rad Appl Instrum* 15: 37–44, 1988

Runge VM et al: Gd DTPA. Future applications with advanced imaging techniques. *Radiographics* 8: 161–179, 1988

Runge BM et al: Contrast enhancement of magnetic resonance images by chromium EDTA: an experimental study. *Radiology* 152: 123–126, 1984

Swartz HM et al: Hypoxia-sensitive NMR contrast agents. *Magn Reson Med* 3: 9–174, 1986

Weinmann HJ et al: Characteristics of gadolinium-DTPA complex: a potential NMR contrast agent. *AJR*: 142: 619–624, 1984

Wesbey GE et al: Intravascular contrast agents suitable for magnetic resonance imaging. *Radiology* 153: 171–176, 1984

Wesbey GE et al: Effect of gadolinium-DTPA on the magnetic relaxation times of normal and infracted myocardium. *Radiology* 153: 165–169, 1984

Wolf GL: NMR contrast agents for proton imaging. *Int J Rad Appl Instrum* 15: 1, 1988

13. Various heart diseases

Been M et al: Myocardial involvement in systemic lupus erythematosus detected by magnetic resonance imaging. *Eur Heart J* 9: 1250–1256, 1988

Boxer RA et al: Cardiac MR imaging in Pompe disease. *J Comput Assist Tomogr* 10: 857–859, 1986

Chandraratna PA et al: Detection of acute myocarditis using nuclear magnetic resonance imaging. *Am J Med* 83: 1144–1146, 1987

Desnos M et al: Polyvisceral echinococcosis with cardiac involvement imaged by two-dimensional echocardiography, computed tomography and nuclear magnetic resonance imaging. *Am J Cardiol* 59: 383–384, 1987

Johnston DL et al: Assessment of tissue iron overload by nuclear magnetic resonance imaging. *Am J Med* 87: 40–47, 1989

Lie JT: Detection of acute myocarditis using nuclear magnetic resonance imaging. *Am J Med* 85: 282–283, 1988

Matsui S et al: Myocardial tissue characterization by magnetic resonance imaging in Fabry's disease. *Am Heart J* 117: 472–474, 1989

Otto R et al: MR and CT findings in infected ventricular aneurysm repair. *J Comput Assist Tomogr* 11: 1069–1070, 1987

Thompson RC et al: Adriamycin cardiotoxicity and proton nuclear magnetic resonance relaxation properties. *Am Heart J* 113: 1444–1449, 1987

von Kemp K et al: Echocardiography and magnetic resonance imaging in cardiac amyloidosis. *Acta Cardiol* 44: 29–36, 1989

Wolf JE: Parietal lesions in arrhythmogenic right ventricular dysplasia disclosed by MRI. *Arch Mal Coeur* 82: 1711–1717, 1989

14. Cardiac and paracardiac masses

Amparo EG et al: Gated MRI of cardiac and paracardiac masses: initial experience. *AJR* 143: 1151–1156, 1984

Applegate PM et al: Two-dimensional echocardiographic and magnetic resonance imaging observations in massive lipomatous hypertrophy of the atrial septum. *Am J Cardiol* 59: 849–491, 1987

Barakos JA et al: MR imaging of secondary cardiac and paracardiac lesions. *AJR* 153: 47–50, 1989

Boxer RA et al: Diagnosis of cardiac tumors in infants by magnetic resonance imaging. *Am J Cardiol* 56: 831–832, 1985

Brown JJ et al: Magnetic resonance imaging of cardiac and paracardiac masses. *J Thorac Imaging* 4: 58–64, 1989

Camesas AM et al: Complementary use of two-dimensional echocardiography and magnetic resonance imaging in the diagnosis of ventricular myxoma. *Am Heart J* 114: 440–442, 1987

Casolo F et al: MRI as an adjunct to echocardiography for the diagnostic imaging of cardiac masses. *Eur J Radiol* 8: 226–230, 1988

Conces DJ Jr et al: Gated MR imaging of left atrial myxomas. *Radiology* 156: 445–447, 1985

Dichek DA et al: Angiosarcoma of the heart: three-year survival and folluw-up by nuclear magnetic resonance imaging. *Am Heart J* 115: 1323–1324, 1988

Dooms GC et al: MR imaging of cardiac thrombi. *J Comput Assist Tomogr* 10: 415–420, 1986

Fisher MS et al: Lipomatous hypertrophy of the interatrial septum. Diagnosis by magnetic resonance imaging. *J Comput Assist Tomogr* 12: 267–269, 1988

Freedberg RS et al: The contribution of magnetic resonance imaging to the evaluation of intracardiac tumors diagnosed by echocardiography. *Circulation* 77: 96–103, 1988

Gindea AJ et al: Biventricular cavity obliteration by metastatic malignant melanoma: role of magnetic resonance imaging in the diagnosis. *Am Heart J* 114: 249–253, 1987

Go RT et al: Comparison of gated cardiac MRI and 2D echocardiography of intracardiac neoplams. *AJR* 145: 21–25, 1985

Gomes AS et al: Cardiac tumors and thrombus: evaluation with MR imaging. *AJR* 149: 895–899, 1987

Johnson DE et al: Comparisons of gated cardiac magnetic resonance imaging and two-dimensional echocardiography for the evaluation of right ventricular thrombi: a case report with autopsy correlation. *Cathet Cardiovasc Diagn* 14: 266–268, 1988

Kaplan KR et al: MR diagnosis of lipomatous infiltration of the interatrial septum. *AJR* 153: 495–496, 1989

Lee R Et al: MR imaging of cardiac metastases from malignant fibrous histiocytoma. *J Comput Assist Tomogr* 13: 126–128, 1989

Levine RA et al: Noninvasive tissue characterization: diagnosis of lipomatous hypertrophy of the atrial septum by nuclear magnetic resonance imaging. *J Am Coll Cardiol* 7: 688–692, 1986

Lund JT et al: Cardiac masses: assessment by MR imaging. *AJR* 152: 469–473, 1989

Magherini A et al: Magnetic resonance and echocardiography in the investigation of cardiac tumour in an infant. *Int J Cardiol* 18: 263–266, 1988

Newell JD 2d et al: MR appearance of an arteriovenous hemangioma of the interventricular septum. *Cardiovasc Intervent Radiol* 11: 319–321, 1988

Pizzarello RA et al: Tumor of the heart diagnosed by magnetic resonance imaging. *J Am Coll Cardiol* 5: 989–991, 1985

de Roos A et al: Calcified right atrial myxoma demonstrated by magnetic resonance imaging. *Chest* 95: 478–479, 1989

Scholz TD et al: Noninvasive diagnosis of recurrent familial left atrial myxoma: observations with echocardiography, ultrafast computed tomography, nuclear magnetic resonance imaging and in vitro relaxometry. *Am J Card Imaging* 3: 142–145, 1989

Sechtem U et al: Diagnosis of left ventricular thrombi by magnetic resonance imaging and comparison with angiocardiography, computed tomography and echocardiography. *Am J Cardiol* 64: 1195–1199, 1989

Watanabe AT et al: Magnetic resonance imaging of cardiac sarcomas. *J Thorac Imaging* 4: 90–92, 1989

Winkler M et al: Suspected intracardiac masses: evaluation with MR imaging. *Radiology* 165: 117–122, 1987

Yasutake M et al: Metastatic cholangiocarcinoma to the right atrial appendage detected by magnetic resonance imaging. *Am Heart J* 116: 566–568, 1988

Zeitler E et al: Magnetic resonance imaging of clots in the heart and vascular system. *Ann Radiol* 28: 105–108, 1985

15. Pericardium

Fisher MR et al: MR imaging of an intrapericardial pheochromocytoma. *J Comput Assist Tomogr* 9: 1103–1105, 1985

Gössinger HD et al: Magnetic resonance imaging findings in a patient with pericardial mesothelioma. *Am Heart J* 115: 1321–1322, 1988

Bibliography

Guttierez FR et al: Diagnosis of congenital absence of left pericardium by MR imaging. *J Comput Assist Tomogr* 9: 551–553, 1985

Im JG et al: MR imaging of the transverse sinus of the pericardium. *AJR* 150: 79–84, 1988

McMurdo KK et al: Magnetic resonance imaging of the superior pericardial recesses. *AJR* 145: 985–988, 1985

Mulvagh SZ et al: Usefulness of nuclear magnetic resonance imaging for evaluation of pericardial effusion, and comparison with two-dimensional echocardiography. *Am J Cardiol* 64: 1002–1003, 1989

Olson MC: CT and MRI of the pericardium. *Radiographics* 9: 633–649, 1989

Rienmüller R et al: Pericardial and congestive heart failure diagnostic with CT- and MR-imaging. *Ann Radiol* 29: 95–100, 1986

Rothschild PA et al: MR diagnosis of herniation of the left ventricle through a pericardial window. *Comput Radiol* 11: 15–20, 1987

Schiavone WA et al: Congenital absence of the left portion of parietal peridcardium demonstrated by nuclear magnetic resonance imaging. *Am J Cardiol* 55: 1439–1440, 1985

Sechtem U et al: MRI of the normal pericardium. *AJR* 147: 239–244, 1986

Sechtem U et al: MRI of the abnormal pericardium. *AJR* 147: 245–252, 1986

Soulen RL et al: Magnetic resonance imaging of constrictive pericardial disease. *Am J Cardiol* 55: 480–484, 1985

Stark DD et al: Magnetic resonance imaging of the pericardium: normal and pathologic findings. *Radiology* 150: 469–474, 1984

Tscholakoff D et al: Evaluation of pleural and pericardial effusions by magnetic resonance imaging. *Eur J Radiol* 7: 169–174, 1987

Vogel HJ et al: Mesothelioma of the pericardium: CT and MR findings. *J Comput Assist Tomogr* 13: 543–544, 1989

16. Thoracic great vessels

Akins EW et al: Preoperative evaluation of the thoracic aorta using MRI and angiography. *Ann Thorac Surg* 44: 499–507, 1987

Akins EW et al: Evaluation of an aortic annular pseudoaneurysm by MRI: comparison with echocardiography, angiography and surgery. *Cardiovasc Intervent Radiol* 10: 188–193, 1987

Akins EW et al: MR imaging of blood pool signal variation with cardiac phase in aortic dissection. *J Comput Assist Tomogr* 11: 543–545, 1987

Amparo EG et al: Magnetic resonance imaging of aortic disease: preliminary results. *AJR* 143: 1203–1209, 1984

Auffermann W et al: MR imaging of complications of aortic surgery. *J Comput Assist Tomogr* 11: 982–989, 1987

Barentsz JO et al: Magnetic resonance imaging of the dissected thoracic aorta. *Br J Radiol* 60: 499–502, 1987

Bouchard A et al: Magnetic resonance imaging in pulmonary arterial hypertension. *Am J Cardiol* 56: 938–942, 1985

Boxer RA et al: Evaluation of the aorta in the Marfan syndrome by magnetic resonance imaging. *Am Heart J* 111: 1001–1002, 1986

Campbell RM et al: Detection of caval obstruction by magnetic resonance imaging after intraatrial repair of transposition of the great arteries. *Am J Cardiol* 60: 688–691, 1987

Casolo GC et al: Magnetic resonance imaging of blood flow in thoracic vessels of patients with impaired left ventricular function. *Chest* 92: 645–650, 1987

Conces DJ Jr et al: Nonangiographic imaging of blood flow in thoracic vessels of patients with impaired left ventricular function. *Chest* 92: 645–650, 1987

de Brux JL et al: Anatomy of the thoracic aorta: magnetic resonance imaging and interpretation of flow phenomena. *Surg Radiol Anat* 9: 141–149, 1987

Dinsmore RE et al: Magnetic resonance imaging of thoracic aortic aneurysms: comparison with other imaging methods. *AJR* 146: 309–314, 1986

Dinsmore RE et al: MRI of dissection of the aorta: recognition of the intimal tear and differential flow velocities. *AJR* 146: 1286–1288, 1986

Dooms GC et al: The potential of magnetic resonance imaging for the evaluation of thoracic arterial diseases. *J Thorac Cardiovasc Surg* 92: 1088–1095, 1986

Friedman MJ et al: Bilateral pulmonary artery stenosis associated with pericarditis. Results of surgery and follow-up by magnetic resonance imaging. *Chest* 883–885, 1988

Fruehwald FX et al: Cine-MR in dissection of the thoracic aorta. *Eur J Radiol* 9: 37–41, 1989

Geisinger MA et al: Thoracic aortic dissections: magnetic resonance imaging. *Radiology* 155: 407–412, 1985

Grenier P et al: Magnetic resonance imaging of aneurysms and chronic dissections of the thoracic aorta. *Ann Vasc Surg* 1: 534–541, 1987

Glazer HS et al: The thoracic aorta studied by MR imaging. *Radiology* 157: 149–155, 1985

Goldman AP et al: The complementary role of magnetic resonance imaging. Doppler echocardiography, and computed tomography in the diagnosis of dissecting thoracic aneurysms. *Am Heart J* 111: 970–981, 1986

Hatabu et al: Pulmonary vasculature: high-resolution MR imaging. Work in progress. *Radiology* 171: 391–395, 1989

Hill JA et al: Ascending aortic dissection: detection by MRI. *Am Heart J* 110: 894–896, 1985

Jeang MK et al: Multiple pulmonary artery aneurysms. New use for magnetic resonance imaging. *Am J Med* 81: 1001–1004, 1986

Jeang MK et al: Aortic root abscess. Initial experience using magnetic resonance imaging. *Chest* 89: 613–615, 1986

Julsrud PR et al: Magnetic resonance imaging of vascular rings. *Mayo Clin Proc* 61: 181–185, 1986
Kersting-Sommerhoff BA et al: MR imaging of the thoracic aorta in Marfan patients, *J Comput Assist Tomogr* 11: 633–639, 1987
Kersting-Sommerhoff BA et al: Aortic dissection: sensitivity and specificity of MR imaging. *Radiology* 166: 651–655, 1988
Lallemand D et al: Magnetic resonance (MR) imaging of aorta and pulmonary circulation. Initial experience with ECG-gating. *Ann Radiol* 28: 289–298, 1985
Lallemand D et al: Cardiosynchronous MRI intensity changes of the great vessels and pulmonary circulation. A preliminary report. *Ann Radiol* 28: 299–307, 1985
LePage JR Et al: Pseudocoarctation of the aorta. *Magn Reson Imaging* 6: 65–68, 1988
Lois JF et al: Magnetic resonance imaging of the thoracic aorta. *Am J Cardiol* 60: 358–362, 1987
Lupetin AR et al: Leiomyosarcoma of the superior vena cava: diagnosis by cardiac gated MR. *Cardiovasc Intervent Radiol* 9: 103–105, 1986
Mazer MJ et al: Practical aspects of gated magnetic resonance imaging of the pulmonary artery. *J Thorac Imaging* 3: 73–84, 1988
Malmgren N et al: Pulmonary artery sling. Diagnosis by magnetic resonance imaging. *Acta Radiol* 29: 7–9, 1988
Medrea M et al: MRI visualization of the aortic nipple. *Cardiovasc Intervent Radiol* 11: 29–31, 1988
Moore EH et al: MRI of chronic posttraumatic false aneurysms of the thoracic aorta. *AJR* 143: 1195–1196, 1984
Pan X et al: Identification of aortic thrombus by magnetic resonance imaging. *J Vasc Surg* 9: 801–805, 1989
Pernes JM et al: MR evaluation of chronic aortic dissection. *J Comput Assist Tomogr* 11: 975–981, 1987
Pucillo AL et al: Magnetic resonance imaging of vascular conduits in coarctation of the aorta. *Am Heart J* 117: 482–485, 1989
Rehr RB et al: magnetic resonance imaging in aortic valve, ascending aortic and isthmic aortic disease. *Am J Cardiol* 55: 1243–1244, 1985
Schaefer S et al: Nuclear magnetic resonance imaging in Marfan's syndrome. *J Am Coll Cardiol* 9: 70–74, 1987
Seed WA: Blood flow patterns in the human aorta studied by magnetic resonance. *Br Heart J* 60: 175–176, 1988
Soulen RL et al: Marfan syndrome: evaluation with MR imaging versus CT. *Radiology* 165: 697–701, 1987
Spielmann RP et al: Magnetic resonance imaging of ruptured aneurysm of the ascending aorta. *Br J Radiol* 62: 373–375, 1989
White RD et al: MR imaging of the aorta after surgery for aortic dissection. *AJR* 150: 87–92, 1988
White RD et al: Advance in imaging thoracic aortic disease. *Invest Radiol* 21: 761–778, 1986
White RD et al: Magnetic resonance imaging of thoracic vascular disease. *J Thorac Imaging* 4: 34–50, 1989
Yamada T et al: Aortic dissection without intimal rupture: diagnosis with MR imaging and CT, *Radiology* 168; 347–352, 1988
Zeitler E et al: Magnetic resonance imaging of aneurysms and thrombi. *Cardiovasc Intervent Radiol* 8: 321–328, 1986

17. Coronary arteries and grafts

Aurigemma G et al: Noninvasive determination of coronary bypass graft patency by cine magnetic resonance imaging. *Circulation* 80: 1595–1602, 1989
Cassidy MM et al: Assessment of coronary artery imaging by gated magnetic resonance. An evaluation of the utility and potential of the currently available imaging method. *Am J Card Imaging* 3: 100–107, 1989
Douard H et al: Magnetic resonance imaging of an anomalous origin of the left coronary artery from the pulmonary artery. *Eur Heart J* 9: 1356–1360, 1988
Frija G et al: A study of coronary artery bypass graft patency using MR imaging. *J Comput Assist Tomogr* 13: 226–232, 1989
Goldfarb A et al: Massive aneurysmal dilatation of saphenous vein grafts used for systemic-pulmonary artery shunts: a role for magnetic resonance imaging in diagnosis. *Am Heart J* 116: 870–873, 1988
Gomes AS et al: Coronary artery bypass grafts: visualization with MR imaging. *Radiology* 162: 175–179, 1987
Jenkins JP et al: Detection of coronary artery bypass graft patency as assessed by magnetic resonance imaging. *Br J Radiol* 61: 2–4, 1988
Nawa S et al: Magnetic resonance evaluation of patency of stented polytetrafluoroethylene graft connecting right atrium to pulmonary artery. *Chest* 94: 1105–1107, 1988
Paulin s et al: MR imaging of the aortic root and proximal coronary arteries. *AJR* 148: 665–670, 1987
Rubinstein RI et al: Magnetic resonance imaging to evaluate patency of aortocoronary bypass grafts. *Circulation* 76: 786–791, 1987
Stehling M et al: Real-time NMR imaging of coronary vessels. *Lancet* 1987 2: 964–965
Strasser SF et al: Mycotic right coronary artery aneurysm: CT and MR diagnosis. *J Comput Assist Tomogr* 10: 667–669, 1986
Wertheimer JH et al: Magnetic resonance imaging and two-dimensional and Doppler echocardiography in the diagnosis of coronary cameral fistula. *Am Heart J* 114: 159–162, 1987
White RD et al: Coronary artery bypass graft patency: noninvasive evaluation with MR imaging. *Radiology* 164: 681–686, 1987
White RD et al: Coronary artery bypass grafts: evaluation of patency with cine MR imaging. *Am J Cardiol* 150: 1271–1274, 1988

Bibliography

18. Cardiac transplantation

Aherne T et al: Magnetic resonance imaging of cardiac transplants: the evaluation of rejection of cardiac allografts with and without immunosuppression. *Circulation* 74: 145–156, 1986

Aherne T et al: Diagnosis of acute and chronic cardiac rejection by magnetic resonance imaging: a non-invasive *invivo* study. *J Cardiovasc Surg* 29: 587–590, 1988

Huber DJ et al: The detection of cardiac allograft rejection by alterations in proton NMR relaxation time. *Invest Radiol* 20: 796–802, 1985

Konstam MA et al: Magnetic resonance imaging with gadolinium-DTPA for detecting cardiac transplant rejection in rats. *Circulation* 78: 87–94, 1988

Nishimura T et al: Cardiac transplantation in dogs: evaluation with gated MRI and Gd-DTPA contrast enhancement. *Heart Vessels* 3: 141–145, 1987

Nishimura T et al: Identification of cardiac rejection with magnetic resonance imaging in heterotopic heart transplantation model. *Heart Vessels* 3: 135–140, 1987

Revel D et al: Magnetic resonance imaging of human orthotopic heart transplantation: correlation with endomyocardial biopsy. *J Heart Transplant* 8: 139–146, 1989

Sasaguri S et al: Early detection of cardiac allograft rejection with proton nuclear magnetic resonance. *Circulation* 72: 231–236, 1985

Tscholakoff D et al: Cardiac transplantations in dogs: evalutation with MR. *Radiology* 157: 697–702, 1985

Wisenberg G et al: Diagnostic applicability of magnetic resonance imaging in assessing human cardiac allograft rejection. *Am J Cardiol* 60: 130–136, 1987

Anatomical index

Anatomical index

SERIES IN RADIOLOGY

1. J.O. Op den Orth: *The Standard Biphasic-contrast Examination of the Stomach and Duodenum.* Method, Results, and Radiological Atlas. 1979 ISBN 90-247-2159-8
2. J.L. Sellink and R.E. Miller: *Radiology of the Small Bowel.* Modern Enteroclysis Technique and Atlas. 1982 ISBN 90-247-2460-0
3. R.E. Miller and J. Skucas: *The Radiological Examination of the Colon.* Practical Diagnosis. 1983 ISBN 90-247-2666-2
4. S. Forgács: *Bones and Joints in Diabetes Mellitus.* 1982 ISBN 90-247-2395-7
5. Gy. Németh and H. Kuttig (eds.): *Isodose Atlas for Use in Radiotherapy.* 1981 ISBN 90-247-2476-7
6. J. Chermet: *Atlas of Phlebography of the Lower Limbs.* Including the Iliac Veins. 1982 ISBN 90-247-2525-9
7. B.K. Janevski: *Angiography of the Upper Extremity.* 1982 ISBN 90-247-2684-0
8. M.A.M. Feldberg: *Computed Tomography of the Retroperitoneum.* An Anatomical and Pathological Atlas with Emphasis on the Fascial Planes. 1983 ISBN 0-89838-573-3
9. L.E.H. Lampmann, S.A. Duursma and J.H.J. Ruys: *CT Densitometry in Osteoporosis.* The Impact on Management of the Patient. 1984 ISBN 0-89838-633-0
10. J.J. Broerse and T.J. Macvittie: *Response of Different Species to Total Body Irradiation.* 1984 ISBN 0-89838-678-0
11. C. L'Herminé: *Radiology of Liver Circulation.* 1985 ISBN 0-89838-715-9
12. G. Maatman: *High-resolution Computed Tomography of the Paranasal Sinuses, Pharynx and Related Regions.* Impact of CT Identification on Diagnosis and Patient Management. 1986 ISBN 0-89838-802-3
13. C. Plets, A.L. Baert, G.L. Nijs and G. Wilms: *Computer Tomographic Imaging and Anatomic Correlation of the Human Brain.* A Comparative Atlas of Thin CT-scan Sections and Correlated Neuro-anatomic Preparations. 1987 ISBN 0-89838-811-2
14. J. Valk: *MRI of the Brain, Head, Neck and Spine.* A Teaching Atlas of Clinical Applications. 1987 ISBN 0-89838-957-7
15. J.L. Sellink: *X-Ray Differential Diagnosis in Small Bowel Disease.* A Practical Approach. 1988 ISBN 0-89838-351-X
16. Th.H.M. Falke (ed.): *Essentials of Clinical MRI.* 1988 ISBN 0-89838-353-6
17. B.D. Fornage: *Endosonography.* 1989 ISBN 0-7923-0047-5
18. R. Chisin (ed.): *MRI/CT and Pathology in Head and Neck Tumors.* A Correlative Study. 1989 ISBN 0-7923-0227-3
19. G. Gozzetti, A. Mazziotti, L. Bolondi and L. Barbara (eds.): *Intraoperative Ultrasonography in Hepato-biliary and Pancreatic Surgery.* A Practical Guide. With Contributions by Y. Chapuis, J.-F. Gigot and P.-J. Kestens. 1989 ISBN 0-7923-0261-3
20. A.M.A. De Schepper and H.R.M. Degryse: *Magnetic Resonance Imaging of Bone and Soft Tissue Tumors and Their Mimics.* A Clinical Atlas. With Contributions by F. De Belder, L. van den Houwe, F. Ramon, P. Parizel and N. Buyssens. 1989 ISBN 0-7923-0343-1
21. J.O. Barentsz, F.M.J. Debruyne and S.H.J. Ruijs: *Magnetic Resonance Imaging of Carcinoma of the Urinary Bladder.* With a Forword by H. Hricak and R. Hohenfellner. 1990 ISBN 0-7923-0838-7
22. C. Depré, J.A. Melin, W. Wijns, R. Demeure, F. Hammer and J. Pringot: *Atlas of Cardiac MR Imaging with Anatomical Correlations.* Foreword by Alexander R. Margulis. 1991 ISBN 0-7923-0941-3